LIFT AND DRAG FORCES ON A SUBMARINE PIPELINE IN STEADY FLOW

by

N.J. KOK

A thesis submitted for the degree of Doctor of Philosophy
in the Faculty of Engineering, University of Cape Town

February 1988

Department of Civil Engineering
University of Cape Town

The University of Cape Town has been given the right to reproduce this thesis in whole or in part. Copyright is held by the author.

The copyright of this thesis vests in the author. No quotation from it or information derived from it is to be published without full acknowledgement of the source. The thesis is to be used for private study or non-commercial research purposes only.

Published by the University of Cape Town (UCT) in terms of the non-exclusive license granted to UCT by the author.

University of Cape Town

To my wife, Jacqueline
and my two sons

DECLARATION

I, Nicolaas Johannes Kok, hereby declare that this thesis is my own work and that it has not been submitted for a degree of another university

February 1988

Signed by candidate

LIFT AND DRAG FORCES ON A SUBMARINE PIPELINE IN STEADY FLOW

Nicolaas J. Kok
11 Sir David Baird Drive
7441 BLOUBERGSTRAND
SOUTH AFRICA

February 1988

ABSTRACT

This thesis describes an experimental investigation into the hydrodynamic forces induced on a cylinder placed transversely to a steady stream. Various cylinder locations near the bed of a water flume were considered. The work relates to pipeline design. The various flow phenomena around a cylinder are theoretically analysed and an explanation of the phenomenon of lift provided.

A thorough literature review was undertaken regarding the classical theory, as well as experimental and theoretical studies carried out on the subject. This revealed that theoretical studies are virtually non-existent.

Measurements have been done in intermediate water depths with both smooth and rough beds. Two different methods, comprising very simple yet novel techniques, were utilised in a water flume 18 m long x 600 mm wide x 450 mm deep. The methods involved a unique pressure determination method as well as the direct measurement of hydrodynamic forces, using a "weighing" method. Very accurate flow velocities were measured using a unique differential manometer.

Experiments were performed in the Reynolds number range 6 000 to 26 000, using 30 and 50 mm diameter cylinders. Comprehensive tests on cylinder roughening were carried out in a flow region which had not been well researched regarding this aspect. Cylinder locations were varied from a gap-to-cylinder diameter ratio of zero to 2,67.

Results revealed that the force coefficients are not appreciably affected by bed roughness. Cylinder roughening produced somewhat contradicting results for the two different cylinders used. The influence on the lift coefficient was inconclusive, but the "rougher" 30 mm cylinder produced a slightly higher drag coefficient.

Although the lift force was predominantly away from the bed, a downward lift force was measured on a few occasions with the cylinder situated further than one cylinder diameter away from the bed. A possible explanation is offered for this and other unexpected results.

Flow visualisation tests were performed to confirm certain features of the flow around the cylinder. These as well as all the other results have been related to published work.

ACKNOWLEDGEMENTS

I am very grateful to my thesis supervisor, Prof. F.A. Kilner, for his guidance and stimulating suggestions. Despite the fact that the project was essentially done during periods of study leave or part-time after hours, over approximately six years, he was always helpful and patient; this has been much appreciated.

The assistance of the workshop staff was also appreciated. In particular I would like to mention Mr. Denis Botha, who did the machining of the various test cylinders and their components, as well as the late Mr. Chris Coetzer for his practical suggestions. I also want to thank the laboratory staff, particularly Mr. Alton Siko, for their assistance.

I also wish to thank undergraduate student Wilfred Manyathi, who helped with certain rough bed test measurements.

Dr. Warren Jones (Shell Development Company, Houston, Texas) had kindly sent me a copy of his Ph.D thesis, as well as copies of the M.Sc and Ph.D theses of Dr. Conrad Smith. His assistance was much appreciated.

Without the three periods of study leave granted to me by my employer, the Cape Technikon, this work would not have been possible. For this concession I am very grateful. I also wish to thank the Rector, Dr. Theo Shippey, for his encouragement.

Many relatives and friends are thanked for their sustained encouragement.

Very special thanks are due to my wife, Jacqueline, and two sons. Their encouragement and selfless support were the main motivating factors in commencing with and completing this work. They created the necessary atmosphere at home to stimulate study and sacrificed many joys of life in the process. Jacqueline's assistance regarding the proof reading of a number of drafts of the thesis has been much appreciated.

Finally, I am grateful to my Heavenly Father for having given me the necessary inspiration and strength to do this study project.

CONTENTS

NOMENCLATURE

a	distance from bed to cylinder centre (mm)
a_1	depth parameter (= (H - D)/H)
a_2	depth parameter (= D/H)
c_1, c_2	centre of vortex
d	subscript, denotes downstream side of separation point inside wake region
f	vortex shedding frequency (s^{-1})
g	gravitational acceleration (m/s^2)
h	height difference of water column in flow velocity recorder; depth of immersion measured at the cylinder centre (mm, cm)
i	imaginary number (= $\sqrt{-1}$)
k	surface roughness height
m	mass readings (gram)
m (θ)	source distribution
p	pressure at a point (N/m^2)
p_o	pressure upstream from the cylinder (N/m^2)
r	radius of the cylinder (mm, cm); polar co-ordinate
s	elevation from bed in shear flow (mm); subscript, denotes upstream side of separation point outside wake region
s_c	distance from bed to stagnating streamline far upstream of cylinder (mm)
s_p	arc length at point p on wake region boundary (Section 9.4.1.2)
u	velocity (m/s); boundary layer displacement effect
u_s	tangential velocity on circle due to source distribution
u_*	friction or shear velocity at the bed (m/s)
v (θ)	normal velocity (see Section 9.4.1)
w	subscript, denotes downstream side of separation point outside wake region
w_ℓ	wake length parameter
x	distance from cylinder centre, in downstream direction (horizontal co-ordinate)
y	elevation above specified point (mm); vertical co-ordinate
y_1	elevation above the bed (mm)
z	complex co-ordinate

A	constant; projected area of a body perpendicular to the flow direction
B	constant
C_p	pressure coefficient
C_{pb}	base pressure coefficient
C_{pm}	minimum pressure coefficient
C_{po}	front centre pressure coefficient
C_{ps}	pressure coefficient at separation point
C_D	drag coefficient
C_D'	measured drag coefficient
C_L	lift coefficient
D	cylinder diameter (mm, cm or m)
F	force (N)
F_r	Froude number (= $U/\sqrt{gh}$)
F_D	drag force per unit length (N/m)
F_{DT}	total drag force (N)
F_L	lift force per unit length (N/m)
G	cylinder-to-bed clearance (mm); velocity due to unit source and unit vortex elements (see Section 9.4.1.2)
H	total pressure head (N/m^2); total water depth (mm, cm)
K	Kármán constant; a constant
K-C	Keulegan-Carpenter period parameter (= U_{max} T/D)
L	cylinder length (mm); significant dimension of the body (mm)
Pstat	static pressure taken at a reference point (N/m^2)
P_θ	pressure at angle θ from front cylinder centre
Q	flow rate of fluid (m^3/s); wake influence function
R_e	Reynolds number based on cylinder diameter (= UD/ν), or on significant body dimension L (= UL/ν)
S	Strouhal number (= fD/U)
T	period of oscillation (s)
U	flow velocity of fluid (m/s); non-dimensional tangential velocity (Section 9.4.1)
U_0	free stream velocity (m/s); far field velocity in shear-free flow (m/s)
U_1	velocity fluctuation (m/s); velocity at elevation y_1 above bed (m/s)
U_{bottom}	velocity at bottom of cylinder (m/s)
U_e	tangential velocity, outside boundary layer region

U_{max}	amplitude of harmonically changing velocity (m/s)
U_s	far field velocity at elevation s from bed in shear flow (m/s)
U_{top}	velocity at top of cylinder (m/s)
$U_{D/2}$	velocity at front cylinder centre (m/s)
V	average velocity from bed to stagnating streamline, distance s_c from bed (m/s)
V_o	velocity of uniform flow field (m/s)
V_{eff}	effective velocity used as reference velocity for calculation of force coefficients (m/s)
δ	viscous boundary layer thickness (mm)
δ^*	boundary layer displacement thickness
$\gamma(\theta)$	vorticity of vortex sheet
μ	dynamic viscosity (N.s/m^2)
ν	kinematic viscosity of the fluid (m^2/s)
ρ	density of fluid (kg/m^3)
θ	angle subtended at cylinder centre, $\theta = \emptyset°$ at front cylinder centre; angle of cylinder to stream velocity; angle measured from rear stagnation point in polar co-ordinates (only used in Section 9.4.1)
θ_{min}	minimum pressure location from front cylinder centre
θ_s	separation angle (Section 9.4)
θ_{sep}	separation angle, measured from front cylinder centre
θ_w	approximate angle to beginning of wake region
τ	shear stress in fluid (N/m^2)
τ_o	shear stress in water, evaluated at the bed (N/m^2)
ϕ	angle of cylinder to approach flow
ω	complex potential

Summary of dimensionless constants used

a_1	depth parameter	$\frac{H-D}{H}$
a_2	depth parameter	$\frac{D}{H}$
k/D	surface roughness ratio	

C_D	drag coefficient	$\frac{F_D}{\frac{1}{2}\rho D V_{eff}^2}$
C_L	lift coefficient	$\frac{F_L}{\frac{1}{2}\rho D V_{eff}^2}$
C_p	pressure coefficient	$\frac{P_\theta - P_{stat}}{\frac{1}{2}\rho V_{eff}^2}$
F_r	Froude number	$\frac{U}{\sqrt{gh}}$
G/D	gap-to-diameter ratio	
G/δ	gap to boundary layer thickness ratio	
K-C	Keulegan-Carpenter period parameter	$\frac{U_{max} T}{D}$
L/D	span-to-diameter ratio	
R_e	Reynolds number based on cylinder diameter	$\frac{V_{eff} D}{\nu}$
S	Strouhal number	$\frac{fD}{U}$

CHAPTER 1 - INTRODUCTION

The effective design of off-shore pipelines, has always been regarded as very important. It is essential that the pipeline designer has a clear understanding of the various factors likely to influence the stability of the structure. Much research has therefore been conducted to determine the hydrodynamic forces exerted on pipelines, as well as on methods to improve the pipeline's stability.

In spite of much capital being spent on research work, the effect of hydrodynamic forces is often not completely appreciated. The result is that pipelines might be underdesigned. Zdravkovich (1985) referred to "1½ miles of a subsea pipeline found floating off the north-east coast of Scotland in 1976". On investigation, it was revealed that the pipeline lost its concrete lining as a result of current-induced forces. Fractured pipelines carrying crude oil, sewerage and other noxious substances could result in a major environmental pollution problem; even a catastrophe. On the other hand, submarine pipelines might be grossly overdesigned. This could result in huge unnecessary expenditure.

A number of experimental studies have been undertaken on the flow past a cylinder placed near a boundary, essentially to determine the hydrodynamic forces induced. However, flow phenomena such as separation and the upward lift force induced on a cylinder situated near a bed in steady and oscillatory flows, have intrigued researchers to this day; some aspects are still not completely understood.

The purpose of this study, was to determine the lift and drag forces exerted on a cylinder at various locations near a boundary, in the turbulent boundary layer of a steady flow, in a subcritical Reynolds number region which had only been researched to a limited degree. Further, the aspect of cylinder roughening required thorough investigation. In the process, various flow phenomena were investigated to obtain a better conception of the various flow

characteristics, to explain how the flow is influenced by boundary proximity.

In formulating the objectives of the present study, much time was devoted to the development of a simple but unique method. The method was required to measure time-averaged pressures and flow velocities, of an order of accuracy, sufficient to explain the motion of fluid particles around and the phenomenon of lift on a submarine pipeline in steady flow conditions. Further, the model had to relate to various field conditions.

Few researchers chose water as the fluid medium; the vast majority performed tests in air. The Reynolds number range of 6 000 to 26 000, in the subcritical flow region chosen for this study, had hardly been investigated. To the author's knowledge, the only other experiments undertaken in the range of Reynolds numbers concerned, were carried out by Fredsoe et al (1985), in the Reynolds number range 20 000 to 30 000, and Roshko et al (1975) at a Reynolds number of 20 000, in water and air respectively. Fredsoe et al's (1985) lift force measurements were performed on smooth cylinders in water. They used a method by which the vertical displacement of a system of springs, from which the cylinder was suspended, was related to the lift force. The method was sensitive to vibrations, and only clearance-to-diameter ratios G/D up to 0,3 were investigated; refer to Section 2.6.2.3 (p.2-40) for further details. In the present study, tests were performed up to G/D ratios of 2,67. Wind tunnel tests are generally regarded as being analogous to water flume experiments. However, it is interesting to note that Beattie et al (1971) showed, that mainly due to variations in free stream turbulence, there are considerable differences when wind tunnel and water flume test results are compared.

The influence of cylinder roughening on the force coefficients of a cylinder located near a boundary, has not been researched thoroughly in the subcritical Reynolds number region. The author believes that the comprehensive tests on cylinder roughening reported in this thesis, make a useful contribution to extend knowledge on the subject field concerned.

To simulate the field conditions, a water flume 18 m long and 600 mm wide, with either a smooth bed or a rough bed was used. The rough bed was composed of 5 mm pebbles closely packed in a single layer on removable mats. The testing area in the flume was chosen a sufficient distance downstream from the inlet end, for a turbulent boundary layer to develop fully along the bed of the flume.

Two smooth aluminium cylinders of 30 mm and 50 mm diameter respectively were chosen to replicate a submarine pipeline. Roughness on the cylinders was achieved by glueing sand grains of uniform size to the cylinders. Due to practical limitations in the laboratory arrangement, maximum flow velocities of only about 0,5 m/sec could be attained. This in turn represents a maximum Reynolds number (based on cylinder diameter) of about 26 000. A free stream velocity of 0,07 m/s was measured in the Severn Estuary (Littlejohns, 1974), which generates a Reynolds number of approximately 27 000 for a 300 mm diameter pipeline. The Reynolds number range used in the experiments performed for this study, is therefore related to real situations in practice. Further, the tests reported in this thesis were carried out in the Reynolds number range 6 000 to 26 000, where the Strouhal number S, which is directly related to the vortex shedding frequency, is independent of the Reynolds number.

A "weighing" method was also developed to measure the time-averaged lift and drag forces directly. This method was essentially used to compare, qualitatively and quantitatively, the generated force coefficients with corresponding values, determined from pressure distributions. A similar and simpler direct force measuring method, has not been encountered before.

A theoretical explanation of the flow mechanism causing the phenomenon of lift, upwards and downwards, is also given in this thesis. It is believed that this explanation could result in a better understanding of the flow features generated, when a cylinder is situated in close proximity of a boundary.

When writing this thesis, the general philosophy was adopted to describe novel or poorly documented concepts in a fair amount of detail; concepts which have been well documented previously, are only broadly outlined. The nomenclature most commonly used was adopted. This has led to some duplication of terms and these cases are clearly noted.

The author believes that the study reported in this thesis, has made a useful contribution to extend the available knowledge on the flow past a cylinder, placed in a steady flow near a boundary.

CHAPTER 2 - LITERATURE REVIEW

2.1 Introduction

A review of published work has been undertaken to present the available experimental and theoretical research on the hydrodynamic forces induced when a cylinder, remote from and near a boundary, is subjected to the steady flow of a fluid.

Numerous studies have examined the flow around a cylinder immersed in a uniform steady transverse flow, particularly the symmetrical flow case. Much research is still currently being undertaken on the topic. The flow around a cylinder is rather complicated and to date not fully understood, both in steady and unsteady flow. The phenomenon of vortex shedding from blunt bodies such as cylinders, "has always been one of the most intriguing problems of fluid dynamics" (Buresti, 1983) and is to date only partly solved by researchers.

The research undertaken on cylinders in steady flow, has developed from investigations in symmetrical flow, remote from a boundary, to those in close proximity of a boundary. In the discussion that follows, the boundary layers along the bed of a flume and along the surface of a cylinder are briefly examined, followed by a summary of some of the research work on hydrodynamic forces in steady flow conditions. Inviscid (non-viscous) and viscous flows are discussed, remote from and near a plane boundary. The discussion below relates to the experimental component of the present study which is described from Chapter 3 to Chapter 8.

2.2 Boundary Layers on a Solid Surface

If the bed of a river or a water flume in a laboratory is considered to be a very smooth flat plate, the flow of fluid

over the plate exhibits interesting properties due to its viscosity.

The viscosity causes the velocity of the fluid to be zero at every point on the surface of the plate. If there is no separation of the flow at the leading edge of the plate, a thin shear layer develops. This thin layer of fluid is called the boundary layer. The boundary layer which forms over the surface of the plate, contains a velocity gradient. The thickness of the boundary layer is denoted by δ ; the velocity of the flow above it is the undisturbed velocity V (see Fig. 2.1) or the free stream velocity.

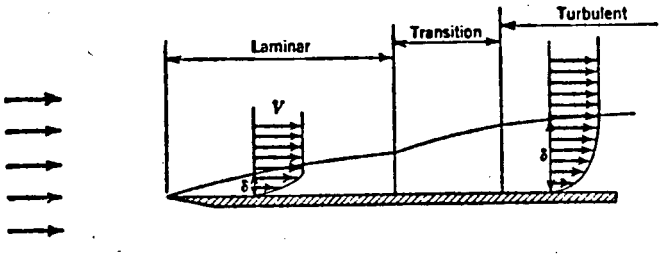

Figure 2.1 : Boundary layers on a flat plate

Viscous action begins at the leading edge of the plate. The layer thus starts from no thickness and increases its thickness in a downstream direction as the increasing viscous action, due to the increasing plate area, extends into the flow. The fluid elements inside the boundary layer decelerate, and in their downstream motion they reduce the velocity of more and more fluid elements and thus extend the boundary layer region by entrainment. This leads to the "growth" of the boundary layer, or increase in boundary layer thickness downstream from the leading edge of the plate.

Where the boundary is thin near the leading edge of the plate, and small quantities of fluid are contained, the boundary layer is laminar. However, as the layer "grows" by becoming thicker and

includes more fluid elements, the flow inside the layer becomes turbulent. When this unstable situation arises, the greater velocity fluctuations of the fluid elements inside the boundary layer region result in more pronounced extension of the boundary layer region.

The change from a laminar to a turbulent boundary layer occurs with an intermediate transition region. In the transition region both viscous and turbulent action are present. Once turbulence effects replace those due to velocity, the boundary layer becomes completely turbulent, with the exception of a thin laminar sub-layer.

2.2.1 Velocity Profiles

In steady flow, the boundary layer on a granular river bed as well as on the bed of the laboratory flume, some distance downstream from its inlet end, is turbulent. Three regions within the turbulent boundary layer can be distinguished (Hinze, 1959, and Schlichting, 1979):

- a thin viscous sub-layer or inner layer
- a buffer zone
- the outer layer

(i) Viscous sub-layer:

A steep velocity gradient exists in this layer. From the relationship between the shear stress and the velocity gradient, the following expression for the velocity profile can be deduced:

$$\frac{U}{u_*} = \frac{u_* y}{\nu} \qquad (2.1)$$

where U = mean water velocity at a height y above the bed,

ν = kinematic viscosity of the water

u_* = friction or shear velocity at the bed

$= \sqrt{\frac{\tau_o}{\rho}}$; τ_o being the shear stress in the water, evaluated at the bed.

(ii) Buffer zone:

In this region, the velocity profiles for smooth and rough walls are respectively given by

$$\frac{U}{u_*} = \frac{1}{K} \ell n \left(\frac{u_* y}{\nu}\right) + A \qquad (2.2)$$

$$\frac{U}{u_*} = \frac{1}{K} \ell n \left(\frac{y}{k}\right) + B \qquad (2.2a)$$

where k = surface roughness height

K = Kármán constant

A and B = constants

(iii)Outer layer:

Jones (1970 and 1971) did a thorough investigation on the turbulent velocity profile in the boundary layer, and suggested the following expression, which was originally proposed by Hama (1954):

$$\frac{U_o - U}{u_*} = 9{,}6 \left(1 - \frac{y}{\delta}\right)^2 \qquad (2.3)$$

where U_o = free stream velocity

According to Jones, Equation (2.3) fits the experimental data of Hama and other investigators very well, for both smooth and rough beds, in the outer region as defined by $\delta > y > 0{,}15\delta$. Further, if the viscous sublayer, of which the thickness is only of the order of $0{,}001\ \delta$ to $0{,}01\ \delta$, is neglected, Equation (2.3) represents the entire boundary layer.

Jones (1971) quotes several investigators who had measured the velocity profile close to a rough bed in a tidal current. They all found their data to fit a logarithmic velocity profile of the form of Equation (2.2a). The same data also fell on the parabolic profile presented by Equation (2.3).

The following relationship is commonly used to approximate the velocity profile in the boundary layer (Hinze,1959):

$$\frac{U}{U_o} = \left(\frac{y}{\delta}\right)^{1/7} \tag{2.4}$$

Equation (2.4) does not give an exact indication of the velocity profile for the 10 % of the boundary layer nearest the bed. For a known velocity value U_1 at a reference height of y_1 from the bed, Equation (2.4) becomes

$$\frac{U_1}{U_o} = \left(\frac{y_1}{\delta}\right)^{1/7} \tag{2.5}$$

The boundary layer thickness δ is eliminated, and an equation relating velocity U at the height y to the known velocity U_1 at the reference height y_1 is established when Equation (2.4) is divided by Equation (2.5):

$$\frac{U}{U_1} = \left(\frac{y}{y_1}\right)^{1/7} \tag{2.6}$$

2.2.2 Pressure Distribution

It is clear that the shear stress τ (= $\mu \frac{dv}{dy}$, where μ is the dynamic viscosity and $\frac{dv}{dy}$ the transverse velocity gradient) is caused by the internal friction of the fluid and acts parallel to

the flow. The influence of the shear stresses perpendicular to the wall (or bed) is therefore small; the acceleration in this direction would then also be small. In addition to shear stress, the only other contributor to acceleration is a longitudinal pressure gradient. It is evident that the pressure gradient perpendicular to the wall, $\partial p / \partial y$ would be small and Goldstein (1950, p118) shows that it is proportional to δ . Further, the pressure distribution across the boundary layer is very nearly constant, and almost equal to its value just above the region.

If the wall is curved, similar results are found. However, a pressure gradient perpendicular to the wall, is required in the decelerated layer to balance the centrifugal force. This means that the pressure is not as constant as the case for a straight wall. Although the pressure gradient at right angles to the wall is larger, it is still small because the total change of pressure takes place over a distance of order δ. Therefore the pressure may still be regarded as being approximately constant over any section of the boundary layer, if the wall is curved.

The situation above can obviously only occur in a laminar boundary layer, i.e. the mentioned very thin inner layer or sub-layer of almost negligible thickness where the viscous effects dominate (Rouse, 1946).

2.3 Symmetrical Flow past a Circular Cylinder in Steady Flow

2.3.1 The Mechanism of Separation

Consider the flow of a fluid along a boundary which curves in such a way as to produce a general increase in velocity, shown by the convergence of the streamlines, and a corresponding decrease in pressure. In this case the previously mentioned tendency of the boundary layer thickness to increase with distance in the flow direction, is restricted by the convergence of the streamlines as well as by the acceleration of the flow in general.

well as upon the Reynolds number R_e of the flow ($R_e = UD/\nu$, where U = flow velocity and D = diameter of the cylinder, for symmetrical flow past a cylinder). The separation point will only remain fixed in position if the boundary is angular in form or has sharp edges. When the boundary has an easy curvature, such as a cylinder, the separation zone will move upstream as the Reynolds number is increased. It suddenly shifts downstream when the boundary layer becomes turbulent; the lateral mixing of the turbulent fluid results in a more uniform velocity distribution which reduces the tendency towards separation. Roughening of the boundary leads to an early commencement of turbulence and therefore separation occurs further downstream.

2.3.2 Drag Force

Due to the existence of the wake, the flow field behind the cylinder changes radically in comparison to non-viscous flow. Separation of the main flow takes place from either side of the cylinder's surface. The flow does not meet directly behind the cylinder, but leaves a region of discontinuity or a "dead zone".

In this zone, the pressure is almost constant on the boundary and very close to its value at the point of separation S. The pressure is always less than that at the foremost point at the front of the cylinder, the front stagnation point.

A large net force will thus act on the cylinder in the downstream direction, due to the pressure differences along its boundary. This force is called "form drag" or "pressure drag".

Form drag is strongly linked with the phenomenon of separation. The subsequent generation of eddies increases the energy loss of the flow. Separation therefore leads to an increase in resistance to motion as well as the rate of energy dissipation due to turbulence and viscous shear. It is clear that a large wake will result in a larger form drag.

where $R_e = \frac{UD}{\nu}$ (for a cylinder)

The drag coefficient can therefore be expressed in terms of the drag force per unit length, F_D, and $\frac{1}{2}\rho U^2$, the pressure at the front stagnation point. Although not indicated here, the drag coefficient is also dependent on other factors such as roughness, vibration, turbulence and proximity of other bodies or boundaries.

2.3.3 Relationship between Drag Coefficient and Reynolds Number

It is reported by Schlichting (1979) and Roshko (1961) that already in 1921 Wieselsberger measured the drag coefficient of circular cylinders immersed in symmetrical steady (air) flow. Wieselsberger used circular cylinders of diameters varying from 0,05 to 300 mm; the generated values fall on a single curve. Fig. 2.3 shows the very familiar relationship between C_D and R_e.

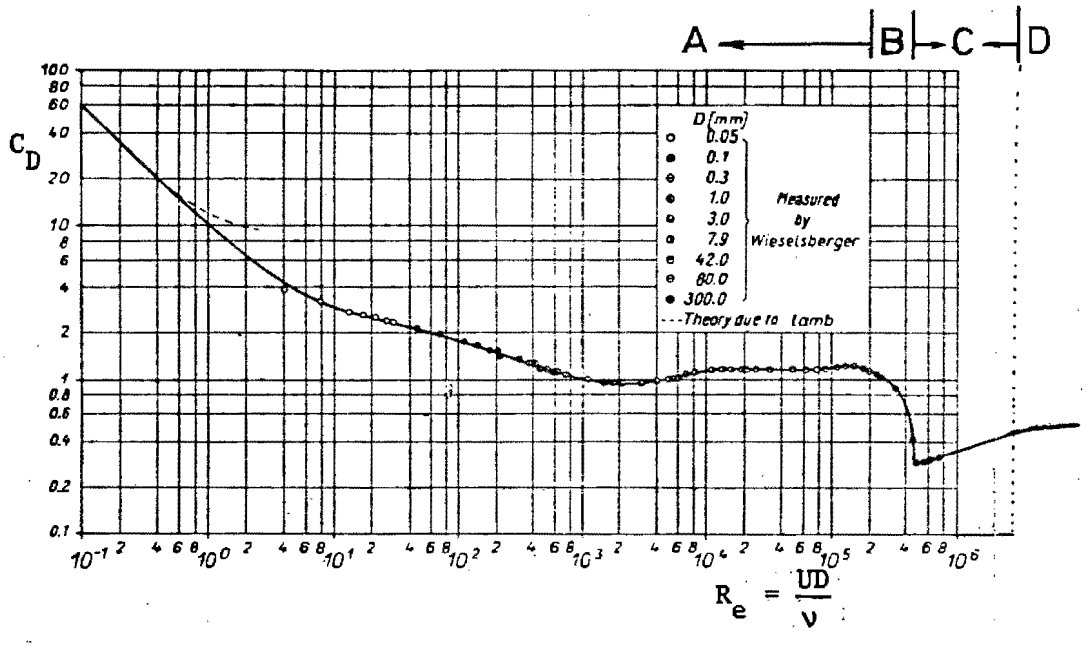

Figure 2.3 : Drag coefficient versus Reynolds number for a smooth circular cylinder in steady flow (from Schlichting (1979), p. 17). The plot is also true for a negligible degree of turbulence intensity.

Some of the characteristics of the drag coefficient curve (Fig. 2.3) are explained in various texts (e.g. Le Mehaute, 1976, and Vennard and Street, 1976). At very low Reynolds numbers, up to approximately Ø,1 (according to Vennard and Street), all the drag is due to viscous effects and no separation of the flow occurs. With a faster flow, separation takes place at a Reynolds number of about 1Ø and a fully developed wake is noticed at a Reynolds number of approximately 1 ØØØ. The total drag now consists of both friction drag and form drag, but the friction drag is estimated at only approximately 5 % of the total drag.

Homann (from Schlichting, 1979) took photographs of the streamlines about circular cylinders in oil in 1936. These are reproduced in Fig. 2.4.

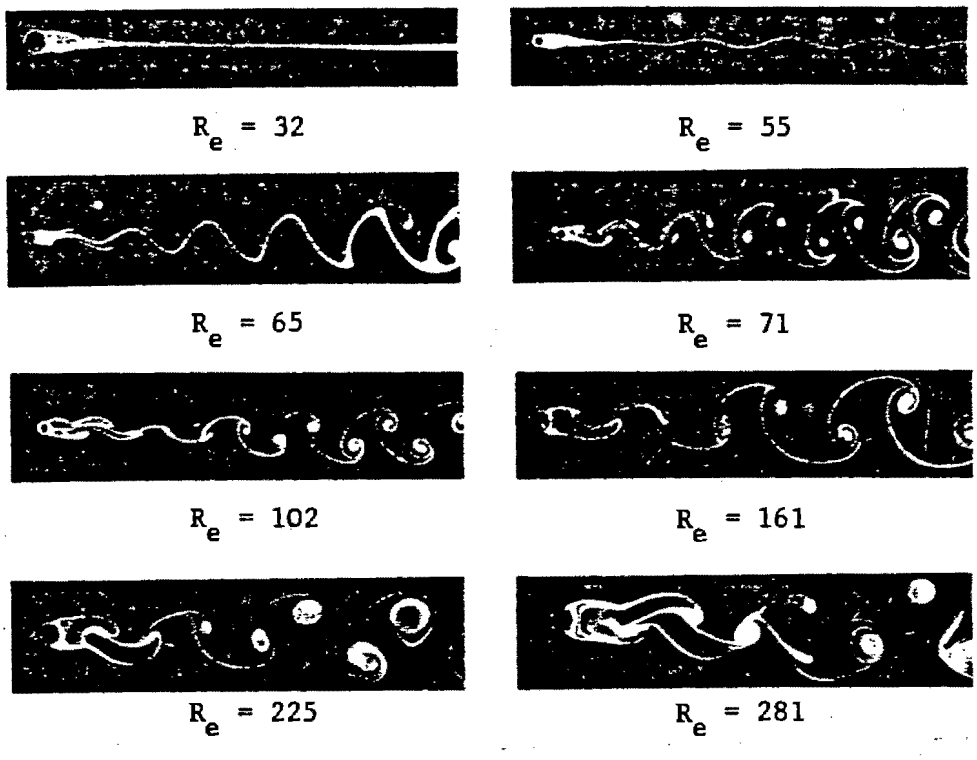

Figure 2.4 : Flow visualisation photographs taken by Homann (from Schlichting (1979) p.18)

The changes in the flow field at various Reynolds numbers are indicated. From the laminar wake at small Reynolds numbers, very regular vortex patterns are formed at increasing Reynolds numbers. These patterns are known as Kármán's vortex street. The regular pattern of vortices alternatively shed from the top and bottom of the cylinder, moves clockwise and counter clockwise respectively. The vortex patterns become irregular and turbulent at Reynolds numbers higher than about 5 ØØØ.

At a Reynolds number of about 2×10^5 , the boundary layer on the cylinder becomes turbulent and the separation points shift further downstream, the width of the wake is reduced and the drag coefficient suddenly decreases to reach a minimum value near $R_e = 5 \times 10^5$. This phenomenon may be explained by examining the energy properties of the laminar and turbulent boundary layers (refer to Fig. 2.5). Let the laminar and turbulent layers have the same thickness δ and the same undisturbed velocity V. From the velocity curve it is clear that the turbulent layer will possess more kinetic energy than the laminar layer.

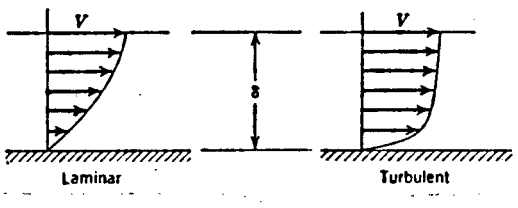

Figure 2.5 : Velocity profiles in laminar and turbulent boundary layers

The transition to a turbulent boundary layer leads to strong mixing of the flow, whereby the fluid elements near the body surface gain sufficient kinetic energy to withstand the adverse pressure gradient better.

The flow consequently continues further around the cylinder before the local surface velocity is reduced to zero, separation occurs and the width of the wake is reduced. The result is a reduction of the drag coefficient.

Roshko (1961) classified four flow regimes based on the Reynolds number. Due to some ambiguity in the description of these regimes, only the terminology used by Sarpkaya and Isaacson (1981) will be quoted:

Reynolds Number	Flow Regime	Boundary layer
$< 2 \times 10^5$	A. Subcritical	laminar
2×10^5 to 5×10^5	B. Critical	transition
5×10^5 to 3×10^6	C. Supercritical	turbulent
$> 3 \times 10^6$	D. Post-supercritical	turbulent

The four flow regimes are also indicated in Fig. 2.3 as A, B, C, and D. The boundary layer in the subcritical flow regime is laminar. As mentioned earlier, the boundary layer becomes turbulent at a Reynolds number of about 5×10^5 after passing through a transitional stage. In the present study the Reynolds number range 6 000 to 26 000 was selected; reasons for selecting this particular range are given in Chapter 1 (pp. 1-1 and 1-3) and Section 2.8 (p. 2-44).

The increase in the drag coefficient beyond a Reynolds number of 5×10^5, may probably be attributed to excessive turbulence.

Although a regular vortex street does not exist in the critical flow regime, Roshko (1961) found that such a regular street does re-appear at a very high Reynolds number of about 4×10^6.

The pressure drag or form drag, which is the dominating component of drag at high Reynolds numbers ($>10^5$) can be reduced by streamlining the body, e.g. an elliptical shaped profile such as an aerofoil. The boundary layer will be attached over most of the body's surface; separation will be delayed and the width of the wake decreased, resulting in a dramatic reduction in drag.

2.3.4 Pressure Distributions: Ideal Fluid Theory and Observations

Consider a two-dimensional steady, frictionless flow (i.e. a perfect fluid) past a circular cylinder (refer to Fig. 2.6). The streamlines represent the actual paths of the fluid particles. The crowding together of the streamlines at points B and D indicates a greater velocity, than the upstream velocity U. The points A and C are stagnation points where the velocity is zero. Mathematically, the velocity at any point P on the cylinder surface is $2\ U \sin\theta$, where θ is the angle subtended by arc AP at the cylinder centre.

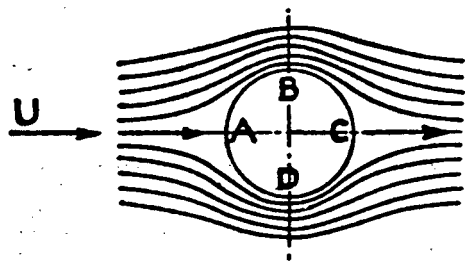

Figure 2.6 : Steady, inviscid (non-viscous) flow past a circular cylinder (from Goldstein (1950), p.23)

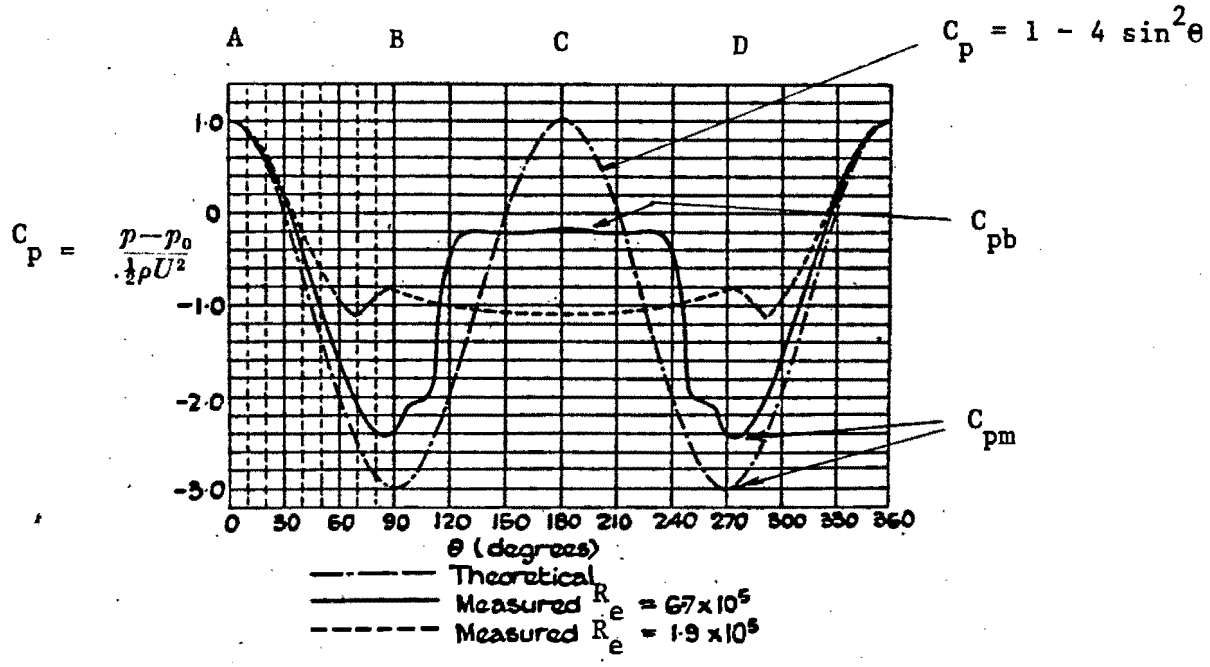

Figure 2.7 : Pressure distributions around a circular cylinder in steady flow (from Goldstein (1950), p.24)

For an ideal fluid the total pressure head H is a constant and is equal to $p + \frac{1}{2}\rho u^2$, where p is the pressure and u the velocity. Goldstein (1950) showed that at a general point P, on a cylinder placed in an ideal fluid, the non-dimensional pressure coefficient

$$C_p = (p - p_o) / (\tfrac{1}{2}\rho U^2) = 1 - 4 \sin^2 \theta \qquad (2.10)$$

Symbol p_o represents the pressure upstream from the cylinder. The pressure is at its maximum at the two stagnation points A and C, and a minimum at B and D. The theoretical dimensionless pressure coefficient is plotted against angle θ in Fig. 2.7. The pressure distribution is symmetrical about the transverse diameter. The

fluid acquires sufficient momentum and energy when moving down the pressure gradient from A to B, to carry it up the pressure gradient to C; naturally in the absence of friction. It is evident that the potential theory considered, generates no net drag.

Two pressure distributions, measured by Flachsbart in 1932, in air, are also indicated in Fig. 2.7. The one distribution ($R_e = 1,9 \times 10^5$) is in the subcritical flow regime, while the other falls in the supercritical regime. At the front of the cylinder there is fair agreement between the measured distributions and the theoretical result, particularly for the larger Reynolds number curve. The discrepancy between the actual and theoretical results becomes large in the rear of the cylinder, due to the large drag of a circular cylinder.

The pressure distribution for the lower (subcritical) Reynolds number curve differs most from the potential theory plot. Separation takes place at 90° and 270° , while it occurs at about 125° and 235° for the larger Reynolds number curve. Further, from the larger negative pressure coefficient of the lower Reynolds number curve, it is evident that a larger drag exists in the subcritical flow regime.

2.4 Vortex Shedding Frequency

A relationship between vortex shedding frequency, the cylinder diameter and the ambient flow velocity was discovered by Strouhal in 1878. The relationship is denoted by the dimensionless Strouhal number S:

$$S = \frac{fD}{U} \tag{2.11}$$

where f is the vortex shedding frequency. The Strouhal number is a useful parameter for determining the vortex shedding frequency in steady flow. Measurements show that it only depends on the

Reynolds number (refer to Fig. 2.8) in the range where the regular Kármán vortex street is observed: from about 60 to 5 000 and beyond 4×10^6. In the subcritical flow regime above $R_e = 500$, the Strouhal number remains approximately constant around 0,20.

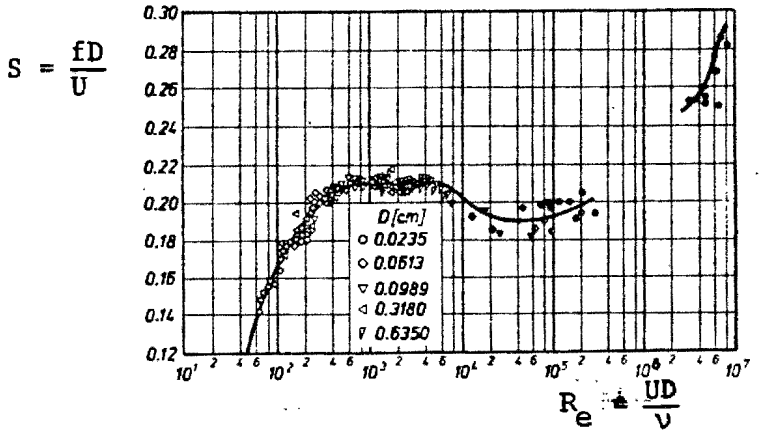

Figure 2.8 : Strouhal number versus Reynolds number, for the flow past a circular cylinder (from Schlichting (1979) p.32)

The vortex shedding phenomenon behind a cylinder, by which vortices are alternately shed from opposite sides, gives rise to an oscillating side thrust that acts in a direction away from the last detached vortex. Therefore unless the cylinder is rigidly supported, it will tend to oscillate from one side to the other. The oscillation is amplified when the natural period of vibration of the cylinder is in resonance with the vortex shedding frequency (Blevins, 1977).

A number of investigations on vortex shedding by cylinders near a boundary had been performed; Bearman and Zdravkovich (1978), Sarpkaya and Isaacson (1981) and Grass et al (1984) are useful references.

2.5 Lift Forces

2.5.1 Symmetrical Flow Field

When a circular cylinder is placed in the infinite, steady, parallel flow field of an ideal fluid (see Fig. 2.6), the pattern

of streamlines is perfectly symmetrical. Mention was already made that the pressure distribution is symmetrical about points B and D in Fig. 2.6, resulting in no net drag. Due to the symmetry of the pressure distribution (Fig. 2.7), there is also no net transverse or lift force on the cylinder.

When, however, the ideal (non-viscous) fluid is replaced by a real fluid, transverse or lift force may be induced due to vortex shedding or rotation of the cylinder. In the previous Section (2.4) it was mentioned that vortex shedding results in an oscillating side thrust always directed away from the last shed vortex. This fluctuating side thrust or lift force exists at a wide range of Reynolds numbers, below 2×10^5 and beyond 4×10^6.

One of the methods devised for the artificial prevention of separation, has led to a large lift being induced on a circular cylinder. Schlichting (1979) mentions that Prandtl showed that the simplest method to prevent separation on a cylinder (and reduce energy losses), is to rotate the cylinder: the cylinder wall is moved with the flow stream to reduce the velocity difference and therefore the cause of boundary layer formation is removed. Although the wall and the stream move in opposite directions on the other side of the cylinder, only slight separation occurs. An asymmetrical pattern of streamlines is created by this method of flow circulation, resulting in a large transverse or lift force, perpendicular to the direction of flow; this is referred to as the Magnus effect. A mathematical expression for this lift force in the case of an inviscid fluid, was deduced by Goldstein (1950).

2.5.2 Steady Flow near a Boundary (Wall)

When the cylinder is placed in the steady flow of an ideal (non-viscous) fluid, near a boundary, transverse forces will be experienced. A steady lift force acting on the cylinder is due to flow asymmetry around the cylinder.

Müller (1929) and Yamamoto et al (1974) showed that for the cylinder placed on the bed, the potential flow theory yields a positive (upward) lift coefficient value of 4,49. With a gap between the cylinder and the wall, the lift force reversed its direction and was directed towards the wall, reducing in magnitude as the gap was increased. The potential flow theory approach is further discussed in Chapter 9 of this dissertation.

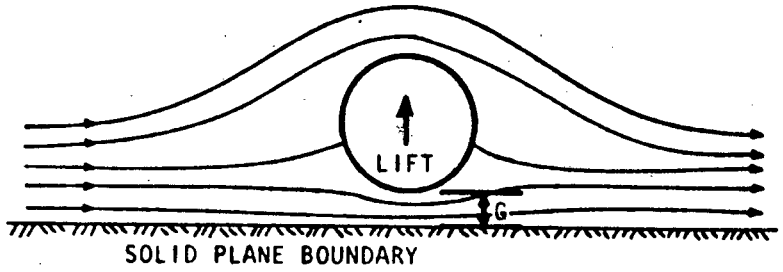

Figure 2.9 : Circular cylinder in the steady flow of a real fluid, near a boundary

When boundary proximity with a real fluid is considered, a totally different situation arises (Fig. 2.9). Apart from the vertical steady lift force, a steady drag force (due to viscous effects) is induced and unsteady lift forces are likely to occur as a result of flow separation.

The transverse or lift forces referred to in this dissertation exclude the force of buoyancy. Therefore, the lift or transverse forces refer only to the hydrodynamic force components.

The proximity of the cylinder to the wall, where a lower energy wall-boundary-layer flow exists, results in the deceleration of the fluid particles closer to the wall, compared to those further

away, due to viscous effects. The flow velocity will therefore be greater over the top of the cylinder, and the cylinder will be subjected to lower pressure on the upper surface than on the lower surface. A resultant steady upward lift force, away from the horizontal wall, will thus be exerted on the cylinder.

Lift forces do not only act vertically upwards. In the case of a vertical pile immersed in a symmetrical, steady, viscous flow, horizontal transverse or lift forces, which are unsteady, are induced due to vortex shedding. Near a vertical boundary, the pile will also experience a horizontal unsteady lift force away from the boundary.

Similar to the expression for the steady drag force (Equation (2.9)), the steady lift force is expressed in terms of the stagnation pressure at the foremost point on the cylinder directed to the approach flow. The expression for the steady lift force per unit length of the cylinder, F_L, is

$$F_L = \tfrac{1}{2} C_L D \rho U^2 \qquad (2.12)$$

where C_L = lift coefficient.

In this study a steady lift force will be regarded as positive when it is directed away from a solid flat wall; a negative value will be towards the wall.

2.6 Experimental Studies

It is evident that for the symmetrical flow case the mechanism by which forces on the cylinder are developed in steady, viscous flow is more complex than in steady, non-viscous flow. With the cylinder near a wall (bed), the boundary layer on the cylinder

interacts with that of the wall and the situation is further complicated. Various variables such as the cylinder clearance, boundary layer thickness, cylinder and bed roughnesses, and approach velocity also have to be considered.

The mathematical analysis of the situation is difficult. It is therefore not surprising that many of the investigators opted for an experimental approach in analysing the situation.

The review of the experimental studies previously undertaken, has been divided into two sections. The first section deals with cylinders placed in a symmetrical flow field. Although the greater portion of this research work was undertaken in wind tunnels for aeronautical purposes, it is analogous to hydrodynamical problems encountered with pipelines. The section is concerned with time-averaged drag (but no nett lift), and the fluctuation in the lift and drag (refer to Fig. 2.10 for definition sketch); vortex shedding is also dealt with.

The second section deals with cylinders in contact with and close to a boundary or solid plane. It is directly related to the topic of the present study and contains information on the various parameters affecting the force coefficients.

All lift and drag forces or coefficients referred to in this dissertation are time-averaged values, unless otherwise stated.

2.6.1 Cylinders in Symmetrical Flow

Considerable research had been done on cylinders suspended in a symmetrical, steady flow field. Measurements have been reported by inter alia Goldstein (1950), Roshko (1961), Gerrard (1961), Bishop and Hassan (1964), Grove et al (1964), Acrivos et al (1968), Achenbach (1968 and 1971), Batham (1973), Tanida et al (1973), Kacker et al (1974), Coutanceau and Bouard (1977), Murphy and Rose (1978) and Savkar et al (1980).

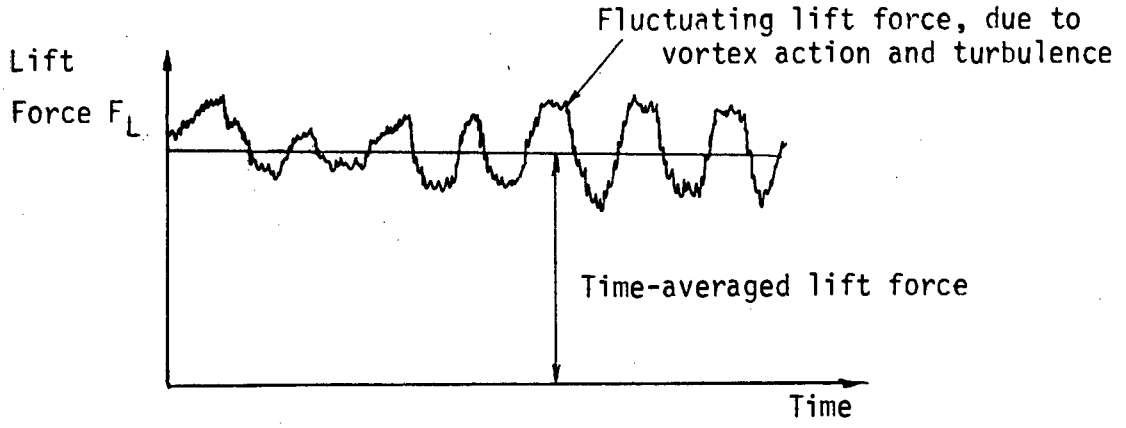

FIG. 2.10: Time-averaged and Fluctuating Lift Force

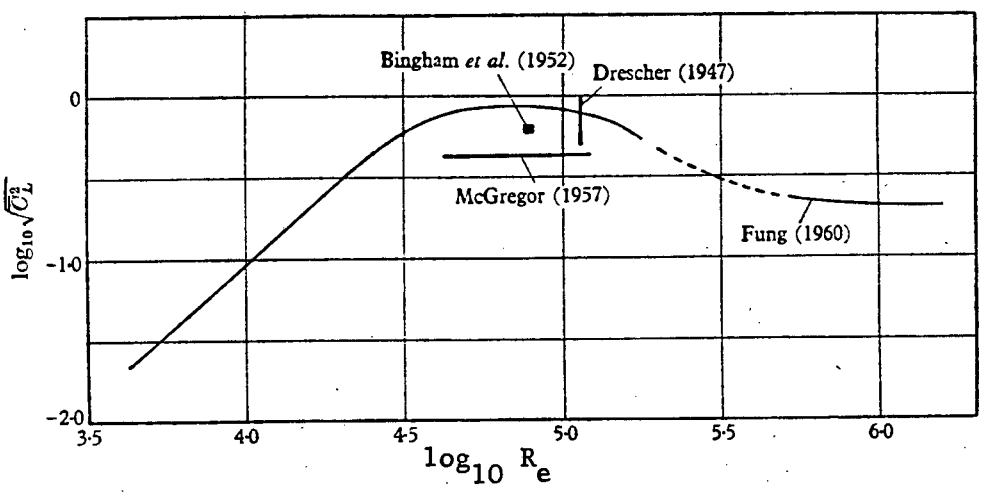

FIG. 2.11: Variation of r.m.s. lift coefficient with Reynolds number. (from Gerrard, 1961)

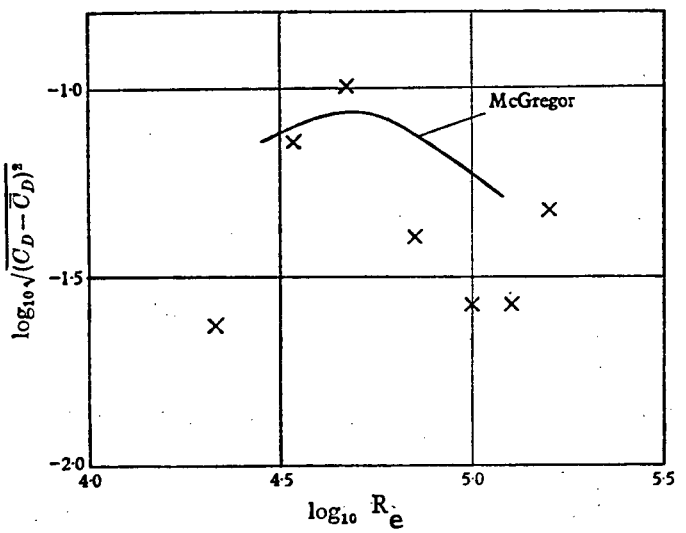

FIG. 2.12: Variation of r.m.s. component of the drag coefficient with Reynolds number (from Gerrard, 1961)

2.6.1.1 Smooth Horizontal Cylinders in Steady Cross Flow

Littlejohns (1972) summarised the experimental research work done until roughly 1970. The vast majority of all research work on the steady, symmetrical, fluid flow around cylinders, had been done in an air medium. Many of the measurements of the drag, to the early 1970's, were done by indirect methods such as measuring the pressure distribution around the cylinder.

Roshko (1961) performed tests, in a wind tunnel, at very high Reynolds numbers from 10^6 to 10^7. He measured the pressures every 10° around a cylinder; pressure orifices were located over half the circumference at the middle section. The pressure measuring system consisted of pressure transducers which were very sensitive at the highest dynamic pressures encountered. A hot wire anemometer, mounted downstream of the cylinder, was fed to a spectral analyser to identify vortex shedding peaks in the scanned frequency spectrum. Roshko found that changes in the drag coefficient relate to changes in the base pressure coefficient C_{pb}, the pressure coefficient on the back of the cylinder. The pressure distribution curve ($R_e = 8,4 \times 10^6$) in the post-supercritical flow regime was similar to that in the subcritical regime, except that separation occurred later (i.e. a larger separation angle). Roshko only observed vortex shedding to commence at a Reynolds number of $3,5 \times 10^6$ (in the 10^6 to 10^7 Reynolds number region investigated).

An interesting technique was used by Gerrard (1961) for investigating the oscillating lift and drag forces on a circular cylinder in steady flow, in a wind tunnel: the fluctuating pressures on the cylinder surface was measured by means of condenser microphones, which had to be calibrated carefully. Integration of the pressures were possible due to the fact that the pressures on one side of the cylinder were out of phase with those on the other side of the cylinder; the lift force could

therefore be calculated. Gerrard found that the root-mean-square (r.m.s.) lift coefficient changed almost linearly from Ø,Ø1 at a Reynolds number of 4 ØØØ, to reach a maximum of Ø,8 at a Reynolds number of 7Ø ØØØ (see Fig. 2.11). In the Reynolds number range 4 ØØØ to 2Ø ØØØ, Gerrard's experiments indicated that the r.m.s. lift coefficient was proportional to $R_e^{1,7}$. The variation in the drag coefficient about the mean was determined for Reynolds numbers beyond 2Ø ØØØ and found to be between 1Ø and 13 times less that the r.m.s. lift coefficient (refer to Fig. 2.12).

Distributions of pressure and skin friction were measured by Achenbach (1968) on a smooth cylinder in an air medium in the Reynolds number range $6 \times 1Ø^4$ to $5 \times 1Ø^6$. Achenbach's work was directed at getting a deeper insight into heat transfer and flow mechanisms around the critical flow regime; the final objective being the design of heat exchangers. Pressures were measured at intervals of 5° around the cylinders by means of single mounted pressure tapping; the cylinder could be rotated. Pressures were recorded by means of a Betz manometer (up to $R_e = 3 \times 1Ø^5$) and electronic pressure transducers. The skin friction distribution was recorded simultaneously with the pressure measurements, by means of a skin friction probe coupled to a precision pressure gauge. The pressure and skin friction distributions very clearly indicated that the beginning and end of the constant pressure zone (wake zone) behind the cylinder, coincides with the zero skin friction locations. These locations are where the boundary layer separates from the cylinder surface. This enabled Achenbach to establish a graphical relationship between the separation angle and the Reynolds number from the subcritical to the post-supercritical flow regimes. The total drag could also be determined from the sum of the form (or pressure) drag and the skin friction drag, and the percentage skin friction drag graphically represented as a function of Reynolds number.

Murphy and Rose (1978) also measured pressure and skin friction distributions on a cylinder in a wind tunnel, but at intervals of 3° . Sets of buried-wire-gauges were installed on the cylinder surface for the measurement of vortex shedding frequencies and skin friction distributions. Although displayed as a function of Mach number, the results were in general agreement with existing literature at the time, for low Mach numbers.

Although flows around a cylinder, immersed in oil, were only investigated at relatively low Reynolds numbers (up to 177) by Grove et al (1964) and Acrivos et al (1968), interesting features regarding the wake region, various pressure locations and the separation angle were disclosed. Both groups used the same experimental arrangement. Pressure distributions were measured by a simple manometer technique. A single pressure tapping was located on a rotatable cylinder. The pressure was accurately read (to the nearest Ø,Ø5 mm) on an oil manometer by means of a cathetometer.

The hyperbolic expression (experimentally determined by Grove et al (1964)) for the pressure coefficient C_p at the front stagnation point ($\theta = Ø$) is given by

$$C_p = 1 + 8/R_e \qquad (2.13)$$

and confirmed the result deduced in a different manner by Homann in 1936. Grove et al also experimentally determined a relationship

$$C_D = Ø,62 + 12,6/R_e \qquad (2.14)$$

between the form drag coefficient C_D and Reynolds number, for the Reynolds number range of 25 to 177. They further found the pressure coefficient C_p at the rear of the cylinder ($\theta = 18Ø°$) to be constant.

Apart from measuring pressures, Acrivos et al (1968) also measured local shear stress along the surface of the cylinder. The shear stress was indirectly measured using the heated surface probe technique (refer to Rotem, 1967). The shear stress curve (for R_e values of 64 to 150) compared extremely well with two theoretical curves which were computed from an approximate solution of the laminar boundary-layer equations. The results of Acrivos et al were in agreement with the prediction of the theoretical model earlier proposed by Acrivos et al (1965). The model which among other things, also predicted pressure distributions (up to about R_e = 180) around a cylinder, was based on the estimated shape of the "wake bubble" boundary. The "wake bubble" boundary forms the perimeter of the relatively stagnant fluid behind the cylinder.

Since the 1960's a number of researchers used strain gauge transducers, whereby the forces exerted on a cylinder are measured from the strains induced. Usually an active cylinder section is placed between two dummy cylinder sections mounted on side beams; the central active section ensures the elimination of end effects on the recorded results. Bishop and Hassan (1964) measured the fluctuations in the lift and drag forces in a water channel using strain gauge transducers, in the Reynolds number range 3 600 to 11 000. The steady average drag force was measured by means of a galvanometer. A common tendency was found between the r.m.s. lift and drag coefficients: they rose and fell at approximately the same Reynolds numbers. Further, they also confirmed the similar shapes between the curves for the time-averaged drag coefficient and 1/S, the reciprocal of the Strouhal number.

Both the direct and indirect force measuring methods were employed by Kacker et al (1974) to measure the r.m.s. lift and drag forces on a cylinder in a wind tunnel, in the Reynolds number range 10^4 to $2{,}5 \times 10^5$. The direct-force-measuring system comprised two load transducers which had to be calibrated meticulously. The oscillating lift and drag forces were also measured indirectly by

obtaining the fluctuating pressure distribution around the cylinder, as an independent check on the force-measuring system. Fluctuating pressures were measured using pressure transducers. Coefficients at a cylinder length to diameter ratio approaching zero, showed good agreement with those of other investigators in the range $4 \times 10^4 < R_e < 10^5$.

2.6.1.2 Cylinder Roughness and Stream Turbulence

Achenbach (1971) investigated the influence of cylinder roughness on the flow around a cylinder in the Reynolds number range 4×10^4 to 3×10^6, using a high-pressure wind tunnel. Pressure and skin friction distributions were measured; the total drag coefficient, percentage skin friction related to Reynolds number and the relative roughness k/D (where k is the surface roughness height), and the location of the separation point could therefore be determined. Achenbach found that the drag coefficient depends also on the roughness ratio. Larger roughness results in a higher skin friction, therefore greater retardation of the boundary layer and earlier separation which leads to a larger drag coefficient. The critical drag coefficients for higher k/D values occurred at lower Reynolds numbers. Further, in the subcritical flow regime the drag coefficient's magnitude was not influenced by surface roughness, but in the other three flow regimes (refer to Section 2.3.3) the drag coefficient increased with roughness.

Measurements were made on smooth and rough cylinders in both laminar and turbulent streams, in a wind tunnel, by Batham (1973) regarding the time-averaged and fluctuating pressure distributions. One of Batham's objectives was to simulate the pressure distributions at high Reynolds numbers of 10^7 to 10^8, by roughening the cylinder surface; the experimental set-up concerned was only capable of Reynolds numbers of order 10^5. Batham found that the introduction of turbulence stabilised

(v) At large Reynolds numbers, the pressure rise to the point of separation, $C_{pb} - C_{pm}$, is essentially a function of the surface roughness.

In later studies by Güven et al (1977 and 1980), their experimental findings indicated in conclusion (ii) above, were well supported by analytical considerations. They used an extension of the Stratford-Townsend theory (Stratford, 1959, and Townsend, 1962), which confirmed the dependence of $(C_{pb} - C_{pm})$ on relative roughness.

In an investigation on the flow around roughened cylinders in transitional regimes, Buresti (1983) confirmed that a link exists among the drag coefficient, the pressure distribution and the vortex shedding frequency in the wake of the cylinder.

Fluctuating lift and drag forces on a cylinder were measured by Savkar et al (1980) in a turbulent flow in a water tunnel. They showed that turbulence results in lower r.m.s. lift and time-averaged drag coefficients and that these values occur at smaller Reynolds numbers, i.e. the critical Reynolds numbers are lowered.

2.6.1.3 Vertical Cylinder in a Water Flume

The steady drag force was measured by Masch and Moore (1960) by placing a cylinder vertically in a water flume; the flow having a free surface. Coefficients were determined from pressure measurements in the subcritical Reynolds number range of 18 500 to 22 500. They found that the local drag coefficient was altered at various locations along the cylinder when the cylinder was approached by a vertical velocity gradient in the flow.

Tanida et al (1973) also undertook tests with a vertical cylinder mounted in a water flume. They measured the steady drag and r.m.s. lift and drag coefficients using the strain gauge method

from a Reynolds number of 40 to 10^4 . Except for the r.m.s. drag coefficient, which was too small to measure accurately, their values showed general agreement with those of other investigators, such as Tritton (1959) and Gerrard (1961).

2.6.1.4 Flow Visualisation

A novel experimental technique was used by Coutanceau and Bouard (1977) to study the main features of the flow past a circular cylinder. They employed a very interesting method to photograph flow patterns around a cylinder immersed in oil at Reynolds numbers of up to 52. Velocity distributions and other features such as the separation angle, wake length and wake boundary were measured from the visualisation photographs. Good comparison was found with known numerical calculations. Further, their results covered more different features of the steady flow around a cylinder than any other investigation in the Reynolds number range concerned.

2.6.1.5 Some Novel Experiments in Unsteady Flow

Although unsteady flow situations are not directly applicable to this study, some interesting experimental methods in unsteady flow conditions are briefly described below.

The vast majority of experimental studies in unsteady approach flow have been concerned with the strain gauge method. Dalton and Chantranuvatana (1980) investigated the flow field around a vertical cylinder which oscillated transversely in a water tank, by means of the average pressure distributions at specific velocities. The cylinder could be rotated about its vertical axis. Two pairs of pressure transducers (each pair consisting of an active and a dummy or reference transducer) were mounted inside the hollow cylinder at different locations to serve as a control.

The pressure signal was transmitted from an opening in the cylinder surface to remote signal amplifiers and a recorder. A pressure distribution (at maximum velocity) did not closely match the steady flow pressure distribution at approximately the same Reynolds number; unfortunately the oscillatory periodic time was too short. Further, the wake vortices present at flow reversal also affected the pressure distribution.

The fluctuation of the drag force, induced on a cylinder suspended in oscillatory water in a large vertical U-tube, was investigated by Shedden and Lin (1983) using a laser-cantilever force transducer. The one end of the cylinder was mounted on a hinge fixed to the vertical wall of the tube while the other was suspended by an inelastic thread, connected to the free end of a cantilever beam mounted above the U-tube. The r.m.s. drag force on the cylinder resulted in small displacements of the cantilever beam. The displacements were projected by a laser beam onto a mirror. The reflected beam was then appropriately magnified via a system of mirrors onto a graph screen. By means of this method, drag forces could be measured which were too small to be determined by standard methods such as strain gauges.

2.6.2 Cylinder on and near a Boundary or Wall, in Steady Flow

The experimental studies reviewed in this section are directly related to the experimental component of this dissertation. The review includes measurements reported by inter alia Dean and Harleman (1966), Brown (1967), Jones (1970 and 1971), Beattie et al (1971), Thomschke (1971), Wilson and Caldwell (1971), Littlejohns (1972 and 1974), Bagnold (1974), Bearman and Zdravkovich (1978), Zdravkovich (1985) and Fredsoe et al (1985).

2.6.2.1 Initial Investigations on Smooth Cylinders

Littlejohns (1972 and 1974) referred to investigations undertaken by the Hydraulics Research Station at Wallingford (in the United Kingdom), in 1961, in a towing tank on 1/3 scale models to determine the lift and drag coefficients for a smooth cylinder resting on a flat plate. The cylinder was fixed to a boundary plate and towed through still water. Measurements were made in the Reynolds number range 5×10^4 to 10^6. For subcritical Reynolds numbers, the drag coefficient values of approximately 1,1 were about 25 % lower than corresponding wind tunnel values recorded. The steady lift coefficient hovered around 1,0 in the same flow region.

One of the first attempts to determine the hydrodynamic forces on a large pipe in contact with the bed of a water channel was reported by Brown (1967). He measured pressure distributions, by means of water manometers, on pipes having diameters of 150 and 250 mm. The water depth was 460 mm, the maximum flow velocity, 1,8 m/s and the Reynolds number varied between 6×10^4 and 3×10^5. The drag coefficient varied from 0,9 to 0,55 and the lift coefficient from 1,3 to 0,8; no graphs were, however, presented by Brown.

According to Wilson and Reid (1963), experiments performed by Dementiev in the U.S.S.R. in 1934 on a cylinder in contact with a wall, presumably in the subcritical flow zone, generated lift and drag coefficients of 0,78 and 1,03 respectively.

In discussing Brown's work, Font (1967) and Sutko (1967) both pointed out that the shallow submergence of the pipe, and the surface waves at the pipe location, could have affected the magnitude of the hydrodynamic forces concerned. Larock (1967)

stated that the Froude number F_r equal to about Ø,8 was appropriate to use in describing shallow submergent flows, while the Reynolds number became important with deep submergent flow situations; he felt that Brown's prototype situation was ill-defined.

In investigating the scour characteristics, and the drag and lift forces exerted on a pipe lying on the bed of a water flume, Townsend and Farley (1973) found that the drag and lift forces are functions of the Froude number. However, from their report it appears that they only considered shallow flows.

2.6.2.2 Reference Velocities for Calculating Lift and Drag Coefficients

An interesting investigation was undertaken by Jones (1970 and 1971) into the forces exerted on cylinders near a boundary in a prototype installation. Jones measured the time-averaged lift and drag forces directly by means of a strain gauge method in the range of Reynolds numbers from about 3×10^4 to 5×10^5. As a submarine pipeline, in a steady current, is usually partially or wholly immersed in a turbulent boundary layer, he did a very useful analysis of the near bed velocity profile. His measurements indicated that turbulent flow existed in the test channel.

Due to the shape of the velocity profile in the channel's boundary layer, it is evident that the free stream velocity will not generate realistic force coefficient values for a cylinder close to the bed. He subsequently deduced an expression for the effective velocity, V_{eff}, which he used as reference velocity. This expression as well as other relevant aspects of the reference velocity are discussed in Chapter 5. Jones recommended that, in the absence of accurate field measurements, the 1/7th power law should be used for approximating the boundary-layer velocity profile.

2.6.2.3 Force Coefficients at Various Cylinder to Bed Clearances

Dean and Harleman (1966) reported on tests, carried out by Knoblock and Troller, at the Guggenheim Airship Institute, on a cylinder mounted at various clearances from a wind tunnel floor. Measurements were apparently performed from a Reynolds number of $1,5 \times 10^5$ to $3,5 \times 10^5$. Dean and Harleman only referred to values obtained for the lift coefficient, C_L, which is indicated in Fig. 2.13.

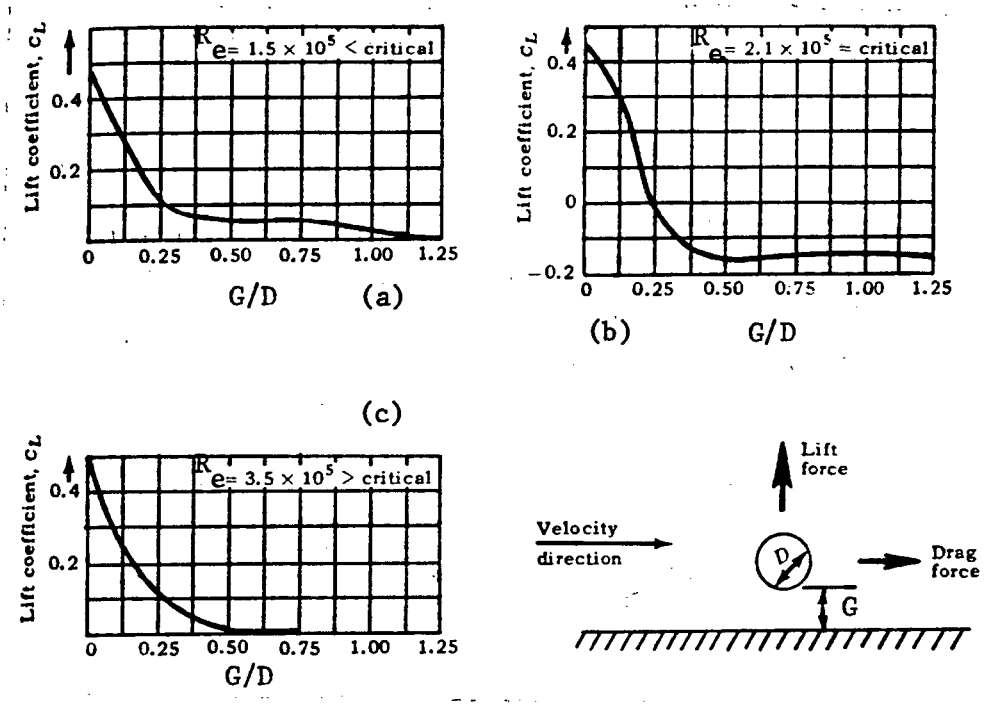

Figure 2.13: Influence of wall proximity and Reynolds number on the lift coefficient (Dean and Harleman, 1966)

Knoblock and Troller's plots indicate a dramatic reduction in the lift coefficient as the cylinder-to-bed clearance, G, increases from the on-bed position. At a gap-to-diameter ratio, G/D, of approximately Ø,25 in the subcritical flow regime (Fig. 2.13 (a)), the slope of the C_L versus G/D curve approached zero and the C value became zero at a G/D ratio of approximately 1,2. It is interesting to note that the lift coefficients were negative, i.e. the lift forces were directed towards the wall for some G/D values

in the critical range of Reynolds numbers (refer Fig. 2.13 (b)). Dean and Harleman (1966) referred to an interpretation for this tendency whereby "the boundary layer remains laminar on the wall side of the cylinder for higher Reynolds numbers than on the unbounded side". This would then result in an asymmetrical wake region behind the cylinder, leading to a downward lift force.

Measurements to determine the mean lift and drag coefficients on a cylinder, placed at various G/D values, were also carried out in a wind tunnel by Wilson and Caldwell (1971). They used a strain gauge method to measure the time-averaged forces exerted. The cylinder of 40 mm diameter was located in relation to a 600 mm long base plate and only two approach flows, generating Reynolds numbers of 33 200 and 56 600, were used. The drag coefficient versus G/D plots were virtually constant for each of the two approach flows, at C_L values of 1,6 and 1,1 respectively. The C_L versus G/D curves showed good agreement with Knoblock and Troller's results. The main objective of Wilson and Caldwell's test programme was, however, to investigate the lift and drag forces on single and double cylinders at different angular orientations with respect to the approach flow.

Investigations regarding hydrodynamic forces on cylinders, located at various clearances from a boundary in a water flume, were undertaken by Jones (1970 and 1971), Thomschke (1971) and Littlejohns (1974). Although the drag coefficient values compared favourably with corresponding wind tunnel values, the lift coefficient values were generally much higher in a water medium. The tests conducted by Jones in a prototype installation are considered to be very reliable, although he did not experiment with a free water surface above the cylinder location. He placed a large sheet of plywood to float on the water surface over the

test cylinder, to avoid the "standing wave" observed by Brown (1967). Jones used a 280 mm diameter cylinder in his prototype installation which comprised a 2 metre deep water flume capable of achieving water velocities of 2,6 m/s.

Thomschke's (1971) investigations into the lift and drag on spheres and cylinders, in close proximity to a wall, were primarily aimed at the identification of the influence of the gap ratio G/D on the force coefficients C_D and C_L. Pressure measurements were carried out on a 110 mm diameter cylinder in a water flume at critical region Reynolds numbers of $9,2 \times 10^4$ and $2,1 \times 10^5$. Both the C_D and C_L versus G/D curves exhibit turning points at G/D values of about 0,1 and 0,2 respectively. These curves are briefly discussed in Chapter 8 and the curves concerned are indicated in Figs. 8.9 and 8.10.

A very interesting field investigation into the hydrodynamic forces on a submarine pipeline, in the turbulent boundary layer of a steady flow which varied gradually, was reported by Littlejohns (1974). The investigation was carried out by the Wallingford Hydraulics Research Station (HRS) in the Severn Estuary. Three standard cylinders of diameter 305 mm, 610 mm and 915 mm were chosen for tests conducted in the range of Reynolds numbers from 3×10^4 to 10^6. Apart from the cylinder to bed clearance G, parameters such as cylinder roughness, angular orientation to the flow and depth of burial (of the cylinder) were also considered. As the investigators had to cope with a gradually increasing or decreasing flow, of varying depth, which depended on the tidal cycle, instantaneous measurements of the forces induced and the flow velocity had to be taken. A strain gauge method was therefore employed for the measurement of forces and an electronic current meter for the flow velocities.

To compensate for the varying depth, Littlejohns (1974) introduced a depth parameter, $a_1 = \frac{H - D}{H}$, where H is the depth of the water. The lift and drag coefficients were then expressed in terms of C_D/a_1 and C_L/a_1 To avoid the possibility of the formation of standing waves, the force measurements for each test were recorded in a water depth of at least five cylinder diameters. The 1/7th power law was used to approximate the boundary-layer velocity profile, for near-bed locations of the small cylinder. The reference velocity, for force coefficient computations, were taken as the velocity at the cylinder centre; however, an effective velocity was used for the small cylinder. As these matters are intimately related to the experimental work of the present study, the depth parameter a_1 and the reference velocity are further discussed in Chapter 5.

Littlejohns defined the variation of turbulence as $\sqrt{\overline{U_1^2}}/U$ where U is the mean velocity and U_1, the velocity fluctuation. The turbulence was at a higher level during the current's decelerating phase. The field tests performed by the HRS, indicated a maximum variation of turbulence intensity of 15 %. Consequently it was decided to investigate the magnitude of the average forces on and the flow around the 305 mm diameter cylinder in low turbulence flow in a large water channel, 2 m deep, 3,66 m wide and flow range capability from 0,5 m/s to 2 m/s. Littlejohns reported that, at the critical Reynolds number, the force coefficients C_D/a_1 and C_L/a_1 for the field tests, were respectively 0,55 and 0,7; these values were 0,2 higher for each of the coefficients in the case of the large water channel. The field test coefficients agreed favourably with corresponding values obtained by Jones (1971); this also applied to near-bed locations.

Bagnold (1974) performed novel experiments in a small flume, 910 mm long and 100 mm deep, using glycerol/water mixtures. He evaluated the lift and drag forces on a sphere and a cylinder using an instrument consisting of two interlinked mechanical balances. The device facilitated investigations with the sphere

or the cylinder as well as various body to bed clearances. Another interesting feature of the apparatus was the moving bed of the flume; smooth and rough surfaced moving-belt beds were used. The moving-bed channel made it possible to study steady flow effects in more viscous liquids (such as glycerol) which could only be made available in small quantities. Bagnold found the flow over the moving bed to be "remarkably steady".

For an increasing gap ratio, G/D, Bagnold found the drag coefficient for a smooth cylinder to decrease from 1,2 to a constant value of 1,Ø at G/D = Ø,25; it increased again close to the water surface. The cylinder diameter was 16 mm, the water depth about 7Ø mm and Reynolds number approximately 3 ØØØ. As expected, the lift coefficient decreased from Ø,57 with increasing G/D. Negative (downward) lift coefficients were recorded with the cylinder located above a G/D value of 3,5. The lift coefficient with the cylinder just surfacing, was -Ø,92. With reference to the theory for a transverse cylinder examined by Jeffreys (1929), Bagnold explained that the free surface behaves in a similar way as the lower solid boundary. With the body close to the bed, there is a decrease in momentum flux, relative to the upper side of the body, resulting in an excess dynamic pressure in the fluid near the bed. A transverse force is consequently exerted on the body away from the boundary. Bagnold was of the opinion that the free surface boundary is deformed by the stagnation pressure with the cylinder in close proximity. According to Bagnold the downward force exerted on the cylinder is equal to the "local excess head of liquid".

Very interesting results were generated by an investigation undertaken by Zdravkovich (1985) into the influence of the gap G, between the cylinder and the wall, and the thickness of the turbulent boundary layer, δ, on the force coefficients.

Tests were conducted in a wind tunnel on 35 mm and 65 mm diameter cylinders. The Reynolds number was varied from $4,8 \times 10^4$ to 3×10^5, G/D from Ø to 2 and the δ/D ratio from Ø,12 to Ø,97. The time-averaged lift and drag forces were measured on a six-component strain gauge balance. The wall boundary layers were artificially thickened by attaching 3 mm tripping wire or fixing a mat of coarse mesh wire, made of interwoven 4 mm wire, to a horizontal partition plate which represented the wall.

Zdravkovich's results revealed tendencies which were not encountered before. The plots of the drag coefficient C_D versus the gap ratio G/D, for the two cylinders, indicated about the same drag coefficient of 1,Ø at the location where the cylinders reached the edge of the wall boundary layer, i.e. at $G/\delta = 1$. It is noteworthy that Bearman and Zdravkovich (1978) found that the base pressure coefficient C_{pb} started to decrease for a gap ratio $G/D < Ø,8$; this location coincided with $G/\delta = 1$. The C_D versus G/D curve of Roshko et al (1975) showed a similar tendency to Zdravkovich's curve for the large cylinder (of 65 mm diameter). In the case under discussion, the $G/\delta = 1$ locations occurred at G/D values of Ø,97 and Ø,52 for the small and large cylinders respectively. Due to the apparent dependence of the drag coefficient on the gap to boundary layer thickness G/δ, Zdravkovich consequently represented the relationship between C_D and G/δ graphically (refer to Fig. 2.14). Good correlation for both cylinders is shown by the graphical presentation in Fig.2.14.

The boundary layer, thickened by mesh wire, also had a marked influence on Zdravkovich's lift coefficient C_L versus G/D curves. A negative lift coefficient was observed in the G/D range Ø,2 to Ø,6 (Fig. 2.15). This meant that the fluid velocity on the gap side of the cylinder was greater than over the top of the cylinder, and the lower pressure below the cylinder then

resulted in a downward transverse (or lift) force. The influence of boundary layer thickening was less significant for the small cylinder of 35 mm diameter, on which measurements were essentially done in a lower subcritical Reynolds number range. A comparison is made in Chapter 8 between Zdravkovich's results, where applicable, and those of the present study.

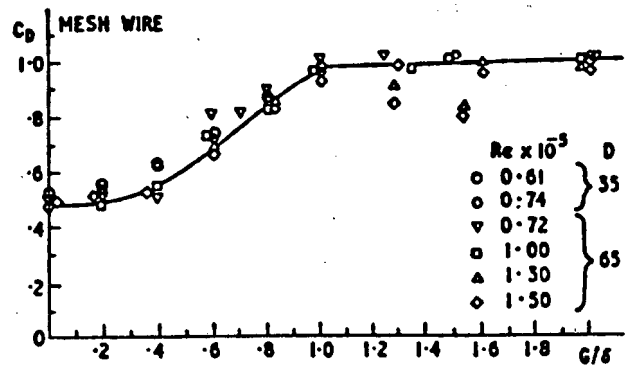

Figure 2.14 : Variation of drag coefficient with gap to boundary layer thickness ratio (Zdravkovich, 1985)

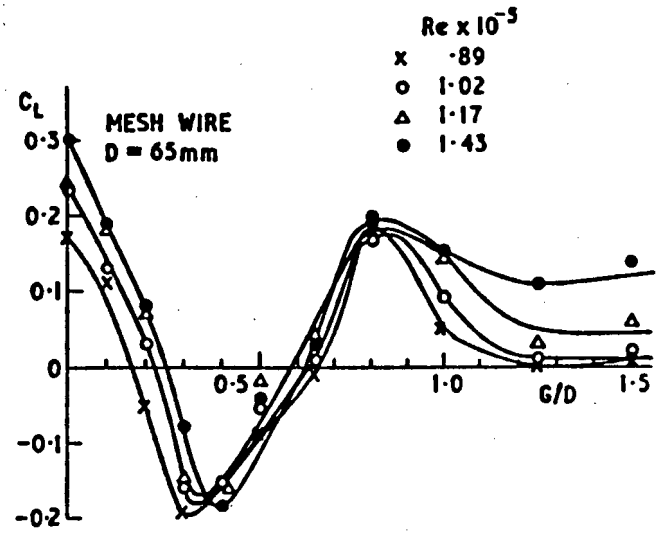

Figure 2.15 : Variation of lift coefficient with G/D, for thickened boundary layer (Zdravkovich, 1985)

Interesting lift force measurements were done by Fredsoe et al (1985) in a 2 metre wide water flume, in the Reynolds number range 20 000 to 30 000. They used an unusual method by which the 89 mm smooth test cylinder was suspended by a system of springs. When the water was allowed to flow past the cylinder, the vertical displacement of the springs was measured by means of a potentiometer. The displacement was related to the lift force induced on the cylinder. The method was very sensitive to vibrations, particularly close to the bed, and tests were only performed up to G/D ratios of 0,3.

Fredsoe et al (1985) found that the lift coefficient was approximately 0,7 at G/D = 0 and dropped to a minimum of 0,16 at G/D = 0,3 (Fig. 9.6). The results exhibited the same trend as those by Thomschke (1971). Fredsoe et al's results are compared to those of the present study in Fig. 8.10.

2.6.2.4 Pressure Distributions

Although a few investigators, such as Brown (1967) and Beattie et al (1971), utilised the pressure distribution method to determine force coefficients, they did not present any pressure distribution diagrams for near-bed locations of the cylinder in their publications known to the author.

Bearman and Zdravkovich (1978) measured the pressure distribution around a 19 mm diameter cylinder in a wind tunnel in a steady flow, at G/D values varying from 0 to 2. Measurements were taken at a Reynolds number of $4,8 \times 10^4$. Pressure distribution diagrams for G/D equal to 0 and 0,1 are shown in Fig. 8.1. Bearman and Zdravkovich found that the maximum pressure point on the front side of the cylinder, is not necessarily at the traditional $\theta = 0^\circ$ position at the front cylinder centre, but displaced towards the bed as the cylinder moved closer to the boundary. They also found that the pressure distributions were almost symmetrical about the front stagnation point ($\theta = 0^\circ$) at G/D = 0,4. For all values of

G/D, Bearman and Zdravkovich's pressure distributions were in general agreement with the measurements carried out by Göktun (1975).

2.6.2.5 Cylinder and Bed Roughness, and Turbulence

The influence of roughness on the force coefficients were investigated by inter alia Beattie et al (1971), Jones (1971), Littlejohns (1974) and Bagnold (1974). All these tests were performed in a water medium and, except for Bagnold's, the measurements were done on large cylinders around the critical Reynolds number, from approximately 10^5 to 10^6.

Experiments by all the mentioned researchers, indicated that roughening of the cylinder, for G/D = Ø, caused the drag coefficient to increase in the transitional and supercritical flow regimes.

According to Littlejohns, this was probably due to the increase in the surface resistance and the retardation of the boundary layer. Cylinder roughening also resulted in increased drag coefficients at higher G/D values. Regarding the effect of roughness, the subcritical region was not thoroughly examined. However, Bagnold observed an increase in the drag coefficient when a cylinder was placed on the bed.

The lift coefficient was extremely sensitive to surface roughness, particularly in the supercritical flow regime. The investigators mentioned above, who experimented in the transitional Reynolds number range, all found that the lift coefficient decreased as the roughness ratio k/D was increased. At increasing cylinder clearances from the bed, the lift coefficient decreased; similarly to smooth cylinders. Bagnold observed an increase in the lift coefficient for the on-bed position of the cylinder. Further away from the bed he noticed very little difference between C_L values for rough and smooth cylinders; he took measurements at a Reynolds number of approximately 3 ØØØ.

Jones (1971) produced lift and drag coefficient curves around the critical Reynolds number which he recommended for the design of submarine pipelines. He also undertook a parametric study (Jones, 1978) regarding the submerged weight and design velocity to ensure on-bottom pipeline stability. His corrected C_D and C_L design curves, extracted from the latter publication, are indicated in Figs. 2.16 and 2.17. The force coefficient values obtained by Beattie et al (1971), Jones (1971) and Littlejohns (1974) are compared to those of the present study in Chapter 8.

The boundary-layer velocity profile has an influence on the forces exerted on a cylinder lying on the bed in a steady flow. Further, the shape of the velocity profile is a function of the bed roughness, and changes in roughness will indirectly affect the forces on the cylinder. Jones (1970 and 1971) showed that, for the same free stream velocity, the lift and drag forces on a cylinder located on the bed, are less for a rough bed than for a smooth bed. However, he found that the lift and drag coefficients concerned were the same for both rough and smooth beds, provided these coefficients were calculated by means of the effective velocity V_{eff}. The effective velocity is given in Equation (5.8), in Chapter 5 of this dissertation.

When Littlejohns' (1974) field and water channel test results are compared, it is observed that an increase in the variation in free stream turbulence intensity, $\sqrt{\overline{U_1^2}}/U$ (up to 15 % in the estuary and less than 2,5 % in the water channel) leads to an increase in both the lift and drag coefficients in the transitional Reynolds number region. This is essentially due to the earlier occurrence of the critical Reynolds number in the case of estuarial flow. However, this tendency is not necessarily applicable to the complete range of Reynolds numbers.

2.6.2.6 Flow Visualisation

Very few flow visualisation studies have been undertaken. The studies of Taneda (1965), and Bearman and Zdravkovich (1978) revealed interesting features about the vortices formed behind a cylinder, near to a wall, in steady flow.

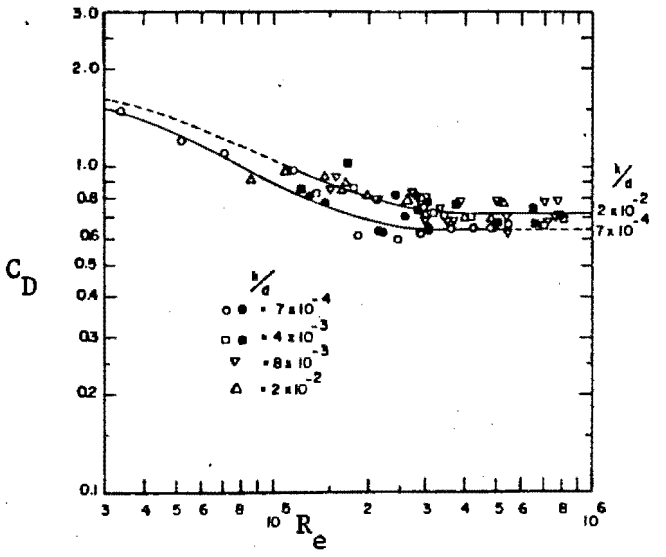

Figure 2.16 : Recommended effective drag coefficient design curves, for the on-bed position of a pipe (Jones, 1978)

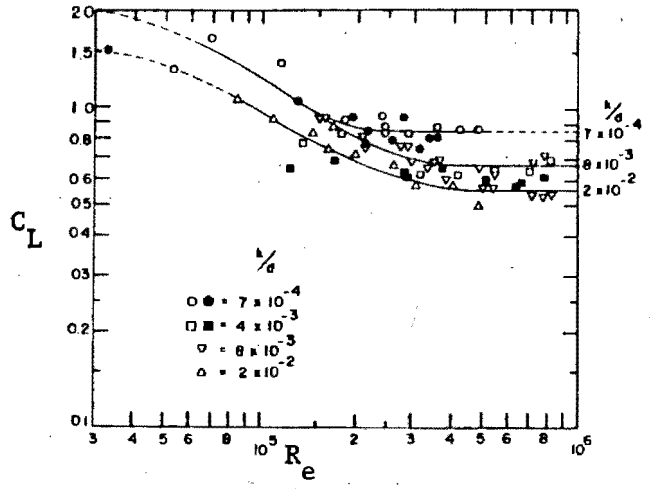

Figure 2.17 : Recommended effective lift coefficient design curves, for the on-bed position of the pipe (Jones, 1978)

Taneda examined the vortex streets behind a cylinder moving parallel to a plane wall, in water. He used aluminium dust and condensed milk to visualise the motion of water. Taneda presented flow visualisation photographs taken at gap ratios G/D of Ø,1 and Ø,6; the Reynolds number was 17Ø. A strong vortex street was noticed at G/D = Ø,6. At G/D = Ø,1 only a single row of vortices was observed. The wavelength of this single row increased downstream from the cylinder, but usually became unstable after a few wavelengths and dispersed.

The flow visualisation experiments on the flow around a cylinder, carried out by Bearman and Zdravkovich (1978), were performed in a wind tunnel at a Reynolds number of $2,5 \times 1Ø^4$. Parallel smoke filaments were used to visualise the streamlines of the flow, while smoke was also ejected into the wake through a small slot running along the back of the cylinder. Flow visualisation photographs were taken at various G/D values from Ø to 2, to reveal the flow pattern around the wake region, as well as the vortex characteristics. It was observed that the wake flow patterns for G/D equal to zero (wall contact) and Ø,2 were similar, even although flow between the cylinder and the wall existed in the latter case. One smoke filament, after having passed through the cylinder-wall-gap, was seen to be entrained into the wake. Irregular vortices were presumably only shed from behind the upper side of the cylinder, i.e. one row of vortices, for G/D values up to almost Ø,4. According to Bearman and Zdravkovich, their measurements of the vortex shedding frequency indicated that regular vortex shedding was suppressed at G/D values less than Ø,3.

Bearman and Zdravkovich's flow visualisation photographs for G/D > Ø,4, showed that regular vortex shedding occurred behind the cylinder. The presence of the wall appeared to have little effect on the flow at these G/D values, and the flow was almost completely symmetrical. Unfortunately, the flow visualisation

experiments were performed with a relatively short cylinder having a length to diameter ratio of only one. Bearman and Zdravkovich commented that, in spite of this shortcoming, the experiments presented a qualitative picture of the flow around a cylinder in close proximity to a plane wall.

2.7 Theoretical Studies

Few theoretical investigations have been done on the unsteady flow around a cylinder near a boundary. Since the 1970's the emphasis with theoretical studies shifted to numerical calculation methods; the phenomenal development of the computer industry has strongly influenced this trend.

Theoretical studies on the steady flow case, regarding wall proximity effects, are almost non-existent. A literature review on theoretical studies, carried out on cylinders placed in unsteady and steady flows close to a boundary, is given in Chapter 9 of this dissertation.

2.8 The Present Study

This Chapter shows that, for "wall cylinders" (i.e. cylinders in close proximity to a boundary), the subcritical flow region had not been well researched, particularly regarding the influence of cylinder roughening on the force coefficients.

In the present study comprehensive experimental tests were undertaken to explain the various flow phenomena in the subcritical region near a boundary. The Reynolds number range of 6 000 to 26 000 was essentially dictated by the practical limitations in the laboratory arrangement, where maximum flow velocities up to only about 0,5 m/s could be achieved; this represents a maximum Reynolds number of approximately 26 000. However, the range selected is related to real situations in practice (refer to page 1-3).

Experimental investigations were performed, in a water flume 18 m long and 600 mm wide, with smooth or rough beds. A smooth or rough cylinder (diameter 30 or 50 mm) was transversely placed in the flume. Unique experimental methods were developed to measure time-averaged pressures and flow velocities very accurately. The hydrodynamic forces were also measured by means of a novel "weighing" technique. The experimental arrangements are discussed in detail in Chapter 3.

The results of the experimental programme are fully discussed and theoretically analysed in Chapter 10.

CHAPTER 3 - EXPERIMENTAL ARRANGEMENTS

3.1 Introduction

The objectives of the experimental section of this study were achieved by using two experimental rigs. The first, the "pressure rig", is shown in Figure 3.1. The rig consisted of a hollow aluminium cylinder, which consisted of two longitudinal half sections, mounted horizontally in a water flume such that the approach flow would always be perpendicular to the cylinder axis. The second rig, the "force rig", was constructed of an aluminium frame resting freely on a sensitive balance while supporting an aluminium cylinder submerged in water. The "force rig" is shown in Fig. 3.2.

The uniqueness of the experimental work centred around the choice of the measuring instruments. Very sensitive non-deflecting Mettler balances were chosen. The use of these balances resulted in the achieving of very accurate pressure values around the cylinder as well as excellent velocity readings for the approach flow in the flume.

Side effect influences on the approach flow due to internal rotatable mountings inside the flume, were taken care of by replacing the glass panels, in the experimental area of the flume, with identical perspex panels. Before mounting the perspex panels, openings were machined at appropriate positions in the panels to accommodate the various cylinders.

The perspex panels could accommodate cylinders of different diameters ranging from 30 to 80 mm. However, due to practical considerations, a maximum cylinder diameter of 50 mm was chosen. Further, the set-up was designed such that the horizontal position of the cylinder in the flume could be adjusted externally, without interrupting the flow of water in the flume.

FIG. 3.1: OVERALL VIEW OF THE PRESSURE RIG.

FIG. 3.2: OVERALL VIEW OF THE FORCE RIG.

Measurements were taken with various combinations of the variables: pipe roughness, bed roughness, height of cylinder above bottom, cylinder diameter and water approach velocity. A micro computer was subsequently used to calculate pressure values and eventually the drag and lift forces and coefficients applicable for every combination of variables.

3.2 Selection of water as the fluid

The use of water as the fluid was chosen as this had definite advantages over the alternative of using air. The reasons are as follows:

Although the kinematic viscosity of air is some ten times greater than that of water, much larger flow velocities could be achieved with air such that the critical Reynolds number of 2×10^5 would be approached. Other investigators such as Bearman and Zdravkovich (1978) did very useful work on cylinders in an air medium. However, it is virtually impossible to simulate a free surface in an air medium. To simulate the flow of a fluid over a submarine pipeline in steady flow conditions, e.g. estuarial flow, a free surface is essential.

University of Cape Town

3.3 Testing Area and the Water Flume

The testing area was the main hydraulics laboratory of the Department of Civil Engineering at the University of Cape Town. The water flume, 18 m long and 600 mm wide, was used for the performing of the experimental work (Fig. 3.3).

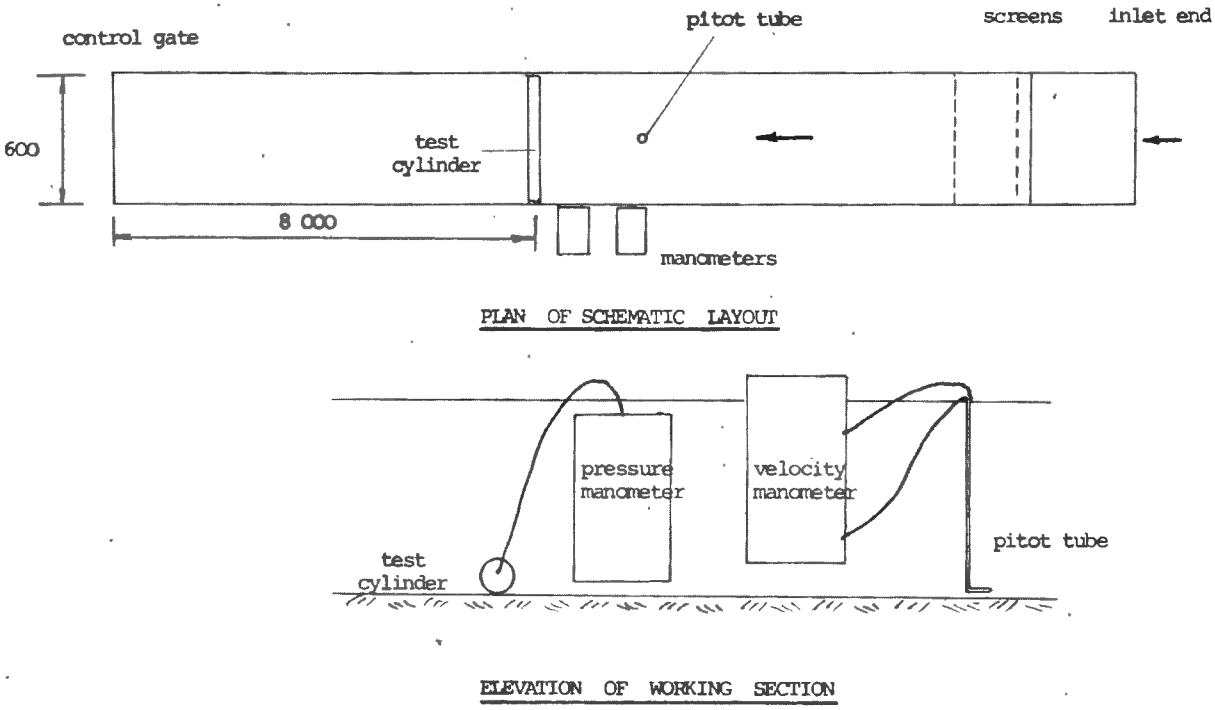

(a) SCHEMATIC LAYOUT

(b) FLUME: VIEW FROM THE DOWNSTREAM END

FIG. 3.3: OVERALL VIEW OF FLUME, SHOWING PRESSURE RIG.

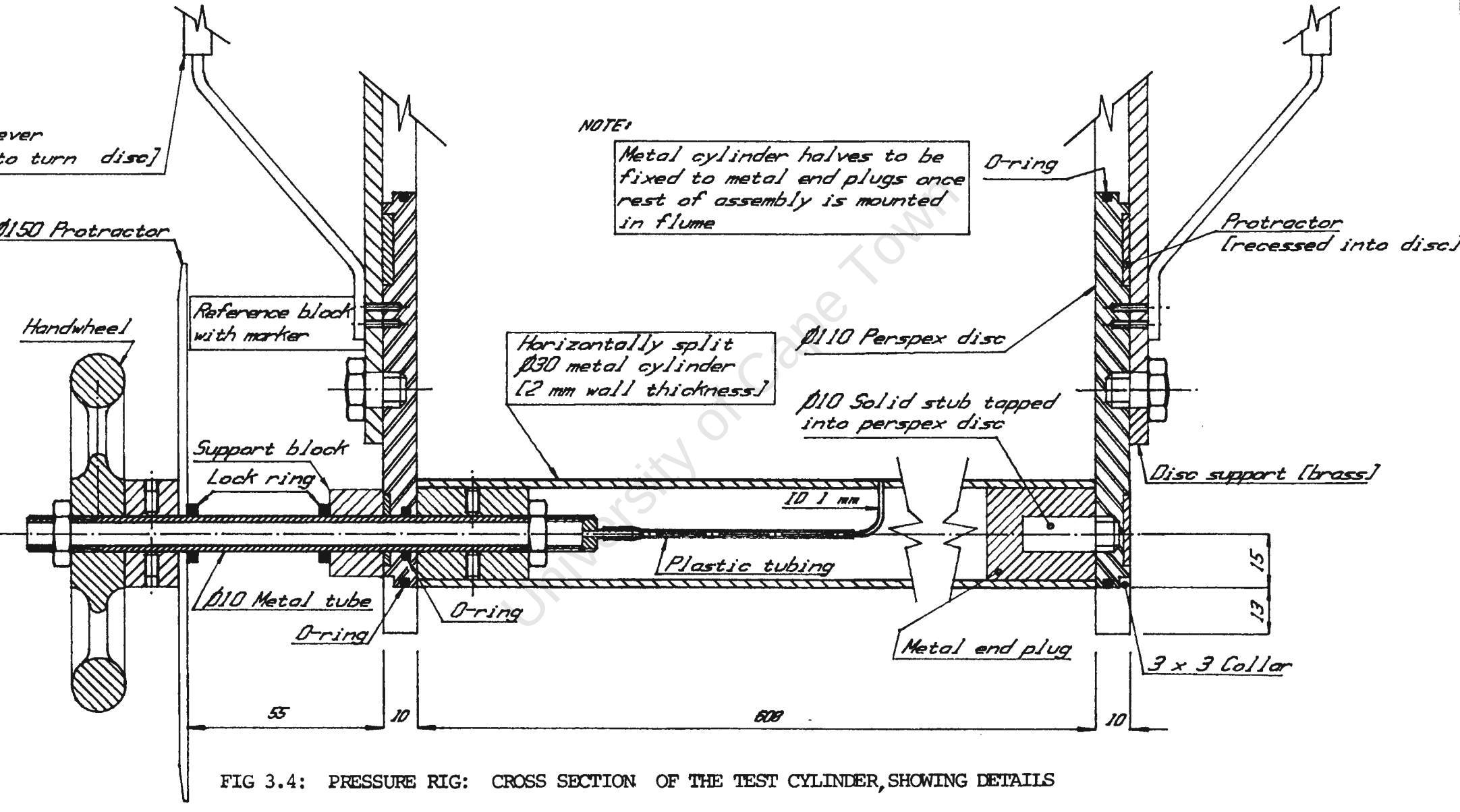

FIG 3.4: PRESSURE RIG: CROSS SECTION OF THE TEST CYLINDER, SHOWING DETAILS

University of Cape Town

The flume was supplied with water from a constant head water tower of approximately 15 metres height. The water supply was limited to 0,1 m^3/sec. With steady flow achieved in the flume, a maximum average flow velocity of only 0,5 metres per second could be obtained, at a depth of 90 mm.

The supply pipe from the tower was equipped with a venturi section, connected in turn to a differential mercury manometer from which the head could be read. The formula $Q = 0{,}019\sqrt{H}$ (with H in inches mercury) was developed to convert head readings to flow in m^3/sec. A control valve at the end of the supply pipe made inflow adjustments possible.

The level of the water flume could be mechanically adjusted. As the whole flume was mounted on a solid steel beam, this adjustment could be systematically performed with relatively little effort.

A control gate at the downstream end of the flume, made it possible to vary the velocity as well as the depth of the water in the flume. The outflow was directed (via sub-floor channels) to a basin from where it was pumped back to the water tower.

University of Cape Town

3.4 Pressure Rig

The "pressure rig" was the main instrument used to perform the experimental work. The layout of the rig is shown in Figs. 3.1, 3.3, and 3.4. It consisted basically of the following components:

- cylinder;
- cylinder mountings to water flume with height adjuster;
- calibrated handwheel to rotate cylinder;
- housing with Mettler balance and perspex beaker.

Although minor elements of the apparatus were similar to that used by Achenbach (1968), such as the central pressure tapping in the cylinder, the main elements of the "pressure rig" were original and unique in many respects.

3.4.1 Accuracy of Measurements

One of the main objectives with the experimental section of the present thesis, was to obtain very accurate pressure and velocity measurements. It was therefore decided to utilise micro manometers based on the principle of weighing a column of water.

The weighing was done by extremely sensitive electronic balances (trade name: Mettler). These digital balances were of a non-deflecting type, except when subjected to sudden impact loads. Further, the balances also had the following useful features:

(i) The balances could be zeroed even when loaded;

(ii) Bodies to be weighed could either be placed in the pan on top of the balance or suspended from a hook under the balance.

(iii) Once loaded and zeroed, mass could be tared off, for example a powder or a liquid; a negative reading would immediately be indicated in the balance's digital screen, provided no more than the original mass is tared off.

Further technical characteristics of the Mettler balances chosen for the "pressure rig" measurements are indicated in Table 3.1.

Mettler balance	Type PE 3000	Type PE 300
Accuracy	0,1 gram	0,01 gram
Range	3 000 g	300 g

Table 3.1: Technical characteristics of Mettler balances

University of Cape Town

The accuracy of the Mettler PE 300 balance was checked by suspending a clean glass beaker from the hook under the balance. The beaker was subsequently filled with clear water, using a 5 cm^3 pipette and the reading on the Mettler's digital screen recorded. Readings were recorded for every 5 cm^3 water up to 90 cm^3. The results are indicated in Table 3.2. and graphically represented in Fig. 3.5.

Water volume in pipette (cm^3)	Mettler balance (PE 300) reading (g)
5	5,00
10	10,01
15	15,01
20	19,98
25	24,99
30	29,99
35	34,99
40	39,98
45	44,98
50	49,98
55	54,98
60	59,98
65	64,96
70	69,96
75	74,98
80	80,00
85	84,96
90	89,98

Table 3.2: Checking accuracy of Mettler PE 300 balance

If possible errors with the pipette volume readings are neglected, the above readings indicate a high degree of accuracy of the Mettler balances. More details regarding the utilisation of the balances are given below in Sections 3.4.6 and 3.5.

3.4.2 Cylinder Construction

The actual testing area, where the test specimen was mounted horizontally in the 18 metres long flume and perpendicular to the

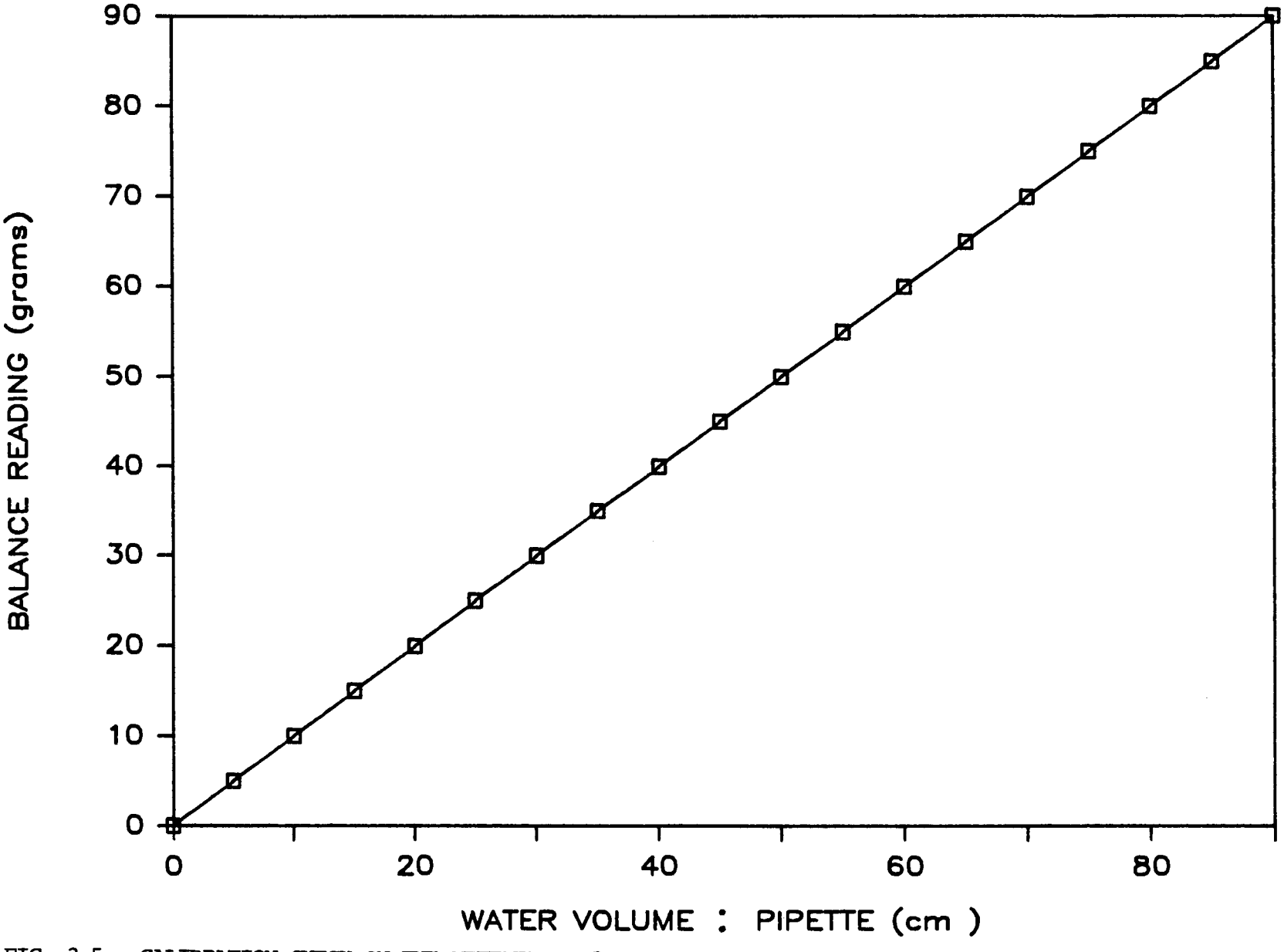

FIG. 3.5: CALIBRATION CHECK ON THE METTLER PE 300 BALANCE

approach flow, was chosen a distance of 8 metres from the tail gate end of the flume. This location was not affected by the turbulence at the inlet end of the flume nor the drawdown, and resulting reduction in depth, at the tail gate end.

The design of the test specimen of the "pressure rig", was essentially governed by the decision to reduce all possible forms of obstruction, to the approach flow in the water flume.

Cylinder supports or protruding mountings inside the flume could adversely influence the approach flow such, that three dimensional flow over the specimen might occur. To accommodate the reduction of side effect influence, the two vertical glass panels of the flume in the chosen testing area, had to be replaced by identical perspex panels.

At the outset it was decided to use two cylinders with different diameters. Due to practical experimental problems, ease of workshop machining and availability of materials, hollow pipe in aluminium was chosen as the test specimen. To avoid the formation of surface waves (as experienced by Brown (1967)) due to the blockage of the specimen, the diameter of the larger cylinder was made 50 mm. The construction of the cylinder was such, that it had to accommodate a 10 mm hollow metal tube extending through one side panel; for manufacturing purposes it was evident that the diameter of the smaller cylinder could not be less than 30 mm (refer to Fig. 3.4).

An unusual feature of the test specimen, was the fact that it was split longitudinally. This technique was used to mount the single pressure tapping at the centre of the cylinder with ease, and assemble the test cylinder comfortably inside the flume.

To split and mount the two halves of a cylinder, the following procedure was followed:

(i) Two identical hollow aluminium pipes, of length 615 mm, were selected (for example, approximately 51 mm outside diameter for the 50 mm diameter cylinder);

University of Cape Town

(ii) Each pipe was then milled longitudinally exactly at its centre to produce one set of halves that would fit perfectly;

(iii) The two halves were subsequently clamped together and machined down to the required diameter.

Circular end blocks of aluminium were machined to act as supports for the cylinder halves, as well as mountings to the rotating perspex discs (refer to Figure 3.4 and Section 3.4.3 below). Fine holes of 1,3 mm were drilled at the centres (along the axes) of the two cylinders, to accommodate the thin steel tube which acted as the single pressure tapping of each cylinder; the openings in the tappings were 1 mm in diameter.

Plastic tubing of 4,5 mm diameter was attached to the thin steel tube. This tubing led through the wall of the flume (via a hollow brass tube and further plastic tubing, both of 10 mm diameter) to the micro manometer. Holes were drilled centrally and along the axes of the aluminium end blocks, to accommodate the mentioned hollow brass tubes. Grub screws were tapped into the end blocks to secure the brass tube and ensure simultaneous rotational motion of the cylinder and the plastic tubing inside it; in this manner twisting of the internal plastic tubing was therefore not possible.

Two aluminium support blocks were also provided for each of the cylinders at approximately one third and two thirds their lengths (Figure 3.6). These blocks proved to be essential for a perfect closure along the longitudinal joints of the cylinders. Brass screws were used to fix the aluminium halves (of 2,5 mm and 2 mm thickness for the 50 mm and 30 mm diameter cylinders respectively) to the end and support blocks. The screws were filed down and filled with plasticine such that the cylinders would be completely smooth circumferentially; any secondary disturbance to the approach flow was therefore eliminated.

University of Cape Town

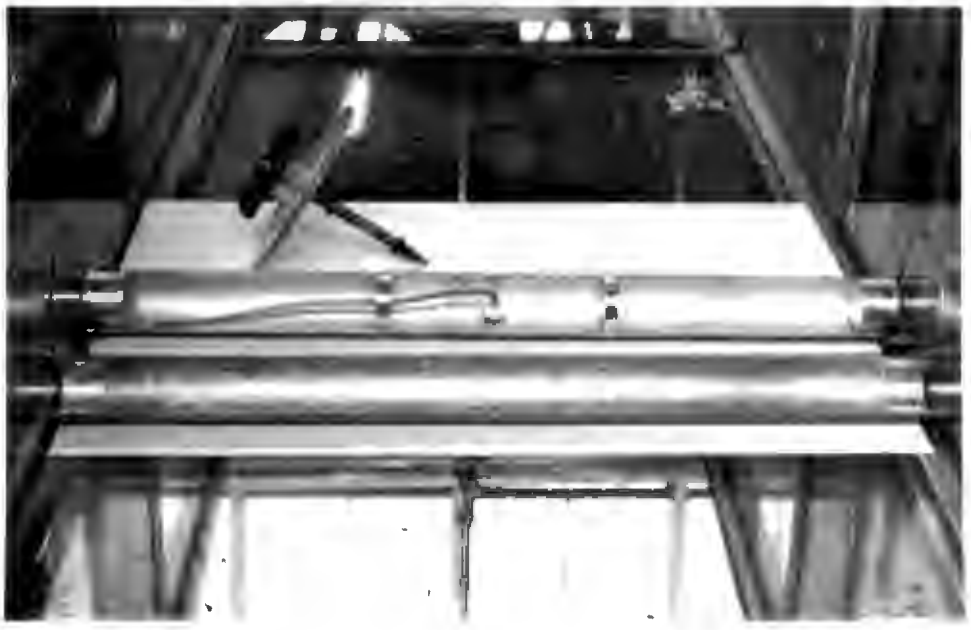

FIG. 3.6: Test cylinder, 50 mm diameter, in the flume; plastic tubing to pressure tapping and handwheel are shown.

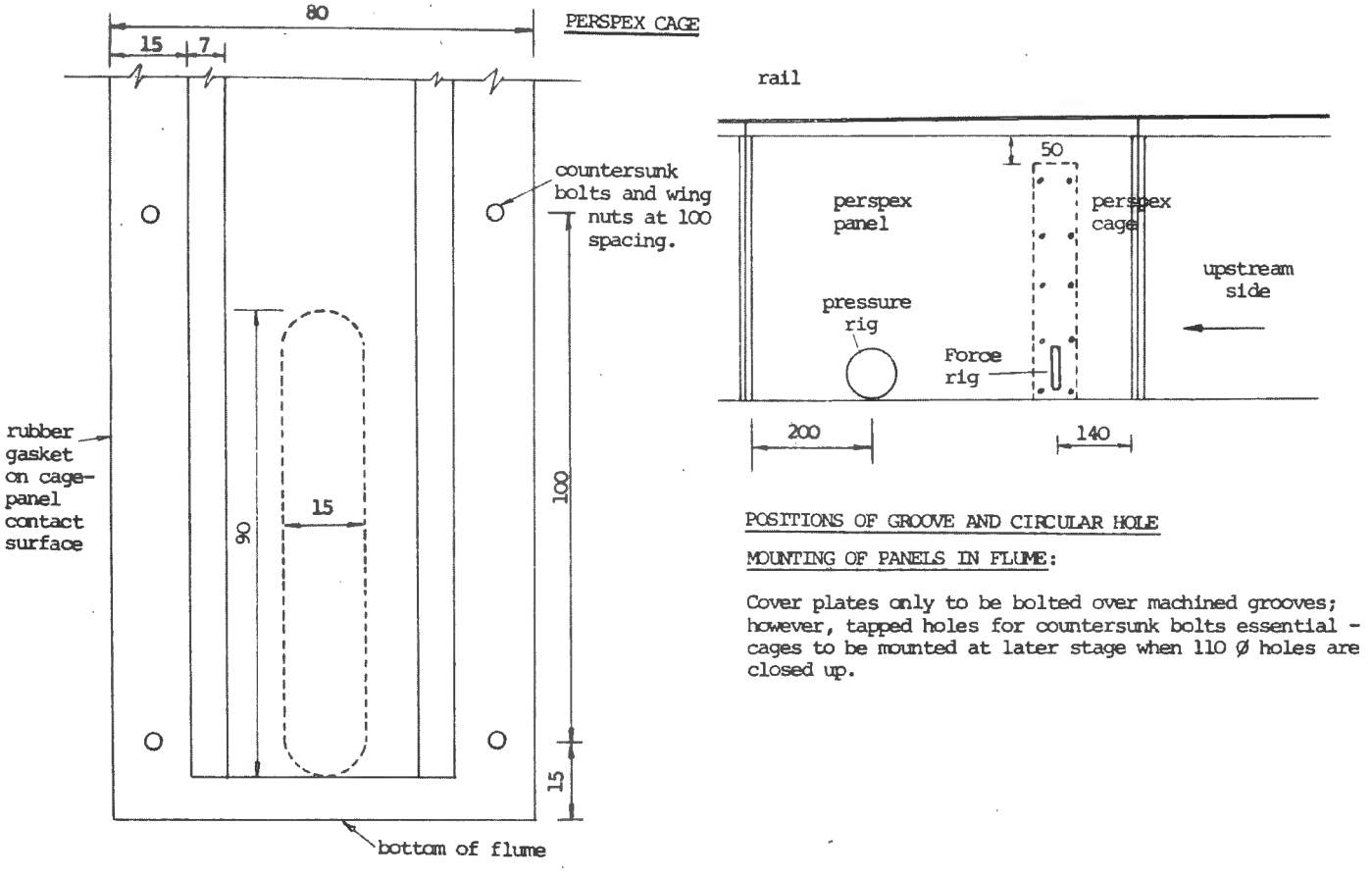

FIG. 3.7: FORCE RIG: POSITIONS OF OPENINGS IN THE PERSPEX PANELS AND DETAILS OF THE PERSPEX CAGE.

The construction of the cylinders was completed by milling each end down, such that there would be 0,5 mm clearance between the cylinders and the side panels when all the components were assembled.

3.4.3 Cylinder Mountings to Water Flume

The cylinder mountings served a multilateral purpose:

(i) The tubing leading from the pressure tapping to the micro manometer had to be accommodated;

(ii) The mountings had to rotate in unison with the cylinder, to facilitate the reading of pressure around the cylinder;

(iii) The mountings had to provide various height locations of the cylinder, as the intention was to take measurements with the cylinder located on the bed of the flume, as well as in proximity of the bottom.

University of Cape Town

Requirement (iii), height adjustment, was essential to avoid dismantling and re-assembling of the cylinder for various clearances above the flume bed. It was therefore decided to remove the two vertical glass panels, approximately 750 mm long, 500 mm high and 9,5 mm thick, of the flume at the testing area and substitute them with identical perspex panels. Before being mounted, openings had to be machined into the panels for the cylinder mountings and the force rig (Fig. 3.7 and Section 3.7.1).

Height adjustment, outside the flume, was achieved by using circular perspex discs of 110 mm diameter. The diameter chosen would allow clearances of 60 mm and 80 mm for the 50 mm and 30 mm cylinders respectively, for smooth cylinders and a smooth flume bed. The maximum clearance had to be limited to avoid the formation of surface waves as experienced by Brown (1967). A collar of 3 mm by 3 mm was machined into the outer circumference

of the perspex discs; the collar ensured that the water inside the flume 'pushed' the disc tight with the vertical side panels (Figure 3.4).

Openings identical to the dimensions of the perspex discs, were machined into the perspex side panels. Grooves were subsequently machined into the circumference of the discs to accommodate O-rings; due to the O-rings, a waterproof fit between the discs and the panels was achieved.

The perspex discs were calibrated by embedding transparent protractors of 100 mm diameter, marked in 1° intervals up to 360°, into their outer flat surfaces. Various height locations of the specimen cylinder could be calculated in degrees and the discs then turned to the required position.

To obtain the previously mentioned maximum clearance of 80 and 60 mm (for the 30 and 50 mm diameter smooth cylinders respectively) as well as zero clearance, two different pairs of discs had to be made for the two cylinders. Holes had therefore to be drilled at eccentricities of 40 mm and 30 mm (for the 30 and 50 mm diameter cylinders) from the disc centre on two separate pairs of discs. Each pair of discs had a solid brass stub (diameter 10 mm) mounted to the one disc and a hollow brass tube passing through the second disc (Figure 3.4); the cylinder concerned was supported at its ends by the stub and the hollow brass tube.

To provide vertical support for and lock the discs, a flat brass bar, 150 mm long, 30 mm wide and 6 mm thick, was fixed to each disc at one end, while the other end was screwed to the perspex panels of the flume (Fig. 3.4). The disc fixture was located at the centre of each disc by means of a threaded brass rod tapped into the disc; however, free rotation of the disc about its centre was still possible.

The disc attachments were rounded off by securing brass handles to the outer edge of each of the discs. The handles were necessary to

University of Cape Town

turn the discs, and naturally also the cylinder concerned, to whichever height location required within the possible range; virtually an unlimited number of locations was possible.

Apart from the openings for the support disc, an opening was also machined into each of the two perspex panels (for the flume) to accommodate the "force rig", of which the details are explained later in this chapter - refer to Figure 3.7 for the locations of the openings in the panels.

3.4.4 Handwheel to Rotate Cylinder

Before all the components explained thus far could be assembled, a handwheel was required outside the flume to rotate the cylinder.

To enable one to rotate the cylinder a degree at a time if required, a transparent protractor of 150 mm diameter was fixed tightly to the brass tube passing through the one perspex disc (Figures 3.4 and 3.8). A handwheel of 90 mm diameter was subsequently secured to the protractor and the brass tube, with the latter passing through it. A reference mark was placed on the brass handle visible behind the larger protractor; the angle of rotation of the cylinder's central pressure tapping, could therefore be determined with ease.

Finally, the length of the brass tube outside the flume, was limited by means of a metal ring, secured with grub screws to the tube. A minimum length of brass tubing was necessary to avoid obstruction from the mountings for the flume's framework.

University of Cape Town

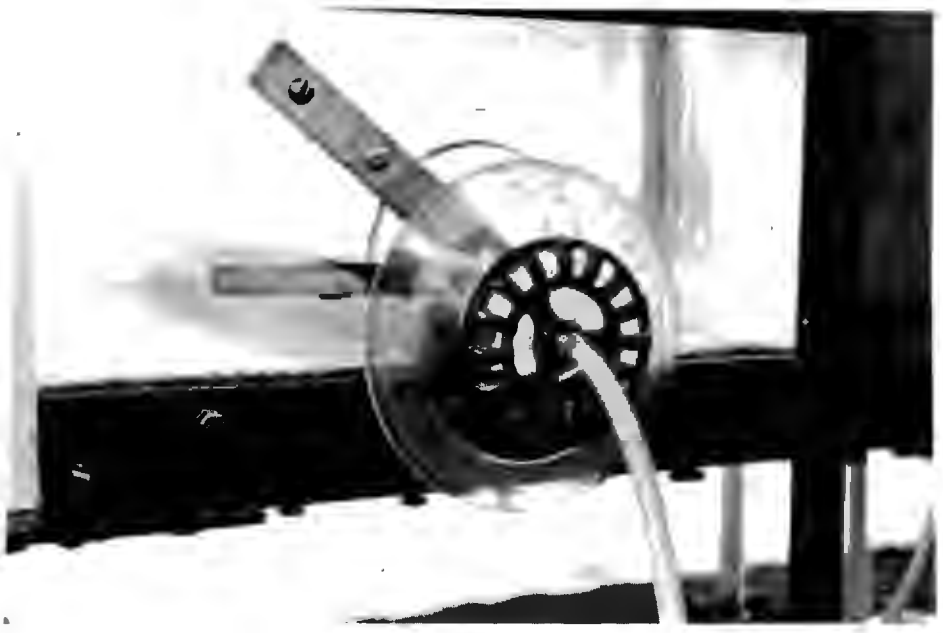

FIG. 3.8: Handwheel and protractor assembly; test cylinder visible in background.

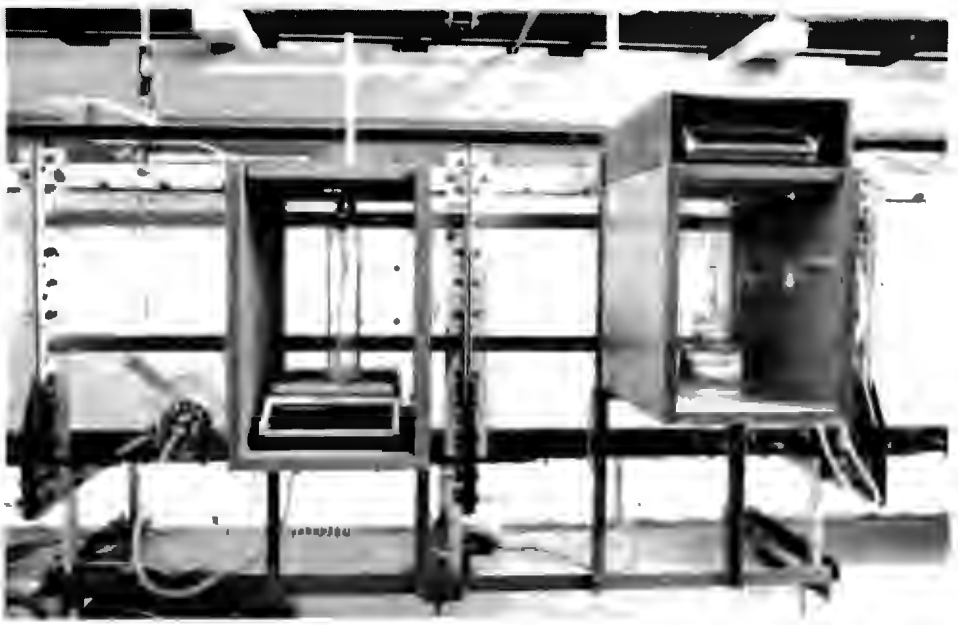

FIG. 3.9: Pressure rig, showing details of pressure and velocity micro manometers.

3.4.5 Assembling of the Pressure Rig

The fitting of the two vertical perspex side panels, proved to be a cumbersome operation before a proper watertight sealing around the edges, making contact with the aluminium supports of the flume, could be obtained.

Due to its design (Figure 3.4), the test cylinder had to be assembled inside the flume. The assembling procedure was as follows:

(i) The perspex discs were pushed into the corresponding openings in the side panels and secured by means of the brass bars to the panels;

(ii) The hollow brass tube, with the handwheel and larger protractor fixture, could now be pushed through the one disc;

(iii) The aluminium end blocks were subsequently fitted to the brass tube and the brass stub respectively;

(iv) The plastic tubing, leading from the central pressure tapping, was tightly fitted to the hollow brass tube;

(v) The two cylinder halves were screwed to the aluminium end blocks and intermediate support pieces. The cylinder was now ready for testing.

University of Cape Town

3.4.6 Housing for Pressure Data Acquisition

Pressure readings were read by means of a Mettler PE 3 000 balance (with an accuracy of 0,1 gram) on which a water column was weighed (Figure 3.9).

The water was contained in a perspex beaker. It was expected that the water level in the beaker would fluctuate above and below the water level in the flume, when pressure readings around the cylinder were taken. It was therefore essential to mount the balance and the "water column" on the side of the flume; close proximity of all the measuring instruments and the test cylinder was also necessary for practical control purposes.

To support a housing for the Mettler balance, a very rigid steel frame was designed (Figure 3.10). The framework was well founded on the heavy metal beam carrying the whole flume. The framework was further bolted to the vertical side supports of the flume (Figure 3.9).

A rectangular wooden box, dimensions 415 mm high, 270 mm wide and 420 mm deep, served as housing for the Mettler balance. Grooves were cut into the wood to accomodate a sliding panel made of perspex, for the front of the box facing the person recording measurements. This perspex panel was used to exclude draughts present in the laboratory; Mettler balances are susceptible to draughts. A perspex panel was fixed to the rear of the box to provide clear visibility of the water in the flume (Figure 3.9). Adjusting screws were also provided in the bottom of the housing for the levelling of the balance.

Holes were drilled through the side and top of the housing for the plastic tubing, attached to the test specimen. A wooden rod was inserted in the top of the housing to support the plastic tubing.

The housing was rigidly bolted to the framework. The Mettler balance was placed inside the housing and coupled to an electric power point. The perspex beaker, used to contain the water, was made of an uniform perspex pipe of 44,7 mm internal diameter and a length of 250 mm. A thin perspex disc (thickness 5 mm) was glued to the pipe, using chloroform, to form a beaker.

University of Cape Town

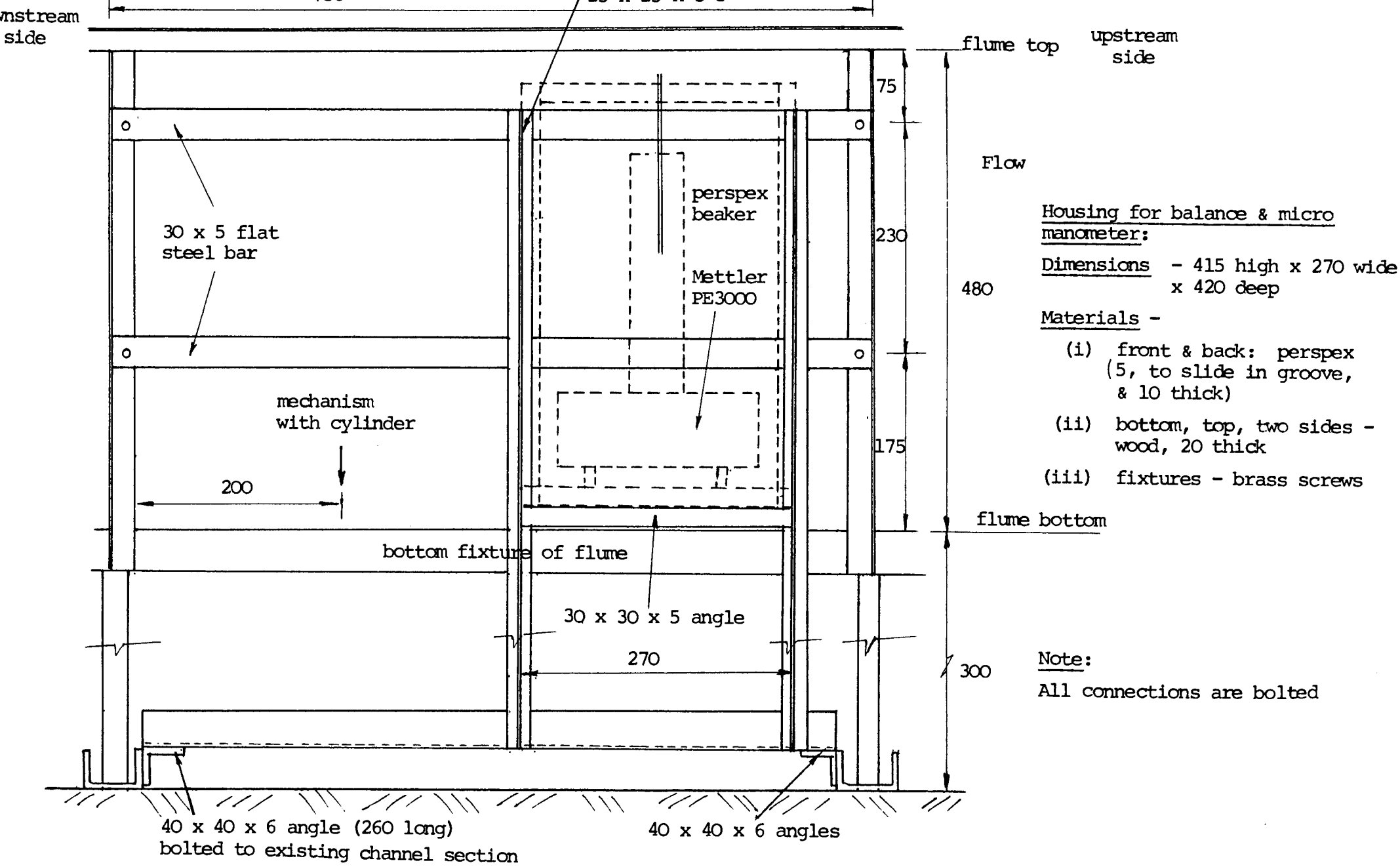

FIG. 3.10: PRESSURE RIG - FRAMEWORK FOR PRESSURE MANOMETER

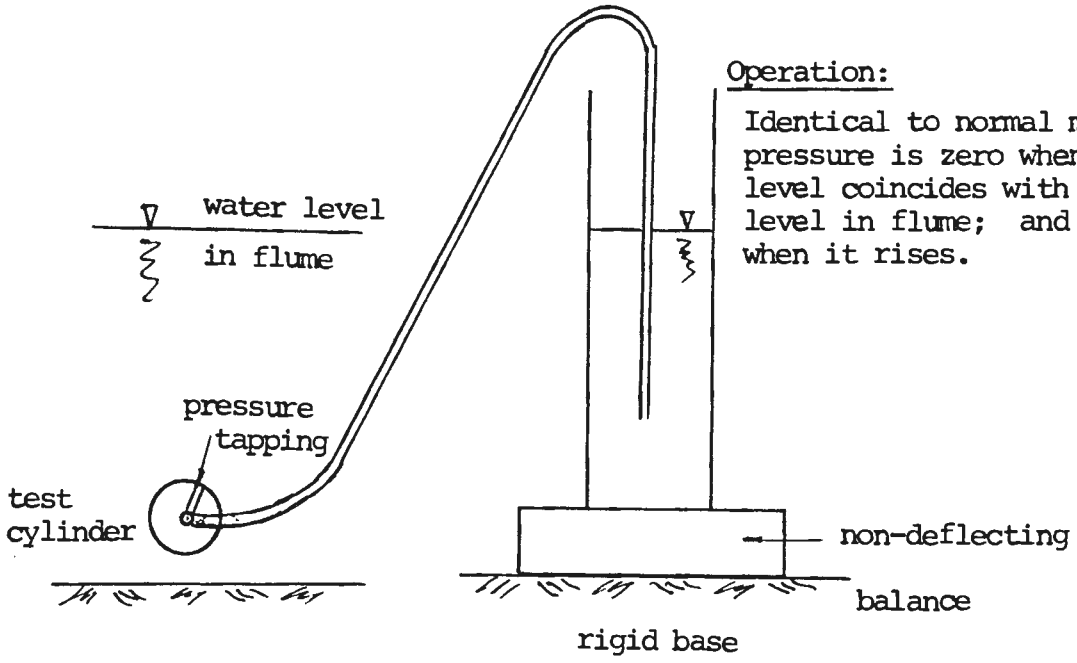

FIG. 3.11: PRESSURE MICRO MANOMETER: PRINCIPLE OF OPERATION

University of Cape Town

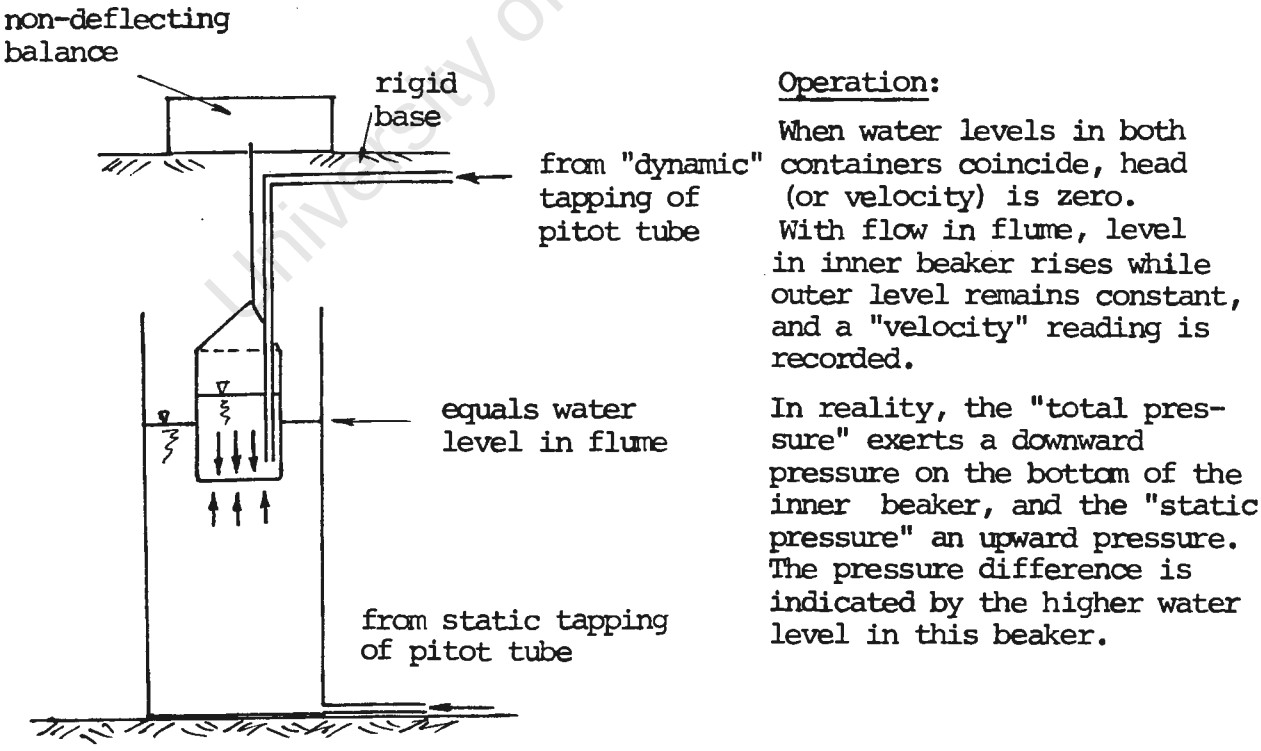

FIG. 3.12: VELOCITY DIFFERENTIAL MICRO MANOMETER: PRINCIPLE OF OPERATION

The "pressure rig" was completed by suspending a plastic tubing of 10 mm diameter into the perspex beaker. To the end of the tubing was attached a perspex pipe of equivalent diameter, to avoid bending or twisting of the end when submerged in water. The other end of the plastic tubing was fixed to the brass tube, protruding from the handwheel mounted to the specimen cylinder (Figure 3.8).

The principle on which the pressure micro manometer operates is illustrated in Figure 3.11. It is briefly explained as follows:

(i) The perspex beaker is placed on the balance;

(ii) The plastic tubing, connected to the cylinder, is primed and water allowed to flow into the beaker while the tubing is hanging in the water column inside the beaker - the tubing should not touch the sides of the beaker;

(iii) When the water in the flume is stationary, the water levels in the beaker and in the flume will correspond - no pressure (zero gauge pressure) is therefore recorded;

(iv) Once the water in the flume starts flowing, the level in the beaker will rise or fall depending on the circumferential position of the pressure tapping, in relation to the approach flow and the proximity of the cylinder to the bed of the flume.

The mass reading on the balance is converted to water head in cm, by dividing the recorded value in grams (or cm^3, as 1 cm^3 weighs 1 gram) by the cross sectional area of the beaker.

3.5 Device for velocity measurement

The device designed for the measurement of flow velocities, was even more unique than that developed for the measurement of pressures.

The apparatus consisted of the following two main components:

- a pitot tube;
- housing for velocity recording.

These components are briefly described below.

3.5.1 Pitot Tube

A pitot tube, in an L-shape and with two inlets was used. As usual the main inlet, directed to the approach flow, formed a stagnation point in the flow. The second inlet was on the side of the tube, perpendicular to the flow; its purpose was to record the static head (or water level) of the flow.

The pitot tube's vertical section was about one metre long and fixed to a mounting which accommodated a linear vernier scale; vertical displacements could be determined accurately to the nearest 0,1 mm.

The pitot tube and its mounting were supported horizontally on a rigid frame made of two steel bars, which could slide on the rails above the flume, upstream or downstream. Marks were made on the horizontal support such that displacements of the pitot tube along the width of the flume could be measured to the nearest millimetre.

Before coupling the pitot tube to a micro manometer by means of two plastic tubes, all joints of the pitot tube that appeared to be vulnerable to leakage, were properly sealed with a quick setting putty.

3.5.2 Housing for Velocity Recording

Analogous to the reading of pressures, the recording of flow velocities was done by means of a Mettler balance. However, a Mettler PE 300 with

University of Cape Town

an accuracy of 0,01 gram was used and the principle of operation was that of a differential micro manometer.

The total head and static head water columns were provided by the pitot tube. The objective of the "velocity recorder" was to register the difference between the total head and the static head directly.

The principle of operation of the differential micro manometer under discussion is explained with reference to Figure 3.12:

(i) A container, for example a transparent beaker, is suspended from the hook under the Mettler balance;

(ii) Simultaneously, the container in (i) is hanging in a second much larger transparent container;

(iii) Water from the static head inlet of the pitot tube, is fed to the larger container, while water from the total head inlet (stagnation point) flows into the smaller container.

(iv) When the water in the flume is stationary, the flume's water level will be at the same elevation as the water levels in the two containers, that is, no head difference or a zero velocity reading is registered;

(v) When the water in the flume flows, the level in the inside container rises and the mass of the water above the static water level is recorded on the sensitive non-deflecting balance.

The mass registered on the balance is easily converted to height h by dividing the mass in grams by the internal cross sectional area (in cm^2) of the inside container. From the formula

$$v = \sqrt{2gh} \qquad (3.1)$$

the velocity of the flow is then calculated.

University of Cape Town

The housing for the "velocity recorder" was mounted on the side of the flume, adjacent to the housing for pressure measurement. The housing was almost identical to the one built for the "pressure recorder", explained in Section 3.4.6 above. However, the Mettler PE 300 balance had to be supported on top of the wooden box of dimensions 350 mm high, 250 mm wide and 420 mm deep, as the weighing operation occurred below the balance. Holes had to be drilled into the top and the sides of the box, to accommodate the vertical support for the "inner" beaker and the plastic tubing attached to the pitot tube respectively (Figure 3.13).

The inner container, was a uniform glass beaker of internal diameter 52,3 mm. It was supported around its rim by a collar made of perspex, to which a brass wire cage was fixed with a hook at its uppermost end. Various lengths of brass wire, with hooks at both ends, were cut such that flow velocities could be measured at different water depths in the flume. Similarly, different lengths of glass tubing had to be provided for the inflow section to the inner beaker. Obviously the glass tubing was not to touch the sides or the bottom of the glass beaker. The glass tubing was bent in an L-shape and fixed to the top panel of the housing (Figure 3.13).

The larger outer container was made of an uniform perspex pipe of about 100 mm in diameter and 300 mm long. A thin perspex pipe was glued into the side of the completed larger beaker, close to its bottom, to act as inlet for the "static head connection".

A draught cover was placed over the Mettler balance on top of the housing, to exclude draughts in the testing area. As with the housing for the "pressure recorder", perspex panels were fixed to the back of the housing and acted as a draught shield at the front.

The housing was bolted to a rigid steel frame on the side of the flume. Although the framework was virtually the same as that indicated in Figure 3.10, the housing was mounted at a higher elevation due to the difference in weighing procedure (from below

University of Cape Town

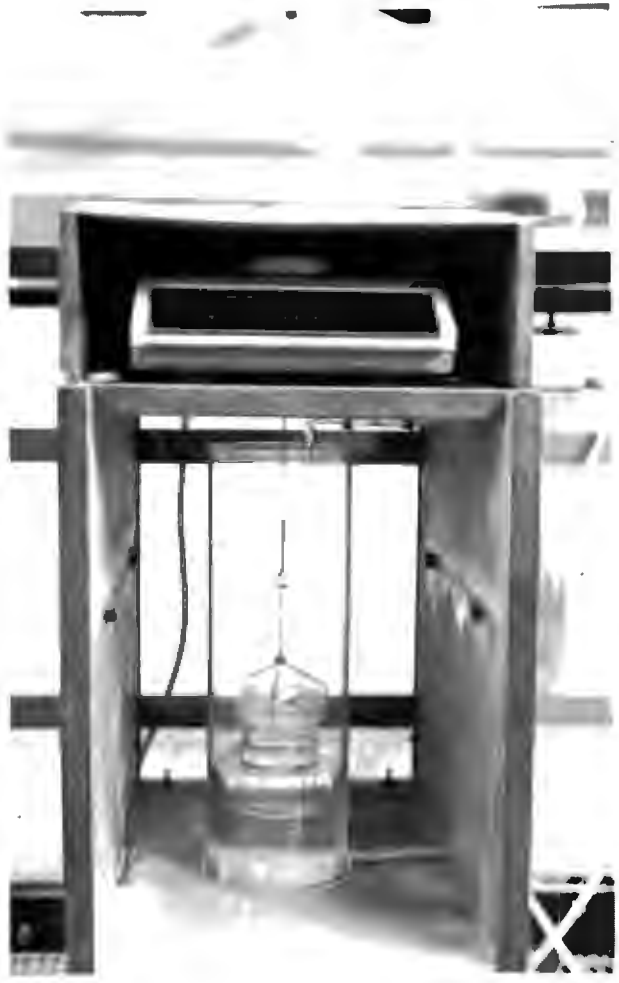

FIG. 3.13: Close-up view of differential micro manometer, used for velocity recording.

FIG. 3.14: Flume with rough bed mats and roughened test cylinder.

instead from above) and the fact that the water level in the flume had to be approximately 250 mm above the flume's bottom; that is, a water depth of approximately five times the cylinder diameter, (the maximum diameter equals 50 mm in this case) is required to avoid standing waves (Littlejohns, 1974).

3.6 Bed and Cylinder Roughness

Cylinders were tested with two conditions of the bed: smooth and a pebble stone bottom. Except for the smooth cylinders, tests were also performed after applying surface roughness to the cylinders.

The smooth condition of the bed was due to the glass and aluminium panels mounted in the bottom of the flume. A machined and sanded (using fine waterpaper) aluminium surface, provided the smooth condition of the test cylinders.

For the bed roughness, hard rubber mats, 10 mm thick, were used. To the rubber mats, 6 mm stone pebbles were glued (Figure 3.14). The pebbles provided an ideal rough bed. The mats could be placed with ease in and removed from the flume.

A fairly coarse sand was used to roughen the cylinders. The sand was thoroughly sieved to obtain virtually uniform particles of 0,9 mm in size. After experimenting with various adhesives for the sand, it was decided to use household varnish. A good coating of varnish was applied to the cylinders, and the sieved sand particles sprinkled evenly over the varnish. The varnish coating was allowed to dry overnight. The roughened 30 mm diameter cylinder is shown in Figure 3.14.

3.7 Force Rig

The "force rig" was essentially a light metal framework, designed to measure the lift and drag forces exerted by a steady flow on the

University of Cape Town

test cylinder directly. As mentioned in Chapter 1, it was found necessary to develop a direct method to compare the force values with those determined indirectly by means of the "pressure rig". The layout of the force rig is shown in Figure 3.2. It consisted of the following two main components:

- framework (fixed to the test cylinder), suspended above the flume;
- housing with flow velocity recorder.

3.7.1 Framework

Soon it was evident that the framework had to be light and rigid to eliminate deflections of its relatively long members. To avoid the possibility of resonance (Blevins, 1977), aluminium was chosen as the material; its Bulk modulus of 75 GN/m^2 and its Young's modulus of 71 GN/m^2 generated a natural frequency, which was removed sufficiently from the vortex shedding frequency. A sketch outlining the design of the frame attached to a test cylinder, is indicated in Figure 3.15.

The mechanical principle on which the "force rig" is based, is illustrated in Figure 3.16. It was of utmost importance that the vertical members were plumb, and that the horizontal members were level throughout a testing session.

All the members of the frame were made of rectangular aluminium tubing, 18 mm by 12 mm in cross section with a wall thickness of 1,5 mm. The members were welded together as shown in Figure 3.15.

A hollow aluminium cylinder of diameter 50 mm was used as test cylinder. Solid aluminium cylinders of length 50 mm were press forced airtight into the ends of the test cylinder. The ends of the cylinder were subsequently machined to the required length of 604 mm. Holes were tapped into the solid end pieces of the cylinder to accommodate solid brass shafts of diameter 10 mm - refer to the sketch in Figure 3.17.

Holes were drilled through the two vertical limbs of the framework at their ends, such that the limbs could be screwed to the brass

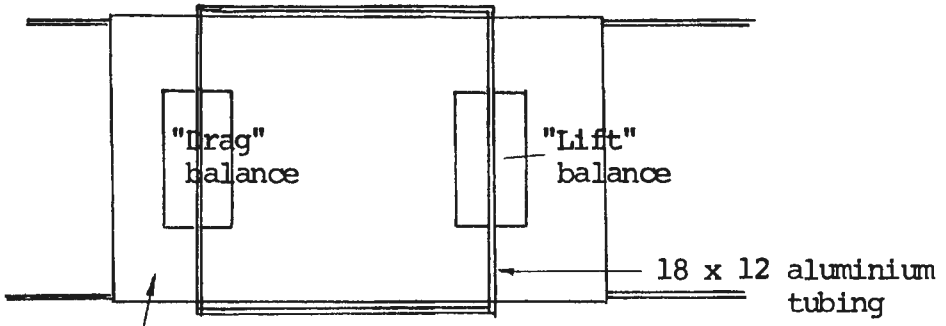

PLAN

wooden platform

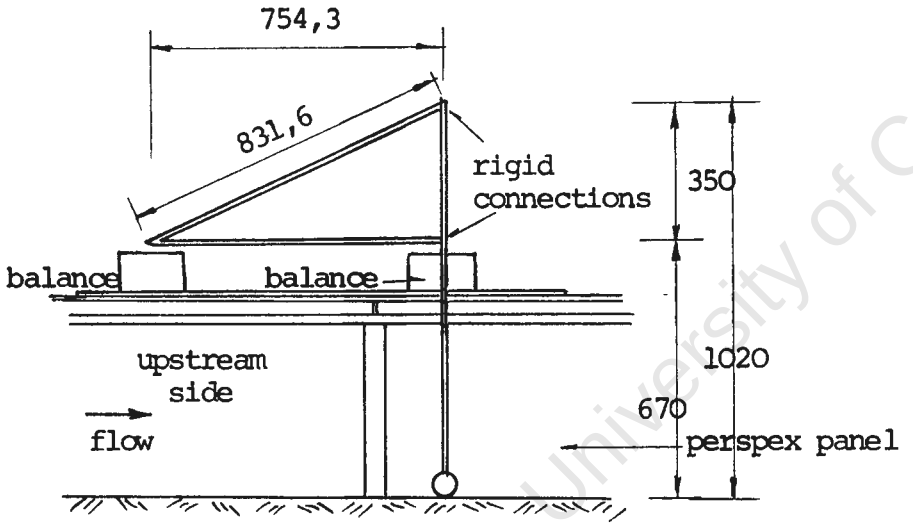

SIDE ELEVATION

Scale 1:20

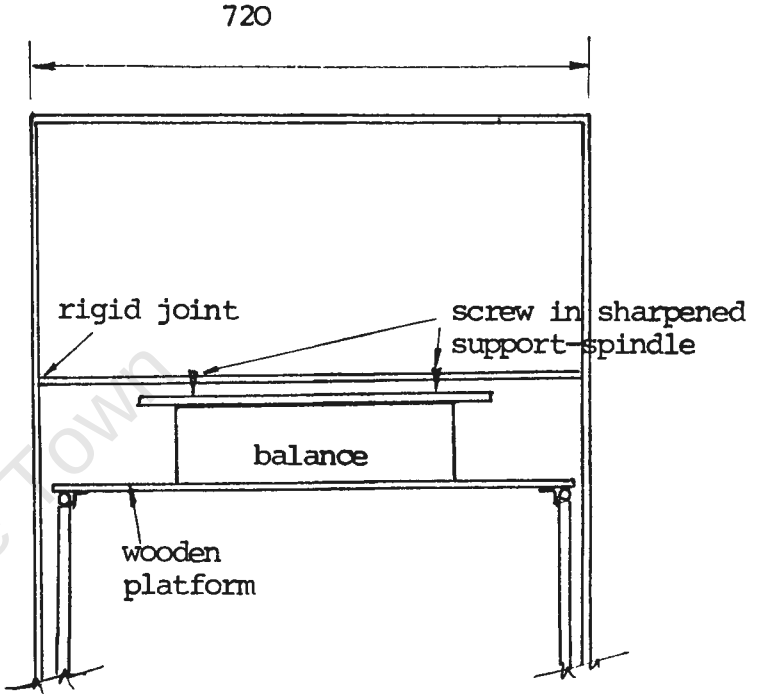

Scale 1:10

CROSS SECTION OF ALUMINIUM FRAME

University of Cape Town

FIG. 3.15: FORCE RIG, SHOWING OVERALL VIEW AND ELEVATIONS

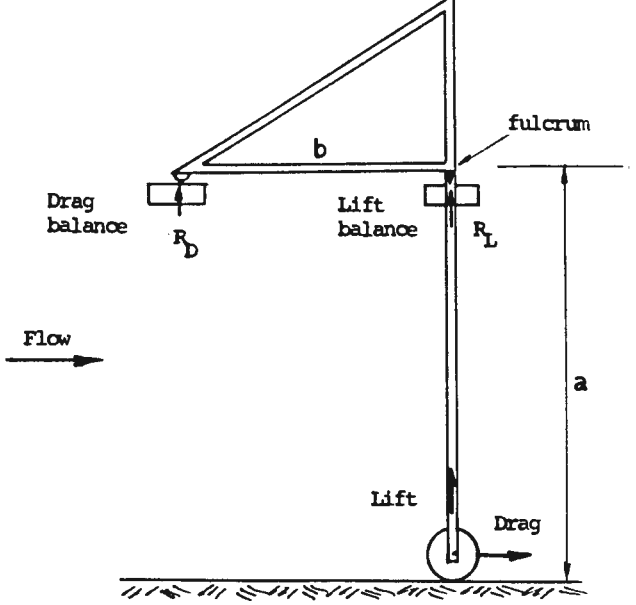

(i) Lift force

Lift force (gram-force) $= -R_L$

= negative reading on lift balance

(ii) Drag force

Drag force x a $= R_D \times b$

Drag force (gram-force) $= \frac{b}{a} \times R_D$

$= \frac{b}{a}$ x reading on drag balance

FIG. 3.16: PRINCIPLE OF THE FORCE RIG: DIRECT RECORDING OF FORCES

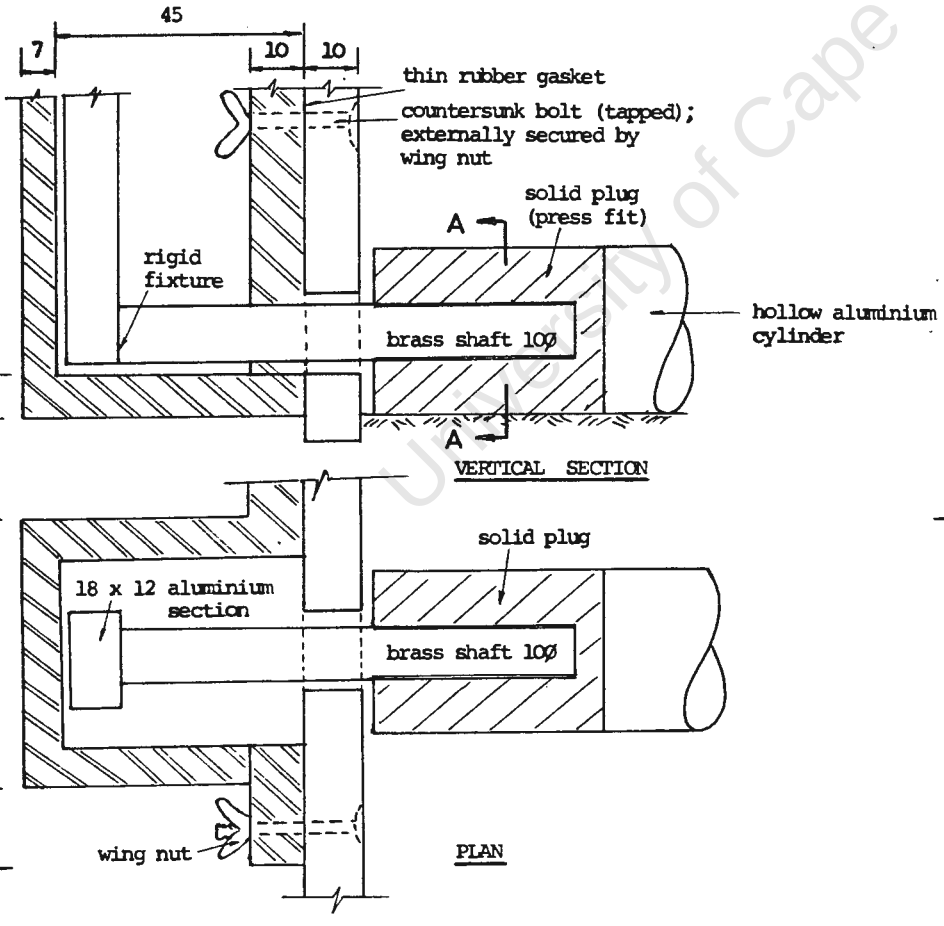

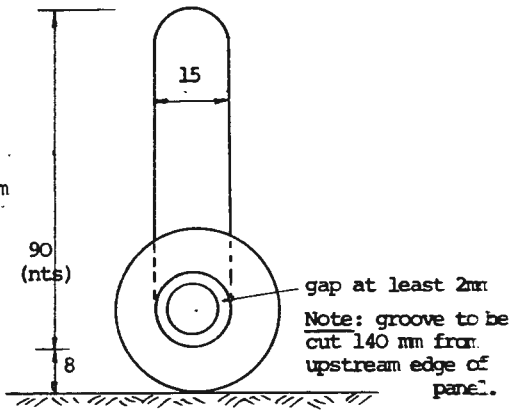

SECTION A:A

FIG. 3.17: FORCE RIG - SKETCHES SHOWING DETAILS OF THE FRAME TO TEST CYLINDER FIXTURE

University of Cape Town

shafts of the test cylinder. Holes were also provided at distances of 30 mm and 60 mm from the first holes, to enable the cylinder to be positioned at these elevations from the bed of the flume. The frame and cylinder weighed 2,8 kg together.

To measure the forces directly, the following Mettler balances were utilised:

(i) Lift force - Mettler PE 6 000 (range: 0 to 6 000 grams), accurate to 0,1 gram;

(ii) Drag force - Mettler PE 3 000 (range: 0 to 3 000 grams), also accurate to 0,1 gram.

A wooden platform was placed firmly on the railings above the flume. The platform supported the mentioned two Mettler balances. A length of 400 mm rectangular aluminium tubing, (as used for the frame) was rigidly fixed to the weighing platform of the Mettler PE 6 000 balance, by means of adjustable steel hooks. Dents were now made in the aluminium tubing close to its ends (Figure 3.15). The vertical section of the frame was supported on the Mettler PE 6 000 balance as follows:

- two sharpened screw-in-spindles were fixed to the bottom horizontal member;

- the two sharp spindles were placed in the dents on the aluminium tubing, fixed to the top of the balance and functioned as frictionless pivots.

The horizontal section of the frame, above the wooden platform, was allowed to be supported by the second Mettler balance, the PE 3 000, such that the frame's horizontal members would be absolutely level at all times. Half round steel bars were strapped to the horizontal member, making contact with this second balance; this ensured uniformly distributed loading on the balance as well as a narrow point type contact.

University of Cape Town

The brass shafts of the test cylinder passed through the holes provided in the perspex panels of the flume. Although this meant that the influence of side effects was reduced inside the flume when testing, the leakage of water through the holes in the side panels had to be taken care of. Perspex cages using 7 mm sheeting, were made (Figure 3.17) to shroud each of the two vertical limbs of the frame. Holes were drilled through the flanges of the cages, such that they could be screwed to the perspex panels of the flume. Rubber gaskets were made to obtain a waterproof seal between the cages and the flume's side panels.

3.7.2 Assembling of the Frame before Testing

Although it might appear logical from the above section, the assembling procedure for the frame and cylinder before testing, was briefly as follows:

(i) The cylinder, without its brass shafts, was placed inside the flume opposite the openings in the side panels;

(ii) The brass shafts were now screwed into the cylinder;

(iii) The platform and the two balances were placed over the testing area (rails were previously fixed to the bottom of the platform, such that it could be pushed away from the testing area);

(iv) The frame was lifted onto the aluminium support fixed to the Mettler PE 6 000 balance;

(v) The two vertical limbs of the frame were now screwed to the brass shafts of the cylinder;

(vi) The procedure was concluded by covering the limbs with the perspex cages, before fixing them watertight (using the rubber gaskets) to the side panels of the flume.

University of Cape Town

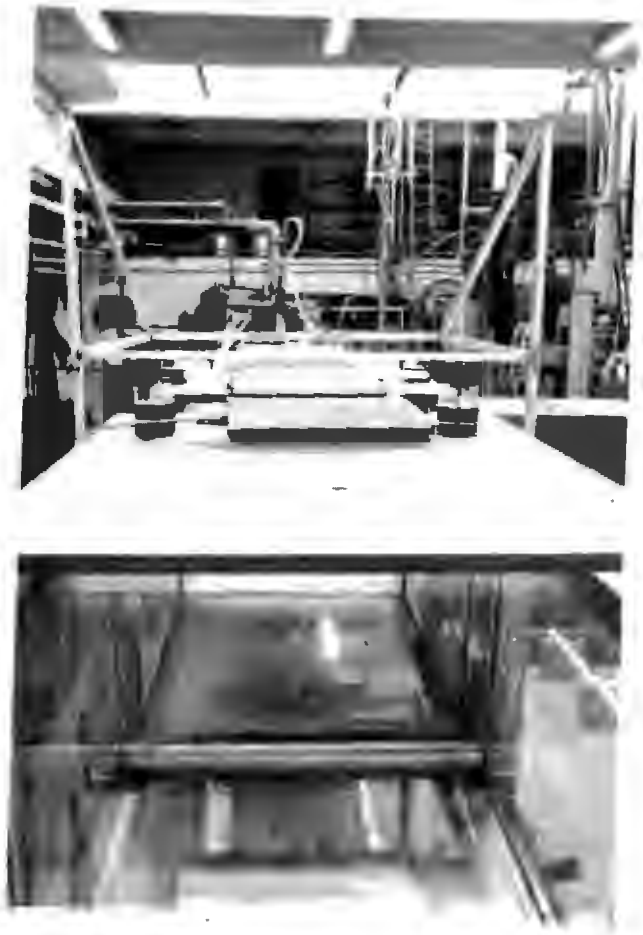

(a) Upstream view, showing pivots above the front balance.

(b) Downstream view, showing four dashpots fixed to frame.

FIG. 3.18: FORCE RIG, SHOWING DETAILS ABOVE PLATFORM, ON TOP OF FLUME.

During preliminary tests performed with the force rig, it was found necessary to dampen the vibrations of the frame. The vibrations were not physically visible, but made reading of the balances very difficult. Four dashpots were therefore placed on the wooden platform to "support" the frame (Figure 3.18); the vibrations were limited to such a degree that the digital screens of the balances could be read comfortably. The dashpots consisted of perspex beakers and circular perspex discs, fixed at one end to thin brass rods; the other ends of the brass rods were rigidly fixed to the two horizontal members of the frame as indicated in Figure 3.18. Transmission oil (SAE 90) was used as the fluid in the dashpots.

3.7.3 Housing with Flow Velocity Recorder

The same housing and differential micro manometer (refer to Section 3.5.2 above) as used with the "pressure rig", was utilised again with the "force rig". However, the velocity profile, along the width of the flume, was also required in this case, specifically for the determination of the effective length of the cylinder. Flow velocity measurements had therefore to be taken at different horizontal and vertical positions of the pitot tube.

CHAPTER 4 - EXPERIMENTAL PROCEDURE

4.1 Preliminary Preparation

Except for the determination of flow velocities, the experimental procedures for both rigs were completely different. Before describing these procedures, certain preliminary preparation work had to be undertaken.

4.1.1 Mercury Manometer

A differential mercury manometer was connected to the venturi section, inserted in the supply pipe for the flume's tank; the manometer was mounted on the side of the tank. As the manometer contained some air and no mercury was visible, it had to be refilled with mercury. The manometer was subsequently primed, to remove the air before being ready for use: the supply flow to the tank was indirectly read in inches mercury and converted to m^3/sec, by means of a conversion formula. The average velocity values subsequently deduced, provided a useful check.

4.1.2 Reducing Turbulence at Upstream End

A reasonable degree of turbulence was observed in the flume at the upstream end, when water was flowing along the flume. To reduce the turbulence, a frame with vertical wire mesh mats fixed to it, was lowered into the flume at the end concerned. The wire mesh mats were placed along the length of the flume and spanned the width of the flume.

4.1.3 Steady Flow

Once water was allowed to flow along the flume, the downstream control gate had to be raised or lowered, until the water depths, five metres upstream and downstream of the test cylinder, were equal. The level of the flume was also slightly adjusted, but did not result in achieving a steady state sooner. For virtually all the runs, the level of the flume was set at 12 in 1 000.

4.2 Pressure Rig

4.2.1 Pressure Distributions

The primary objective with the pressure rig, was to measure the pressure distribution around the test cylinder, while an accurate velocity profile of the approach flow was simultaneously recorded at a point 2,65 metres upstream from the cylinder.

As mentioned earlier, smooth cylinders with diameters of 30 mm and 50 mm were used as test specimens. The height of the test cylinder above the flume bed was varied. Tests were also performed with roughened cylinders and smooth and rough flume beds; the flume bed was smooth in its "undisturbed" state. For each combination of parameters, of which there were 28 combinations, tests were performed with approximately five different approach flows. Each of the runs took almost three hours to perform. Table 4.1 on the following page, gives a summary of the various combinations of tests performed.

Pressure readings were taken at intervals of 10° around the cylinder, starting from the front cylinder centre. By means of the handwheel, fixed to the cylinder, the single pressure tapping could be rotated comfortably and set accurately to 1° on the protractor concerned. Before every series of readings, taken at the same

height above flume bed, the 90° position of the tapping was very carefully determined by means of a sensitive plumb level and a vernier scale. This position was noted on the protractor, and the cylinder rotated back to its zero position at the front centre of the cylinder.

Cylinder Diameter (mm)	Cylinder Surface: Smooth/ Rough	Flume Bottom: Smooth/ Rough	Clearance between cylinder and bottom (mm)	Number of Runs
50	Smooth	Smooth	0; 2,73; 5; 10; 30; 60	26
52	Rough	Smooth	0; 10; 28,8; 59	24
50	Smooth	Rough	0; 10; 45,5	15
52	Rough	Rough	0; 10; 42,2	15
30	Smooth	Smooth	0; 10; 80	12
31,8	Rough	Smooth	0; 10; 79	12
30	Smooth	Rough	0; 10; 65,7	15
31,8	Rough	Rough	0; 10; 64,4	15
			Total	134

Table 4.1: Summary of Various Combinations Tested

Before pressure readings could be taken, the tubing leading to the pressure manometer had to be primed; this could obviously only be done with the water stationary in the flume and the test cylinder completely covered with water. When priming the tubing, care was taken in not spilling water on the balance and wetting the sides of the perspex beaker when filling it. The rationale of the pressure determination method is described in Figure 3.11.

The water depths of the various approach flows were seldom the same. The zero "pressure" reading (in grams) on the balance, was therefore simply established (before the daily continuous series of tests) as follows:

(i) With the perspex end of the tubing submerged under the water in the beaker, the beaker with its contents was raised above the platform of the balance;

(ii) The balance was zeroed and the beaker lowered onto the platform.

The pressure manometer was now operational. The zero reading was checked, after each set of pressure readings taken from cylinder positions 0^{o} to 360^{o}.

The readings on the Mettler balances took a long period of time (between 10 and 15 minutes in some cases) to settle; this resulted in some runs taking as long as three hours or longer to perform.

4.2.2 Static Water Pressure Checks

A reference pressure was required for every set of pressure readings, to establish how the "live" pressure tapping readings related to the static water pressure for the run concerned.

After every continuous series of tests, a static water pressure check had to be done. With the "pressure" balance still operational, the downstream control gate was raised and the approach flow valve closed. The water level inside the flume was allowed to stabilise (it usually took at least ten minutes) and the pressure reading on the balance noted as well as the corresponding water depth, of the flume, using a vernier depth gauge. The water level in the flume was raised or lowered and at least three similar pairs of "static water" readings recorded. An

example of static water pressure readings is graphically represented in Figure 4.1.

Reference static water pressures for every run, could be read from the graph concerned or interpolated from a set of water depth and pressure readings.

4.2.3 Velocity Distributions

Velocity readings were taken exactly along the longitudinal axis of the flume and 2,65 metres upstream from the cylinder. The velocity measurements were not influenced by the cylinder; a check one metre upstream from the cylinder, generated equivalent velocity readings. The velocity measurements can therefore be taken as the velocity that would exist near the bed, if the cylinder was not present. Velocity profiles were recorded for each test run.

Although the principle on which the differential "velocity" micro manometer functioned, is explained in Section 3.5.2 and Figure 3.12, its priming and zeroing were of utmost importance. The latter procedure is therefore fully described here, with reference to the sketch in Figure 4.2:

(i) Tubes b and d (total and static pressure tubes respectively) from the pitot tube are primed and the flow stopped by means of laboratory clamps;

(ii) The inner glass beaker suspended from the balance, is vertically positioned at the water level of the flow along the flume;

(iii) The two beakers are filled with water from a container placed above the housing, via tubes a and c;

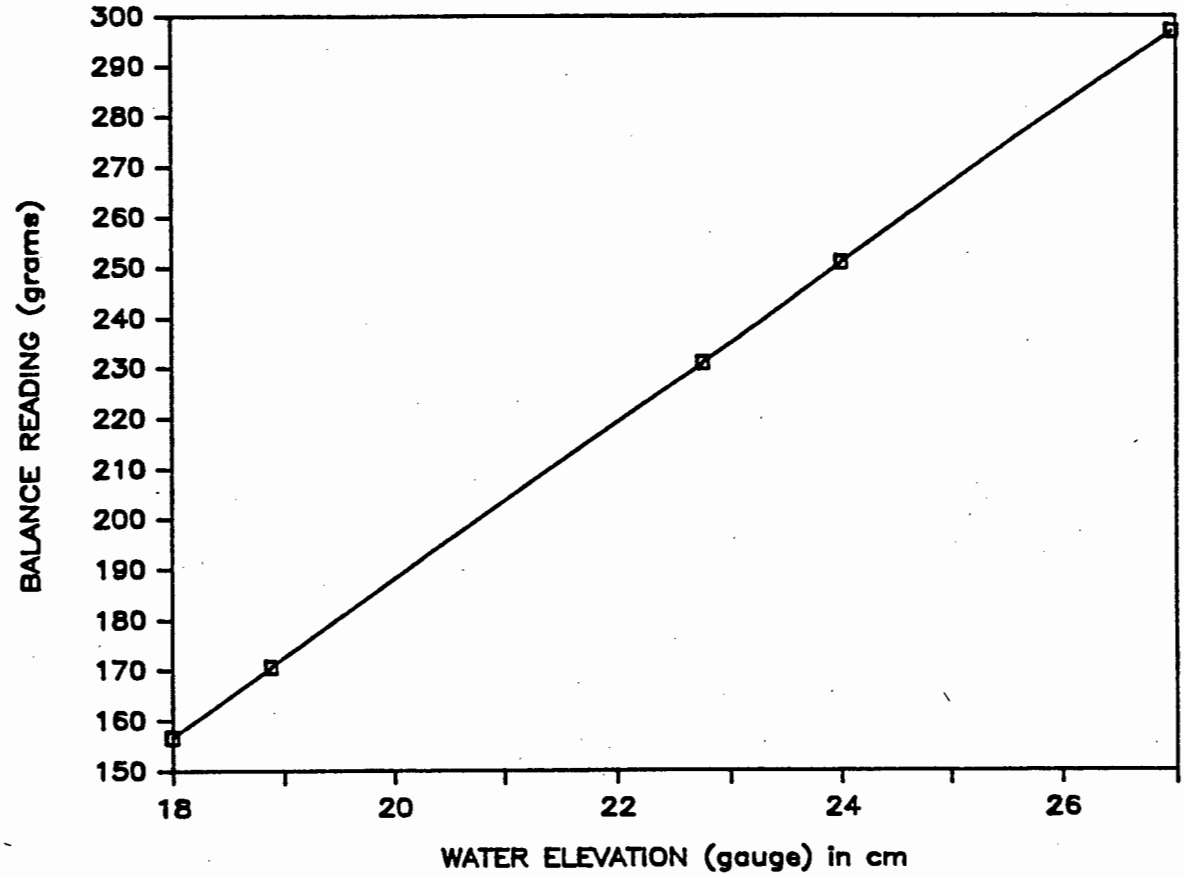

FIG 4.1: GRAPH SHOWING A SET OF STATIC WATER PRESSURE READINGS

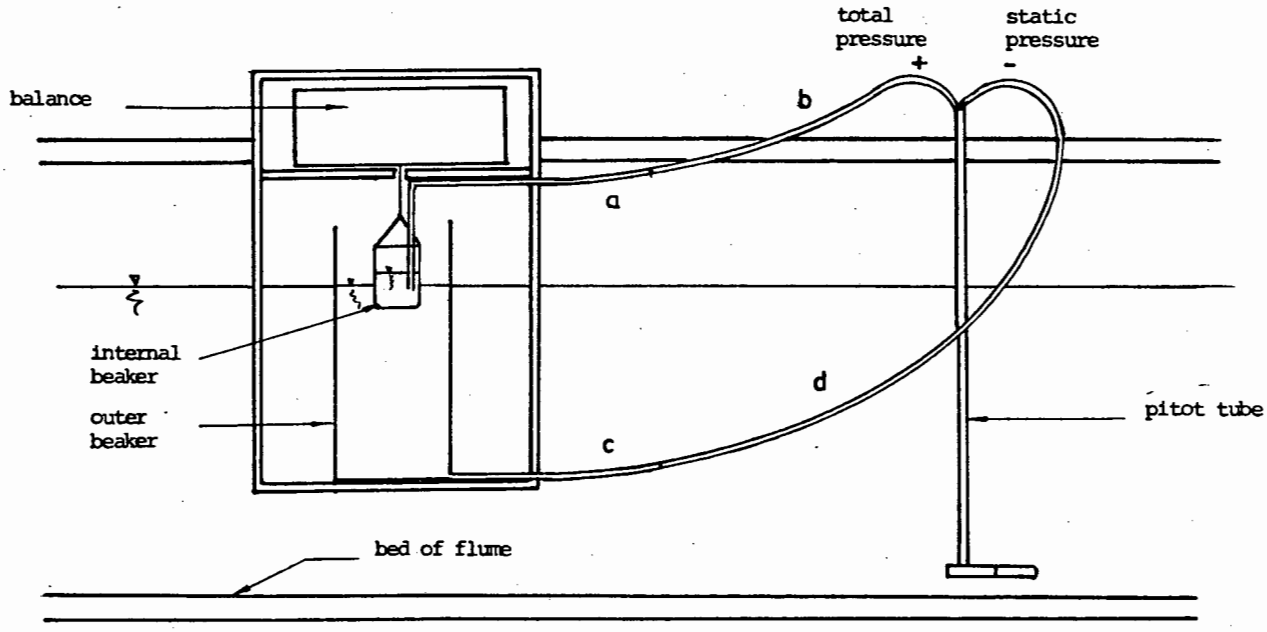

FIG 4.2: VELOCITY MICRO MANOMETER

(iv) The outflow from the beakers are prevented by means of two further laboratory clamps;

(v) Once a steady flow state is achieved in the flume, the tubes a, c and d are joined using a three way connector;

(vi) The system is now left a period of time until the water levels in the two beakers are exactly the same, when the balance is zeroed;

(vii) Tube c is carefully connected to tube d, and tube a to tube b - care has to be taken to avoid entrapped air in the system.

The system is now operational and "velocity" readings will be recorded on the digital screen of the balance.

4.2.4 Other Measurements

For each run the water temperature was recorded (as it affected the kinematic viscosity of water) and the water depths at various positions along the length of the flume.

The various roughness conditions of the test cylinders and the flume bottoms, as mentioned in Section 3.6., were:

(i) 0,9 mm sand particles glued to the cylinder surfaces ($k/D = 2 \times 10^{-2}$ and 3×10^{-2} for the 50 and 30 mm cylinders);

(ii) 6 mm stone pebbles fixed to rubber mats to serve as rough bottom.

The various heights above the flume, at which tests were performed, are indicated in the Table 4.1. The perspex discs, with embedded protractors, functioned extremely well as height adjusters.

4.3 Force Rig

Before the force rig was set up, the openings in the side panels for the pressure rig were closed by means of circular perspex discs, which had O-rings embedded along their perimeter edges.

4.3.1 Zeroing of "Force" Balances

To zero the "force" balances described in Section 3.7.1, the water in the flume had to be completely stationary at a convenient water depth, approximately at the operational depth, that is, 5 x cylinder diameter. Both balances were now zeroed and the water depth measured with a vernier depth gauge. "Lift" balance readings and water depth measurements were subsequently taken at at least two stationary water levels, above and below the original "zero" level. For higher water levels the "lift" balance recorded negative readings and positive readings for lower levels; this was due to an apparent loss of weight, as the vertical limbs of the frame were further submerged under water as the water level rose in the flume and the perspex cages. No change was recorded on the "drag" balance.

The apparent loss of or gain in weight (of the frame) versus the water depth, is represented graphically in Figure 4.3. The centimetre change in water level was equivalent to 3,9317 gram-force loss/gain of weight.

4.3.2 Force Readings

The system was now ready for testing. Due to the susceptibility of the system to vibrations, the zeroing procedure was repeated for every set of force readings, with each different approach

flow. The four dashpots "cushioning" the framework on the platform, dampened the vibrations to a large degree. Care was also taken to ensure that the vertical limbs of the frame were not touching the sides of the flume, and that the cylinder was free to move inside the openings in the side panels.

Once the zeroing procedure was completed, the stationary water in the flume was allowed to flow along the flume, until a steady flow state was achieved. The average readings on the "lift" and the "drag" balances were taken separately. Initially the readings fluctuated continuously on the "lift" balance over a range of as much as 30 grams, while the "drag" balance readings were almost constant. The apparent instability of the frame was solved by loading the frame, directly above the two vertical limbs, by means of 500 gram weights on each side. This reduced the range of the "lift" readings to about one gram, representing a 0,42% deviation.

In calculating the lift force applicable, the gain in or loss of (frame) weight was taken into account.

Twenty-one sets of force readings were taken for a smooth cylinder (diameter 50 mm) and a smooth flume bed for the following height above bottom values:

		Number of runs (sets)
(i)	0 mm (on bottom)	5
(ii)	*10 mm	5
(iii)	*30 mm	6
(iv)	*60 mm	5
	Total	21

(* Heights were varied by means of wooden blocks and thin metal plates placed under the balances on the platforms, without removing the perspex cages fixed to the side panels).

In common with the pressure rig tests, the temperature of the water, the water depths at various locations in the flume, and the average flow velocity were also measured.

4.3.3 Velocity Distribution

The velocity readings were similar to those done with the pressure rig, except that a velocity profile along the width of the flume at the centre of the cylinder, was now required. As a check a number of velocity readings were also taken at other elevations. The horizontal velocity profile was necessary to determine the effective length of the cylinder.

4.4 Murky Water

The murkiness of the water made it almost impossible to observe the test cylinder, particularly the centre tapping when performing tests with the pressure rig. The cause of the murkiness was essentially due to tests performed with sand and clay particles in a nearby experimental project, using the same water supply. Although the recirculated water was filtered, it did not succeed in reducing the turbidity of the water substantially.

CHAPTER 5 - RESULTS OF PRESSURE RIG TESTS

5.1 Introduction

The experimental results included in this chapter, constitute the major component of the entire experimental programme.

Experiments were conducted at various approach flow velocities, which generated Reynolds numbers in the range 6 000 to 26 000 for the two cylinders (diameters 30 mm and 50 mm) used. These Reynolds numbers are within the range where the drag coefficient and the Strouhal number of a circular cylinder are relatively independent of the Reynolds number. The Strouhal number, S = 0,21 for the range of Reynolds numbers mentioned above (Le Méhauté, 1976).

Pressure and velocity measurements were carried out at the various combinations of the variables, indicated in Table 4.1: cylinder size, clearance (between cylinder and bed), cylinder roughness, bed roughness and approach velocity. The original data of which Table 5.1 (complete set of readings for Run 50) is a typical example, is available from the writer.

5.1.1 Three-dimensional Effects

One of the main objectives with the design of the pressure rig was to eliminate three-dimensional effects as far as possible. Except for the test cylinder, no other obstruction was therefore placed in the water flume.

No influences on pressure and velocity readings, due to three-dimensional effects, were detected. This showed that the single central pressure tapping and the pitot tube, were placed in an essentially two-dimensional flow.

5.1.2 Free-surface Effects

Since the tests were performed in a flume with a free surface, it was necessary to observe the effect of the free surface on the

PRESSURE DISTRIBUTION

Clearance G = 10 mm
Cylinder : Rough ; Diameter = 52 mm $k/D = 2 \times 10^{-2}$)
Bottom : Smooth (Roughness k = 1,0 mm;

Static head = 269,2 g (Level of flume = 0)

RUN NO. = 50
DATE = 26/9/85
TEMP = 19,2 C
H = 30,1 inches
Q = 0,0191 $\sqrt{H}$ = 0,1048 m^3/s
Elevation surf = 41,81 cm.
Bottom = 8,00 cm
Depth = 33,81 cm
Average vel. = 0,5097 m/s

θ	Mettler (g)	θ	Mettler (g)
0	287,2	190	253,6
10	283,7	200	253,1
20	276,4	210	253,1
30	267,8	220	252,9
40	256,6	230	252,6
50	246,8	240	252,2
60	241,7	250	250,2
70	243,6	260	249,6
80	250,5	270	250,7
90	251,5	280	254,6
100	252,9	290	259,1
110	253,9	300	266,9
120	254,1	310	274,7
130	254,1	320	279,7
140	254,1	330	282,3
150	254,2	340	286,1
160	254,0	350	287,4
170	253,9	360	287,2
180	253,7		

VELOCITY DISTRIBUTION

Elevation (cm)	Mettler PE300 (grams)
5,25(=0,84 cm	17,1 grams
5,6 above	19,4
6 bed)	20,3
6,5	21,8
7	22,5
7,5	23,6
8	24,4
8,5	25,1
9	25,4
9,5	26,1
10	26,3
11	26,9
12	27,1
14	27,8
17	28,4
22	28,0
30	28,5

Dia = 52,3 mm
(glass beaker)

Dia = 44,7 mm
(perspex
beaker)

STATIC WATER
zero = 8,00 cm

Mettler (g)	Depth gauge (cm)	Depth (cm)
288,2	43,05	35,05
186,6	36,43	28,43

REMARKS:

The static head is the reference static pressure, as measured on the flume bed directly below the cylinder; it is expressed in grams to relate to the pressure distribution.

TABLE 5.1: EXAMPLE OF SET OF MEASUREMENTS (PRESSURE RIG)

results, as the cylinder may generate surface waves. Such surface waves possess energy which is carried away; this causes the test specimen to experience a wave resistance (Bishop and Hassan, 1964). The maximum wave resistance is dependent upon the Froude number, F_r and occurs when

$$F_r = \frac{U}{\sqrt{gh}} = 1 \qquad (5.1)$$

where h is the depth of immersion measured to the centre of the cylinder, and U the velocity of the free stream. In the tests reported here, the wave resistance was kept very small by carefully choosing the depth and velocity range. The maximum Froude number was Ø,443 (Run 54). Measurements in the present study revealed a maximum drawdown of 3 mm, of the water flowing over the cylinder, at the cylinder location.

5.1.3 Blockage Effect

The length-to-diameter ratios of the two test cylinders, were 12 and 2Ø respectively. Although the flume had a finite width of 6ØØ mm, the length-to-diameter ratios in excess of 1Ø, suggest that the sizes of the test cylinders were of reasonable dimensions, without the flow being affected much by the presence of the walls of the flume. Jones (197Ø) performed tests with length-to-diameter ratios of 5,5 to 11 and Zdravkovich (1985) with ratios of 13,5 and 25.

The traditional blocking ratio, equal to the ratio of cylinder diameter to total depth, was between Ø,15 and Ø,3Ø for the 5Ø mm cylinder (but mostly about Ø,2Ø) and between Ø,1Ø and Ø,21 for the 3Ø mm cylinder. Blocking ratios were calculated for all tests, but no blockage correction was applied to the plots of the pressure distributions, which are included at the end of this chapter. Modified blocking ratio adjustments (explained in Section 5.2.2) were, however, made to compare the results with those of other investigators in Chapter 8.

5.2 Experimental Data Reduction

5.2.1 Lift and Drag Forces

As stated in Chapter 2, only time-averaged pressures were measured. The measured pressures were integrated around the surface of the cylinder concerned, to provide the drag force as the horizontal component and the lift force as the vertical component, after multiplying by a constant which included the area between two adjacent pressure tapping positions. The effective pressure was therefore taken as the arithmetic mean of the two pressures on adjacent taps, which were positioned every 10° by rotation.

With reference to the elemental section in Figure 5.1 below, the deduction of the effective force is as follows:

$$\text{Force, } F = \text{Pressure}_{elem} \times \text{Area}_{elem}$$
$$= \rho g h \times r\Delta\theta \text{ for one metre length of cylinder}$$

The horizontal component,

$$\text{Total Drag Force, } F_D = \frac{\pi g r}{18} \times 10^3 \, \Sigma \, h \cos\theta \qquad (N/m) \quad (5.2)$$

Similarly, the vertical component,

$$\text{Total Lift Force, } F_L = \frac{\pi g r}{18} \times 10^3 \, \Sigma \, h \sin\theta \qquad (N/m) \quad (5.3)$$

$$\text{where } h = \frac{4m}{100\pi D_i^2} \qquad (m)$$

and m = mass readings in grams

D_i = beaker diameter in centimetres.

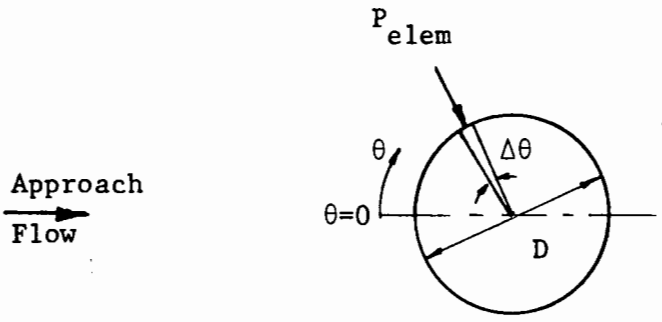

Figure 5.1 : Pressure on an elemental section of a cylinder

A computer program was written to process the pressure readings for the 134 test runs. Details of the program are included in Appendix 1. An example of the calculated forces, indicating the various angles of rotation and the pressure readings, is shown in Table 5.2.

5.2.2 Lift and Drag Coefficients

For a cylinder within the boundary layer, the lift and drag forces depend on the same quantities, as when the cylinder is in a free stream. These variables are:

D, cylinder diameter
k, surface roughness height
G, gap between bed and cylinder
ϕ, angle of cylinder to stream velocity (= 90° for this study)
H, depth of water
U, approach velocity
ν, kinematic viscosity
ρ, water density
and turbulence intensity

PRESSURE DISTRIBUTION (Run 50)

Cylinder Diameter = 52 cm; Clearance = 10 mm; Beaker dia. = 44,7 mm

Cylinder = Rough; Bottom = Smooth; R_e = 24 492

Static Head = 269,2 g; Water depth = 33,81 cm; Ave. vel. = 0,509 m/s

ANGLE	MASS (g)	HEAD h (cm)	h SIN θ	h COS θ
0	287.200	18.301	0.000	18.301
10	283.700	18.078	3.139	17.804
20	276.400	17.613	6.024	16.551
30	267.800	17.065	8.532	14.779
40	256.600	16.351	10.510	12.526
50	246.800	15.727	12.047	10.109
60	241.700	15.402	13.338	7.701
70	243.600	15.523	14.587	5.309
80	250.500	15.963	15.720	2.772
90	251.500	16.026	16.026	0.000
100	252.900	16.116	15.871	-2.798
110	253.900	16.179	15.204	-5.534
120	254.100	16.192	14.023	-8.096
130	254.100	16.192	12.404	-10.408
140	254.100	16.192	10.408	-12.404
150	254.200	16.198	8.099	-14.028
160	254.000	16.186	5.536	-15.209
170	253.900	16.179	2.809	-15.933
180	253.700	16.166	0.000	-16.166
190	253.600	16.160	-2.806	-15.915
200	253.100	16.128	-5.516	-15.156
210	253.100	16.128	-8.064	-13.967
220	252.900	16.116	-10.359	-12.345
230	252.600	16.096	-12.331	-10.347
240	252.200	16.071	-13.918	- 8.035
250	250.200	15.943	-14.982	- 5.453
260	249.600	15.905	-15.664	- 2.762
270	250.700	15.975	-15.975	0.000
280	254.600	16.224	-15.977	2.817
290	259.100	16.511	-15.515	5.647
300	266.900	17.008	-14.729	8.504
310	274.700	17.505	-13.409	11.252
320	279.700	17.823	-11.457	13.653
330	282.300	17.989	-8.994	15.579
340	286.100	18.231	-6.235	17.132
350	287.400	18.400	-3.180	18.036
		TOTALS:	-4.834	13.913

LIFT FORCE: -2.152 N/m
DRAG FORCE: 6.194 N/m

TABLE 5.2: Calculation of Drag and Lift Forces, by Pressure Integration

It is well known (see e.g., Littlejohns, 1974) that the non-dimensional parameters between the above variables can be written in the form:

$$\frac{2\,F_D}{\rho D U^2} = C_D = f_1\left(\frac{k}{D}, \frac{G}{D}, \phi, \frac{H-D}{H}, R_e\right) \tag{5.4}$$

and similarly

$$\frac{2\,F_L}{\rho D U^2} = C_L = f_2\left(\frac{k}{D}, \frac{G}{D}, \phi, \frac{H-D}{H}, R_e\right) \tag{5.5}$$

where R_e = Reynolds number;
F_D = Drag force (in N/m);
F_L = Lift force (in N/m);
C_D = Drag coefficient;
C_L = Lift coefficient.

For all cases in this study, the cylinder was perpendicular to the approach flow. Further, for the cylinder positioned at a specific elevation (i.e. G/D value) and for a given surface roughness k/D, the drag coefficient C_D can be written:

$$C_D = f_1\left(\frac{H-D}{H}, R_e\right)$$

In studies on the flow past bluff bodies, Shaw (1971) showed that there exists a linear relationship between C_D and the blocking ratio D/H, for the range of blocking ratios (0,15 to 0,25) considered in this study. This was confirmed by Ramamurthy and Ng (1973), admittedly only for cylinders placed in a symmetrical flow. It therefore follows that

$$\frac{C_D}{a_1} = f_1(R_e) \tag{5.6}$$

where $a_1 = \frac{H-D}{H}$

Littlejohns' (1974) results for wall cylinders, using Eq. (5.6), produced very little scatter. He also assumed the relationship

$$\frac{C_L}{a_1} = f_2(R_e) \tag{5.7}$$

with very satisfactory results.

According to Littlejohns (1974), standing waves form, due to cylinder obstruction at cylinder depths of less than 5D, i.e. at Froude numbers less than about 0,8. As mentioned earlier, the magnitude of the forces acting on a cylinder in contact with the bed, will be affected by surface waves. It is evident that the force coefficients are related to the water depth. The parameter a_1 enables one to make a direct comparison with tests performed earlier. As it was impossible to keep the water depth constant for different approach flows, the parameter a_1 was calculated for each test run in the present study.

Smith (1969) investigated the influence of the variation of the water depth on the lift and drag coefficient of a body on or near the bottom of a stream. He showed that the shallow-water drag coefficient could be predicted, within an accuracy of 10 % , if the deep-water coefficient is known. The same method generates a deep-water drag coefficient if the shallow water coefficient is given or determined from tests. No variation was however observed in the lift coefficient under similar circumstances. Smith (1971) also found that the drag force is influenced by the proximity of the free water surface. As tests were performed in intermediate water depths in the present study, Smith's method was not used; the parameter a_1 (refer Littlejohns, 1974), as indicated above, was applied to compensate for the varying water depth in successive test runs.

Jones (1970 and 1971) also identified two further dimensionless groups which are related to C_D and C_L. These two groups are

$$\frac{\delta}{D} \quad , \quad \frac{u_*}{U_o}$$

where δ is the boundary layer thickness,

u_* is known as the friction velocity

($u_* = \sqrt{\frac{\tau_o}{\rho}}$ with $\tau_o =$ shear stress in the fluid, evaluated at the bed),

U_o is the free stream velocity.

Jones' work is valuable, regarding the effective velocity experienced by the test cylinder in the boundary layer. The velocities used in the calculation of C_D and C_L are explained in the next section.

The values of C_D generated by the pressure integration process, do not account for the skin friction component, and C_D can therefore only be regarded as the form drag coefficient or pressure drag coefficient. According to Achenbach (1968), the friction coefficient for a circular cylinder, remote from a boundary, accounts for no more than 2 % of the total drag coefficient in the subcritical region. The friction coefficient for free cylinders can be assumed to be applicable to wall cylinders regarding the order of magnitude.

5.2.3 Reference Velocities

The velocity profile in the boundary layer is affected by bottom roughness. Velocity profiles were recorded for each test run. The velocity measurements were taken at a location 2,65 metres upstream from the cylinder; identical velocity values were also measured one metre upstream from the cylinder. The velocities upstream from the cylinder were therefore not influenced by the presence of the cylinder.

For all the on-bottom positions of the cylinders, the boundary layer thickness was in excess of the cylinder diameter. At clearances of one diameter or more, the test cylinder was generally in the free stream velocity region. However, an analysis of the test data was done with the reference velocity $U_{D/2}$ taken at the elevation of the cylinder centre. In a further analysis, account was taken of the depth parameter a_1, in calculations of C_D and C_L (Table 5.3).

Computed Forces and Lift and Drag coefficients, from Pressure Distributions

Smooth bed: Runs 1 to 74; Rough bed: Runs 75 to 134 (* S = smooth; R = rough)

Run No.	*Dia of Cylinder D (mm)	Gap G (mm)	G/D	Temp (°C)	Velocity(m/s)		Flow Q (m^3/s)	Water Depth H (cm)	Reynolds No.	Forces		Coefficients		Depth parameter a_1	Coefficient	
					Average (m/s)	$U_{D/2}$ (m/s)				F_D (N/m)	F_L (N/m)	C_D	C_L		C_D/a_1	C_L/a_1
1	50S	0	0	19,1	0,219	0,215	0,0311	23,31	10 750	1,282	0,770	1,109	0,666	0,785	1,41	0,848
12	50S			19	0,219	0,194	0,0273	20,51	9 700	1,506	0,917	1,601	0,974	0,756	2,12	1,29
13	50S			19,2	0,323	0,337	0,049	25,13	16 850	3,226	2,174	1,136	0,766	0,801	1,42	0,96
14	50S			19,5	0,376	0,37	0,0602	26,34	18 500	4,075	3,061	1,190	0,894	0,810	1,47	1,10
15	50S			19,5	0,401	0,397	0,0602	24,66	19 850	4,986	3,762	1,265	0,955	0,797	1,59	1,20
2	50S	60	1,2	19,5	0,24	0,251	0,033	22,64	12 550	1,805	-0,547	1,146	-0,347	0,779	1,47	-0,45
3	50S			19	0,28	0,274	0,0384	22,30	13 700	3,081	-0,041	1,642	-0,021	0,776	2,12	-0,03
4	50S			19,2	0,318	0,347	0,045	23,3	17 350	3,961	-0,179	1,316	-0,059	0,785	1,68	-0,08
5	50S			19,4	0,341	0,358	0,045	21,7	17 900	4,665	-0,343	1,456	-0,107	0,770	1,89	-0,14
6	50S			19,7	0,386	0,418	0,0535	22,8	20 900	6,143	-0,091	1,406	-0,021	0,781	1,80	-0,03
7	50S	30	0,6	19	0,30	0,32	0,0423	23,21	16 000	3,586	0,050	1,401	0,020	0,785	1,78	0,03
8	50S			19	0,391	0,405	0,0505	21,22	20 250	6,541	0,113	1,595	0,028	0,764	2,09	0,04
9	50S			19,5	0,443	0,471	0,061	22,65	23 550	8,178	0,158	1,475	0,028	0,779	1,89	0,04
10	50S			19,5	0,461	0,491	0,0649	23,14	24 550	9,136	0,005	1,516	0,001	0,784	1,93	0,001
11	50S			19,8	0,439	0,454	0,0648	24,27	22 700	7,781	0,251	1,510	0,049	0,794	1,90	0,06
16	50S	2,73	0,055	18,9	0,28	0,246	0,0357	20,96	12 300	2,395	0,720	1,583	0,476	0,761	2,08	0,63
17	50S	5	0,1	19	0,336	0,322	0,044	21,53	16 100	3,825	0,730	1,476	0,282	0,768	1,92	0,37
18	50S			19,4	0,409	0,4	0,0563	22,67	20 000	5,502	1,342	1,376	0,336	0,779	1,77	0,43
19	50S			19,7	0,435	0,481	0,0636	24,07	24 050	5,866	1,520	1,014	0,263	0,792	1,28	0,33
20	50S			20	0,416	0,404	0,0598	23,62	20 200	5,343	1,539	1,309	0,377	0,788	1,66	0,48
21	50S			18,8	0,306	0,296	0,038	20,43	14 800	3,201	0,832	1,461	0,380	0,755	1,94	0,50
22	50S	10	0,2	19,8	0,328	0,321	0,0357	17,93	16 050	4,284	0,769	1,663	0,299	0,721	2,31	0,41
23	50S			20,2	0,35	0,356	0,0462	21,69	17 800	4,120	0,620	1,300	0,196	0,769	1,69	0,25
24	50S			20,8	0,385	0,39	0,0525	22,42	19 500	4,690	0,771	1,233	0,203	0,777	1,59	0,26
25	50S			20,7	0,409	0,417	0,059	23,71	20 850	5,140	0,848	1,182	0,195	0,789	1,50	0,25
26	50S			21,5	0,421	0,437	0,0639	24,97	21 850	5,30	0,893	1,110	0,187	0,80	1,39	0,23
27	52R	59	1,135	20,3	0,269	0,281	0,033	20,04	14 612	3,506	0,103	1,708	0,050	0,741	2,31	0,067

TABLE 5.3: Computed Forces and Lift and Drag coefficients, from Pressure Distributions

Computed Forces and Lift and Drag coefficients, from Pressure Distributions

Smooth bed: Runs 1 to 74; Rough bed: Runs 75 to 134 (* S = smooth; R = rough)

Run No.	*Dia of Cylinder D (mm)	Gap G (mm)	G/D	Temp (°C)	Velocity(m/s)		Flow Q (m^3/s)	Water Depth H (cm)	Reynolds No.	Forces		Coefficients		Depth parameter a_1	Coefficient	
					Average (m/s)	$U_{D/2}$ (m/s)				F_D (N/m)	F_L (N/m)	C_D	C_L		C_D/a_1	C_L/a_1
28	52R	59	1,135	20,6	0,325	0,36	0,0425	21,5	18 720	4,839	0,357	1,436	0,106	0,758	1,87	0,14
29	52R			20,7	0,372	0,405	0,0507	22,42	21 060	6,057	0,305	1,420	0,072	0,768	1,85	0,09
30	52R			21	0,40	0,429	0,0573	23,7	22 308	7,550	0,526	1,578	0,110	0,781	2,02	0,14
31	52R			21	0,425	0,458	0,0642	24,85	23 816	7,213	0,534	1,323	0,098	0,791	1,67	0,12
47	52R			20,2	0,486	0,487	0,086	29,07	25 324	7,047	0,926	1,143	0,150	0,821	1,39	0,18
32	52R	0	0	20,3	0,224	0,218	0,0311	22,86	11 336	1,512	1,059	1,224	0,857	0,773	1,58	1,11
33	52R			20,3	0,413	0,405	0,0602	23,97	21 060	4,518	4,137	1,059	0,970	0,783	1,35	1,24
34	52R			20,5	0,331	0,322	0,0493	24,48	16 744	3,235	2,727	1,200	1,012	0,788	1,52	1,28
35	52R			20,6	0,29	0,267	0,0412	23,35	13 884	2,770	1,991	1,494	1,074	0,777	1,92	1,38
36	52R			20,7	0,43	0,415	0,0633	24,43	21 580	4,954	4,169	1,106	0,931	0,787	1,41	1,28
48	52R			20,5	0,488	0,435	0,0859	28,95	22 620	5,761	4,966	1,171	1,009	0,82	1,43	1,23
49	52R			19	0,509	0,455	0,1047	33,81	23 660	5,523	5,235	1,026	0,973	0,846	1,21	1,15
37	52R	28,8	0,554	19,7	0,303	0,327	0,0421	22,88	17 004	3,648	0,532	1,312	0,191	0,773	1,70	0,25
38	52R			20,2	0,392	0,419	0,0504	21,14	21 788	6,296	1,010	1,379	0,221	0,754	1,83	0,29
39	52R			19	0,443	0,471	0,0608	22,55	24 492	7,812	0,965	1,354	0,167	0,769	1,76	0,22
40	52R			19,7	0,374	0,440	0,0642	22,76	22 880	7,635	0,974	1,517	0,193	0,772	1,97	0,25
41	52R			20	0,448	0,432	0,0666	24,43	22 464	7,023	0,598	1,447	0,123	0,787	1,84	0,16
46	52R			19,7	0,489	0,474	0,0847	29,07	24 648	6,926	1,134	1,186	0,231	0,821	1,44	0,28
42	52R	10	0,192	19,5	0,332	0,303	0,036	17,84	15 756	4,183	1,083	1,752	0,454	0,709	2,47	0,64
43	52R			19,7	0,389	0,354	0,0525	22,19	18 408	4,770	1,545	1,464	0,474	0,766	1,91	0,62
44	52R			20,2	0,42	0,382	0,0641	25,06	19 864	4,968	1,500	1,309	0,309	0,792	1,65	0,50
45	52R			19,5	0,489	0,458	0,0865	29,07	23 816	6,449	2,118	1,182	0,388	0,821	1,44	0,47
50	52R			19,2	0,509	0,471	0,1048	33,81	24 492	6,194	2,152	1,074	0,373	0,846	1,27	0,44
51	30S	80	2,67	22	0,296	0,301	0,0401	22,28	9 309	1,917	-0,006	1,411	-0,004	0,865	1,63	-0,005
52	30S			22	0,38	0,399	0,0554	24,04	12 340	3,098	-0,097	1,297	-0,041	0,875	1,48	-0,05
53	30S			22,5	0,46	0,477	0,076	27,27	14 906	4,476	-0,084	1,311	-0,025	0,890	1,47	-0,03
54	30S			23	0,592	0,590	0,0993	28,21	18 632	6,698	-0,050	1,283	-0,010	0,894	1,44	-0,01
55	30S	0	0	23,5	0,474	0,409	0,0764	26,51	13 053	2,493	1,700	0,994	0,678	0,887	1,12	0,76
56	30S			23,7	0,59	0,506	0,1018	28,34	16 235	4,247	2,406	1,106	0,626	0,894	1,24	0,70

TABLE 5.3 (continued)

Computed Forces and Lift and Drag coefficients, from Pressure Distributions

Smooth bed: Runs 1 to 74; Rough bed: Runs 75 to 134 (* S = smooth; R = rough)

Run No.	*Dia of Cylinder D (mm)	Gap G (mm)	G/D	Temp (°C)	Velocity(m/s)		Flow Q (m^3/s)	Water Depth H (cm)	Reynolds No.	Forces		Coefficients		Depth parameter a_1	Coefficient	
					Average (m/s)	$U_{D/2}$ (m/s)				F_D (N/m)	F_L (N/m)	C_D	C_L		C_D/a_1	C_L/a_1
57	30S	0	0	24	0,41	0,351	0,0552	22,2	11 446	2,272	1,355	1,229	0,733	0,865	1,42	0,85
58	30S			24,2	0,33	0,270	0,0382	19,22	8 901	1,526	0,912	1,396	0,834	0,844	1,65	0,99
59	30S	10	0,333	24,4	0,31	0,274	0,0377	19,89	9 133	1,663	0,221	1,477	0,196	0,849	1,74	0,23
60	30S			24,2	0,43	0,394	0,0554	21,11	13 061	3,037	0,262	1,304	0,113	0,858	1,54	0,13
61	30S			24,3	0,52	0,470	0,0768	24,31	15 667	4,383	0,437	1,323	0,132	0,877	1,51	0,15
62	30S			24,5	0,55	0,502	0,0987	29,12	16 733	3,488	0,330	0,923	0,897	0,897	1,03	0,10
63	31,8R	79	2,484	24,8	0,34	0,341	0,0389	18,94	12 050	3,149	-0,081	1,703	-0,004	0,832	2,047	-0,005
64	31,8R			24,5	0,43	0,438	0,0557	21,43	15 476	4,564	-0,181	1,496	-0,059	0,852	1,756	-0,069
65	31,8R			24,8	0,51	0,529	0,0759	21,48	18 691	6,075	-0,278	1,365	-0,062	0,870	1,569	-0,071
66	31,8R			25	0,57	0,581	0,1007	29,3	20 760	7,360	-0,432	1,371	-0,080	0,891	1,539	-0,09
67	31,8R	10	0,314	25,2	0,58	0,527	0,1009	28,86	18 830	5,691	0,574	1,288	0,130	0,890	1,447	0,146
68	31,8R			25,5	0,52	0,468	0,0759	24,21	16 816	5,094	0,416	1,463	0,119	0,869	1,68	0,14
69	31,8R			25,6	0,46	0,410	0,0557	19,98	14 732	4,480	0,404	1,676	0,151	0,841	1,99	0,18
70	31,8R			25,2	0,35	0,282	0,0387	18,2	10 076	2,557	0,254	2,022	0,201	0,825	2,45	0,24
71	31,8R	0	0	25,4	0,33	0,279	0,0382	18,78	9 991	1,941	1,022	1,568	0,826	0,831	1,89	0,99
72	31,8R			25,7	0,43	0,379	0,0547	20,7	13 664	3.012	1,491	1,319	0,653	0,846	1,56	0,77
73	31,8R			25,9	0,54	0,456	0,0766	23,42	16 478	4,491	2,190	1,358	0,662	0,864	1,57	0,77
74	31,8R			26	0,58	0,494	0,1012	28,76	17 851	4,637	2,126	1,195	0,548	0,889	1,34	0,62
75	52R	42,2	0,812	19	0,226	0,22	0,027	19,4	11 440	2,2	-0,3	1,75	-0,238	0,732	2,39	-0,33
76				20	0,518	0,45	0,105	33,24	23 400	7,26	1,42	1,379	0,270	0,844	1,64	0,32
77				20	0,44	0,38	0,075	27,92	19 760	5,46	1,17	1,45	0,317	0,814	1,78	0,39
78				17	0,363	0,31	0,054	24,47	15 065	4,30	0,48	1,72	0,190	0,787	2,19	0,24
79				17	0,297	0,26	0,041	22,42	12 636	2,99	0,23	1,70	0,132	0,768	2,21	0,17
80	52R	10	0,192	18	0,453	0,36	0,077	27,82	17 829	4,53	1,87	1,343	0,556	0,813	1,65	0,68
81				18	0,541	0,41	0,105	31,81	20 305	6,11	2,38	1,40	0,544	0,837	1,67	0,65
82				20	0,388	0,31	0,054	23,02	16 120	3,94	1,47	1,576	0,590	0,774	2,04	0,76
83				20	0,317	0,26	0,041	21,26	13 520	3,12	0,95	1,775	0,541	0,755	2,35	0,72
84				20	0,297	0,27	0,029	17,06	14 040	3,12	0,79	1,645	0,4164	0,695	2,37	0,60

TABLE 5.3 (continued)

Computed Forces and Lift and Drag coefficients, from Pressure Distributions

Smooth bed: Runs 1 to 74; Rough bed: Runs 75 to 134 (* s = smooth; R = rough)

Run No.	*Dia of Cylinder D (mm)	Gap G (mm)	G/D	Temp (°C)	Velocity (m/s)		Flow Q (m^3/s)	Water Depth H (cm)	Reynolds No.	Forces		Coefficients		Depth parameter a_1	Coefficient	
					Average (m/s)	$U_{D/2}$ (m/s)				F_D (N/m)	F_L (N/m)	C_D	C_L		C_D/a_1	C_L/a_1
85	52R	0	0	20	0,274	0,25	0,028	16,99	13 000	3,21	1,42	1,978	0,875	0,694	2,85	1,00
86				20	0,379	0,26	0,041	20,71	13 520	3,14	1,63	1,784	0,9275	0,749	2,38	1,24
87				20	0,391	0,30	0,054	22,86	15 600	3,62	1,93	1,549	0,825	0,773	2,00	1,07
88				20	0,458	0,33	0,077	27,52	17 160	4,51	2,44	1,594	0,862	0,811	1,97	1,06
89				21	0,552	0,42	0,105	31,39	21 840	5,85	3,37	1,276	0,736	0,834	1,53	0,88
90	50S	45,5	0,91	21	0,559	0,52	0,105	30,99	26 000	8,98	0,27	1,329	0,0402	0,839	1,58	0,05
91				22	0,47	0,42	0,076	26,59	21 000	6,78	0,17	1,538	0,0374	0,812	1,89	0,05
92				22	0,388	0,35	0,055	23,34	17 500	5,26	0,08	1,718	0,0254	0,786	2,19	0,03
93				22	0,327	0,32	0,041	20,39	16 000	4,15	-0,01	1,62	-0,0025	0,755	2,15	-0,003
94				21,5	0,257	0,27	0,03	18,95	13 500	2,62	-0,06	1,438	-0,0353	0,736	1,95	-0,05
95	50S	10	0,20	21,5	0,289	0,28	0,03	17,21	14 000	3,07	0,46	1,565	0,234	0,709	2,21	0,33
96				21,5	0,327	0,28	0,041	20,60	14 000	3,09	0,53	1,579	0,269	0,757	2,09	0,36
97				21	0,373	0,32	0,055	24,28	16 000	3,41	0,54	1,33	0,2099	0,794	1,68	0,26
98				21	0,473	0,38	0,077	26,64	19 000	5,61	1,24	1,429	0,3427	0,812	1,76	0,42
99				21	0,572	0,47	0,105	30,08	23 500	6,87	1,83	1,244	0,3311	0,834	1,49	0,40
100	50S	0	0	20,5	0,537	0,38	0,105	32,10	19 000	5,31	3,82	1,47	1,059	0,844	1,74	1,25
101				20,5	0,428	0,32	0,076	29,34	16 000	3,86	1,44	1,509	0,564	0,83	1,82	0,68
102				22	0,353	0,26	0,055	25,61	13 265	2,84	0,78	1,678	0,463	0,805	2,08	0,58
103				22	0,32	0,25	0,041	21,54	12 755	2,88	0,87	1,846	0,554	0,768	2,40	0,72
104				22	0,257	0,23	0,028	18,13	11 735	2,14	0,99	1,619	0,7513	0,724	2,24	1,04
105	30S	65,7	2,19	22	0,509	0,47	0,077	24,77	14 388	4,83	-0,17	1,459	-0,050	0,879	1,66	-0,06
106				22	0,616	0,55	0,105	28,09	16 837	6,65	-0,29	1,465	-0,0631	0,893	1,64	-0,07
107				22	0,406	0,4	0,054	22,0	12 249	3,32	-0,21	1,385	-0,0886	0,864	1,60	-0,10
108				22	0,345	0,36	0,041	19,30	11 020	2,56	-0,30	1,315	-0,154	0,845	1,56	-0,18
109				23	0,277	0,3	0,029	17,21	9 375	1,85	-0,18	1,373	-0,133	0,826	1,66	-0,16
110	30S	10	0,333	23	0,388	0,34	0,041	17,37	10 625	2,25	0	1,299	-0,001	0,827	1,57	-0,001
111				23	0,451	0,36	0,055	19,95	11 250	2,64	0,06	1,357	0,0332	0,85	1,6	0,04
112				22	0,529	0,4	0,077	23,83	12 245	3,09	0,20	1,285	0,0843	0,874	1,47	0,10

TABLE 5.3 (continued)

Computed Forces and Lift and Drag coefficients, from Pressure Distributions

Smooth bed: Runs 1 to 74; Rough bed: Runs 75 to 134 (* S = smooth; R = rough)

Run No.	*Dia of Cylinder D (mm)	Gap G (mm)	G/D	Temp (°C)	Velocity(m/s) Average (m/s)	Velocity(m/s) $U_{D/2}$ (m/s)	Flow Q (m^3/s)	Water Depth H (cm)	Reynolds No.	Forces F_D (N/m)	Forces F_L (N/m)	Coefficients C_D	Coefficients C_L	Depth parameter a_1	Coefficient C_{D/a_1}	Coefficient C_{L/a_1}
113				22	0,625	0,45	0,105	27,54	13 760	4,22	0,32	1,389	0,1054	0,891	1,56	0,12
114				22	0,279	0,25	0,027	15,95	7 653	1,17	-0,04	1,248	-0,046	0,812	1,54	0,06
115	30S	0	0	21	0,284	0,23	0,027	15,64	6 900	1,21	0,21	1,528	0,265	0,808	1,89	0,33
116				21	0,366	0,28	0,041	18,42	8 400	1,54	0,37	1,309	0,317	0,837	1,56	0,38
117				21	0,418	0,30	0,055	21,53	9 000	1,73	1,00	1,283	0,739	0,861	1,49	0,86
118				21	0,498	0,33	0,076	25,24	9 900	2,31	1,20	1,412	0,737	0,881	1,60	0,84
119				22	0,581	0,40	0,105	29,64	12 245	2,66	1,41	1,1093	0,589	0,899	1,23	0,66
120	31,8R	64,4	2,025	21,5	0,491	0,05	0,076	25,52	14 636	4,64	0,20	1,424	0,0617	0,875	1,63	0,07
121				21,5	0,401	0,37	0,054	22,18	12 034	3,34	-0,02	1,515	-0,0112	0,857	1,77	-0,01
122				21,5	0,33	0,31	0,041	20,44	10 083	2,32	0,02	1,50	0,0104	0,844	1,78	0,012
123				20	0,212	0,27	0,027	17,45	8 694	1,63	0,10	1,385	0,0864	0,818	1,69	0,11
124				20	0,597	0,54	0,105	28,82	17 388	6,35	0,15	1,353	0,0313	0,890	1,52	0,04
125	31,8R	10	0,314	21	0,619	0,46	0,105	27,79	14 812	4,29	0,55	1,259	0,161	0,886	1,80	0,18
126				21	0,534	0,40	0,076	23,52	12 880	3,44	0,30	1,337	0,115	0,865	1,55	0,13
127				21	0,422	0,33	0,054	21,04	10 626	2,56	0,16	1,462	0,0925	0,849	1,72	0,11
128				21,5	0,367	0,31	0,041	18,14	10 083	2,11	0,13	1,363	0,0822	0,825	1,65	0,10
129				21,5	0,295	0,27	0,028	15,43	8 782	1,62	0,12	1,38	0,101	0,794	1,74	0,13
130	31,8R	0	0	21,5	0,289	0,22	0,027	15,37	7 156	1,35	0,37	1,726	0,469	0,793	2,18	0,59
131				21,5	0,357	0,28	0,041	18,65	9 107	1,89	0,65	1,495	0,518	0,829	1,80	0,63
132				21	0,413	0,30	0,054	21,50	9 660	2,12	0,67	1,464	0,4625	0,852	1,72	0,54
133				21	0,498	0,35	0,077	25,32	11 270	2,40	1,42	1,218	0,7225	0,874	1,39	0,83
134				22	0,578	0,4	0,105	29,77	13 143	3,09	1,20	1,201	0,4658	0,893	1,35	0,52

TABLE 5.3 (continued)

Run	Cyl. dia (mm)	$U_{D/2}$ (m/s)	V_{eff} (m/s)	R_e	C_D	C_L	C_{D/a_1}	C_{L/a_1}
1	50S	Ø,215	Ø,209	10 470	1,17	Ø,70	1,49	Ø,90
12		Ø,194	Ø,189	9 447	1,69	1,Ø3	2,24	1,36
13		Ø,337	Ø,328	16 411	1,20	Ø,81	1,50	1,Ø1
14		Ø,37	Ø,36	18 Ø18	1,25	Ø,94	1,55	1,17
15		Ø,397	Ø,386	19 333	1,33	1,Ø1	1,68	1,26
55	30S	Ø,474	Ø,462	12 713	1,Ø4	Ø,71	1,18	Ø,80
56		Ø,59	Ø,575	15 812	1,17	Ø,66	1,31	Ø,74
57		Ø,41	Ø,4Ø	11 148	1,3Ø	Ø,77	1,5Ø	Ø,9Ø
58		Ø,33	Ø,32	8 67Ø	1,47	Ø,88	1,74	1,Ø4
32	52R	Ø,218	Ø,212	11 Ø4Ø	1,29	Ø,9Ø	1,67	1,17
33		Ø,4Ø5	Ø,394	2Ø 511	1,Ø8	1,Ø2	1,42	1,31
34		Ø,322	Ø,314	16 3Ø8	1,27	1,Ø7	1,6Ø	1,35
35		Ø,267	Ø,26	13 522	1,57	1,13	2,Ø2	1,45
36		Ø,415	Ø,4Ø4	21 Ø18	1,17	Ø,98	1,49	1,35
48		Ø,435	Ø,424	22 Ø31	1,23	1,Ø6	1,51	1,3Ø
49		Ø,455	Ø,443	23 Ø44	1,Ø8	1,Ø3	1,28	1,21
71	31,8R	Ø,279	Ø,272	9 731	1,65	Ø,87	1,99	1,Ø4
72		Ø,379	Ø,369	13 3Ø8	1,39	Ø,69	1,64	Ø,81
73		Ø,456	Ø,444	16 Ø5Ø	1,43	Ø,7Ø	1,66	Ø,81
74		Ø,494	Ø,481	17 4ØØ	1,26	Ø,58	1,41	Ø,65

$G/_D$ = Ø; Smooth bed only

(S = smooth; R = rough)

TABLE 5.4(a): LIFT AND DRAG COEFFICIENTS, USING EQUATION (5.9) - VALUES CORRECTED FOR VARYING DEPTH

Run	Cyl. dia (mm)	$U_{D/2}$ (m/s)	V_{eff} (m/s)	R_e	C_{D/a_1}	C_{L/a_1}
100	50S	0,38	0,37	18 505	1,83	1,32
101		0,32	0,312	15 583	1,92	0,72
102		0,26	0,253	12 919	2,19	0,61
103		0,25	0,243	12 423	2,53	0,76
104		0,23	0,224	11 429	2,36	1,10
115	30S	0,23	0,224	6 720	1,99	0,35
116		0,28	0,273	8 181	1,64	0,40
117		0,30	0,292	8 766	1,57	0,91
118		0,33	0,321	9 642	1,69	0,89
119		0,40	0,39	11 926	1,30	0,70
85	52R	0,25	0,243	12 661	3,00	1,05
86		0,26	0,253	13 168	2,51	1,31
87		0,30	0,292	15 194	2,11	1,13
88		0,33	0,321	16 713	2,08	1,12
89		0,42	0,409	21 271	1,61	0,93
130	31,8R	0,22	0,214	6 970	2,30	0,62
131		0,28	0,273	8 870	1,90	0,66
132		0,30	0,292	9 408	1,81	0,57
133		0,35	0,341	10 976	1,47	0,87
134		0,40	0,39	12 801	1,42	0,52

$G/_D$ = 0; Rough bed only

(S = smooth; R = rough)

TABLE 5.4(b): LIFT AND DRAG COEFFICIENTS, USING EQUATION (5.9) - VALUES CORRECTED FOR VARYING DEPTH

Bed condition	Run	Cylinder dia D (mm)	Gap G (mm)	G/D	$U_{D/2}$ (m/s)	V_{eff} (m/s)	R_e	C_{D/a_1}	C_{L/a_1}
S	22	50S	10	0,2	0,321	0,316	15 802	2,38	0,42
	23				0,356	0,351	17 525	1,74	0,26
	24				0,39	0,384	19 200	1,64	0,27
	25				0,417	0,411	20 528	1,55	0,26
	26				0,437	0,430	21 513	1,43	0,24
	42	52R	10	0,192	0,303	0,298	15 513	2,55	0,66
	43				0,354	0,439	18 124	1,97	0,64
	44				0,382	0,376	19 557	1,70	0,52
	45				0,458	0,451	23 448	1,49	0,48
	50				0,471	0,464	24 114	1,31	0,45
	59	30S	10	0,333	0,274	0,271	9 042	1,78	0,23
	60				0,394	0,39	12 930	1,57	0,13
	61				0,470	0,465	15 510	1,54	0,15
	62				0,502	0,497	16 566	1,05	0,10
	67	31,8R	10	0,314	0,527	0,522	18 642	1,48	0,15
	68				0,468	0,463	16 648	1,71	0,14
	69				0,410	0,406	14 585	2,03	0,18
	70				0,282	0,279	9 975	2,50	0,24
	7	50S	30	0,6	0,32	0,319	15 952	1,79	0,03
	8				0,405	0,404	20 189	2,10	0,04
	9				0,471	0,47	23 479	1,90	0,04
	10				0,491	0,49	24 476	1,94	0,001
	11				0,454	0,453	22 632	1,91	0,06
	37	52R	28,8	0,554	0,327	0,326	16 953	1,71	0,25
	38				0,419	0,418	21 723	1,84	0,29
	39				0,471	0,47	24 419	1,77	0,22
	40				0,44	0,439	22 811	1,98	0,25
	41				0,432	0,431	22 397	1,85	0,16
	46				0,474	0,473	24 574	1,44	0,28
R	80	52R	10	0,192	0,36	0,354	17 554	1,70	0,70
	81				0,41	0,394	19 991	1,72	0,67
	82				0,31	0,305	15 871	2,10	0,78
	83				0,26	0,256	13 311	2,42	0,74
	84				0,27	0,266	13 823	2,44	0,62
	95	50S	10	0,20	0,28	0,276	13 783	2,28	0,34
	96				0,28	0,276	13 783	2,16	0,37
	97				0,32	0,315	15 753	1,73	0,27
	98				0,38	0,374	18 707	1,82	0,43
	99				0,47	0,463	23 137	1,54	0,41
	110	30S	10	0,333	0,34	0,337	10 519	1,60	-0,001
	111				0,36	0,356	11 138	1,63	0,04
	112				0,4	0,396	12 123	1,50	0,10
	113				0,45	0,446	13 622	1,59	0,12
	114				0,25	0,248	7 576	1,57	0,06
	125	31,8R	10	0,314	0,46	0,455	14 664	1,84	0,18
	126				0,40	0,396	12 751	1,58	0,13
	127				0,33	0,327	10 520	1,75	0,11
	128				0,31	0,307	9 982	1,68	0,10
	129				0,27	0,267	8 694	1,78	0,13

TABLE 5.4(C): LIFT AND DRAG COEFFICIENTS, USING REFERENCE VELOCITY BASED ON EQUATION (5.13) - values corrected for varying depth

Smooth bed only									Equation (5.10)		Equation (5.12)	
Cyl. dia (mm)	G (mm)	U mean (m/s)	U top (m/s)	s_c (mm)	U_s (m/s)	R_e	C_D/a_1	C_L/a_1	R_e	C_D	C_D/a_1
50S	2,7	0,19	0,39	5,73	0,20	10 000	3,15	0,95	14 000	1,06	1,39
	5	0,23	0,47	10,1	0,27	13 500	2,73	0,53	18 000	1,02	1,33
		0,28	0,57	10,2	0,34	17 000	2,45	0,60	22 500	1,00	1,28
		0,34	0,70	10,40	0,45	22 500	1,46	0,38	26 000	0,8	1,01
		0,28	0,56	10,00	0,35	17 500	2,21	0,64	22 500	0,98	1,24
		0,21	0,40	9,7	0,25	12 500	2,72	0,70	17 000	0,98	1,30
	10	0,23	0,43	19,1	0,30	15 000	2,64	0,47	19 000	0,95	1,32
		0,25	0,47	18,7	0,33	16 500	1,97	0,29	20 300	0,93	1,21
		0,27	0,50	18,5	0,37	18 500	1,77	0,29	21 800	0,01	1,17
		0,29	0,53	18,3	0,38	19 000	1,81	0,30	23 400	0,90	1,14
		0,31	0,55	17,7	0,40	20 000	1,66	0,27	24 900	0,88	1,09
30S	10	0,19	0,37	19,4	0,26	8 666	1,93	0,26	9 700	1,23	1,45
		0,28	0,53	18,9	0,38	12 600	1,66	0,14	13 900	1,12	1,30
		0,33	0,64	19,5	0,45	15 000	1,65	0,16	16 700	1,16	1,33
		0,35	0,66	18,7	0,48	16 000	1,13	0,11	17 300	0,85	0,95

TABLE 5.5 : LIFT AND DRAG COEFFICIENTS, USING EQUATIONS (5.10) AND (5.12) - VALUES CORRECTED FOR VARYING DEPTH

Jones (1971) found that his experimental results were correlated best, by using the effective velocity V_{eff}, as the reference velocity in calculating the lift and drag coefficients. He defined the effective velocity as

$$V_{eff}^2 = \frac{1}{D} \int_o^D \left[U\ (y)\right]^2\ dy \qquad (5.8)$$

where U(y) is the velocity that would exist in the boundary layer, if the cylinder was not present. To calculate the effective velocity, Jones suggested one of the following procedures:

(i) If the velocity profile has been measured, equation (5.8) can be applied. It implies that the area under the U^2 versus y curve between y = o and y = D has to be obtained. This area divided by D generates V_{eff}^2.

(ii) The velocity profile in the boundary layer of the flume can be approximated by using the 1/7th power law. The following expression for the effective velocity for a cylinder resting on the flume bed was derived:

$$V_{eff}^2 = 0{,}778\ U_1^2\ \left(\frac{D}{y_1}\right)^{0{,}286} \qquad (5.9)$$

where U_1 is the measured at the height y_1 above the bed.

An analysis of both procedures suggested by Jones was done for a few situations. Very good correlation was found between the two methods, with the graphical methods being very time consuming. The results are indicated in Tables 5.4 (a) and (b).

The variation in position of the front stagnation point, due to shear flow over a pipe was investigated by Fredsoe and Hansen (1984). They explained that the lift acting on pipelines with a small gap, is caused by the fact, that the front stagnation point moves towards the bottom. They further stated that the lift force must be based on U_s, the far field velocity at distance s from the bed in shear flow; refer to Figure 5.2 below.

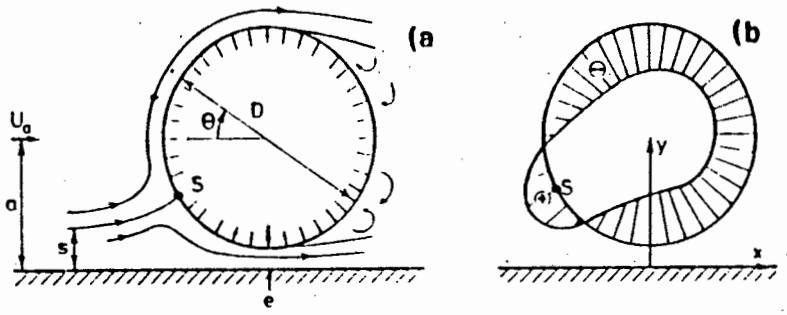

Fig. 5.2: (a) Flow around cylinder; (b) Pressure distribution on cylinder (Fredsoe and Hansen, 1984).

They consequently deduced the following expression for s_c, the distance from the bed to the stagnating streamline far upstream of the cylinder:

$$s_c = \frac{U_{top}}{V} G \qquad (5.10)$$

where U_{top} is the velocity at the top of the cylinder, with the cylinder in place; V is the average velocity from the bed to the stagnating streamline, distance s_c from the bed.

Values for s_c were calculated for some of the present test runs. Lift and drag coefficients could then be determined, using the measured velocities U_s from the recorded velocity profiles (Table 5.5).

Roshko (1961) corrected velocities and drag coefficients for blockage effects by making use of the formulae of Allen and Vincenti:

$$\text{Corrected } U = U_{D/2} \left[1 + \frac{1}{4} C_D' \left(\frac{D}{H}\right) + 0{,}82 \left(\frac{D}{H}\right)^2\right] \tag{5.11}$$

$$\text{Corrected } C_D = C_D' \left[1 - \frac{1}{2} C_D' \left(\frac{D}{H}\right) - 2{,}5 \left(\frac{D}{H}\right)^2\right] \tag{5.12}$$

where C_D' = measured drag coefficient
$U_{D/2}$ = measured velocity

However, he investigated symmetrical flow around a cylinder in air. Equations (5.11) and (5.12) enabled Roshko to correct for wall interference effects. To facilitate comparison with other methods, these equations were applied to some situations (refer to Table 5.5).

5.2.4 Kinematic Viscosity due to Temperature Changes

The following known values for the kinematic viscosity of water, ν, were used to calculate Reynolds number:

Temperature (°C)	Kinematic viscosity (m^2/s) (x 10-6)
14	1,172
15	1,141
16	1,112
17	1,Ø84
18	1,Ø57
19	1,Ø32
2Ø	1,ØØ7
21	Ø,983
22	Ø,96Ø
23	Ø,938
24	Ø,917
25	Ø,897
26	Ø,877
27	Ø,858

Kinematic viscosities for intermediate temperatures were determined by interpolation.

All the calculated results, including R_e, F_D, F_L, C_D, C_L, a_1 and the reference velocities, are indicated in Tables 5.3 and 5.4.

5.3 Pressure Distributions

Pressure distribution profiles for each of 26 different combinations of variables, are shown in Figs. 5.4 to 5.29. The various sets of pressure readings are not included in this dissertation, but are available from the author.

Various flow velocities generated similar pressure distributions for the same combination of variables. Three plots, respectively of velocities $U_D/2$ of Ø,35 m/s, Ø,42 m/s and Ø,52 m/s, are shown in Fig. 5.3 for a 5Ø mm smooth cylinder, at a clearance distance of 45,5 mm from a rough bed. Due to this similarity, only plots of different combinations are indicated (Figs. 5.4 to 5.29). Pressure values on the plots are indicated in centimetres water, and the value of the static water pressure is shown as a horizontal line in each case. All the plots are grouped together at the end of the chapter, for easy reference.

A summary of the 26 different testing combinations mentioned above, is given in Table 5.6; approximate locations of the front stagnation and separation points, are also indicated in the table. Comments on various characteristics of the plots are given below.

The pressure coefficients of various cylinder to bed locations are discussed in Section 5.6.

5.3.1 Front Stagnation Point

The front stagnation point is considered the location at the front of the cylinder, where the maximum positive pressure reading occurs. These locations, as measured and represented graphically, are indicated in Table 5.6.

(i) Clearance = Ø:

When the cylinder was positioned on the bed, an almost constant maximum pressure was measured in the region 28Ø° to 36Ø° (i.e. the zone from the front centre point towards the bed), for the smooth 5Ø mm diameter cylinder.

Run	Fig.	Cylinder Dia (mm) S = smooth, R = rough	Bed	Clearance (mm)	G/D	R_e	Angle of Rotation	
							Front stagnation point (estimated)	Separation point (estimated)
15	5.4	50S	S	0	0	19 333	280 to 360	105
49	5.5	52R	S	0	0	23 044	280 to 360	105
56	5.6	30S	S	0	0	15 812	290 to 360	105
74	5.7	31,8R	S	0	0	17 400	300 to 360	105
26	5.8	50S	S	10	0,2	21 513	360^-	90; 260
50	5.9	52R	S	10	0,192	24 114	360^-	110; 240
61	5.10	30S	S	10	0,333	15 510	360^-	100; 260
67	5.11	31,8R	S	10	0,314	18 642	360^-	110; 260
10	5.12	50S	S	30	0,6	24 476	360^-	90; 260
46	5.13	52R	S	28,8	0,554	24 574	360^-	110;240
6	5.14	50S	S	60	1,2	20 900	360^+	90;270
47	5.15	52R	S	59	1,135	25 324	360	110; 250
54	5.16	30S	S	80	2,67	18 632	360^+	90; 270
66	5.17	31,8R	S	79	2,484	20 760	360^+	100; 260
101	5.18	50S	R	0	0	15 583	360^-	100; 240
89	5.19	52R	R	0	0	21 271	360^-	105; 235
119	5.20	30S	R	0	0	11 926	360^-	90
134	5.21	31,8R	R	0	0	12 801	360^-	100
99	5.22	50S	R	10	0,2	23 137	360^-	90; 245
81	5.23	52R	R	10	0,192	19 991	360^-	100; 240
113	5.24	30S	R	10	0,333	13 622	360^-	90; 250
125	5.25	31,8R	R	10	0,314	14 664	360^-	105; 230
90	5.26	50S	R	45,5	0,91	26 000	360	90; 260
78	5.27	52R	R	42,2	0,812	15 065	360	100; 245
106	5.28	30S	R	65,7	2,19	16 837	360^+	90; 270
124	5.29	31,8R	R	64,4	2,025	17 388	360	110; 250

TABLE 5.6: PRESSURE PROFILES: APPROXIMATE LOCATIONS OF FRONT STAGNATION POINT AND SEPARATION POINT

With a rough bed, the maximum pressure with the same cylinder, was recorded at 360°.

The pressures at 10° and 350° indicate that the maximum pressure occurs between 350° and 360°; the pressure at 350°, is higher than that measured at 10°. The location of the stagnation point concerned, is therefore indicated as 360⁻ in Table 5.6. The same principle was applied when determining the stagnation points for the other combinations of variables, and is indicated as such in Table 5.6.

The smaller cylinder (smooth), experienced maximum pressures in the region 290° to 360° (smooth bed) and 360⁻ (rough bed).

With the roughened 50 mm cylinder, placed on the bed, the locations of the maximum pressure point were at almost identical locations in comparison to the smooth 50 mm cylinder.

(ii) Clearances of 10 mm to 30 mm ($0,2 \leq G/D \leq 0,6$):

From all the pressure distributions measured at these clearances, there is a clear indication that the stagnation point is located between 350° and 360°, i.e., slightly towards the bed from the centre point at the front of the cylinder. The pressure distributions at clearances beyond 10 mm ($G/D > 0,2$), are virtually symmetrical around the zero point; the pressure at 350° exceeds that at 10° by a small margin (Figs. 5.12, 5.13 and 5.22 to 5.25).

(iii) Clearances beyond 30 mm (G/D > 0,6):

The pressure distributions indicate that the stagnation point is indeed at 0° or 360°, the front centre point of the cylinder. In some cases (with G/D > 1.2) the front stagnation point appears to be located slightly above the front cylinder centre, i.e. displaced towards the 10° pressure recording location. These cases are indicated as 360+ in Table 5.6. The location of the front stagnation point possibly resulted in a net downward force on the cylinder.

The above observations are in accordance with the findings of Fredsoe and Hansen (1984): As the gap, between cylinder and bed, becomes very small, the front stagnation point moves towards the bed.

5.3.2 Separation Point

The flow follows the shape of the cylinder, until it separates from its wall at the point where the skin friction vanishes. Geometrically, this separation point of the boundary layer coincides with the point (e.g. point A in Fig. 5.3) where the pressure profile's linearly increasing gradient (beyond the maximum negative turning point) suddenly drops to become zero in the wake region behind the cylinder. The pressure value at the separation point is therefore approximately equal to the base pressure, i.e. the average pressure in the wake zone. Depending on the clearance between the cylinder and the bed, a similar second separation point could occur near the bottom of the cylinder; refer to point B in Fig. 5.3.

With all the cylinders on the bed, only one separation point was geometrically identified, except with the smooth and rough 50 mm diameter cylinders on a rough bed. A second separation point at

approximately 240° occurred as a result of "leakage" through the cylinder-rough-bed interface.

The position of the separation point was experimentally determined by Achenbach (1968), when he obtained pressure and skin friction distributions around a cylinder in symmetrical flow, in air. From his results, one can gather that in the subcritical region ($R_e < 3 \times 10^5$), the position of the separation point was

(i) not seriously influenced by the span-diameter ratio of various test cylinders;

(ii) independent of the Reynolds number, except at $R_e = 1{,}5 \times 10^5$ where there was a sudden rise in the separation angle, indicating the beginning of the decreasing trend of the total drag coefficient C_D.

From the pressure plots (Figs. 5.4 to 5.29), it is evident that the span-diameter ratio (12 and 20 for the 50 mm and 30 mm cylinders respectively), does not affect the shape of the pressure profiles or the location of the separation points. Deduction (ii) above, regarding the separation point being independent of R_e, is also applicable to the Reynolds number range of the present study.

Further, Fig. 5.3. shows that a change in Reynolds number (or different flow velocities for the same cylinder arrangement) does not influence the shape of the pressure profile; the separation angle is therefore not affected.

The relationship between the separation angle and G/D (gap-diameter ratio), is graphically indicated in Fig.5.30 for a smooth bed only. From the graph it is clear that for roughened cylinders the boundary layer separates from the cylinder at a later stage, than is the case with smooth cylinders. Except for the one

separation point, when the cylinder is on the bed, two separation points occur at all clearances and generally at corresponding angular positions (also refer to Table 5.6).

5.3.3 Minimum Pressure Point

The relationship between the minimum pressure angle and G/D, is graphically indicated in Fig. 5.31 for a smooth bed. All the minimum pressure locations for the 74 smooth bed runs are shown in Table 5.8. As with the separation angle, these locations are independent of Reynolds number and are essentially determined by the G/D ratio.

The minimum pressure locations θ_{min} for both smooth and rough cylinders occur at approximately the same angles on the upper side of the cylinders, i.e. from 60° to 70°, with θ_{min} for the rough cylinder at a slightly larger angle up to G/D = 0,5 and beyond 1,4. At the lower side of the cylinder, all the minimum pressure points (or maximum velocity points) for rough cylinders were located further from the front centre point of the cylinder, in comparison to smooth cylinders.

5.3.4 Shape of Pressure Profiles

General comments on the shapes of the pressure plots at various clearances are as follows:

(i) Clearance = 0:

The roughened cylinders (on a smooth bed) experienced a fair increase in pressure at the rear of the cylinder, in the wake zone (Figs. 5.4 to 5.7). The same situation, although not as

pronounced, was observed with the cylinders on a rough bed (Figs. 5.18 to 5.21). However, the shapes of the pressure profiles are similar for all smooth bed cases; rough bed profiles are also similar. As expected, the smooth bed situations showed a very sudden increase at 270°, the contact point with the bed.

(ii) Clearance = 10 mm; 50 mm cylinder (G/D = 0,2):

Roughening of the cylinder again generated an increase in the almost constant wake zone pressure, behind the cylinder. The same phenomenon was observed for smooth and rough bed tests. (Figs. 5.8, 5.9, 5.22, 5.23).

(iii) Clearance = 10 mm; 30 mm cylinder (G/D = approx 0,3):

The same situation, as observed in (ii) above, is noted here (Figs. 5.10, 5.11, 5.24, 5.25). Further, it is noticed from the pressure profiles that a symmetrical flow situation is starting to develop.

(iv) Clearance = 30 mm; 50 mm cylinder (G/D = approx 0,6):

Except for a hump in the wake zone of the smooth cylinder, the trend of the pressure profile was similar to what is reported in (iii) above (Figs. 5.12 and 5.13).

Gap-diameter ratios of 0,81 and 0,91, with the same cylinder produced similar plots (Figs. 5.26 and 5.27). Gap-diameter ratios beyond 1,1 (Figs. 5.14 to 5.17, 5.28 and 5.29), indicated further

development of the pressure distributions towards the approaching of symmetrical flow. In all situations, roughening of the cylinders resulted in a larger increase in the pressure behind the cylinder.

5.4 Velocity Profiles

A total of 134 velocity profiles for the flume was plotted. The velocities at the centre of the cylinder were measured directly, by means of the differential micro manometer, as well as read from the velocity profiles as a check; the values corresponded in all cases. The velocity values at the cylinder centre, $U_{D/2}$, are indicated in Table 5.3.

A selection of some velocity profiles is included as Figs. 5.32 to 5.36. Plots of various flows and cylinder arrangements are shown in Figs 5.32 to 5.34 for a smooth bed. The Reynolds numbers indicated on the figures, are based on the velocity at the centre of the cylinder. It is evident that the velocity measurements were not influenced by the cylinder, due to

(i) the shapes of the velocity profiles being similar;

(ii) the thickness of the boundary layer δ, in the flume, is approximately equal to 90 mm for the various test runs in the case of the smooth bed (refer Fig. 5.32).

From the above it is clear that the velocity measurements can also be taken as the velocities that would exist near the bed if the cylinder was not in place.

Similar velocity profiles were plotted for a rough bed (Fig. 5.35). Due to turbulence, the boundary layer was too thick to measure.

The velocity profiles with a smooth and a rough bed, for the same free stream velocity, were also compared (test runs 15 and 101 in Fig. 5.36). The difference in boundary layer thickness is clearly illustrated by the plot. The drag and lift forces, for a smooth 50 mm diameter cylinder on bottom, were calculated from pressure distributions for the smooth bed (Run 15) and the rough bed (Run 101) respectively; the force values are indicated in Table 5.3: The lift and drag forces are less for a rough bed than for a smooth bed, for the same free stream velocity. The same result was obtained by Jones (1971).

5.5 Lift and Drag Coefficients

Lift and drag coefficients were computed for every test run, using equations (5.4) and (5.5); the velocity measured upstream, (and from the velocity profiles) at the elevation of the cylinder centre, was applied. The results are indicated in Table 5.3.

It was evident that the varying depth of the different approach flows, in cases where all the other variables were kept constant, caused an irregular pattern of C_D and C_L values. The depth parameter a_1 was therefore taken into account and C_D/a_1 and C_L/a_1 values calculated (refer to Table 5.3). Nevertheless, there was still a degree of scattering in the data, which could possibly be attributed to the following factors:

(i) The bottom glass panel of the flume, in the testing area, was not sufficiently uniform to prevent leakage under the cylinder, when $G/D = 0$. The panel "sagged" about 1 mm near the centre of the flume, resulting in an estimated "flow" error of less than 0,5%)

(ii) Very slight fluctuations occurred in the micro manometer readings, due to the pulsating approach flow;

(iii) For a few test runs, with the 50 mm cylinder, very slight drawdown of the water surface of approximately 3 mm was measured over the test cylinder.

It was interesting to note that corresponding coefficients were higher for the 50 mm diameter cylinder in comparison to the 30 mm cylinder. As mentioned before, the span-diameter ratios were 12 and 20 respectively. Further, the "vertical" blocking ratio, D/H, was on average 0,2 and 0,15 for the two cylinders concerned. On the whole, the 50 mm cylinder caused more blockage. It is therefore not surprising that the results for the 30 mm cylinder, were more consistent.

Almost all the lift and drag coefficients, illustrated in various graphs for this study, were divided by the depth parameter a_1, to take care of the varying depths for different test runs.

5.5.1 Coefficients computed, using various Velocities

The correct choice of the reference velocity proved to be extremely important. A small error in the velocity represents a larger percentage error in the lift and drag coefficients, which are inversely proportional to the square of the velocity.

(i) Jones' method:

Coefficient computations, by means of Jones' equation (eq. (5.9)), produced values exhibiting the same trend and an increase of 5 % in magnitude, in comparison to calculations based on $U_D/2$, the velocity at the cylinder centre. This was essentially due to the velocity V_{eff} being equal to 0,974 times $U_D/2$. Computed coefficients are indicated in Tables 5.4 (a) and (b).

From the determination of the front stagnation point on the test cylinder (Section 5.3.1 and Table 5.6), at small bed-cylinder clearances, it is evident that the maximum pressure point is not at the front centre of the cylinder. This result and the fact that the cylinders were completely covered in the flume's boundary layer, indicate that the reference velocity should not be taken as the upstream velocity, measured at the centre of the cylinder, for these particular situations. Further, the degree of consistency of coefficients generated by means of equation (5.9) (from Jones, 1971), derived for on-bed locations in the boundary layer, leaves no doubt regarding its applicability in this study.

(ii) Fredsoe and Hansen's method:

Velocities, using equation (5.10), generated coefficients which were 9 % to 50 % higher compared to computations with $U_{D/2}$ (Table 5.5). As these values were too inconsistent, mainly due to insufficient information on the velocities measured directly above the cylinder when in place, they were not used in this study.

(iii) Roshko's correction:

"Blockage corrections" using Eq. (5.12) resulted in an almost 40 % reduction in the drag coefficient in some cases (Table 5.5). The equation was intended for a stream of infinite width, flowing symmetrically over a cylinder. Further, only drag coefficient and velocity corrections are taken into account. As both Roshko's correction and the correction deduced by Shaw (1971) were applicable to a symmetrical flow situation, they were not utilised in the present study.

(iv) Reference velocity finally applied:

As the cylinders were partly or wholly immersed in the flume's boundary layer for all clearances up to 30 mm, the reference velocity based on Jones' method was applied to

these cases. For the on-bed location, equation (5.9) was directly applied. An adapted graphical version was used to determine the effective velocity at the other clearances concerned. The following expression was used:

$$V^2_{eff} = \frac{1}{D} \int_G^{G+D} [U(y)]^2 \, dy \qquad (5.13)$$

The integral refers to the area under the U^2 versus y curve between y = G (the gap between bed and cylinder) and y = G+D, i.e. over the projected diameter of the cylinder.

For all clearances beyond 30 mm, the velocity at the cylinder centre, $U_{D/2}$, was used to calculate all lift and drag coefficients.

The calculated lift and drag coefficients finally used in this study, can be found in the various tables indicated in the schedule below.

TABLES	CYLINDER DIAMETER (mm)	Gap G (mm)	G/D	REFERENCE VELOCITY APPLIED (% of $U_{D/2}$)
5.4 (a) & (b)	30 & 50	0	0	*97,4
5.4 (c)	50	10	0,2	*98,46
5.4 (c)	30	10	0,33	*99,0
5.4 (c)	50	30	0,6	*99,7 %
5.3	30 & 50	>30	>0,6	100

(* as determined graphically and mathematically by means of equations (5.8), (5.9) and (5.13) from a selection of test runs.)

5.5.2 Cylinders Resting on the Bed

Fig. 5.37 indicates plots for drag coefficients C_D and C_D/a_1, and Fig. 5.40 for lift coefficients C_L and C_L/a_1. All other figures up to Fig. 5.42, illustrate values for either C_D/a_1, or C_L/a_1. The downtrends of all these drag coefficient plots are possibly an indication of the start of the critical region.

A linear relationship between the force coefficients and Reynolds number was assumed. Linear regression lines were therefore determined for all such relationships. The equations of the various regression lines are included in Appendix 2.

As mentioned earlier in Section 5.5 (see pp. 5-19 and 5-20), factors such as the pulsating approach flow presumably caused some scattering in the calculated force coefficients; refer Fig. 5.37. The smooth 50 mm cylinder produced curvilinear relationships for the drag and lift coefficients with a smooth bed (Figs. 5.38 and 5.41), and the lift coefficient with a rough bed (Fig. 5.42).

Although the on-bed location of this cylinder probably caused more flow blockage than the other test combinations, a thorough analysis of the experimental data revealed the existence of at least one deviating value in each of the cases mentioned. These deviating values were generated by test run 12 (R_e = 9 447; a_1 = 0,756) in Figs. 5.38 and 5.41, and test run 104 (R_e = 11 429; a_1 = 0,724) in Fig. 5.42. It is interesting to note that in both these test runs, the water depth was less than four cylinder diameters and about 3 mm drawdown of the water surface occurred visibly over the cylinder. A total of eight such cases were identified for $G/D \leq 0,2$ (see Table 5.3). It is estimated that a slightly larger drawdown (about 3 mm) of the water surface, which is characteristic of relatively shallower water in the flume, could influence the force coefficients by as much as 10%.

The drawdown of the water over the cylinder, results in a reduction in pressure at the top of the cylinder; i.e. a smaller minimum pressure value and wake region pressure. With reference to Fig. 10.1(b) and the calculations in Section 10.5, it is evident

that a smaller minimum pressure results in an increase in the lift coefficient, while a smaller wake pressure is associated with a higher drag coefficient. In the plots concerned, both linear and curvilinear interpretations are given (refer Figs. 5.38, 5.41, 5.42 and 5.44). Due to the abovementioned conclusion, only the linear interpretations were however considered.

The least-squares straight-line analysis of the sets of lift and drag coefficients, generated for both 30 and 50 mm cylinders (smooth and rough on a smooth bed), revealed very interesting information. When smooth and rough cylinders of similar dimensions were compared, the slopes of the linear regression lines were the same for each pair compared, with the roughened cylinders' coefficient slightly higher in most cases. Figures 5.37, 5.38, 5.40 and 5.41 illustrate this situation for a smooth bed.

The same situation only applied to the drag coefficient plots for a rough bed (Figs. 5.39) up to R_e = 16 000. Due to the similarity between corresponding situations and the fact that the Reynolds number range was essentially from 10 000 to 20 000, average values of C_D/a_1 and C_L/a_1 were calculated for each combination of variables. These average results, indicated in Table 5.7, facilitate relative comparisons between various situations with the same cylinder.

In the smooth bed case, it was not practical to seal the very small gap (due to the non-uniformity of the bottom panel) under the cylinder, as the cylinder with the single pressure tapping had to be rotated. This aspect (i.e. a very small gap) did not seem to have any marked influence on the results; Ø,5% error estimated.

Comparisons between the drag coefficient plots for smooth and rough beds (Fig. 5.38 compared to Fig. 5.39), revealed conflicting results for the 30 and 50 mm cylinders. Regarding the lift coefficient, no conclusive results were produced, as the corresponding plots (Figs. 5.41 and 5.42) for the smooth and rough beds intersect.

The lift coefficient for both the smooth and rough 30 mm cylinders, on a smooth bed, revealed an interesting phenomenon: with an increase in Reynolds number, the lift coefficient decreased by roughly 30 %, over the Reynolds number range 9 000 to 17 000 (Table 5.3 and Fig. 5.40). The rough bed generated a less pronounced decreasing tendency in the lift coefficient.

5.5.3 Cylinders Near the Bed

When considering various bed conditions separately, the drag coefficient did not appear to be substantially influenced by an increase in the gap under the cylinder. A graphical representation of the drag coefficients of the rough 30 mm cylinder, at various clearances, is shown in Fig. 5.43.

The tests performed with the smooth 50 mm cylinder, with a smooth bed, were more comprehensive than those with any of the other cylinders. It was interesting to note that the average C_D/a_1 value for this cylinder increased slightly from 1,71 to 1,93, when G/D was reduced from 1,2 to 0,6. With further reductions in G/D, the average drag coefficient C_D/a_1 decreased to 1,55. Roshko et al (1975), Göktun (1975) and Haffen (1975) found a similar trend; Roshko et al carried out experiments in air at a Reynolds number of 20 000. According to Roshko et al the decrease closer to the bottom, could be attributed to the cylinder being completely immersed in the lower energy boundary layer of the bed, and the interference of the bed with vortex shedding.

The lift coefficient was very dependent on the G/D ratio. With a gap of 5 mm (G/D = 0,1), the C_L/a_1 value for the smooth 50 mm cylinder decreased from approximately 1,1 at G/D = 0 to 0,44. Further away from the bottom, the lift coefficient approached zero. Lift coefficient curves are shown in Figs. 5.44 and 5.45.

Some test runs (at $G/D > 1.0$) produced negative lift coefficients; the front stagnation points for these runs were located slightly above the front centre of the cylinder (refer Table 5.6). Zdravkovich (1985) also obtained negative lift coefficients, for G/D values between 0,3 and 1,5 in the subcritical Reynolds number region.

5.5.4 Graphs of Average Lift and Drag Coefficients versus G/D

From the average coefficients summarised in Table 5.7, graphs were plotted with the coefficient concerned and G/D as the primary variables. On the same diagram, plots with parameters such as cylinder size, cylinder roughness and bed roughness were shown.

Plots of the average drag coefficient versus G/D are shown in Figs. 5.46 and 5.47. The coefficients for the larger cylinder were somewhat higher. Bed roughness produced inconsistent comparisons between corresponding force coefficients. Except for the larger cylinder on a smooth bed, cylinder roughening apparently led to higher drag coefficients.

Various plots of the average lift coefficient versus G/D are shown in Figs. 5.48 to 5.51. Various combinations of the 50 mm cylinders are illustrated in Fig. 5.48, while similar combinations for the smaller cylinders are shown in Fig. 5.49. All the smooth bed combinations are plotted in Fig. 5.50 and the all rough bed situations in Fig. 5.51.

Virtually all the average lift coefficient versus G/D-curves approach zero (symmetrical flow), at a G/D value of approximately 1,5. Only the curves for the 50 mm cylinder (Fig. 5.48) indicated that cylinder roughening causes a higher lift coefficient; the smaller 30 mm cylinder produced conflicting results (Fig. 5.49).

The lift curves for a smooth bed, reveal that except for the rough 50 mm cylinder, lift coefficient values almost coincide (Fig. 5.50). Although not as pronounced, a similar tendency is noticeable in the plots for the rough bed below $G/D < 0,3$ (Fig. 5.51).

If the lift coefficient results for the larger cylinder are ignored, due to its higher blocking ratio, it is evident that cylinder roughening and a rough bed do not have any marked

Smooth Bed				Rough Bed			
Cylinder dia (mm)	$G/_D$	$C_D/_{a_1}$	$C_L/_{a_1}$	Cylinder dia (mm)	$G/_D$	$C_D/_{a_1}$	$C_L/_{a_1}$
50S	Ø	1,55	1,14	50S	Ø	2,17	Ø,90
	Ø,1	1,78	Ø,44		Ø,2	1,91	Ø,36
	Ø,2	1,75	Ø,29		Ø,910	1,95	Ø,02
	Ø,6	1,93	+Ø,Ø3				
	1,2	1,71	-Ø,Ø7				
52R	Ø	1,57	1,31	52R	Ø	2,26	1,11
	Ø,192	1,81	Ø,55		Ø,192	2,Ø8	Ø,7Ø
	Ø,554	1,76	Ø,24		Ø,812	2,Ø4	Ø,16
	1,135	1,855	Ø,11				
30S	Ø	1,43	Ø,87	30S	Ø	1,63	Ø,64
	Ø,333	1,49	Ø,15		Ø,333	1,58	Ø,Ø4
	2,667	1,51	-Ø,Ø2		2,19	1,62	-Ø,11
31,8R	Ø	1,68	Ø,83	31,8R	Ø	1,78	Ø,65
	Ø,314	1,93	Ø,18		Ø,314	1,72	Ø,13
	2,484	1,73	-Ø,Ø6		2,Ø25	1,68	Ø,Ø4

TABLE 5.7 AVERAGE LIFT AND DRAG COEFFICIENTS vs. G/D (corrected for varying depth and blockage)

Smooth bed (* S = smooth; R = rough)

Run No.	*Dia of Cylinder D (mm)	Gap G (mm)	$G/_D$	δ (mm)	$G/_\delta$	$G/_D$	V_{eff} (m/s)	Reynolds No	Θ_{sep}	Θ_{min}	Pressure Coefficients			
											C_{po}	C_{pm}	C_{pb}	C_{pb} - C_{pm}
1	50S	0	0	166,5	0	1,17	0,209	10 470	105	70	0,83	-0,83	-0,773	0,057
12	50S			-	-	1,69	0,189	9 447	105	70	0,385	-1,96	-1,785	0,175
13	50S			105,7	0	1,20	0,328	16 411	105	70	0,686	-1,069	-0,813	0,256
14	50S			117,8	0	1,25	0,36	18 018	105	70	0,627	-1,312	-0,974	0,338
15	50S			105,9	0	1,33	0,386	19 333	105;	60	0,638	-1,477	-1,116	0,361
2	50S	60	1,2	-	-	1,146	0,251	12 550	90;270	70;290	0,357	-2,123	-2,104	0,02
3	50S			155,6	0,386	1,64	0,274	13 700	90;270	70;290	0,883	-2,315	-2,182	0,133
4	50S			121,4	0,494	1,32	0,347	17 350	90;270	75;280	0,800	-1,609	-1,547	0,062
5	50S			170,9	0,351	1,46	0,358	17 900	90;270	70;290	0,927	-1,892	-1,736	0,156
6	50S			105,6	0,568	1,41	0,418	20 900	90;270	65;290	0,923	-1,603	-1,417	0,186
7	50S	30	0,6	155,5	0,193	1,41	0,319	15 952	90;260	70;280	0,848	-1,585	-1,474	0,111
8	50S			90,5	0,331	1,60	0,404	20 189	90;260	70;280	1,149	-1,647	-1,57	0,077
9	50S			95,9	0,313	1,48	0,47	23 479	90;260	70;280	1,053	-1,613	-1,500	0,113
10	50S			79,3	0,378	1,52	0,49	24 476	90;260	70;280	0,974	-1,562	-1,526	0,036
11	50S			117,1	0,256	1,52	0,453	22 632	90;260	70;290	1,151	-1,535	-1,45	0,085
16	50S	2,73	0,055	100,0	0,027	1,58	0,24	12 017	105;250	70;270	0,608	-1,084	-1,758	0,326
17	50S	5	0,1	117,6	0,043	1,48	0,316	15 778	100;250	70;270	0,914	-1,728	-1,477	0,25
18	50S			113,6	0,044	1,38	0,392	19 600	100;250	80;270	0,984	-1,399	-1,172	0,228
19	50S			117,5	0,043	1,01	0,471	23 570	100;250	70;270	0,902	-0,913	-0,727	0,186
20	50S			102,9	0,049	1,31	0,396	19 800	100;250	70;270	1,148	-1,244	-0,997	0,247
21	50S			115,1	0,043	1,46	0,29	14 500	100;250	70;270	0,728	-1,769	-1,516	0,253
22	50S	10	0,2	-	-	1,66	0,316	15 802	90;260	70;270	0,839	-2,304	-2,003	0,30
23	50S			127,5	0,078	1,3	0,351	17 525	90;260	70;270	0,842	-1,603	-1,38	0,223
24	50S			108,3	0,092	1,23	0,384	19 200	90;260	60;270	1,068	-1,289	-1,068	0,22
25	50S			100,2	0,10	1,18	0,411	20 528	90;260	60;270	1,036	-1,258	-1,021	0,237
26	50S			127,5	0,078	1,11	0,430	21 513	90;260	60;270	0,947	-1,217	-0,98	0,237
27	52R	59	1,135	98,8	0,597	1,71	0,281	14 612	110;250	70;270	0,947	-1,231	-0,987	0,244
28	52R			96,1	0,614	1,44	0,36	18 720	110;250	75;280	0,945	-1,524	-1,375	0,145
29	52R			120,1	0,491	1,42	0,405	21 060	110;250	80;280	0,96	-1,57	-1,387	0,183
30	52R			96,4	0,612	1,58	0,429	22 308	80;250	80;250	1,066	-1,433	-1,433	0
31	52R			96,4	0,612	1,32	0,458	23 816	110;250	80;280	0,93	-1,537	-1,240	0,298
47	52R			126,3	0,467	1,14	0,487	25 324	110;250	60;275	1,097	-1,755	-1,155	0,6
32	52R	0	0	136,4	0	1,29	0,212	11 040	105	70	0,529	-1,613	-1,057	0,556
33	52R			116,4	0	1,08	0,394	20 511	105	70	0,813	-1,667	-0,854	0,813
34	52R			86,4	0	1,27	0,314	16 308	105	70	0,558	-1,825	-1,141	0,685
35	52R			116,4	0	1,57	0,26	13 522	105	70	0,666	-2,108	-1,554	0,555
36	52R			90,4	0	1,17	0,404	21 018	105	70	0,834	-1,517	-0,797	0,72

TABLE 5.8: Boundary layer thickness (from velocity profiles) and Pressure Coefficients (from measured pressures)

Smooth bed (* S = smooth; R = rough)

Run No.	Dia of Cylinder D (mm)	Gap G (mm)	$G/_D$	δ (mm)	$G/_\delta$	$G/_D$	V_{eff} (m/s)	Reynolds No	θ_{sep}	θ_{min}	Pressure coefficients			
											C_{po}	C_{pm}	C_{pb}	$C_{pb}-C_{pm}$
48	52R			125,9	0	1,23	0,424	22 031	105	60	0,508	-1,579	-1,154	0,424
49	52R			95,9	0	1,08	0,443	23 044	105	65	0,765	-1,612	-0,841	0,771
37	52R	28,8	0,554	86,4	0,333	1,31	0,326	16 953	110;240	70;270	0,871	-1,565	-1,388	0,176
38	52R			111,3	0,259	1,38	0,418	21 723	110;240	70;270	0,945	-2,039	-1,474	0,565
39	52R			109,6	0,263	1,35	0,47	24 419	110;240	70;265	1,115	-1,80	-1,319	0,481
40	52R			-	-	1,52	0,439	22 811	110;240	70;270	1,336	-2,173	-1,524	0,649
41	52R			-	-	1,45	0,431	22 397	110;240	70;270	1,171	-1,803	-1,380	0,424
46	52R			120,9	0,238	1,19	0,473	24 574	110;240	65;260	1,101	-1,956	-1,224	0,732
42	52R	10	0,192	-	-	1,81	0,298	15 513	110;240	60;265	0,943	-2,717	-2,125	0,591
43	52R			-	-	1,51	0,439	18 124	110;240	60;265	0,675	-1,375	-0,928	0,448
44	52R			-	-	1,35	0,376	19 557	110;240	60;265	1,123	-2,043	-1,30	0,743
45	52R			145,7	0,069	1,22	0,451	23 448	110;240	60;265	1,070	-1,764	-1,088	0,676
50	52R			95,9	0,104	1,11	0,464	24 114	110;240	60;260	1,045	-1,597	-0,900	0,697
51	30S	80	2,67	-	-	1,41	0,301	9 309	90;270	70;280	0,98	-2,164	-2,065	0,098
52	30S			-	-	1,30	0,399	12 340	90;270	70;280	0,528	-1,639	-1,559	0,08
53	30S			-	-	1,31	0,477	14 906	90;270	80;280	0,873	-1,332	-1,264	0,067
54	30S			105,9	0,755	1,28	0,590	18 632	90;270	65;290	1,053	-1,316	-1,152	0,164
55	30S	0	0	145,9	0	1,04	0,462	12 713	105	70	0,376	-0,823	-0,668	0,155
56	30S			145,9	0	1,17	0,575	15 812	105	70	0,435	-0,751	-0,651	0,1
57	30S			-	-	1,30	0,40	11 148	105	70	0,294	-1,018	-0,947	0,072
58	30S			-	-	1,47	0,32	8 670	105	70	0,249	-1,144	-1,007	0,137
59	30S	10	0,333	-	-	1,51	0,271	9 042	100;260	70;270	1,023	-1,56	-1,421	0,139
60	30S			-	-	1,35	0,39	12 930	100;260	70;280	0,594	-1,64	-1,481	0,159
61	30S			-	-	1,35	0,465	15 510	100;260	65;270	0,654	-1,507	-1,395	0,112
62	30S			106,7	0,094	0,94	0,497	16 566	60;290	60;290	0,855	-0,727	-0,727	0
63	31,8R	79	2,484	-	-	1,70	0,341	12 050	100;260	80;280	0,58	-2,058	-2,047	0,011
64	31,8R			-	-	1,50	0,438	15 476	100;260	80;290	0,796	-1,559	-1,546	0,013
65	31,8R			125,9	0,627	1,37	0,529	18 691	100;260	80;280	0,423	-1,415	-1,324	0,091
66	31,8R			121,0	0,653	1,37	0,581	20 760	100;260	85;280	0,826	-1,260	-1,161	0,099
67	31,8R	10	0,314	85,9	0,116	1,32	0,522	18 642	110;260	75;270	1,000	-1,154	-0,944	0,21
68	31,8R			-	-	1,49	0,463	16 648	110;260	80;270	0,814	-1,562	-1,413	0,148
69	31,8R			-	-	1,71	0,406	14 585	110;260	80;270	0,934	-1,753	-1,629	0,124
70	31,8R			-	-	2,02	0,279	9 975	110;260	80;270	0,589	-2,666	-2,584	0,082
71	31,8R	0	0	-	-	1,65	0,272	9 731	105	80	0,568	-1,669	-1,531	0,138
72	31,8R			-	-	1,39	0,369	13 308	105	80	0,168	-1,73	-1,449	0,28
73	31,8R			-	-	1,43	0,444	16 050	105	80	0,497	-1,517	-1,272	0,245
74	31,8R			123,9	0	1,26	0,481	17 400	105	80	0,737	-1,078	-0,847	0,231

TABLE 5.8 (Continued)

influence on the lift coefficient in the Reynolds number range concerned.

5.6 Pressure Coefficients

Pressure coefficients were calculated for all the smooth bed test runs for the front centre point, the minimum pressure point and the average wake pressure zone. These coefficients are respectively indicated by the symbols C_{po}, C_{pm} and C_{pb}, and are given in Table 5.8. The pressure coefficients were calculated using

$$C_p = (p_\theta - p_{stat}) / \tfrac{1}{2}\rho V_{eff}^2 \qquad (5.14)$$

where p_θ = pressure at angle θ from the front centre of the cylinder

p_{stat} = static pressure measured on the flume bed directly below the cylinder (this was determined for every run)

V_{eff} = effective flow velocity at the elevation of the front stagnation point, determined according to the method outlined in Section 5.5.1 (iv) above; calculated V_{eff} values are indicated in Table 5.8.

Graphical representations of C_{po}, C_{pm}, C_{pb} and $(C_{pb} - C_{pm})$ versus Reynolds number, at various G/D ratios, are shown in Figs. 5.52 to best lines through the points plotted. The deviating values generated by test run 12 are not included in the plots.

5.6.1 Front centre pressure coefficient C_{po}

Plots indicating the variation of C_{po} with Reynolds number are shown in Fig. 5.52. It is interesting that the G/D = 0 line for the 30 mm cylinder, has lower C_{po} values than the other lines. This is due to the maximum pressure point concerned, being displaced further towards the bed.

5.6.2 Minimum pressure coefficient C_{pm}

The C_{pm} plots (Fig. 5.53) show a similar tendency to the C_{po} plots. However, the gradient of the G/D = 0 line for the 50 mm cylinder, differs from the other G/D lines. As also indicated in Fig. 5.52, only plots for smooth cylinders are shown.

5.6.3 Base pressure coefficient C_{pb}

Base pressure coefficient plots for smooth cylinders are indicated in Fig. 5.54. Except for the gradient of the G/D = 0 line for the 50 mm cylinder, all the C_{pb} lines display an increasing slope; this latter tendency was expected.

A comparison between the base pressure coefficient plots for smooth and rough cylinders, provided interesting information about the 50 and 30 mm cylinders (Figs. 5.55 and 5.56); surface roughness ratios were 2×10^{-2} and 3×10^{-2} respectively. The "smooth" and "rough" plots for the 50 mm cylinder (Fig. 5.55), intersect for corresponding G/D values, and therefore give no clear indication about the influence of roughness. However, regarding the 30 mm cylinder (Fig. 5.56), the "rough" plots consistently have somewhat smaller C_{pb} values, which imply a higher drag coefficient.

The variation of the base pressure coefficient C_{pb} with the gap ratio G/D, at a Reynolds number of approximately 20 000, is shown in Fig. 5.57 for both smooth and rough cylinders. For virtually all G/D values up to 2,5, the curve for the rough cylinder has a higher C_{pb} value than the smooth cylinder. Although the curves shown in Fig. 5.57 are essentially based on C_{pb} values for the 50 mm cylinder, some values for the 30 mm cylinder were also accommodated; i.e. length to diameter ratios L/D of 12 and 20 respectively. It is therefore evident that the base pressure coefficient is not appreciably influenced by the L/D ratio.

5.6.4 Difference between C_{pb} and C_{pm}

Plots of $(C_{pb} - C_{pm})$ versus Reynolds number (Fig. 5.58) show a substantial difference between the G/D = Ø lines (on bed locations) for the rough and smooth 5Ø mm cylinders. The much higher $(C_{pb} - C_{pm})$ values for the rough cylinder, imply a smaller drag coefficient for roughened cylinders. The "symmetrical" flow lines (G/D equal to about 1,2) for the smooth and rough cylinders virtually coincide. A careful analysis of the $(C_{pb} - C_{pm})$ values for the 3Ø mm cylinder, showed little difference between corresponding "rough" and "smooth" combinations; the slight degree of scatter confirmed the fact that it was difficult to find C_{pm} exactly.

5.7 Drag Coefficient variation with G/δ

The boundary layer thickness (refer to Fig. 5.34 for definition) was geometrically determined for all the smooth bed test runs from the velocity profiles obtained. In a few cases the boundary layer was too thick to measure due to a degree of free stream turbulence being present; for the same reason no boundary layer measurements were possible for the rough bed test runs. Boundary layer thicknesses as well as the gap to boundary layer thickness ratios G/δ for the various test runs are indicated in Table 5.8.

The variation of the drag coefficient C_D/a_1 with G/δ for smooth cylinders is shown in Fig. 5.59, and for both smooth and rough cylinders in Fig. 5.6Ø. The C_D/a_1 values were calculated using V_{eff} (refer Table 5.8) as the reference velocity. The scatter of the C_D/a_1 values, particularly for a rough bed, is essentially due to free stream turbulence. A least-squares straight-line analysis for the 17 points plotted up to G/D = Ø,4 (Fig. 5.59), revealed an increasing tendency in C_D/a_1 as G/δ progressed; a further three possible measurements indicated a decreasing trend beyond G/D = Ø,4.

Zdravkovich (1985) performed similar tests in air near the critical Reynolds number (refer to Fig. 2.14) and found that the dependence of the drag coefficient C_D on G/δ was a "more relevant parameter" than the gap to diameter ratio G/D. Comparisons between the various C_D/a_i versus G/D and C_D/a_i versus G/δ plots shown in this Chapter, indicated that the latter relationship is more consistent at near-bed locations of the cylinder.

5.8 General Comments

The results obtained by means of the unique methods, described in Chapters 3 and 4, were very satisfactory. The apparatus responded well and the pressure and velocity measurements were fairly accurate.

The following measures are, however, recommended for similar tests performed in future:

(i) The average approach velocity should be limited to Ø,4 m/s, to minimise fluctuations in manometer readings, caused by very slight changes in the flume's water level;

(ii) The water in the flume should be at least five cylinder diameters deep, to reduce the blocking ratio of the test cylinder.

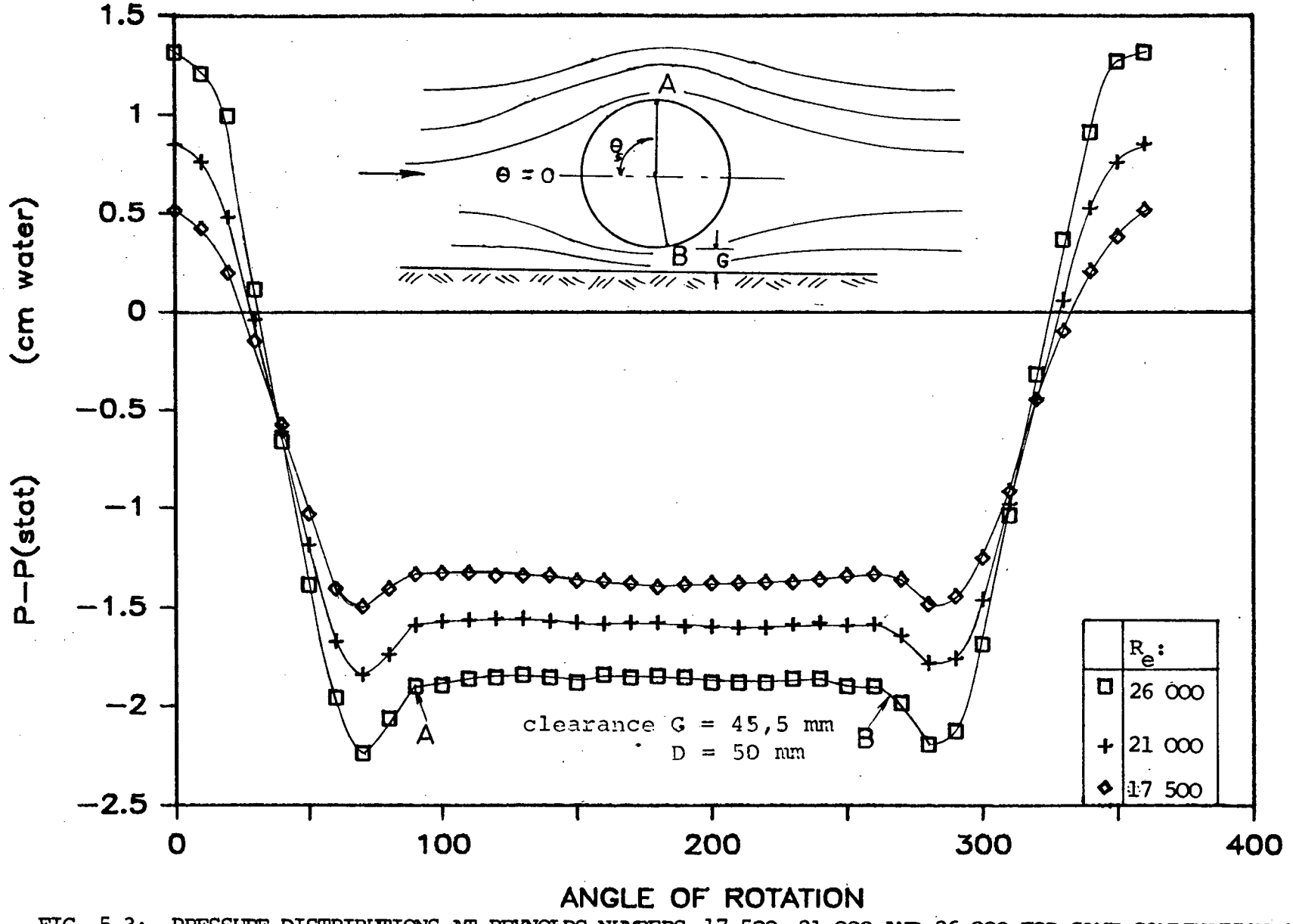

FIG. 5.3: PRESSURE DISTRIBUTIONS AT REYNOLDS NUMBERS 17 500, 21 000 AND 26 000 FOR SAME COMBINATION OF VARIABLES

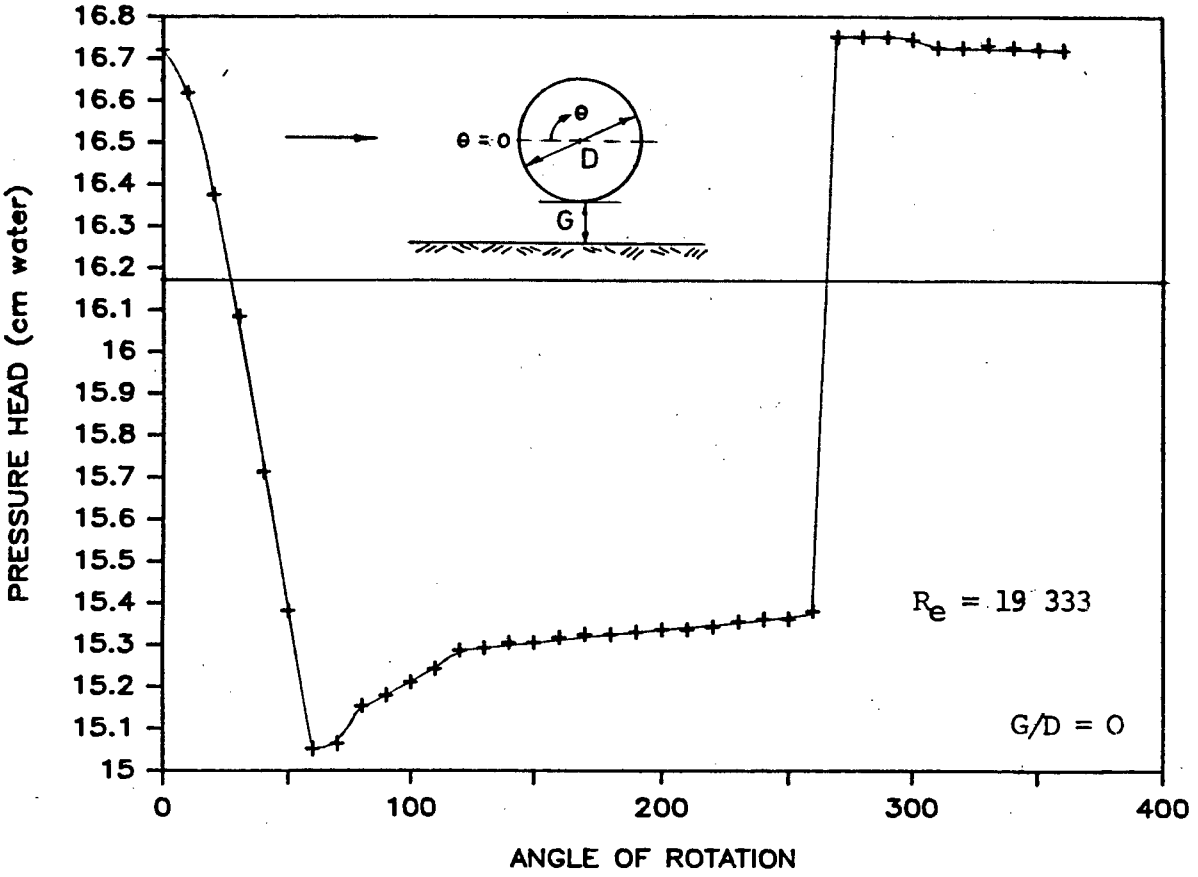

FIG 5.4: PRESSURE DISTRIBUTION WITH SMOOTH 50 mm CYLINDER; SMOOTH BOTTOM; CLEARANCE = 0

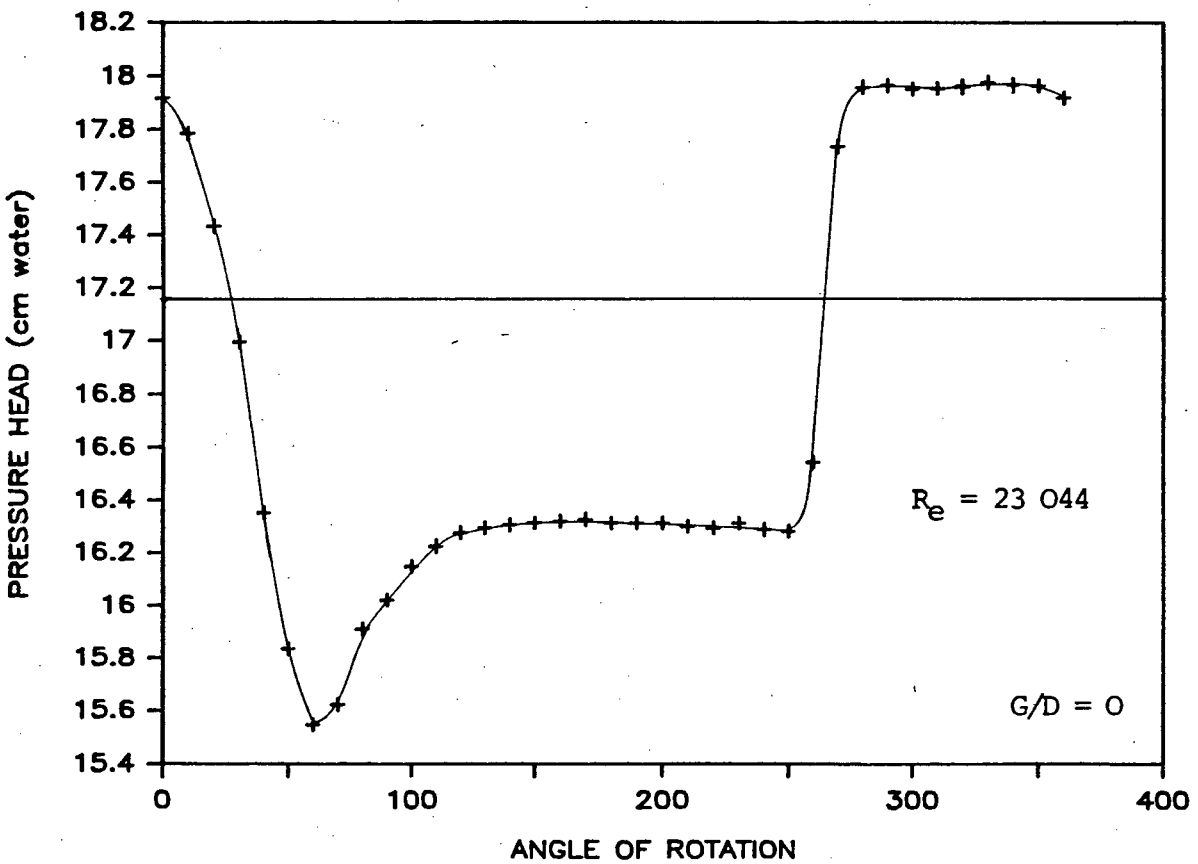

FIG. 5.5: PRESSURE DISTRIBUTION WITH ROUGH 52 mm CYLINDER; SMOOTH BOTTOM; CLEARANCE = 0

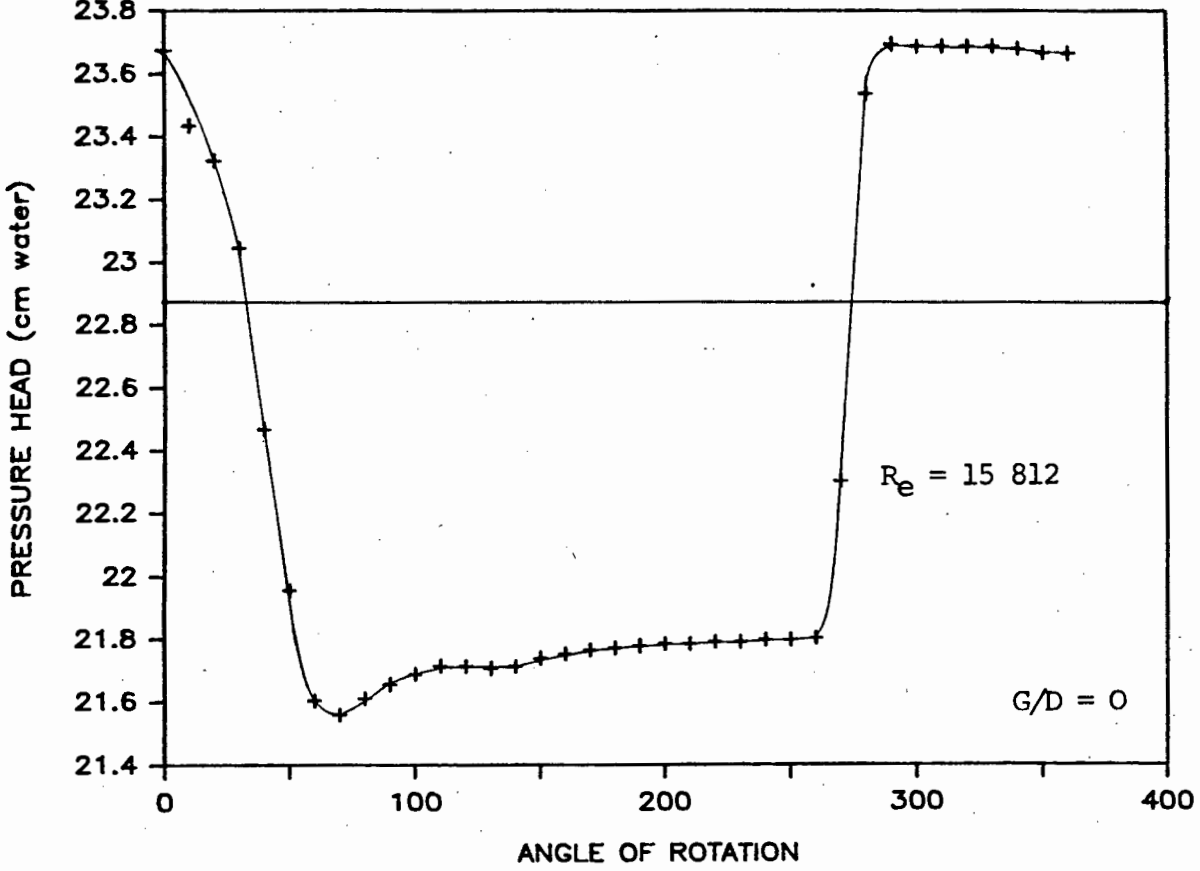

FIG. 5.6: PRESSURE DISTRIBUTION WITH SMOOTH 30 mm CYLINDER; SMOOTH BOTTOM; CLEARANCE = 0

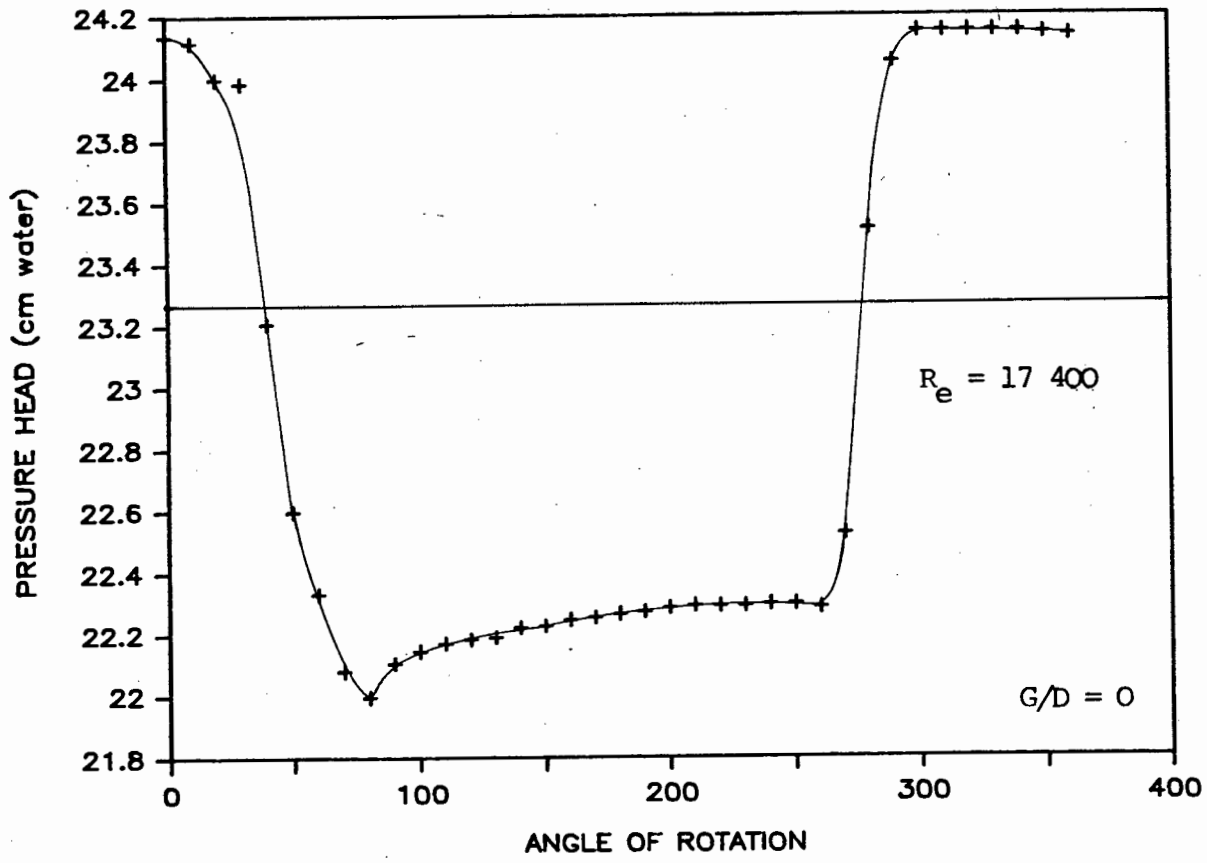

FIG. 5.7: PRESSURE DISTRIBUTION WITH ROUGH 31,8 mm CYLINDER; SMOOTH BOTTOM; CLEARANCE = 0

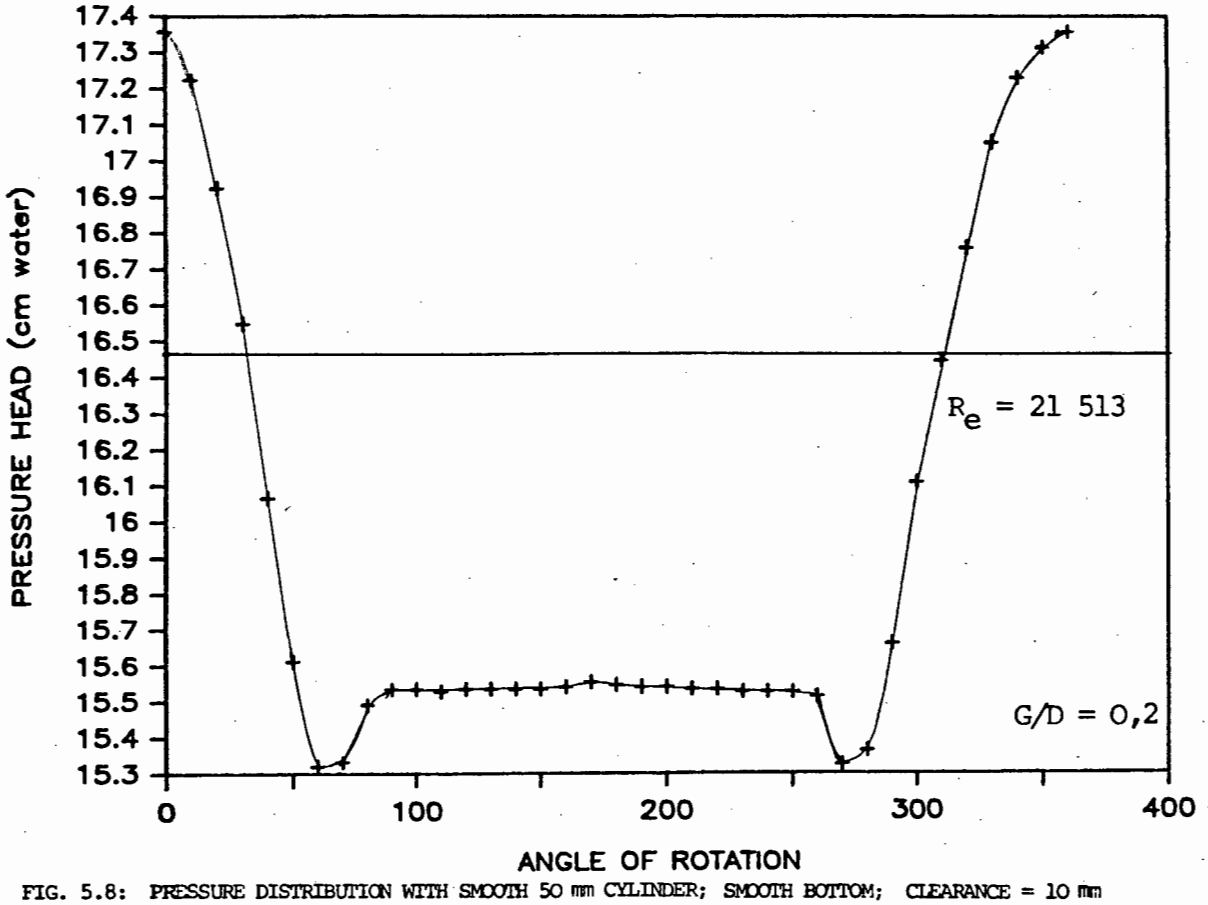

FIG. 5.8: PRESSURE DISTRIBUTION WITH SMOOTH 50 mm CYLINDER; SMOOTH BOTTOM; CLEARANCE = 10 mm

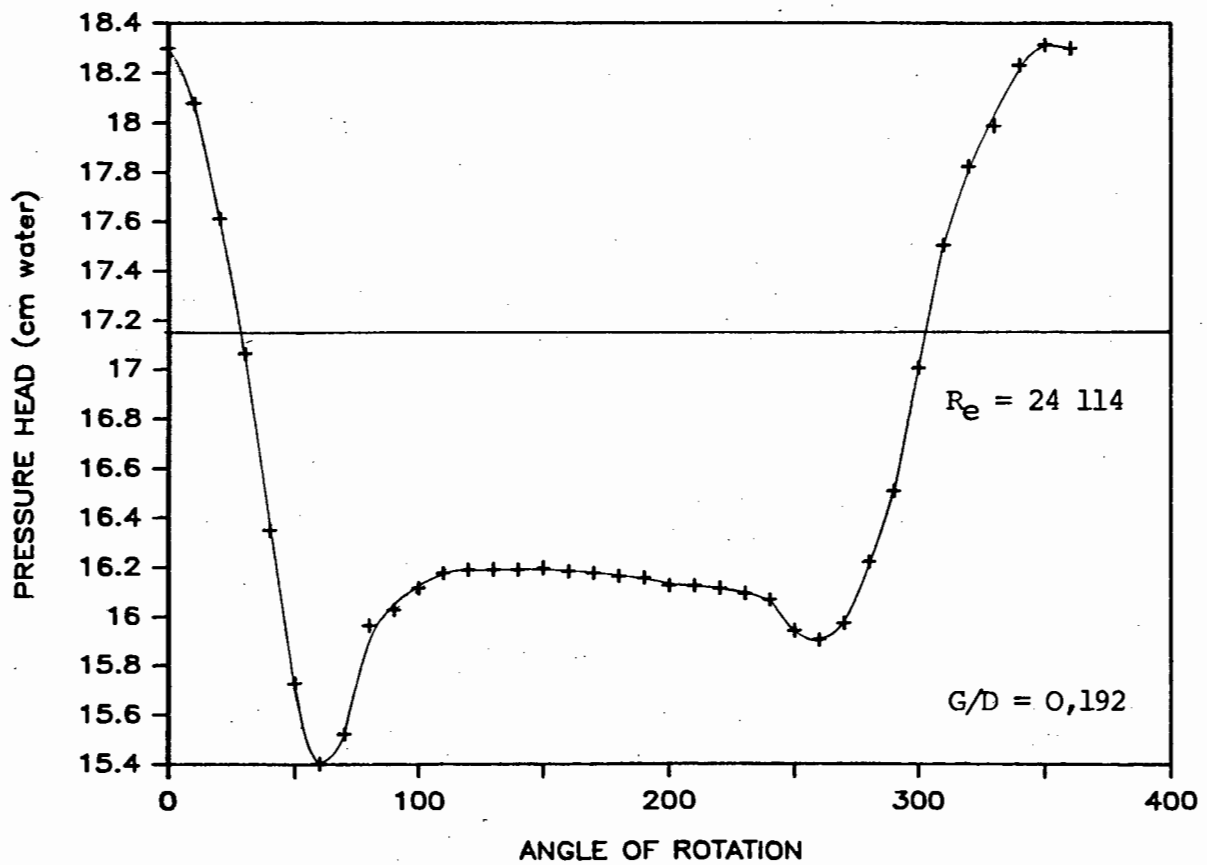

FIG. 5.9: PRESSURE DISTRIBUTION WITH ROUGH 52 mm CYLINDER; SMOOTH BOTTOM; CLEARANCE = 10 mm

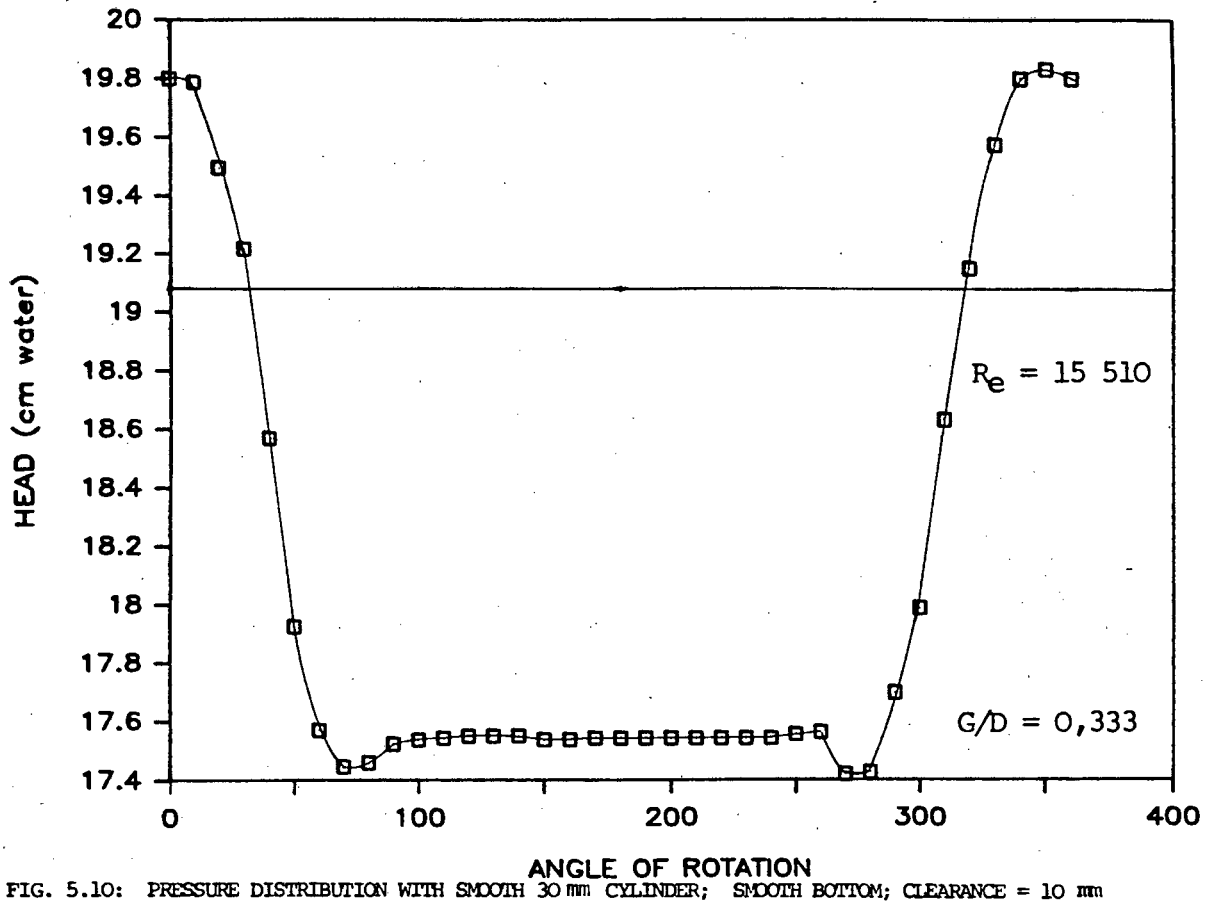

FIG. 5.10: PRESSURE DISTRIBUTION WITH SMOOTH 30 mm CYLINDER; SMOOTH BOTTOM; CLEARANCE = 10 mm

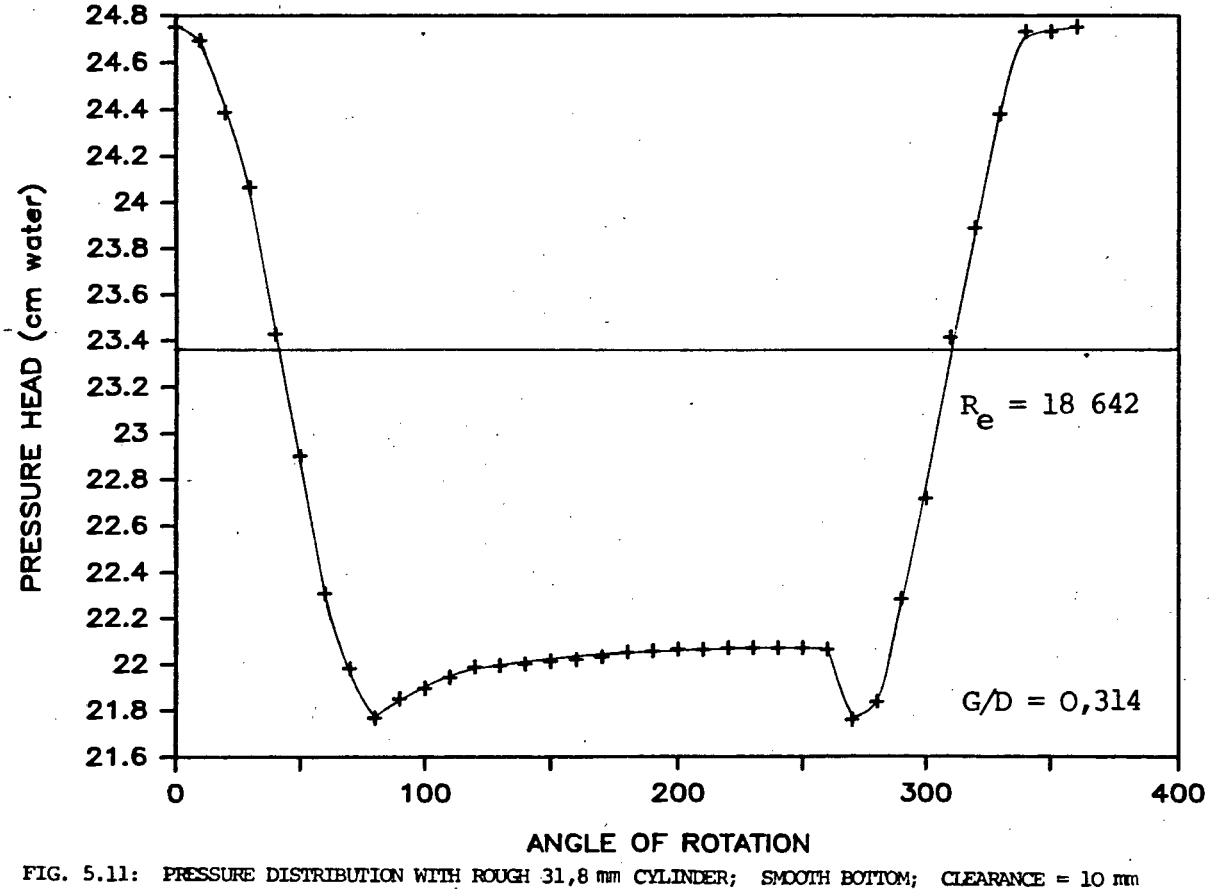

FIG. 5.11: PRESSURE DISTRIBUTION WITH ROUGH 31,8 mm CYLINDER; SMOOTH BOTTOM; CLEARANCE = 10 mm

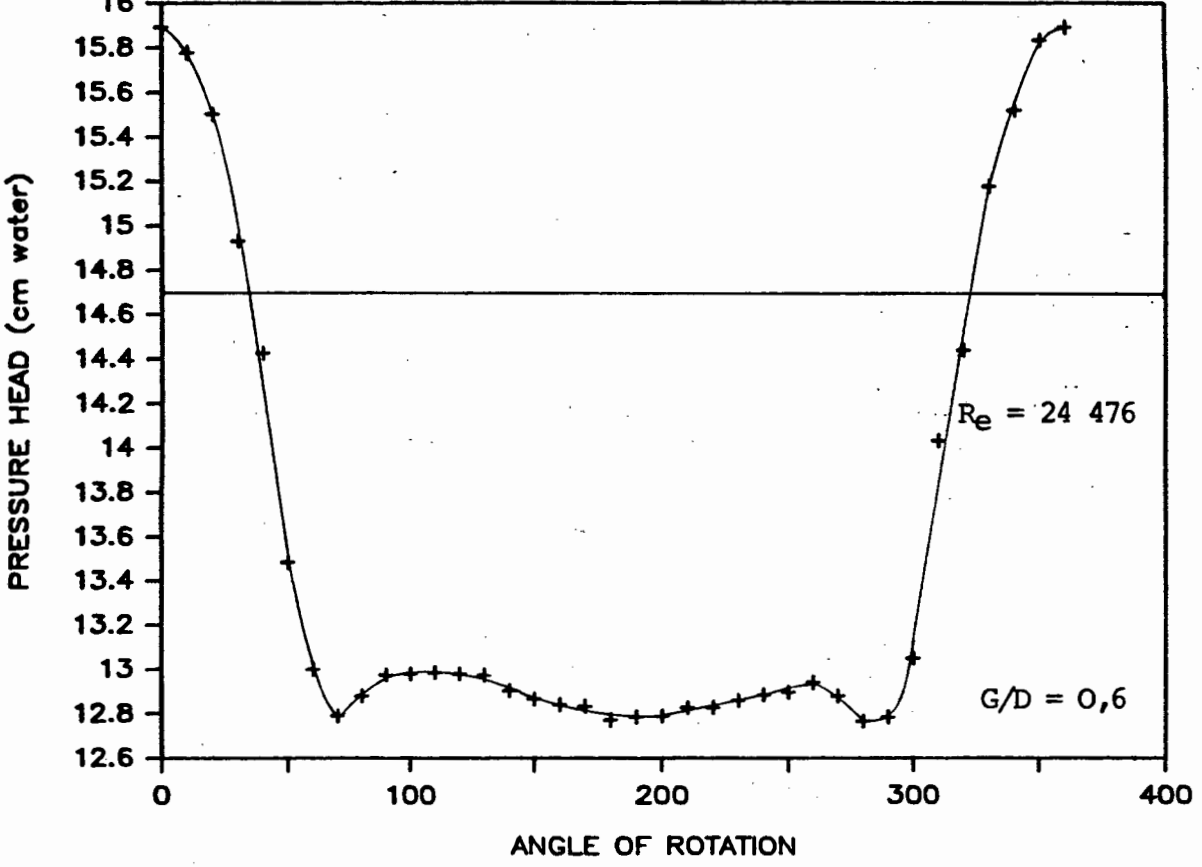

FIG. 5.12: PRESSURE DISTRIBUTION WITH SMOOTH 50 mm CYLINDER; SMOOTH BOTTOM; CLEARANCE = 30 mm

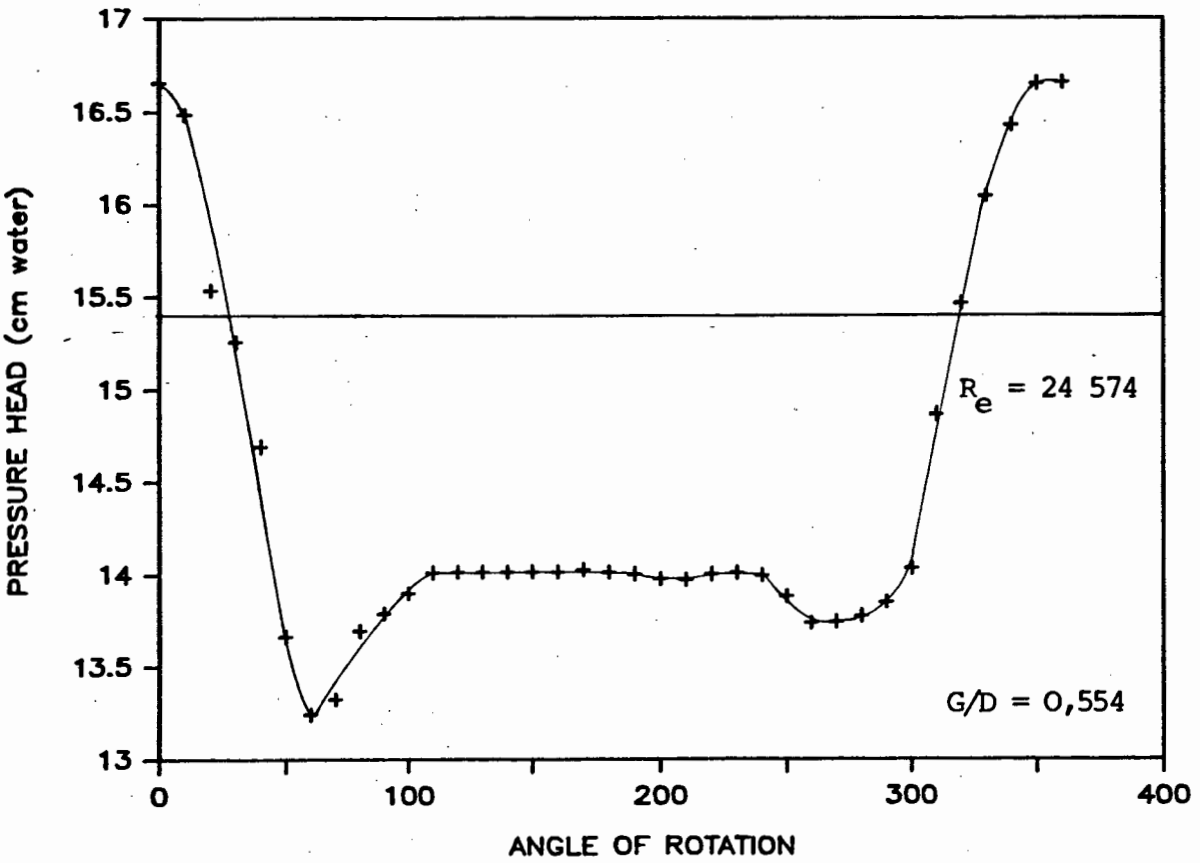

FIG. 5.13: PRESSURE DISTRIBUTION WITH SMOOTH 52 mm CYLINDER; SMOOTH BOTTOM; CLEARANCE = 28,8 mm

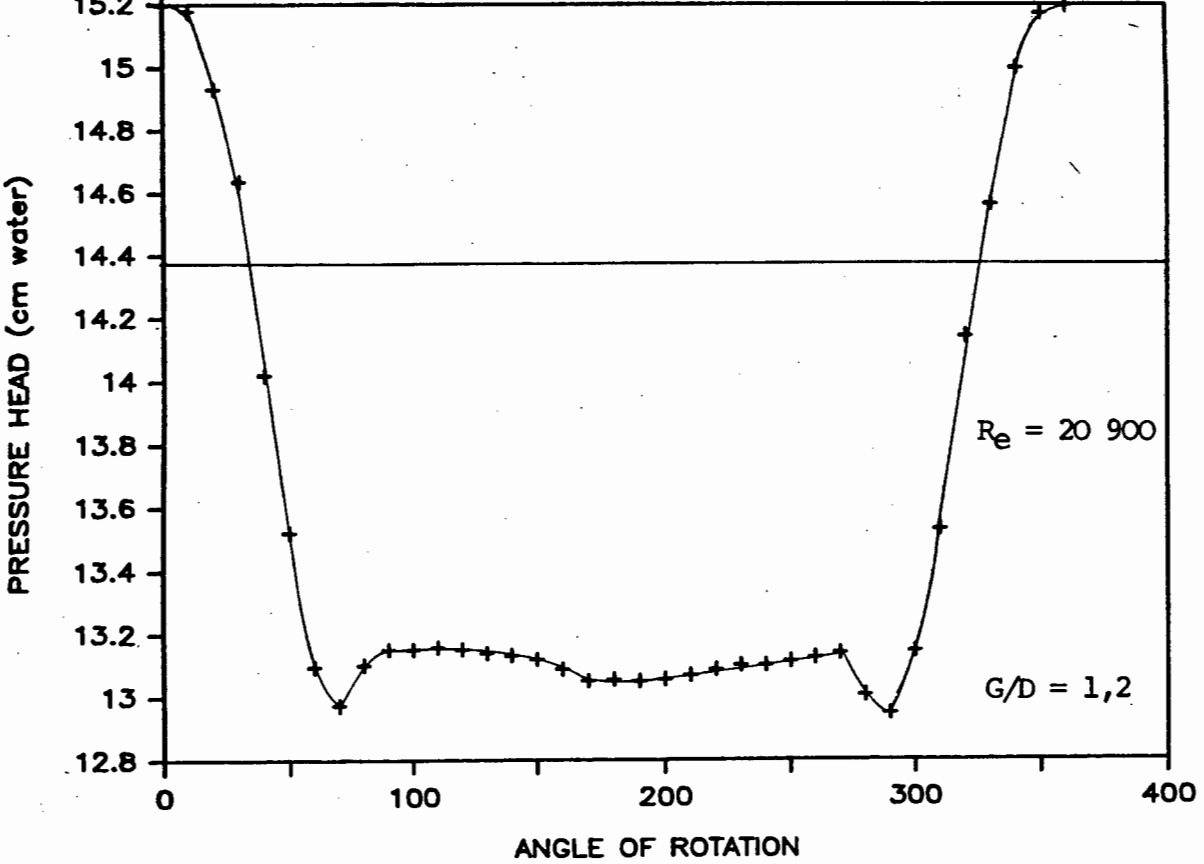

FIG. 5.14: PRESSURE DISTRIBUTION WITH SMOOTH 50 mm CYLINDER; SMOOTH BOTTOM; CLEARANCE = 60 mm

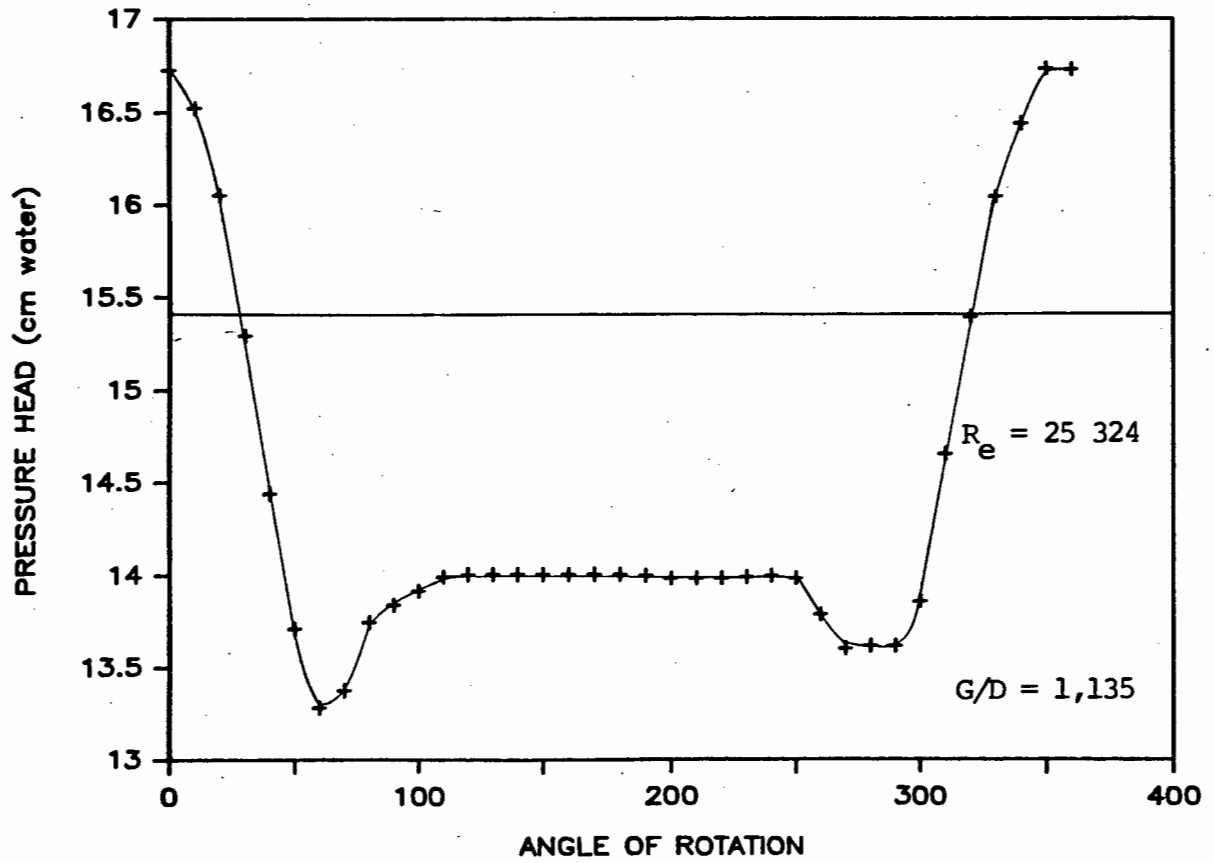

FIG. 5.15: PRESSURE DISTRIBUTION WITH ROUGH 52 mm CYLINDER; SMOOTH BOTTOM; CLEARANCE = 59 mm

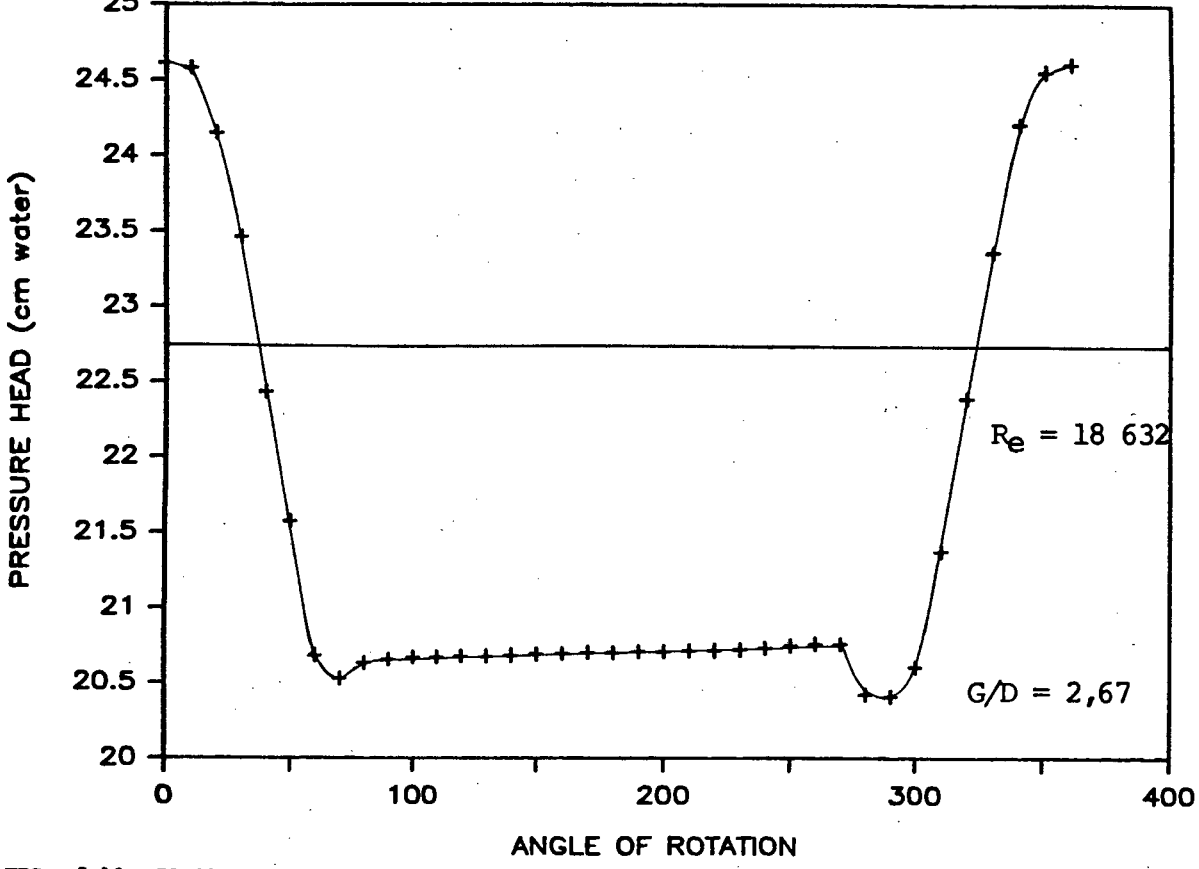

FIG. 5.16: PRESSURE DISTRIBUTION WITH SMOOTH 30 mm CYLINDER; SMOOTH BOTTOM; CLEARANCE = 80 mm

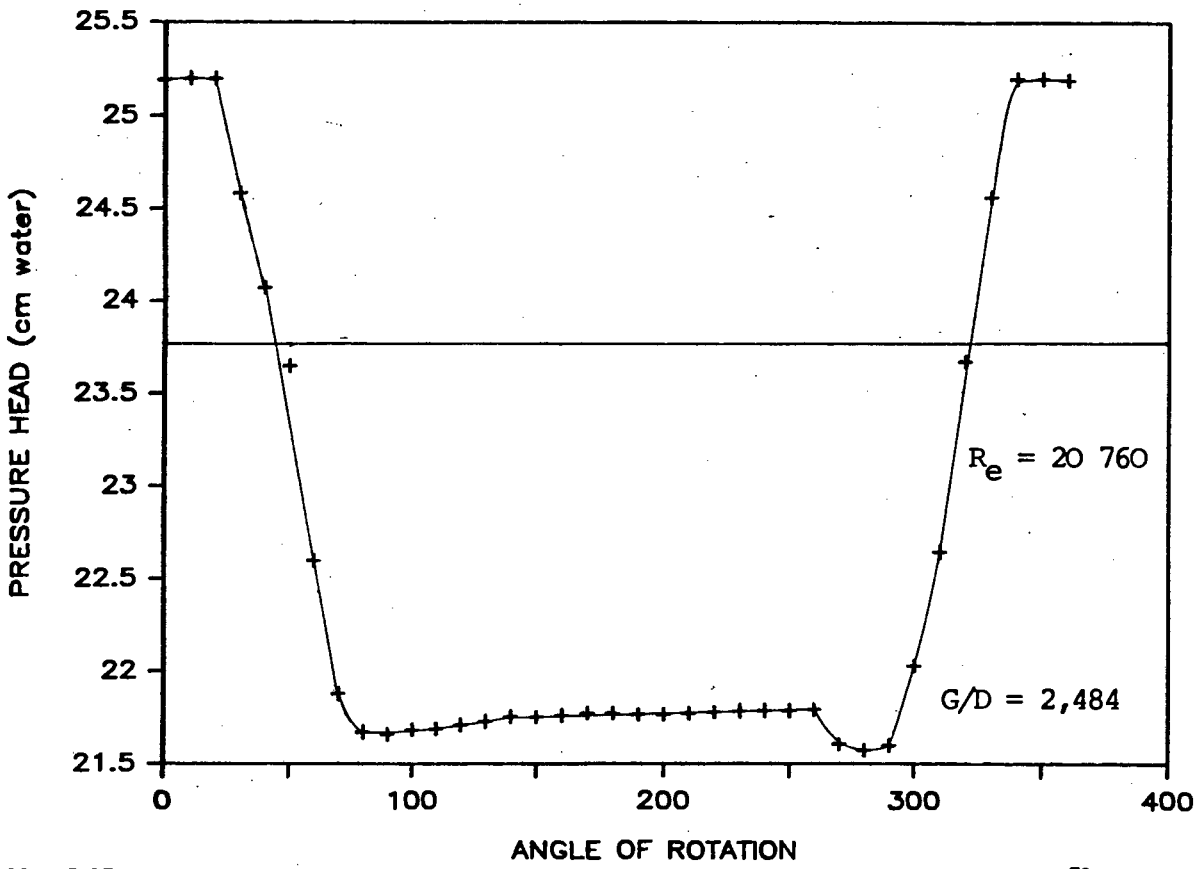

FIG. 5.17: PRESSURE DISTRIBUTION WITH ROUGH 31,8 mm CYLINDER; SMOOTH BOTTOM; CLEARANCE = 79 mm

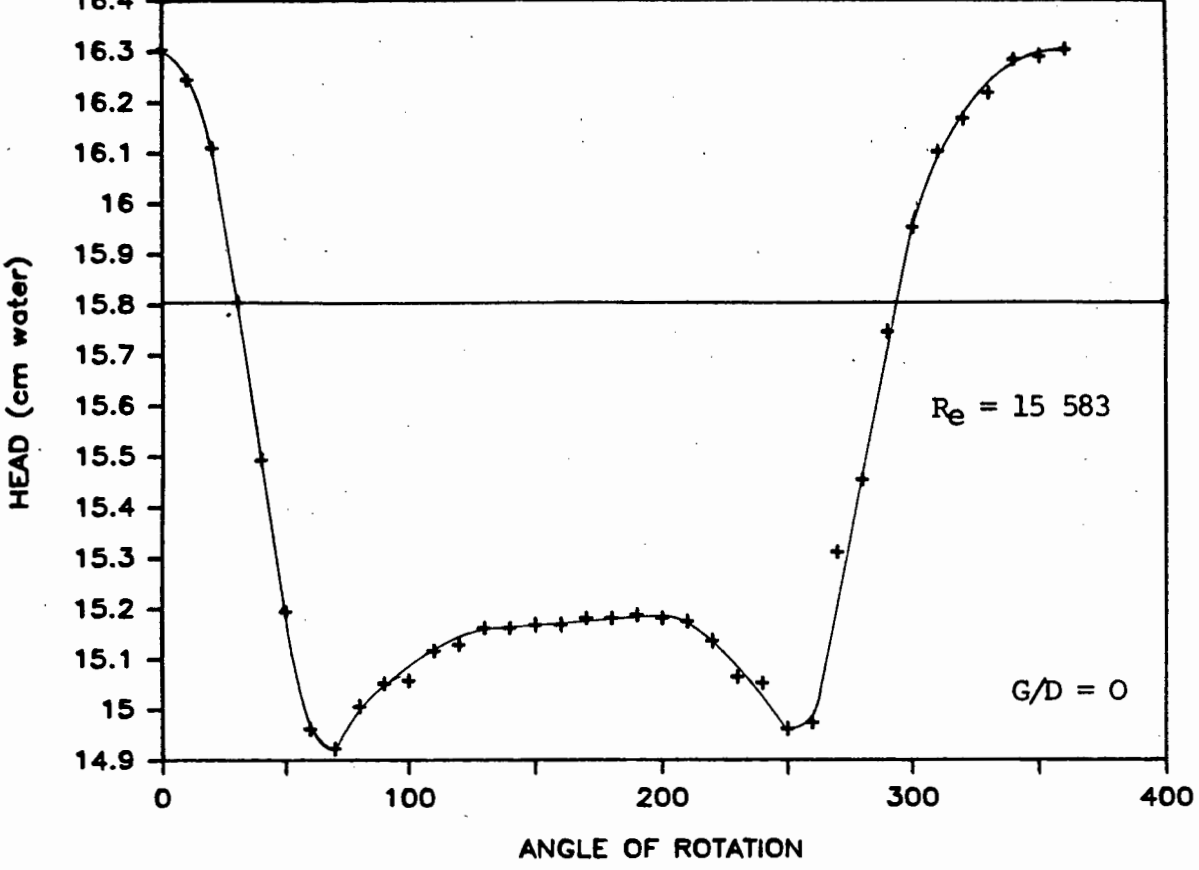

FIG. 5.18: PRESSURE DISTRIBUTION WITH SMOOTH 50 mm CYLINDER; ROUGH BOTTOM; CLEARANCE = 0

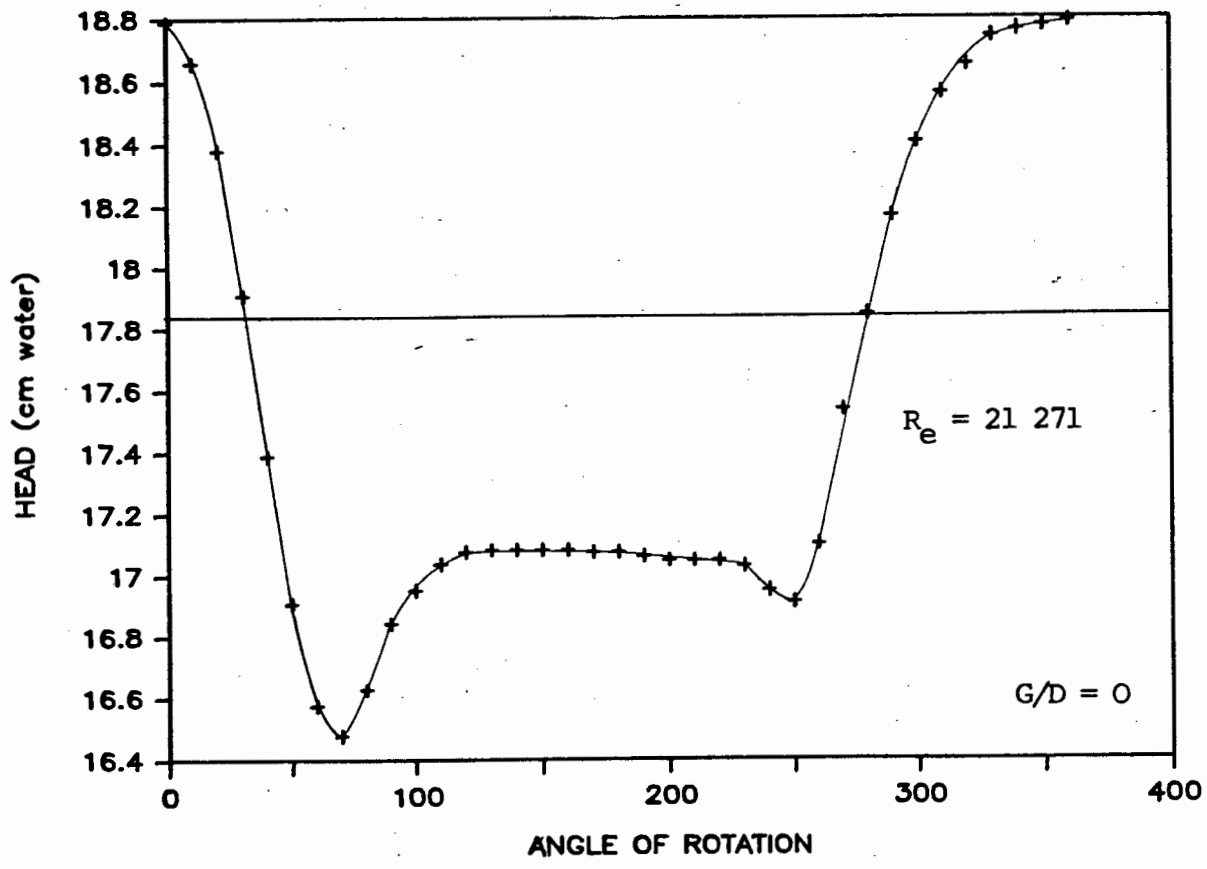

FIG. 5.19: PRESSURE DISTRIBUTION WITH ROUGH 52 mm CYLINDER; ROUGH BOTTOM; CLEARANCE = 0

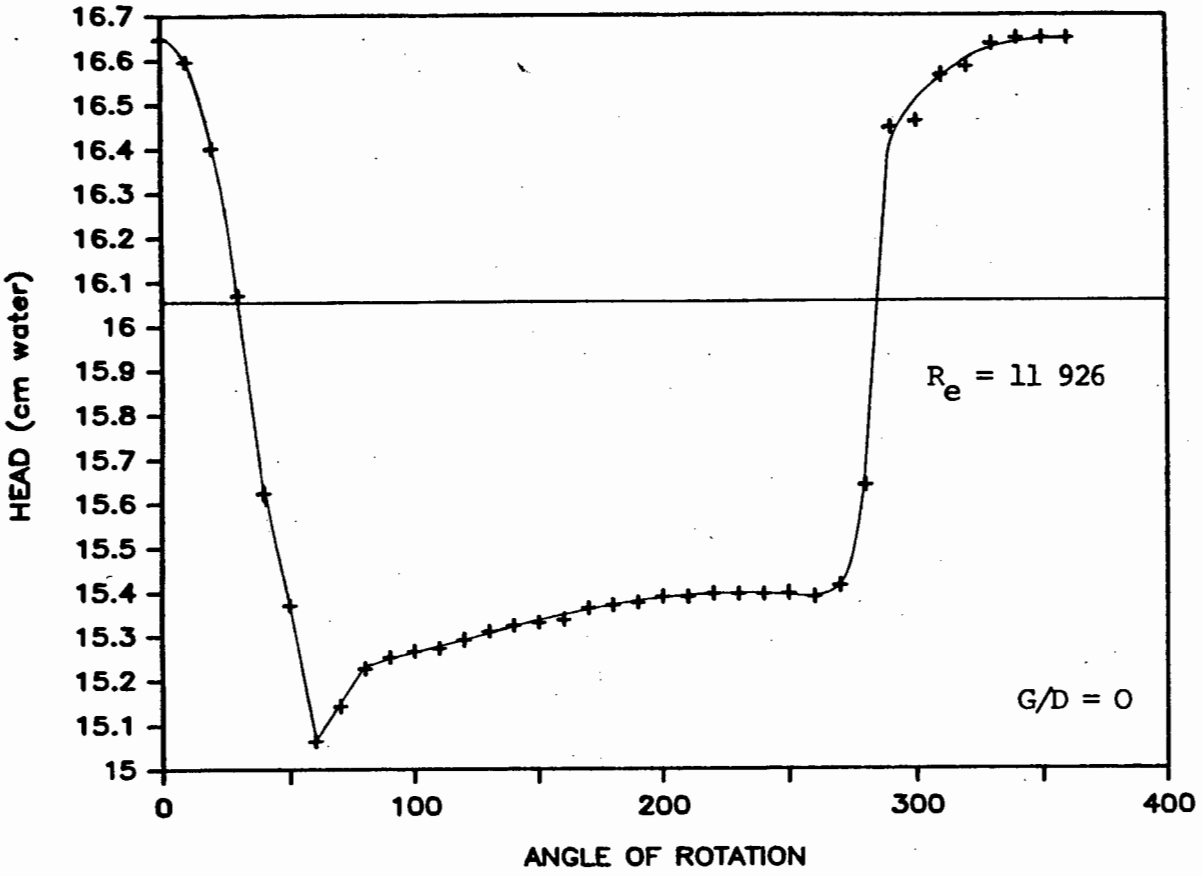

FIG. 5.20: PRESSURE DISTRIBUTION WITH SMOOTH 30 mm CYLINDER; ROUGH BOTTOM; CLEARANCE = 0

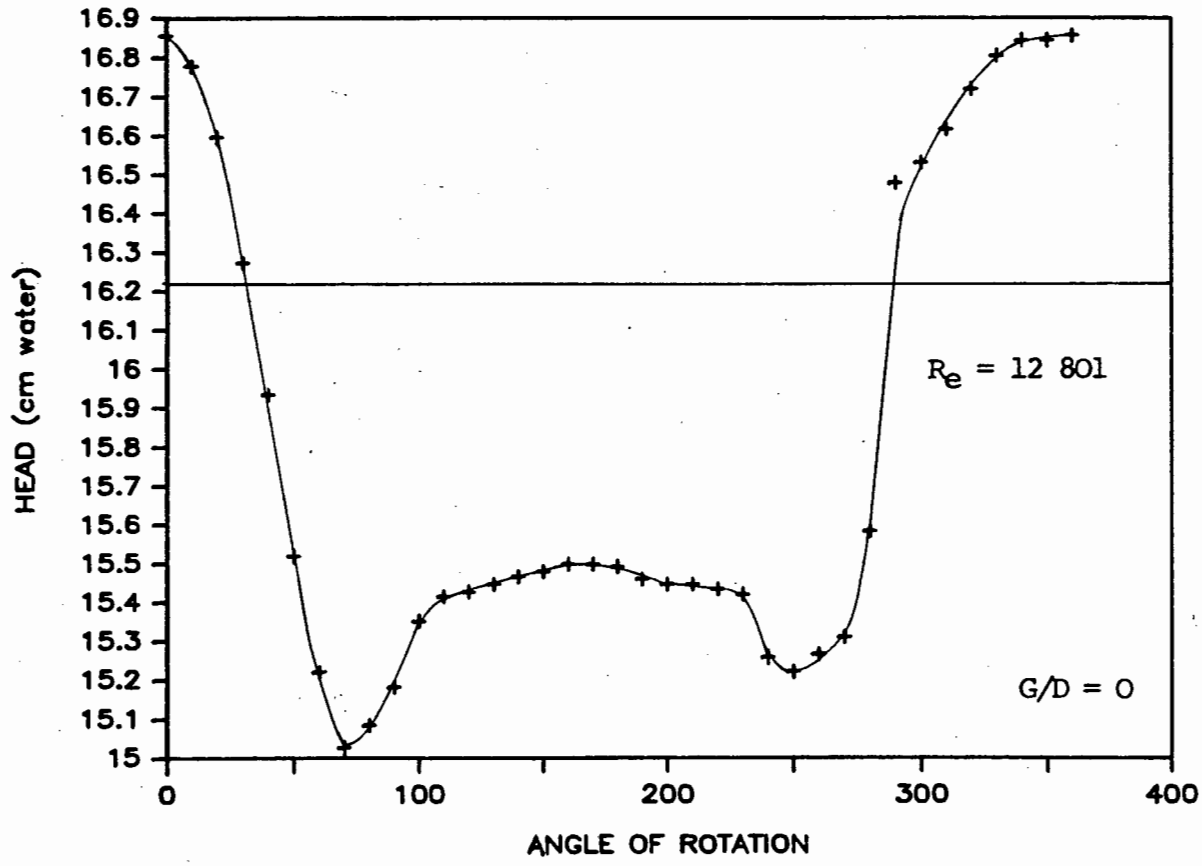

FIG. 5.21: PRESSURE DISTRIBUTION WITH ROUGH 31,8 mm CYLINDER; ROUGH BOTTOM; CLEARANCE = 0

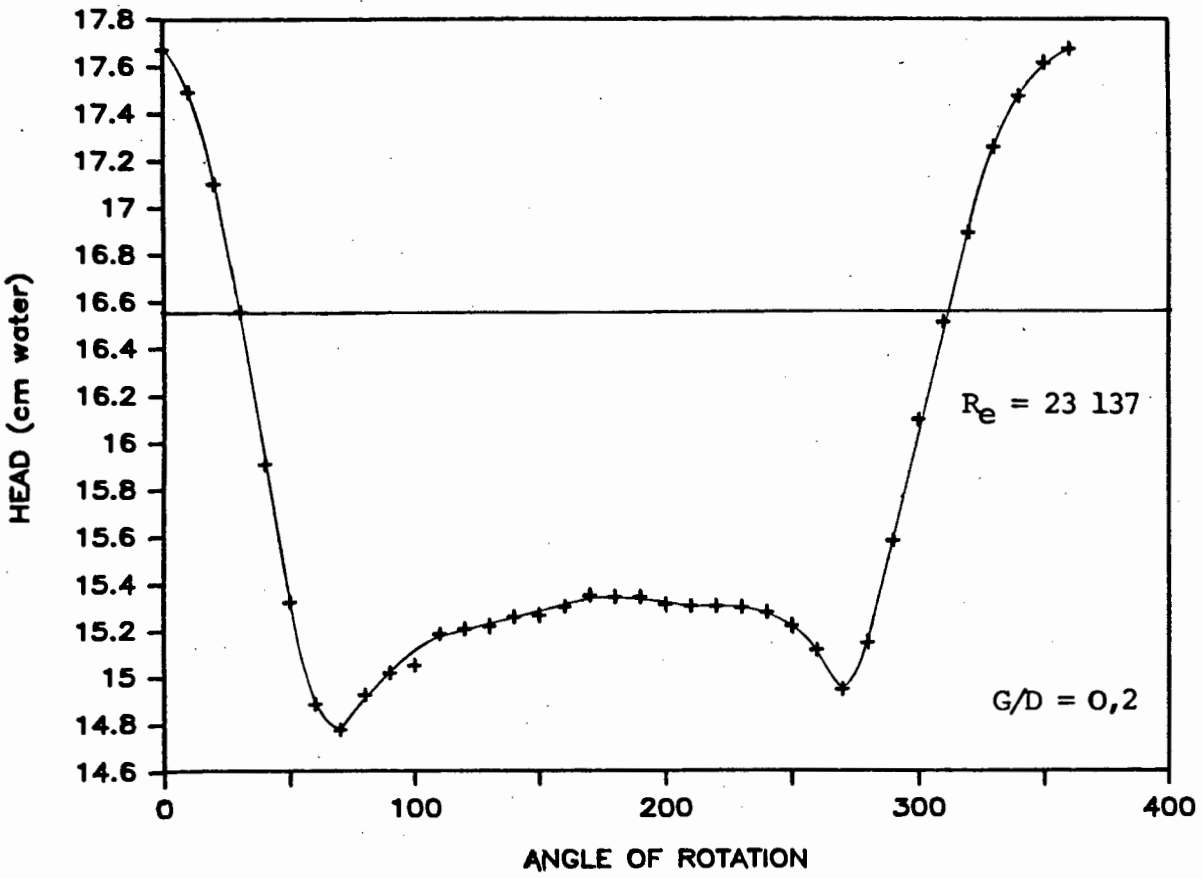

FIG. 5.22: PRESSURE DISTRIBUTION WITH SMOOTH 50 mm CYLINDER; ROUGH BOTTOM; CLEARANCE = 10 mm

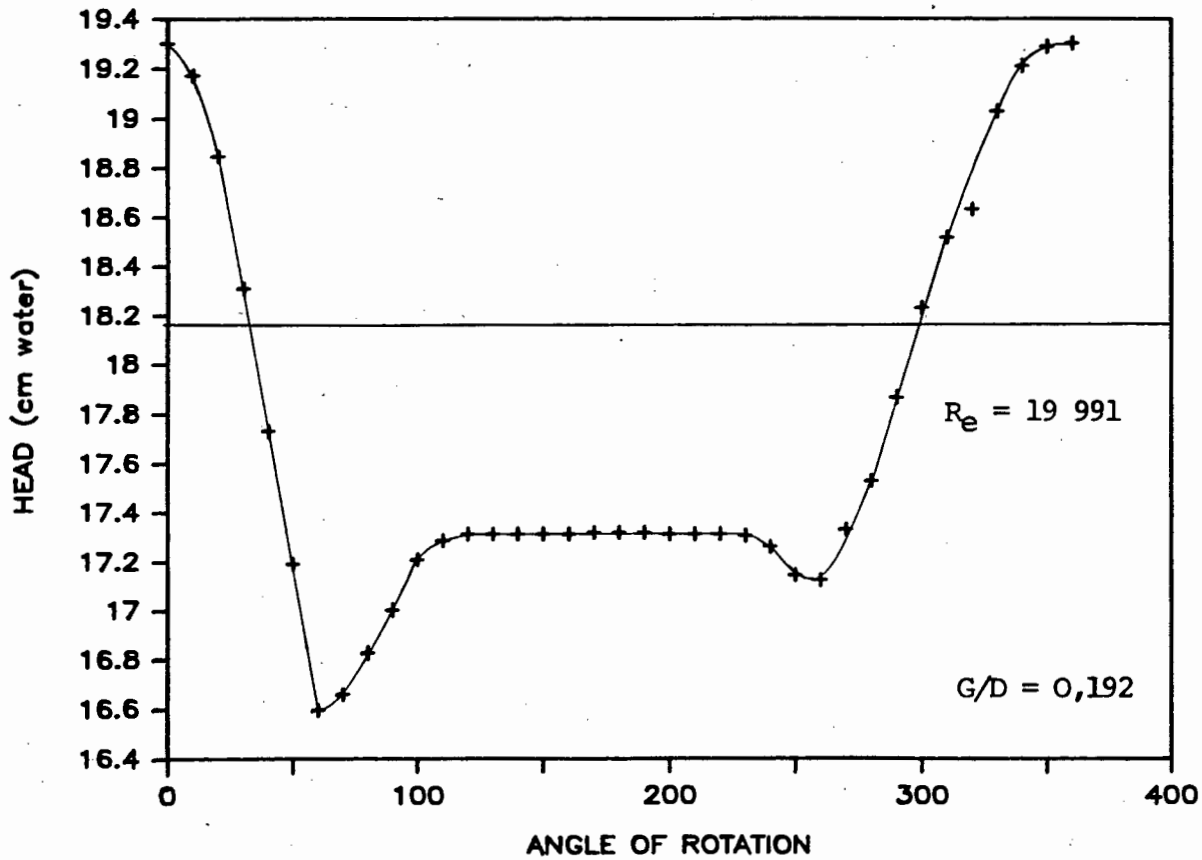

FIG. 5.23: PRESSURE DISTRIBUTION WITH ROUGH 52 mm CYLINDER; ROUGH BOTTOM; CLEARANCE = 10 mm

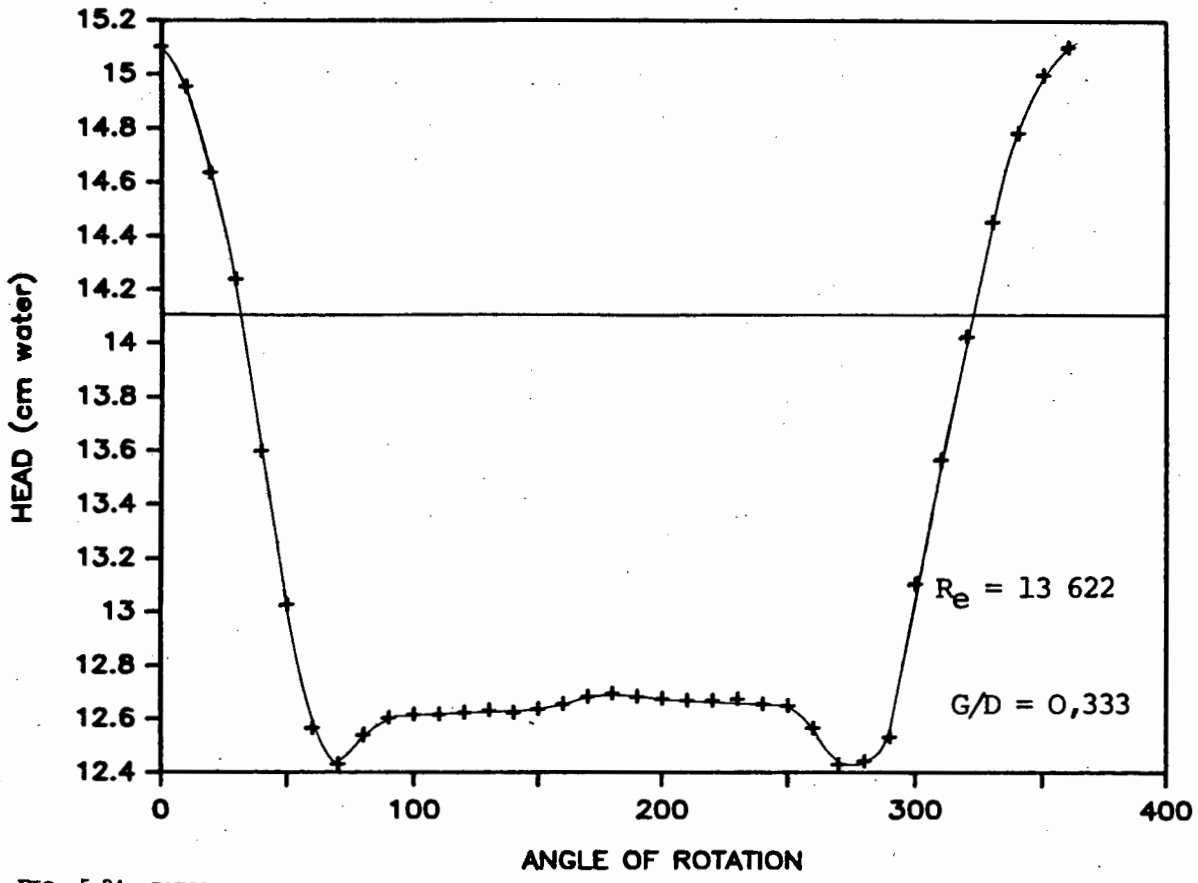

FIG. 5.24: PRESSURE DISTRIBUTION WITH SMOOTH 30 mm CYLINDER; ROUGH BOTTOM; CLEARANCE = 10 mm

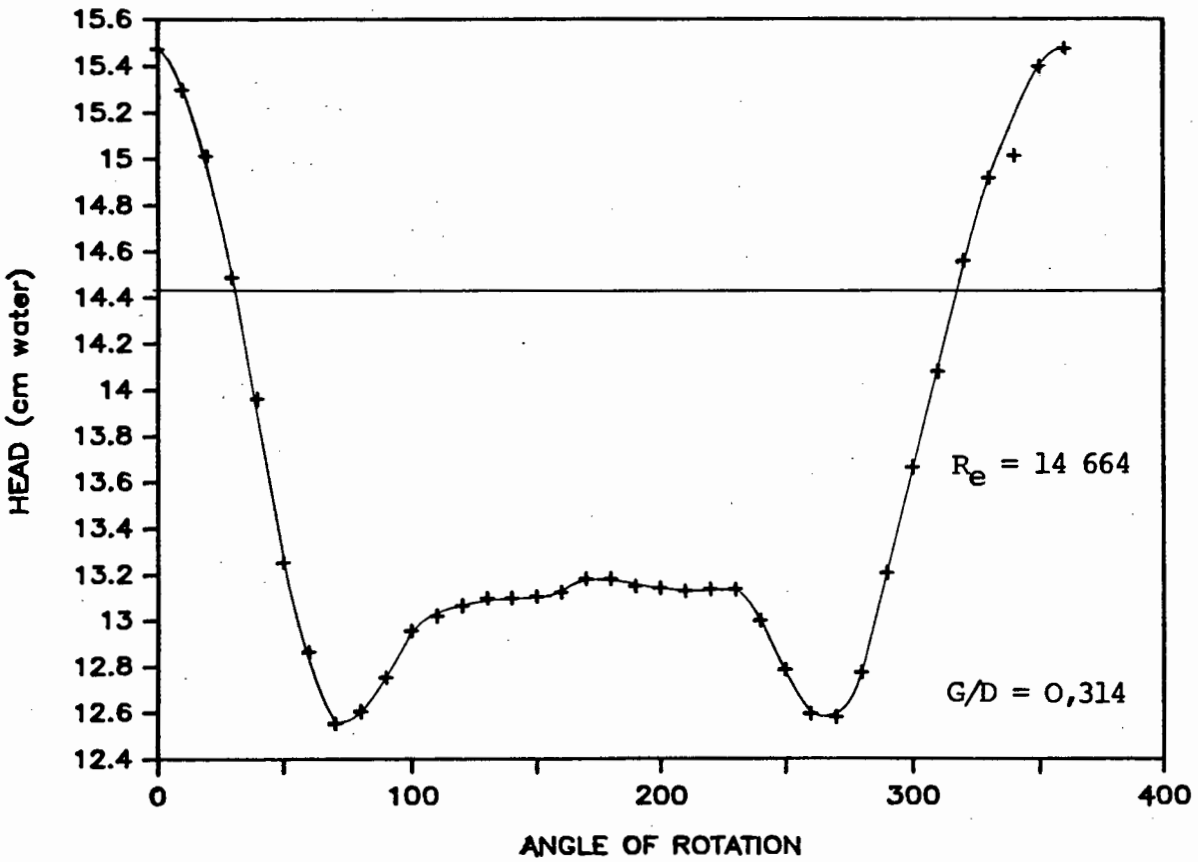

FIG. 5.25: PRESSURE DISTRIBUTION WITH ROUGH 31,8 mm CYLINDER; ROUGH BOTTOM; CLEARANCE = 10 mm

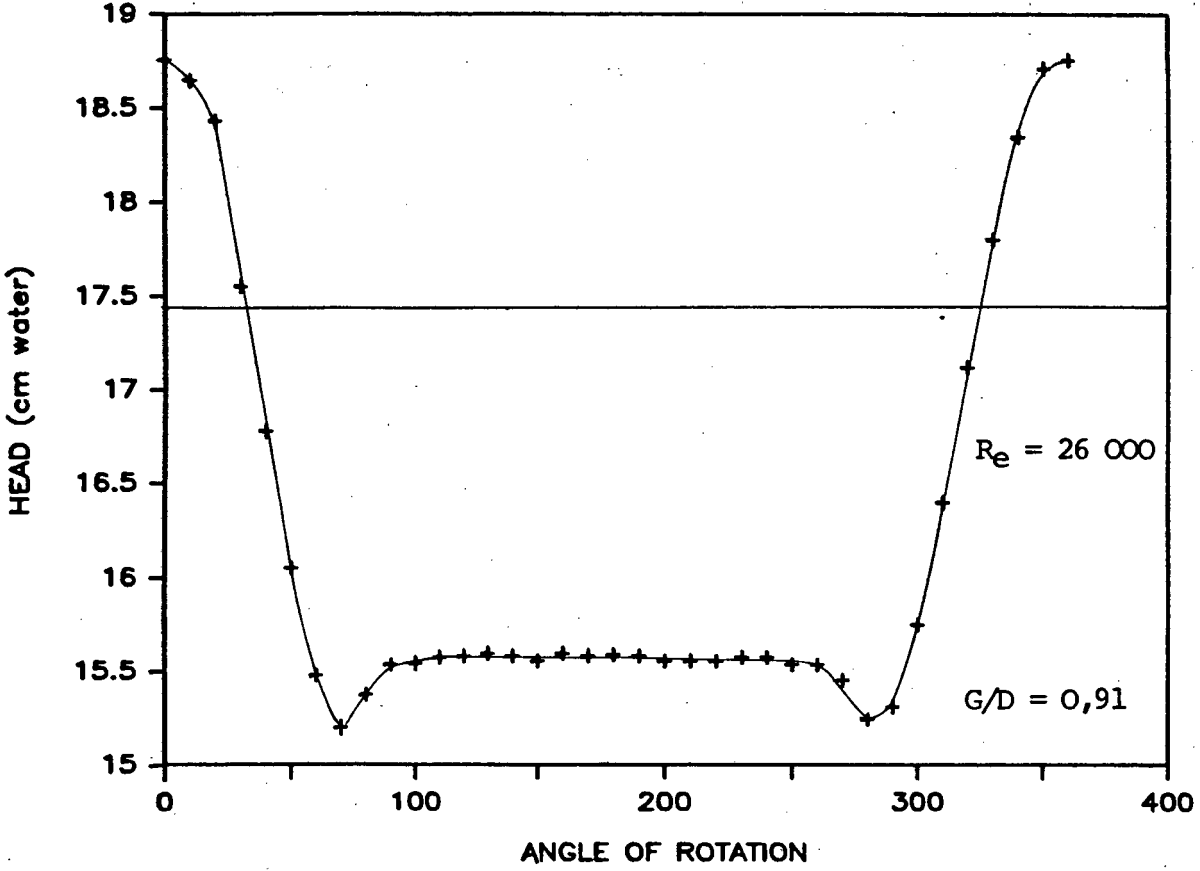

FIG. 5.26: PRESSURE DISTRIBUTION WITH SMOOTH 50 mm CYLINDER; ROUGH BOTTOM; CLEARANCE = 45,5 mm

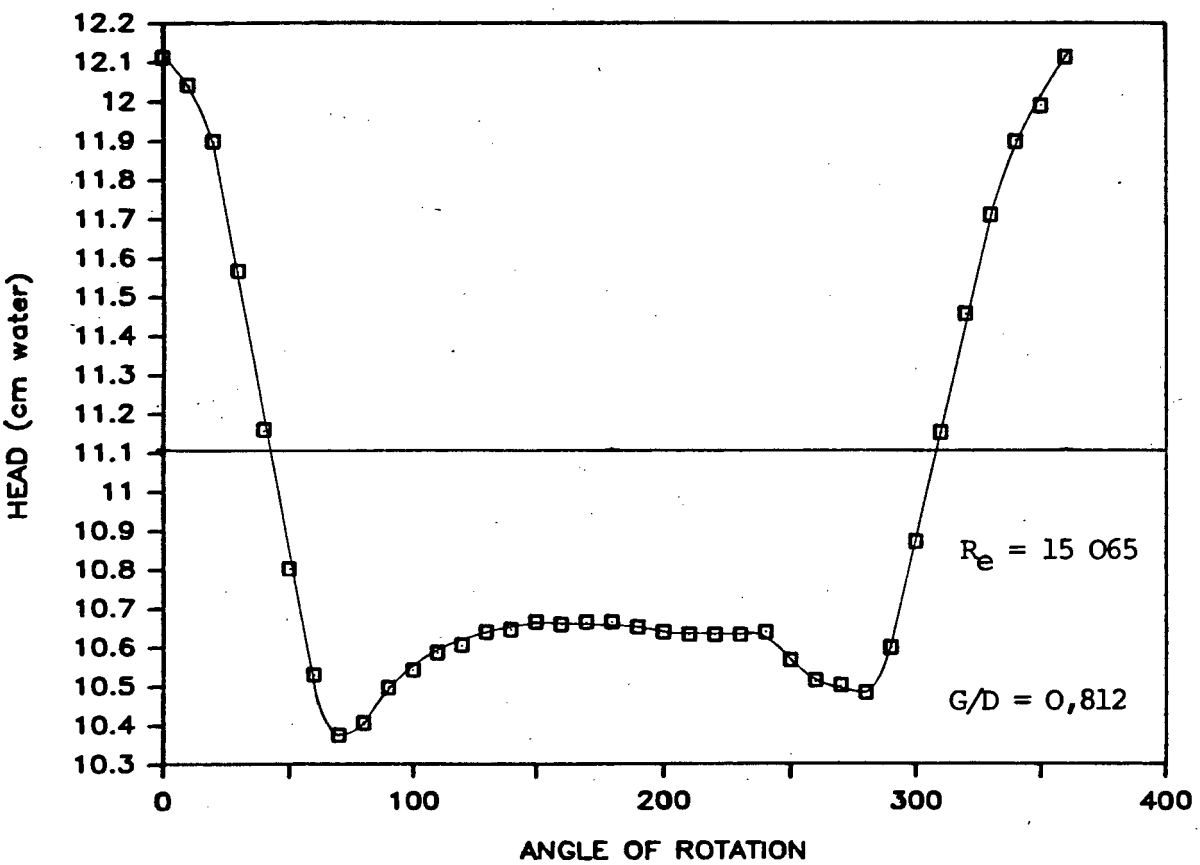

FIG. 5.27: PRESSURE DISTRIBUTION WITH ROUGH 52 mm CYLINDER; ROUGH BOTTOM; CLEARANCE = 42,2 mm

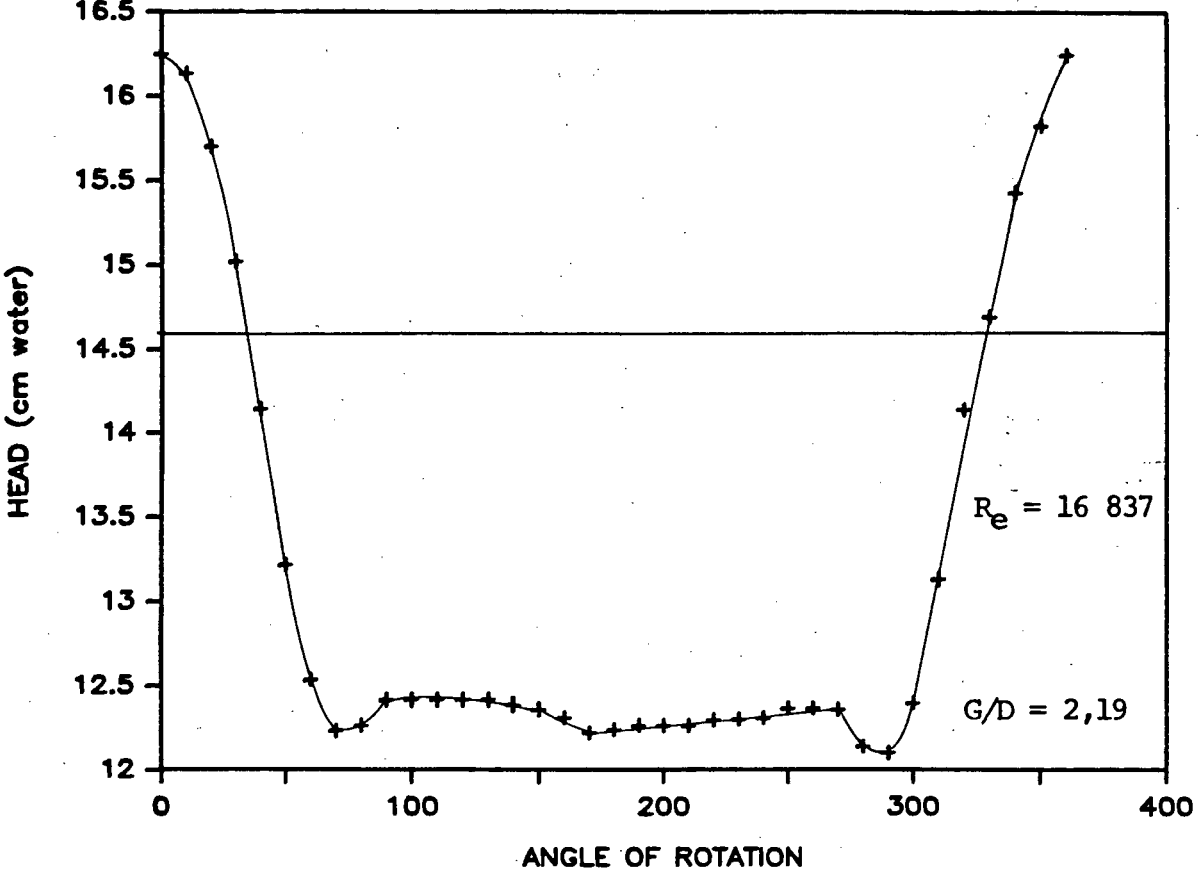

FIG. 5.28: PRESSURE DISTRIBUTION WITH SMOOTH 30 mm CYLINDER; ROUGH BOTTOM; CLEARANCE = 65,7 mm

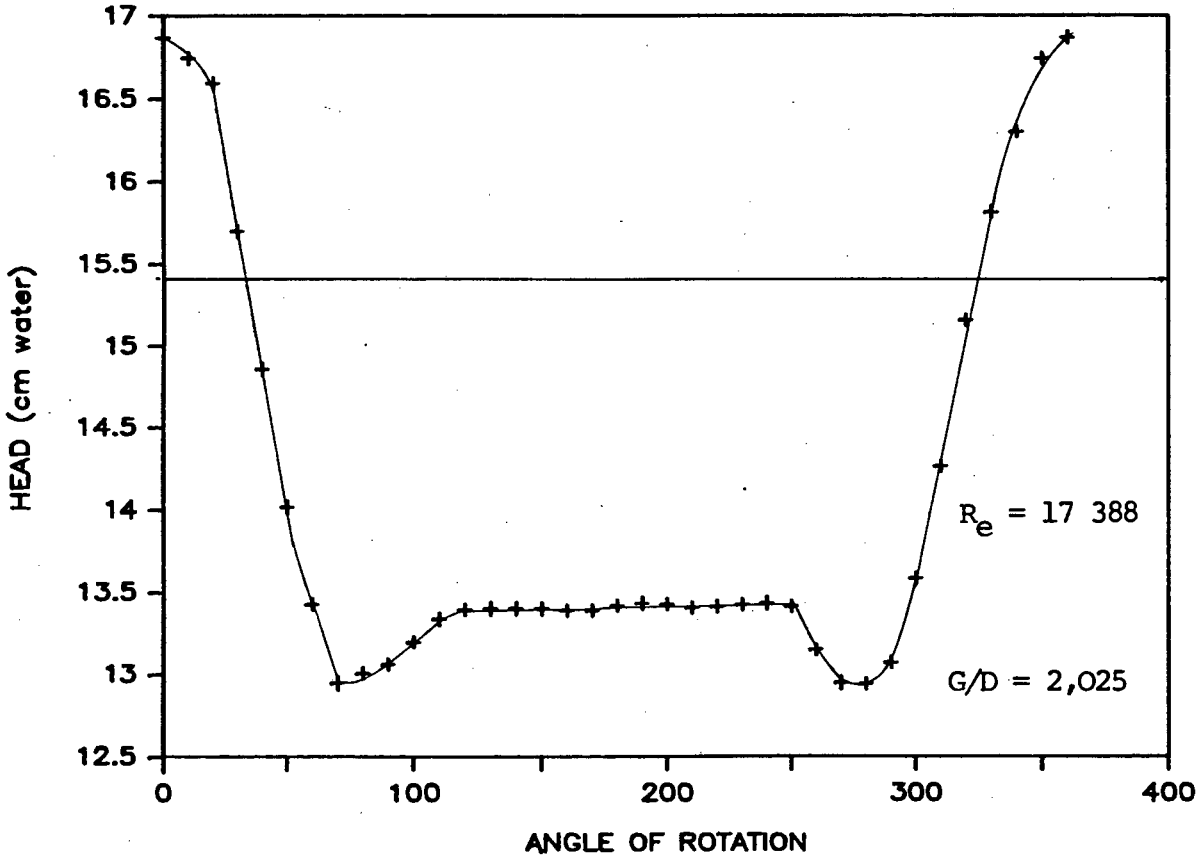

FIG. 5.29: PRESSURE DISTRIBUTION WITH ROUGH 31,8 mm CYLINDER; ROUGH BOTTOM; CLEARANCE = 64,4 mm

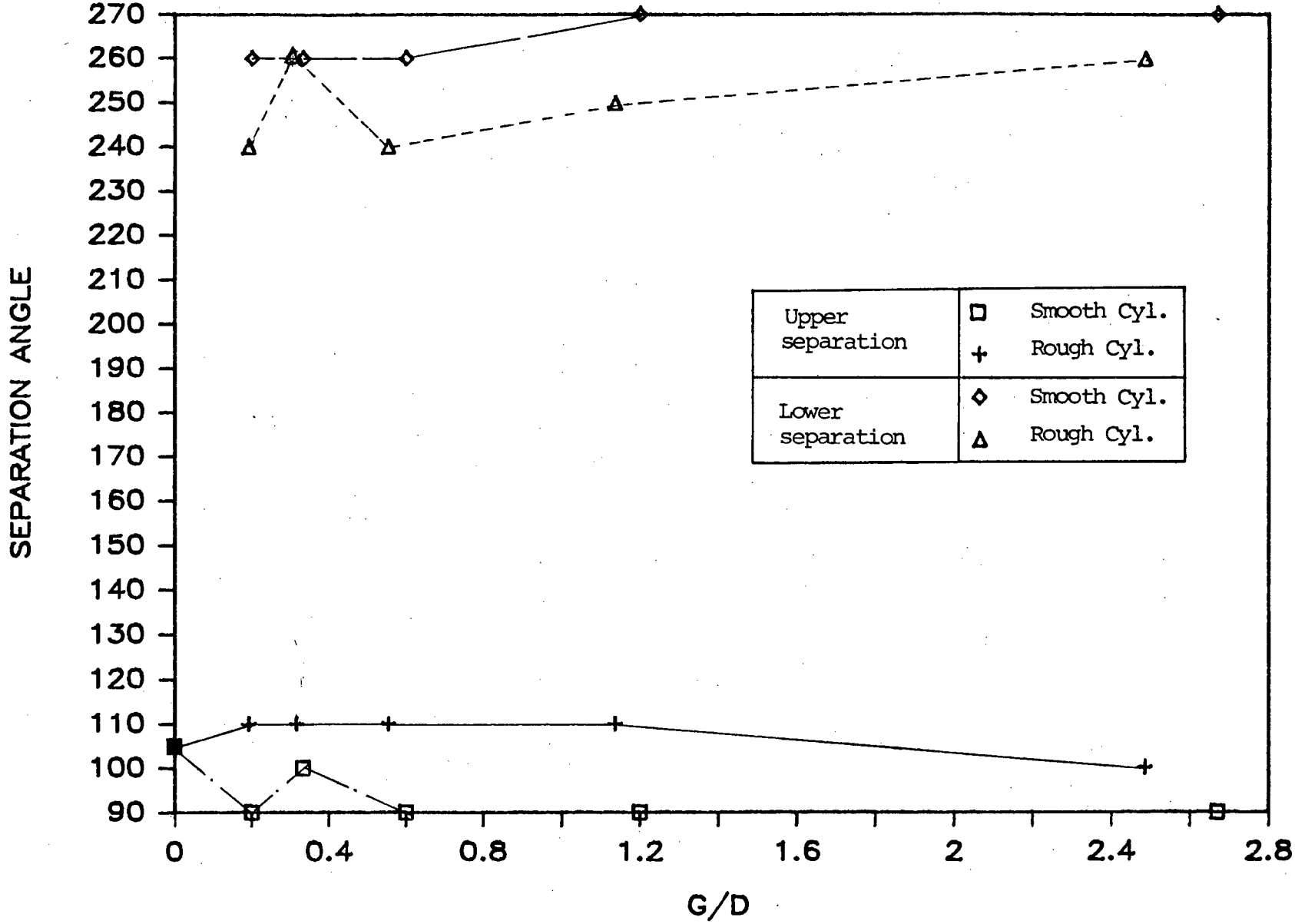

FIG. 5.30: PLOTS OF SEPARATION POINT VERSUS $G/_D$, FOR SMOOTH AND ROUGH CYLINDERS

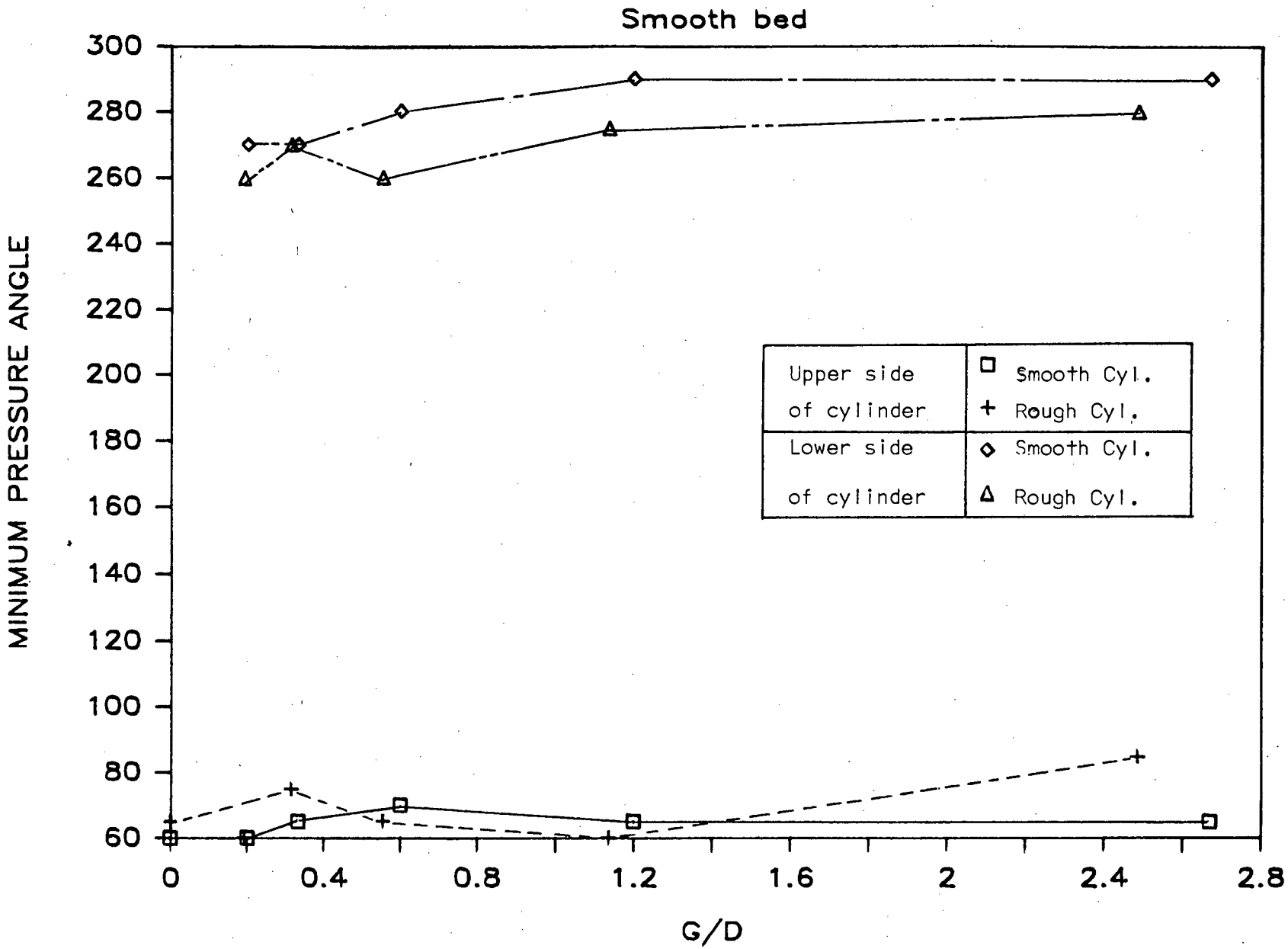

FIG. 5.31: PLOTS OF MINIMUM PRESSURE POINT VERSUS G/D, FOR SMOOTH AND ROUGH CYLINDERS

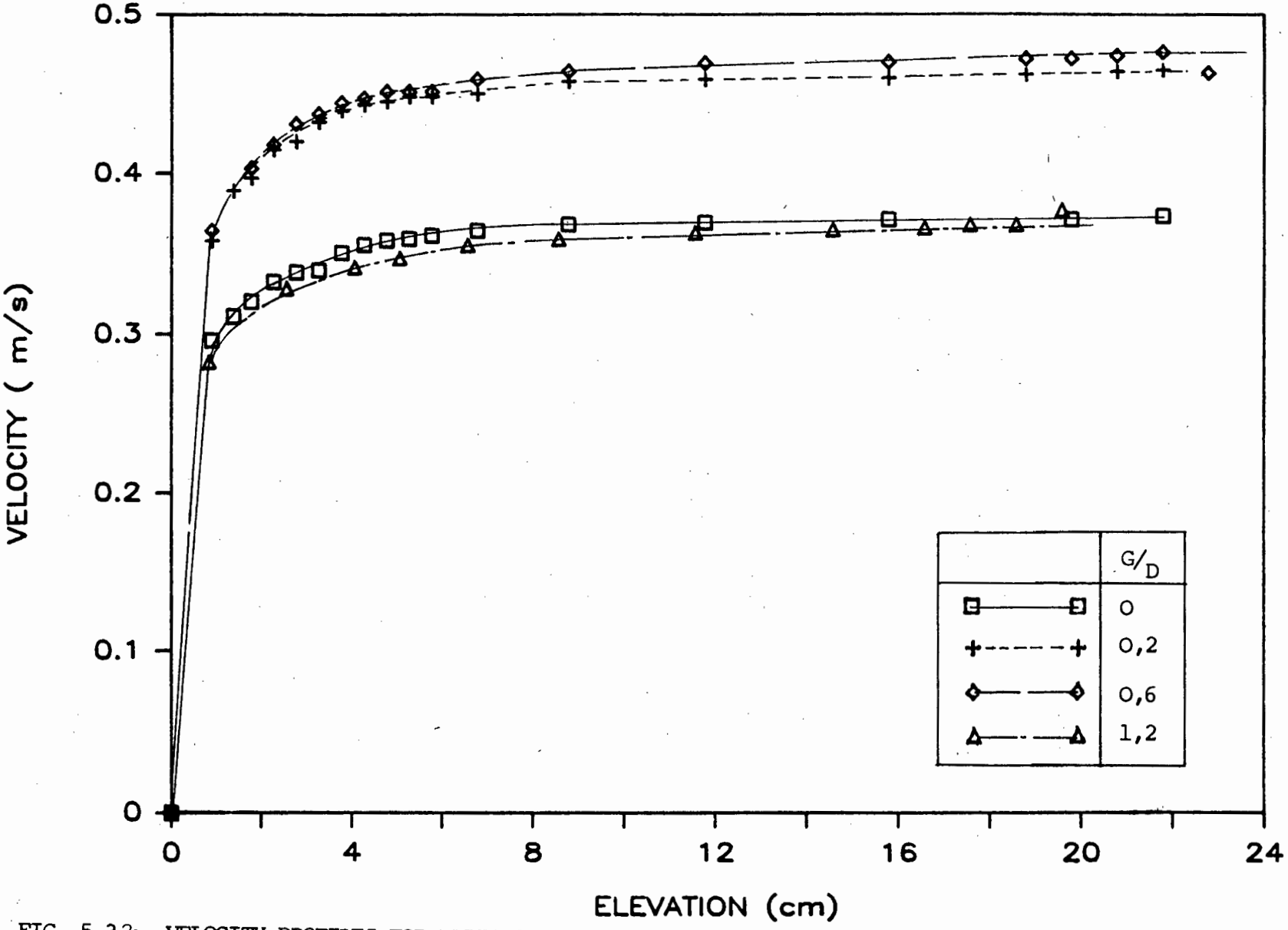

FIG. 5.32: VELOCITY PROFILES FOR VARIOUS RUNS; SMOOTH BED AND VARYING $G/_D$

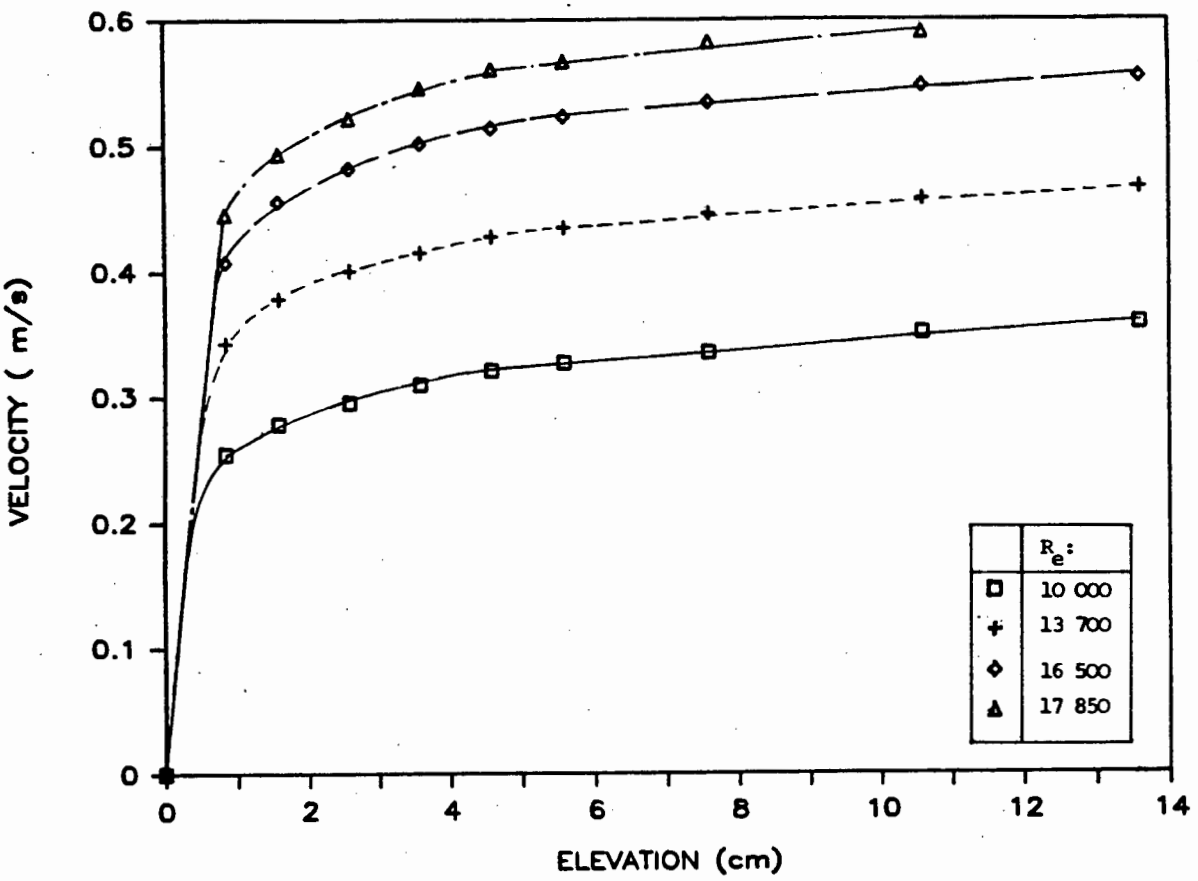

FIG. 5.33: VELOCITY PROFILES FOR VARIOUS RUNS; SMOOTH BED AND ROUGH CYLINDER, G/D = o

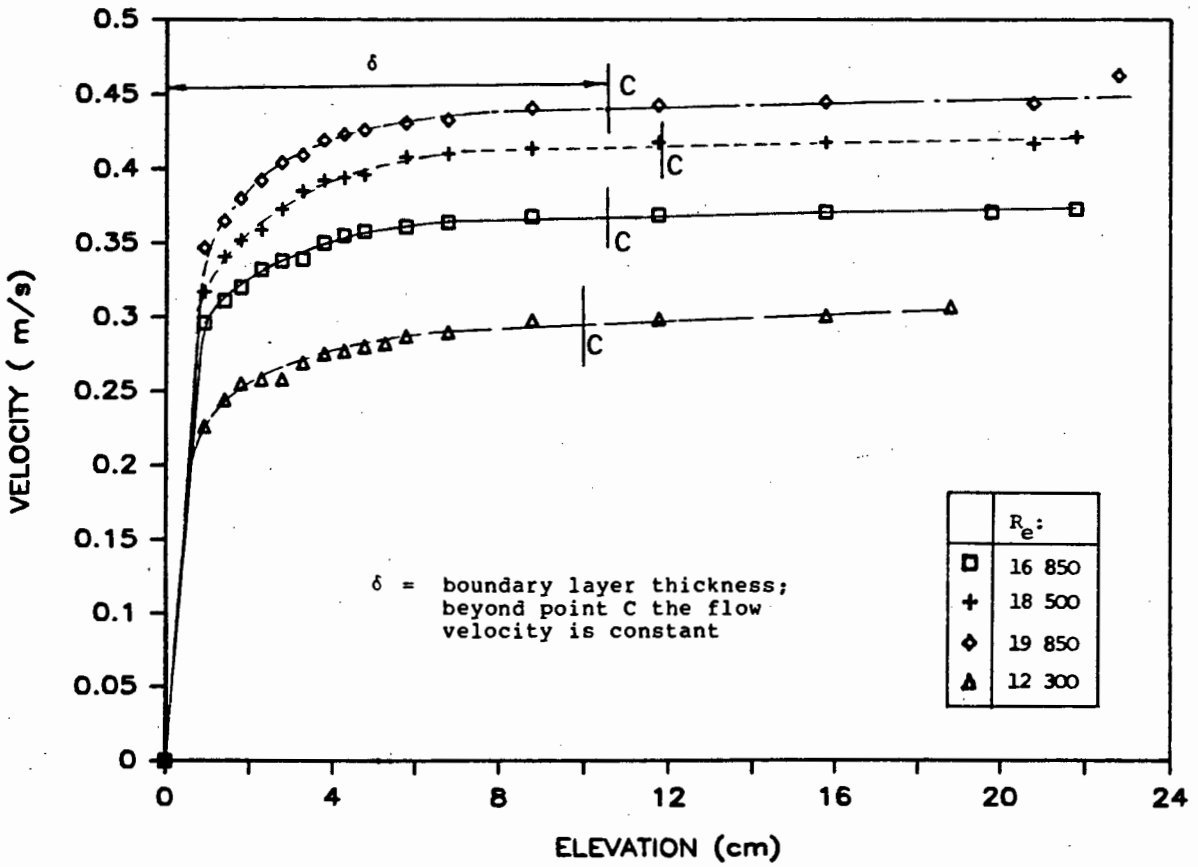

FIG. 5.34 VELOCITY PROFILES FOR VARIOUS RUNS; SMOOTH BED, SMOOTH CYLINDER AND G/D = O

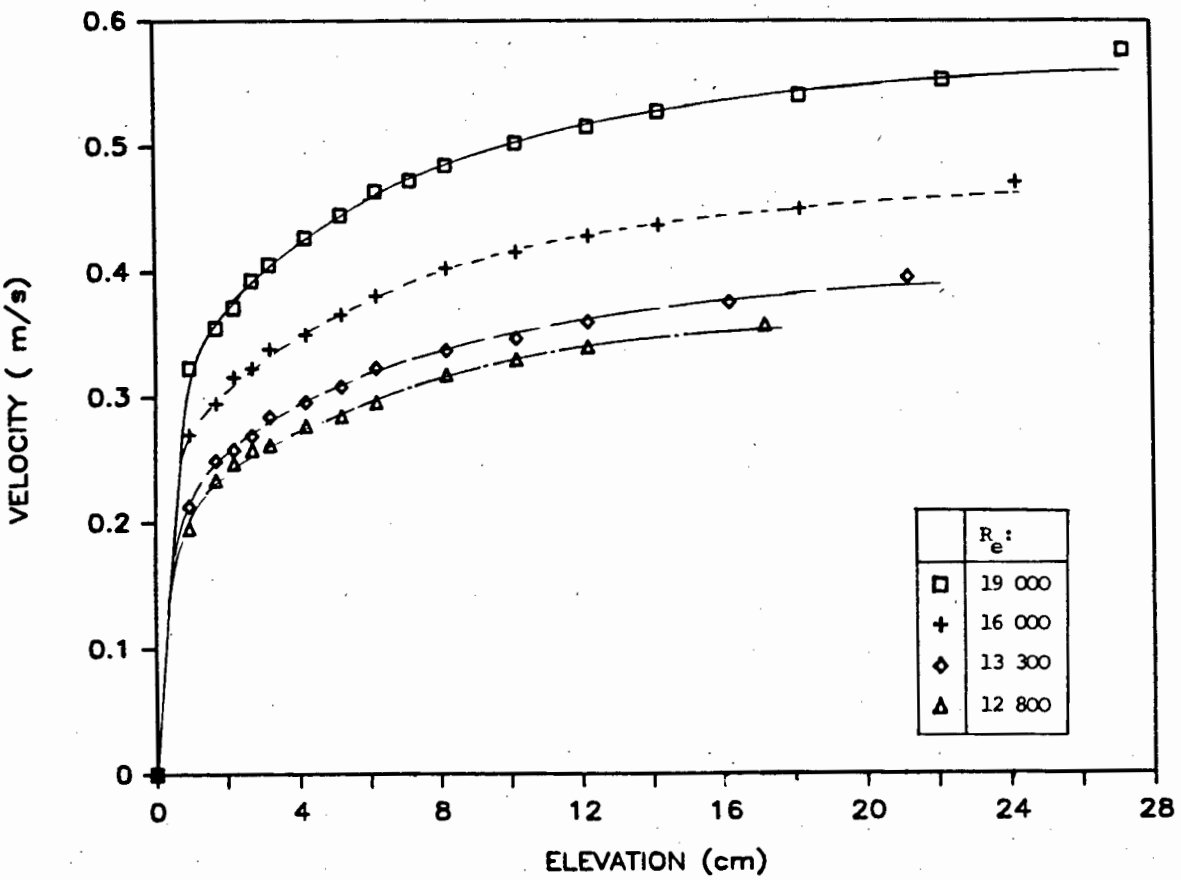

FIG. 5.35: VELOCITY PROFILES FOR A ROUGH BED

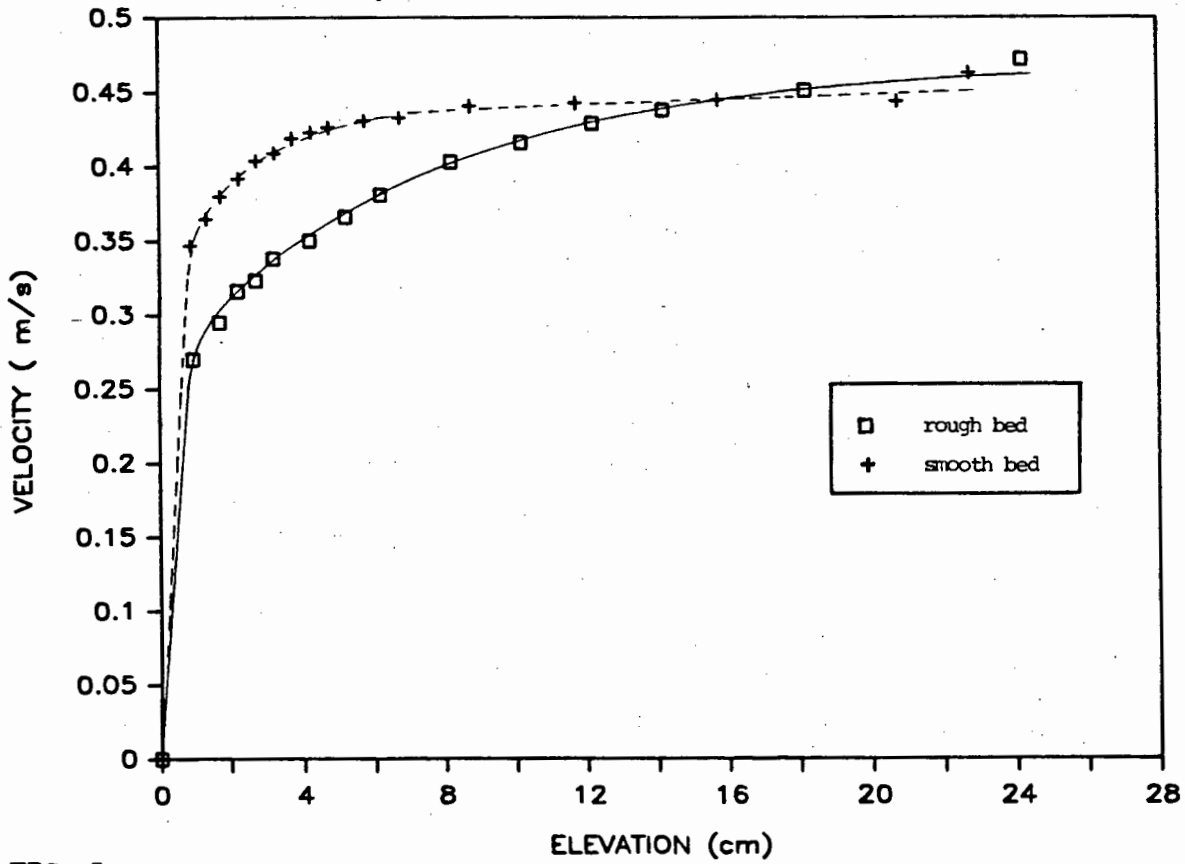

FIG. 5.36: COMPARISON OF VELOCITY PROFILES FOR ROUGH AND SMOOTH BEDS.

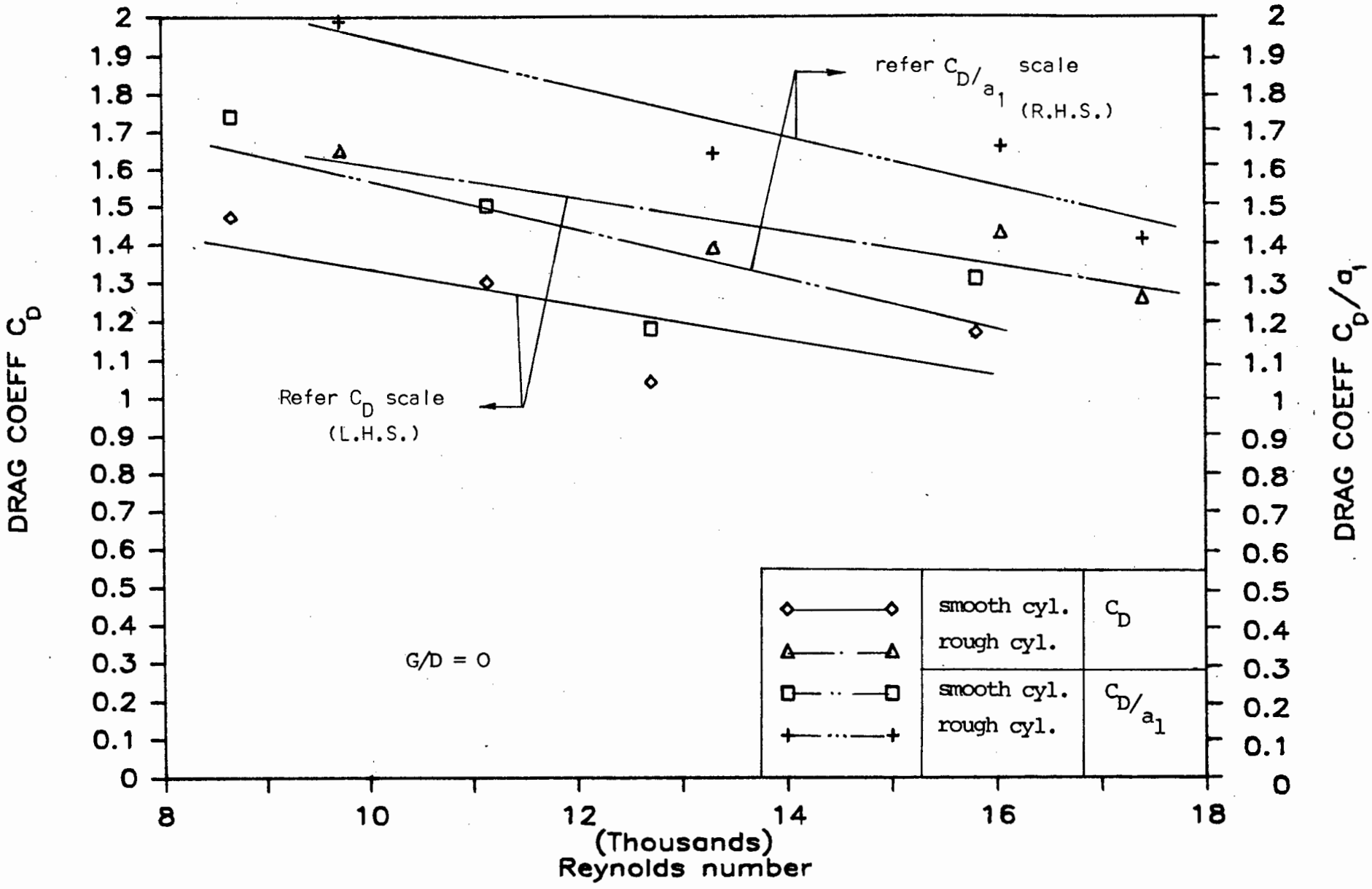

FIG. 5.37: DRAG COEFFICIENTS FOR SMOOTH AND ROUGH 30 mm CYLINDERS; SMOOTH BED

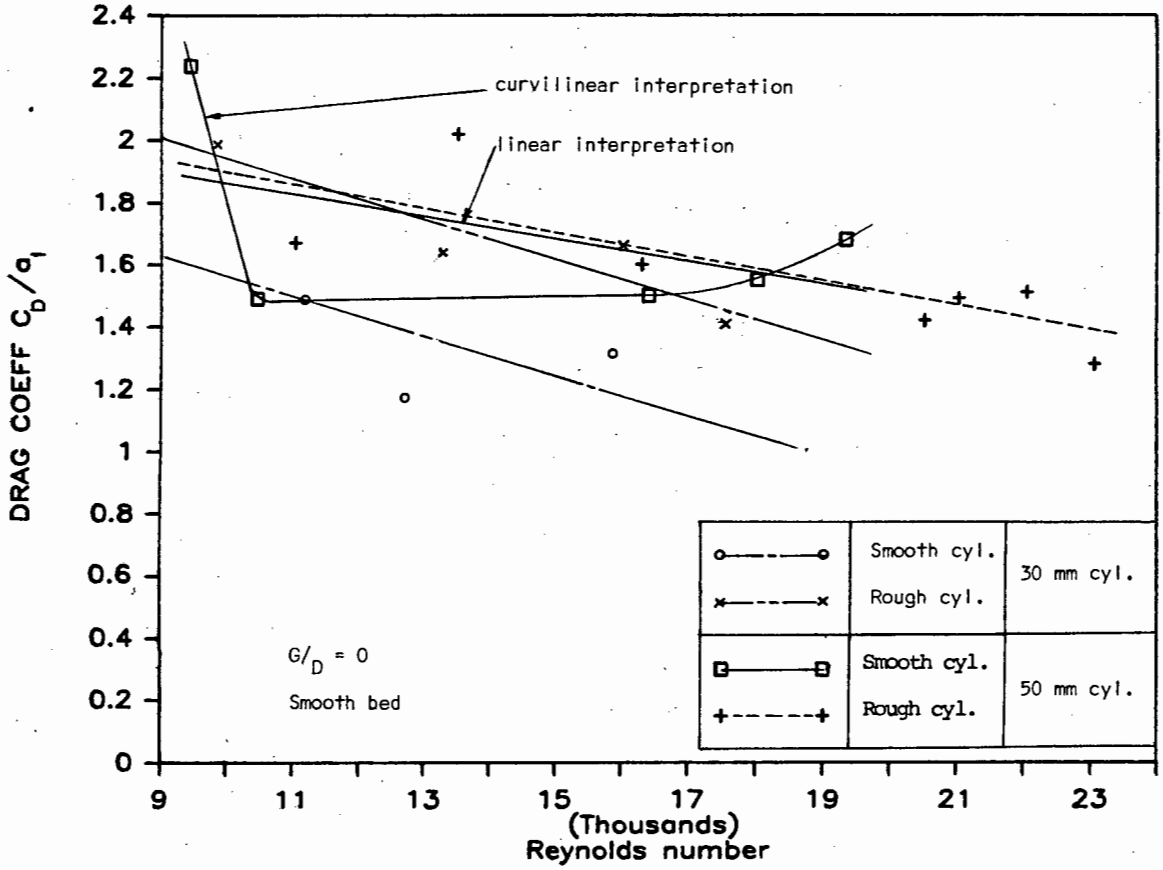

FIG. 5.38: DRAG COEFFICIENTS FOR SMOOTH AND ROUGH CYLINDER; SMOOTH BED

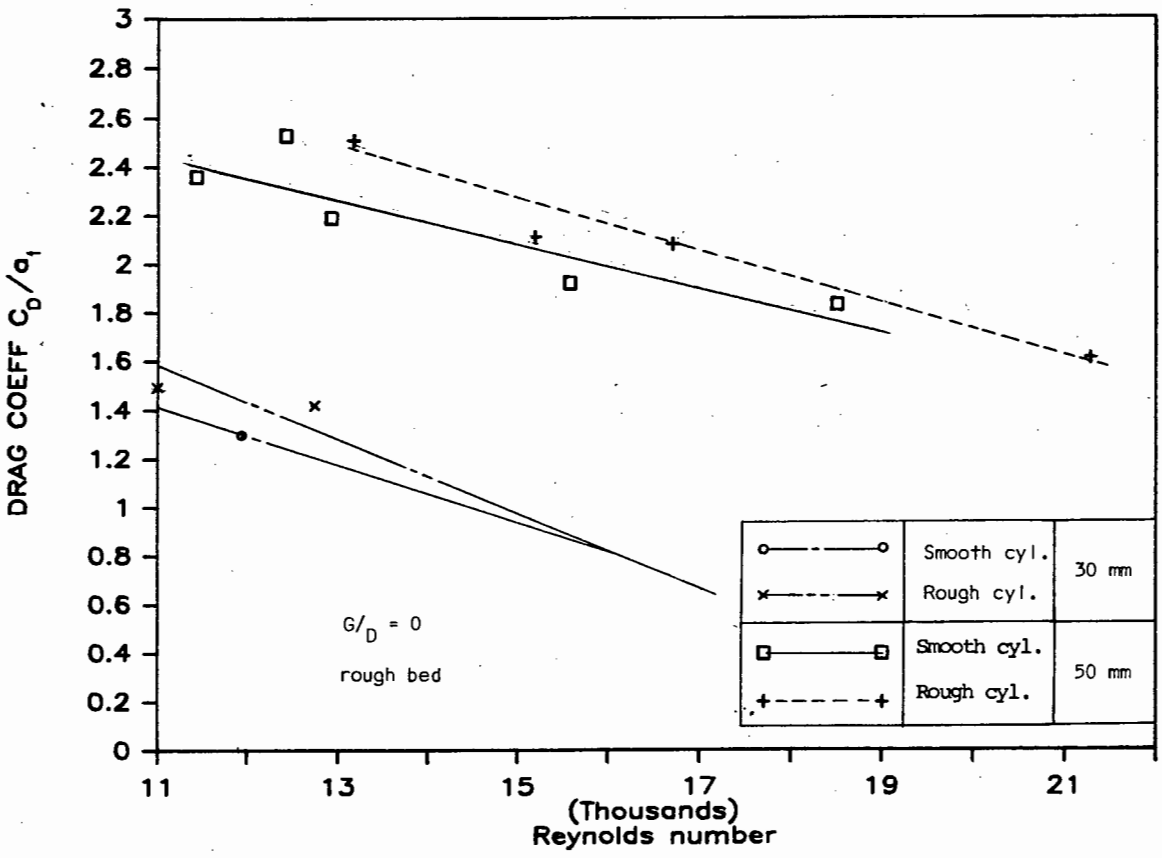

FIG. 5.39: DRAG COEFFICIENTS OF SMOOTH AND ROUGH CYLINDERS; ROUGH BOTTOM

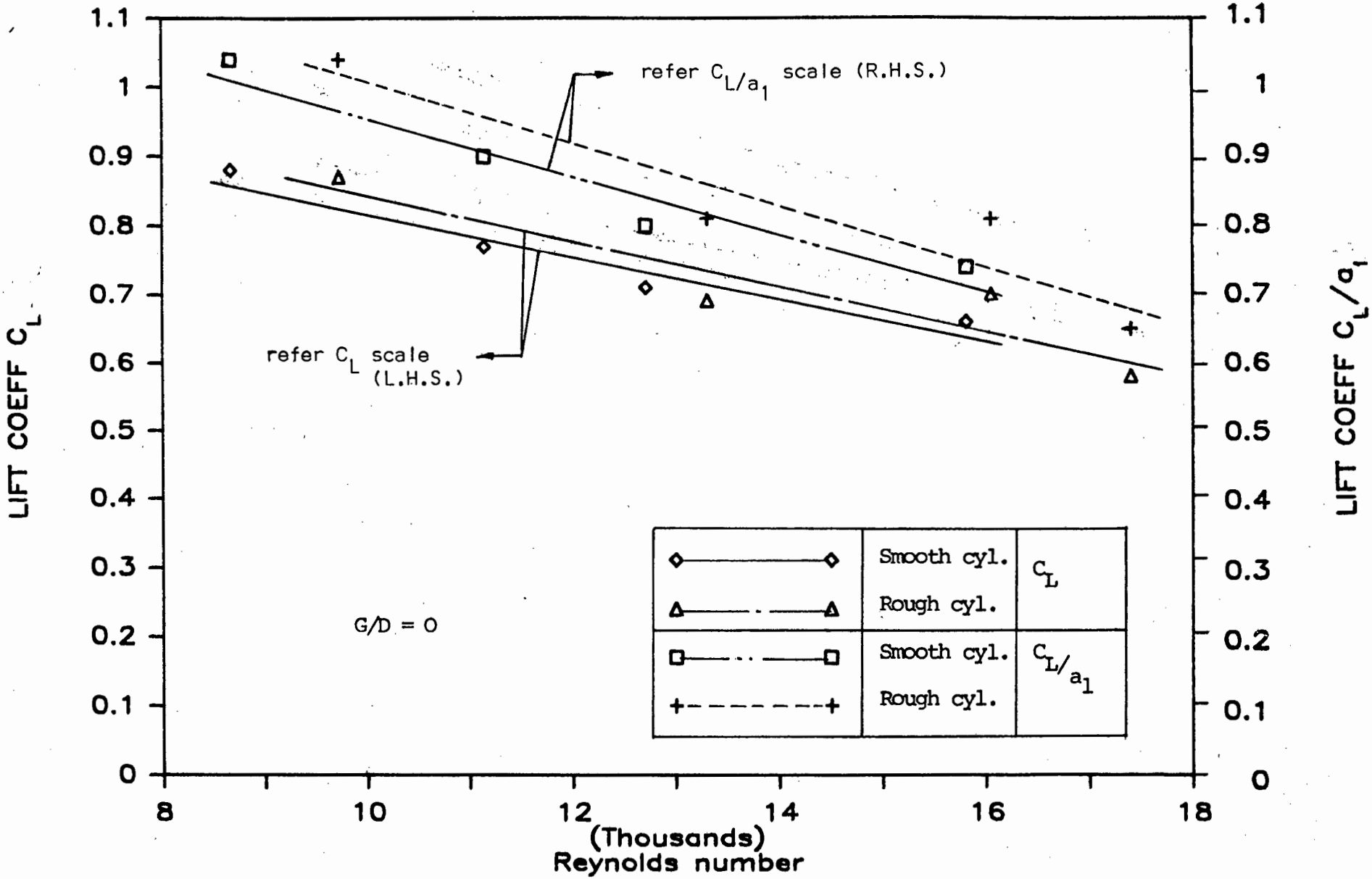

FIG. 5.40: LIFT COEFFICIENTS FOR SMOOTH AND ROUGH 30 mm CYLINDERS; SMOOTH BED

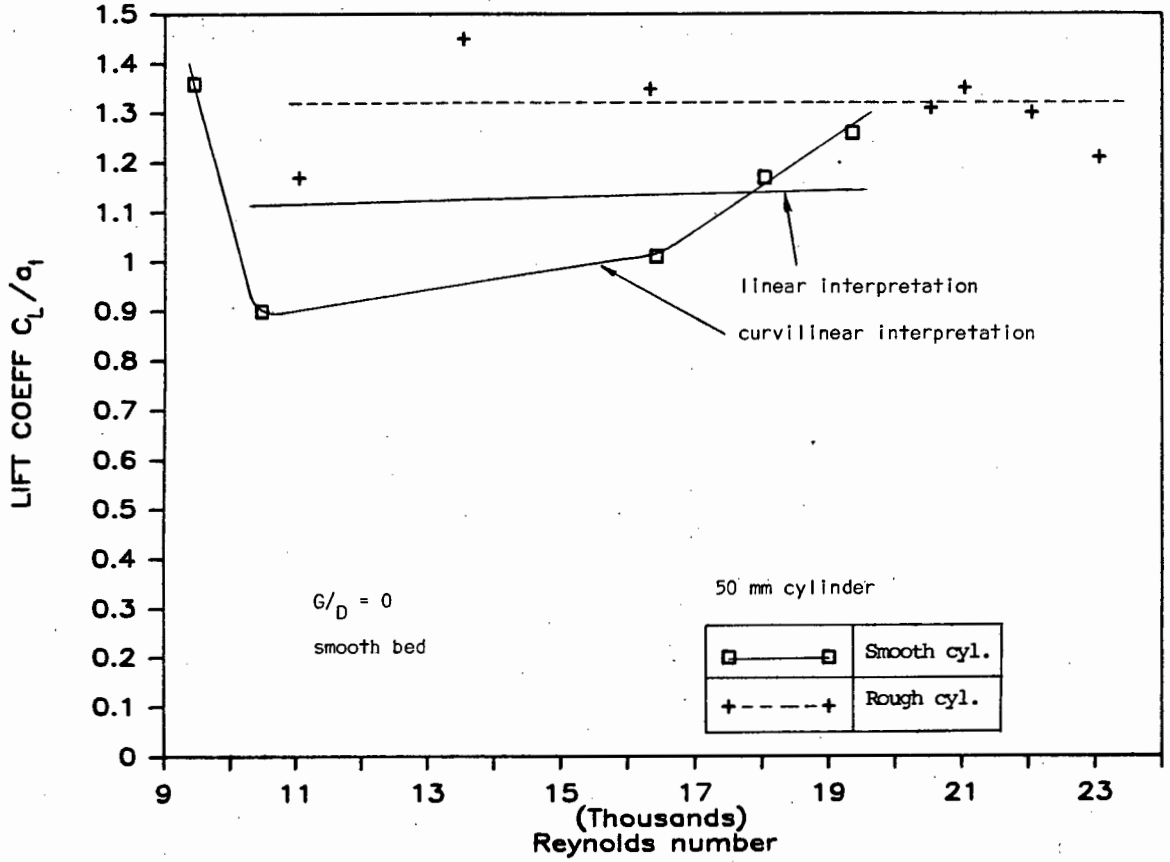

FIG. 5.41: LIFT COEFFICIENTS FOR SMOOTH AND ROUGH 50 mm CYLINDERS; SMOOTH BED

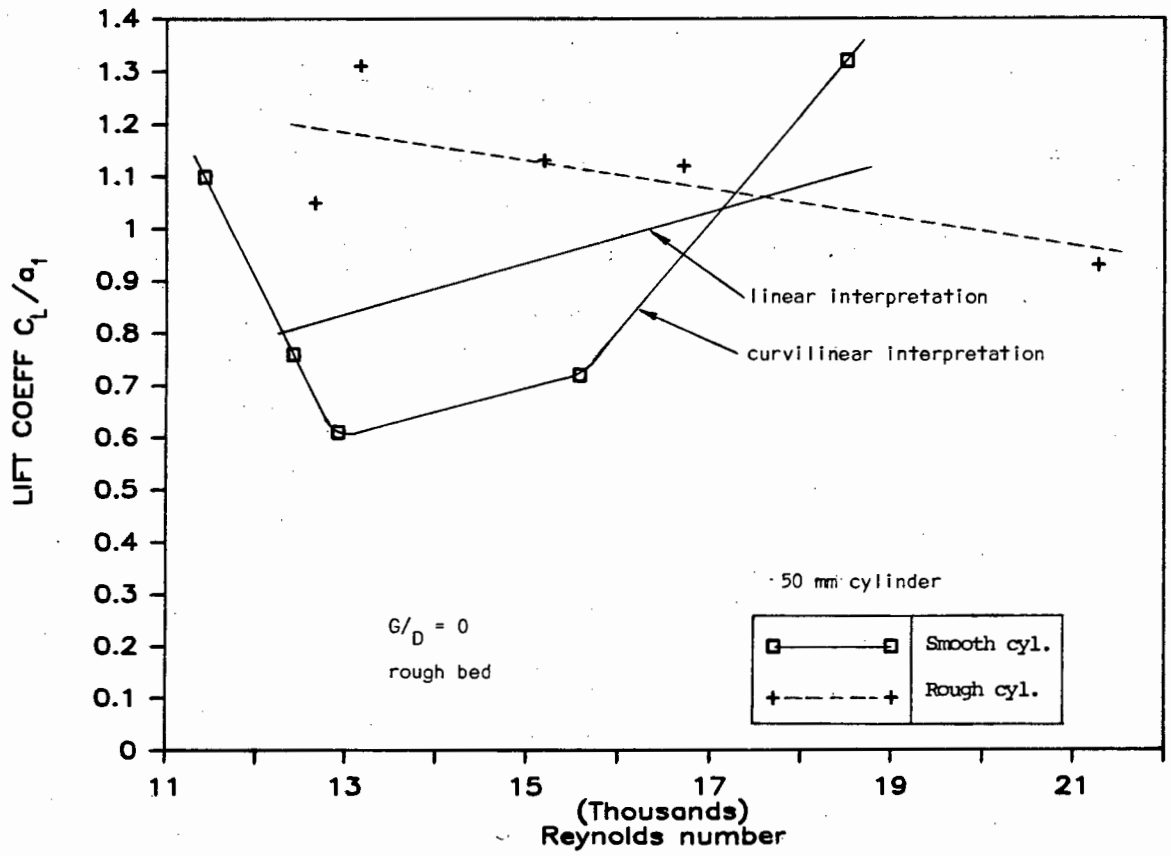

FIG. 5.42: LIFT COEFFICIENTS FOR SMOOTH AND ROUGH 50 mm CYLINDERS; ROUGH BED

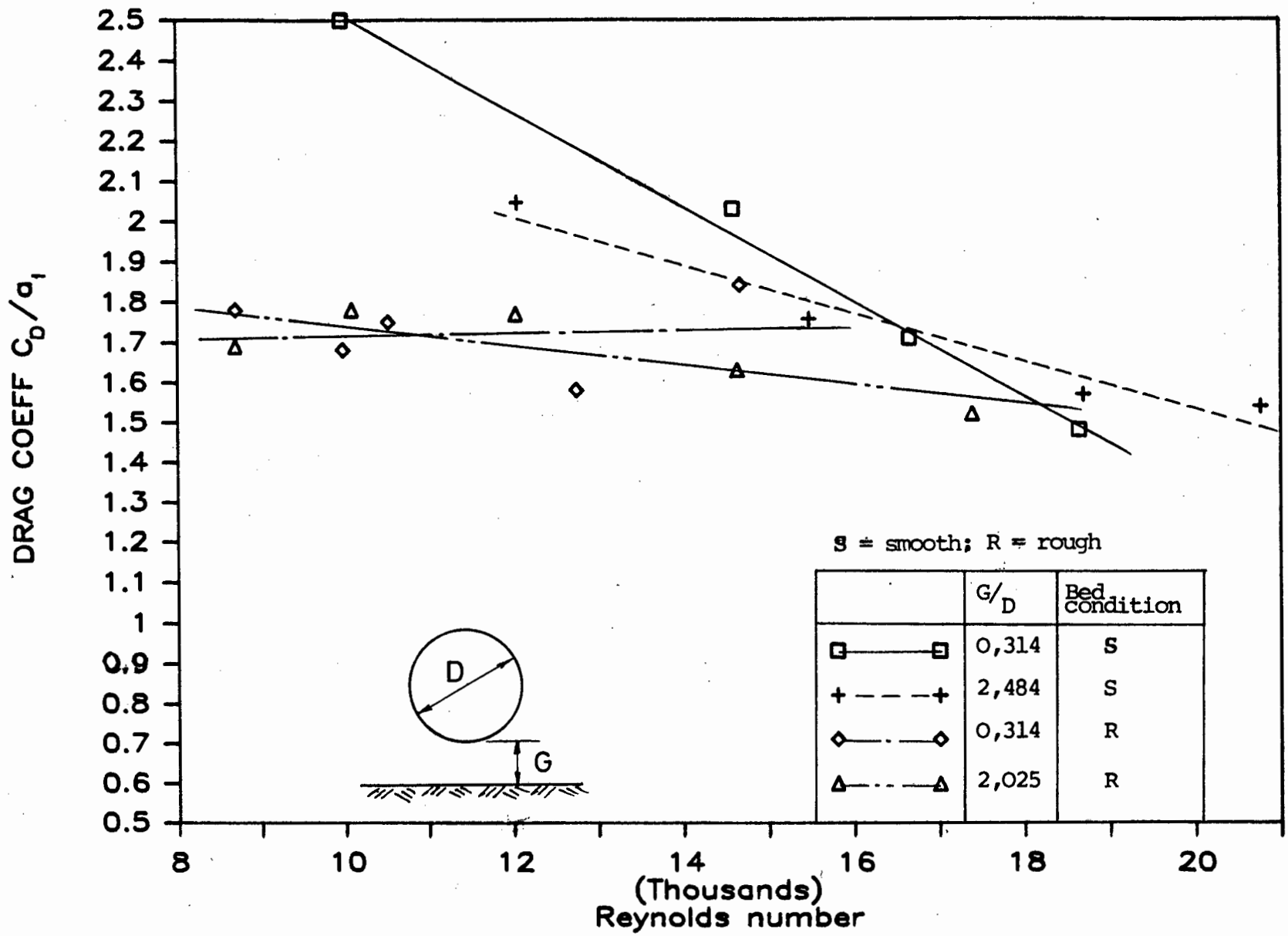

FIG. 5.43: DRAG COEFFICIENTS FOR VARIOUS $G/_D$, BED ROUGHNESSES AND 31,8 mm ROUGH CYLINDER

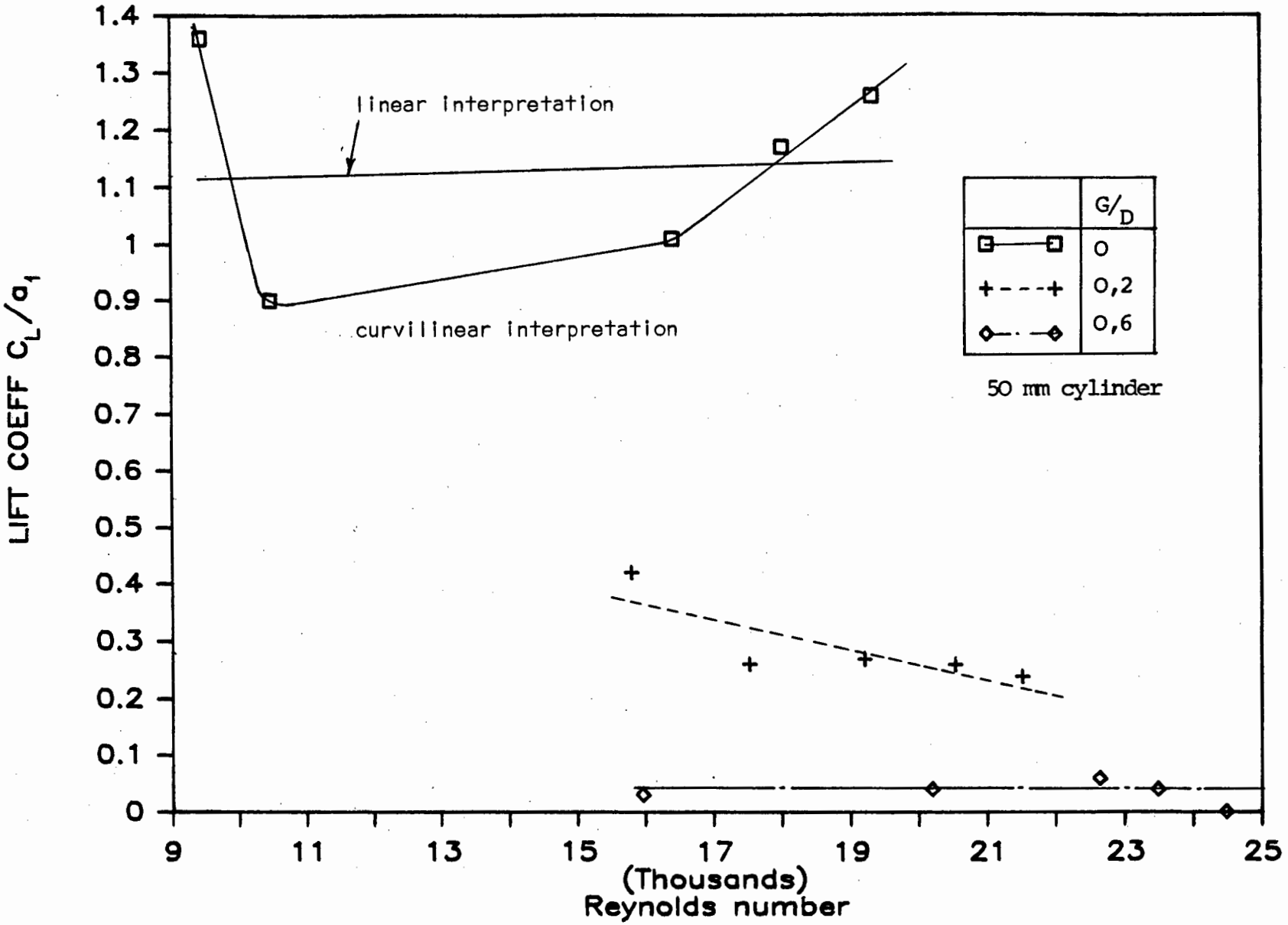

FIG. 5.44: LIFT COEFFICIENTS FOR VARIOUS $G/_D$; SMOOTH 50 mm CYLINDER AND SMOOTH BED

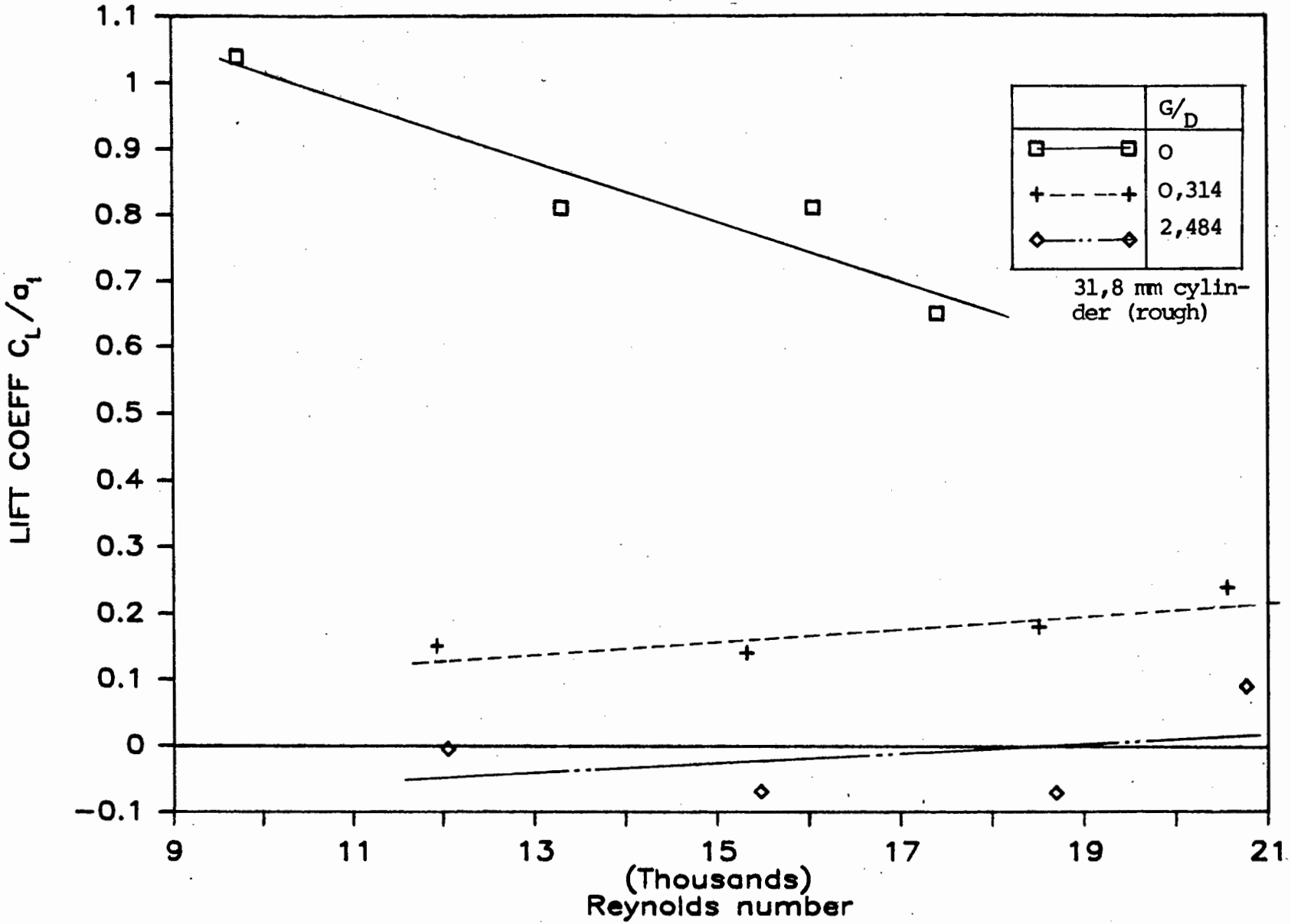

FIG. 5.45: LIFT COEFFICIENTS FOR VARIOUS $G/_D$; SMOOTH BED, ROUGH 31,8 mm CYLINDER

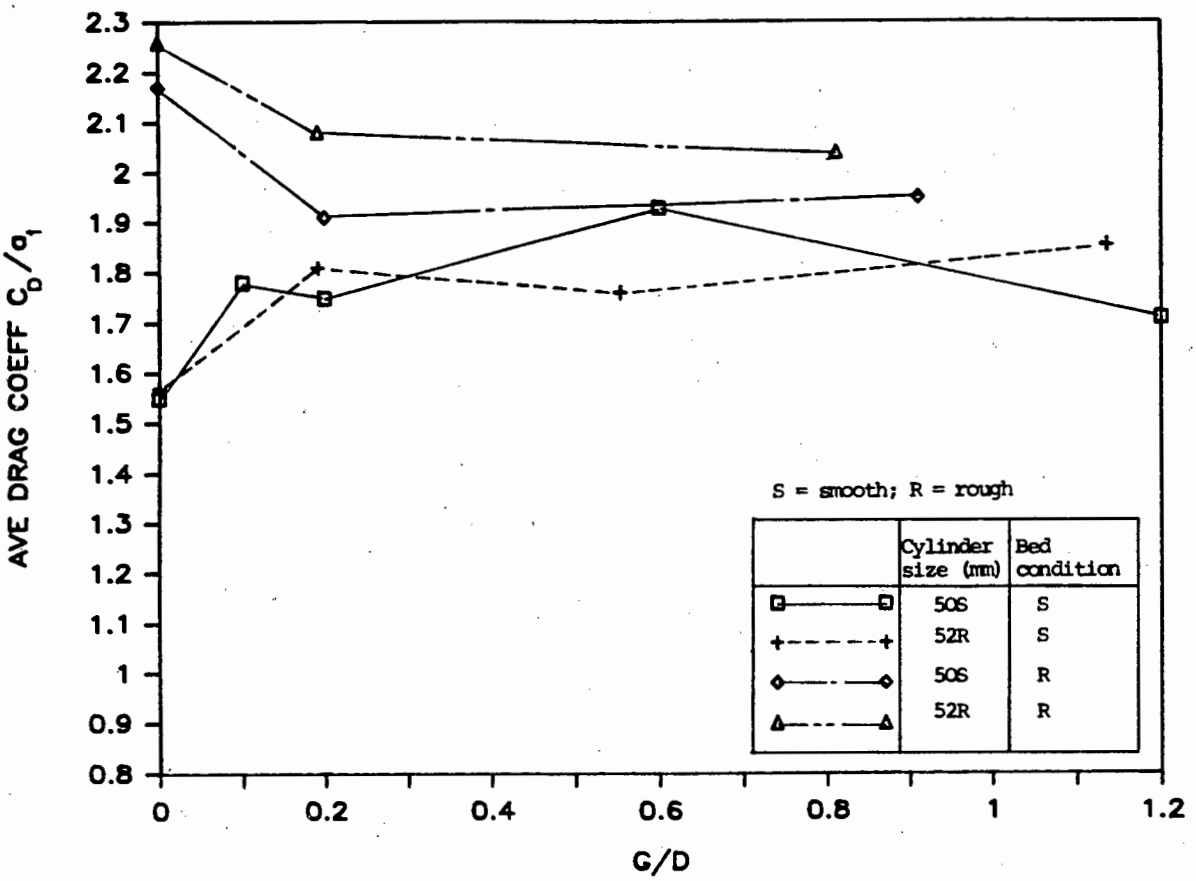

FIG. 5.46: AVERAGE DRAG COEFFICIENTS FOR VARIOUS $G/_D$; 50 mm CYLINDER

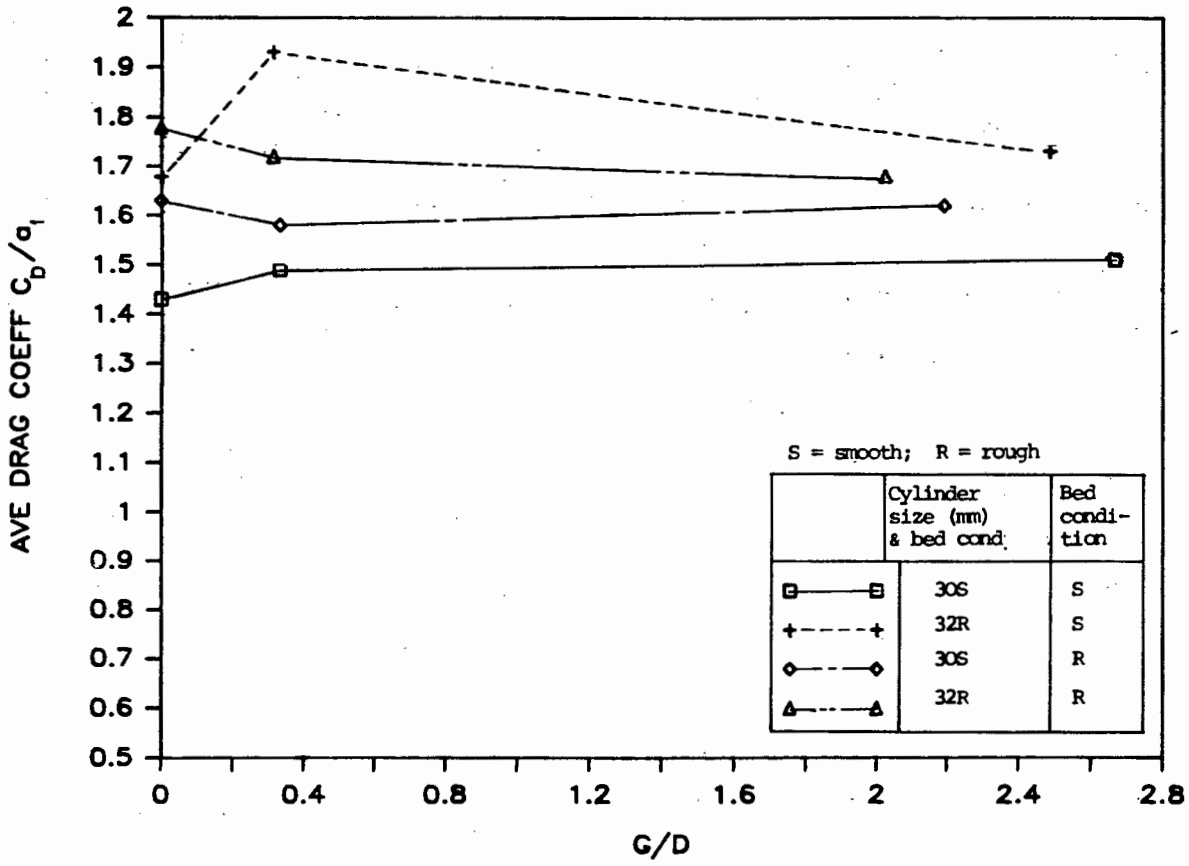

FIG. 5.47: AVERAGE DRAG COEFFICIENTS FOR VARIOUS $G/_D$; 30 mm CYLINDER

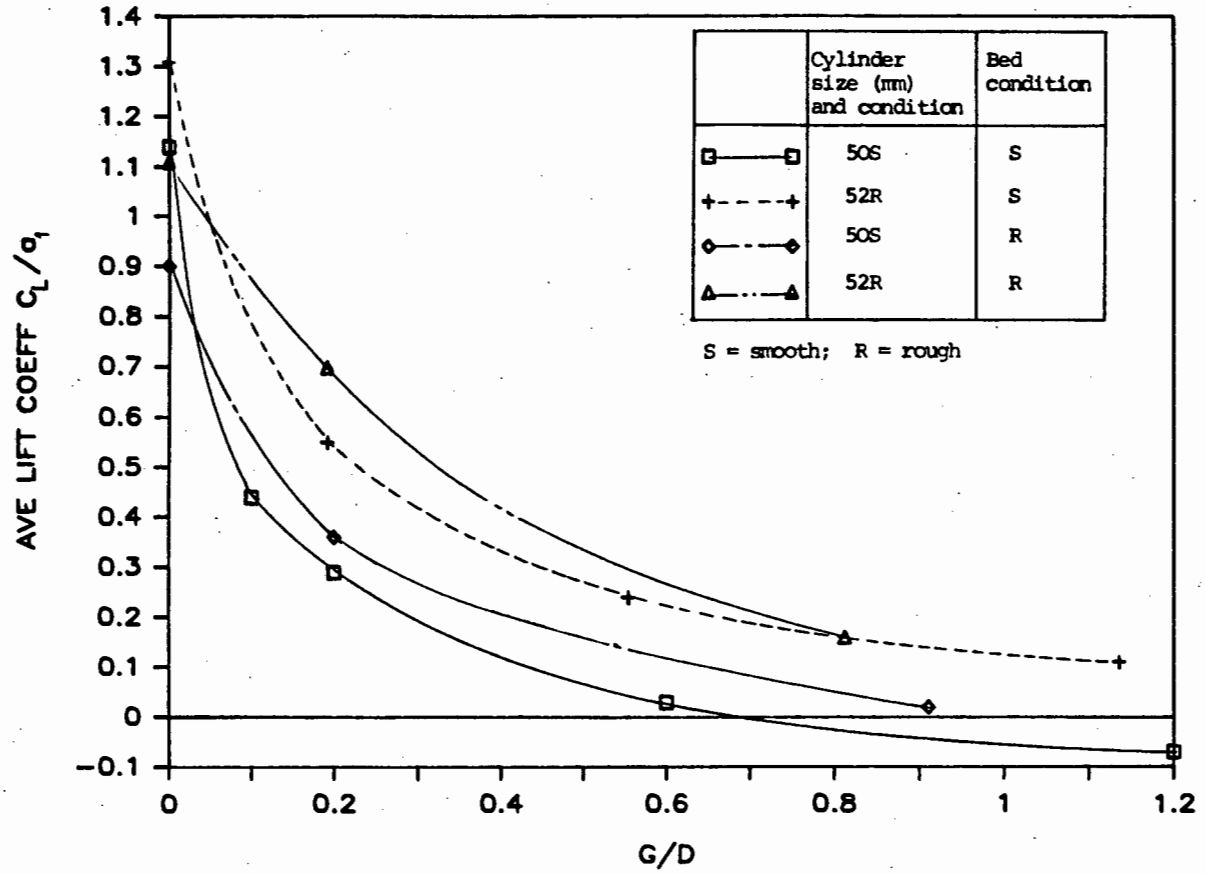

FIG. 5.48: AVERAGE LIFT COEFFICIENTS FOR VARIOUS $G/_D$; 50 mm CYLINDER

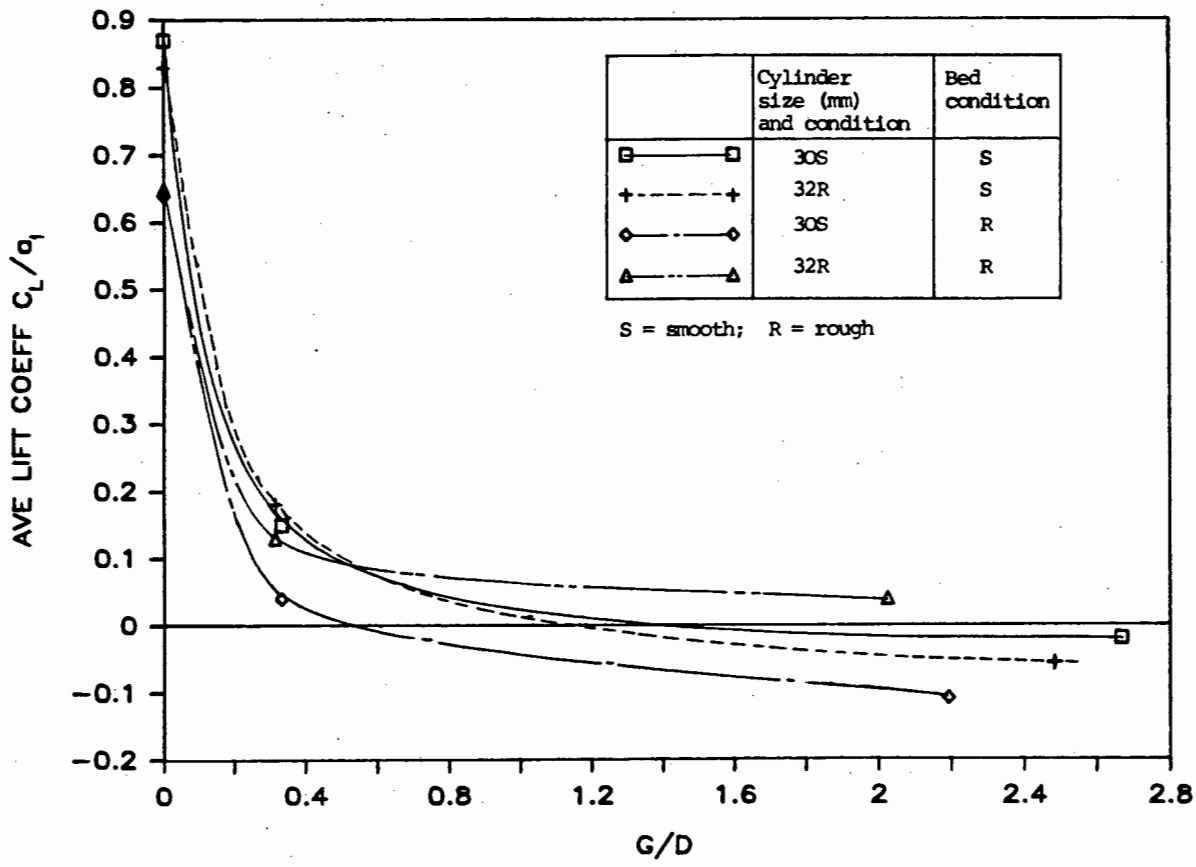

FIG. 5.49: AVERAGE LIFT COEFFICIENTS FOR VARIOUS $G/_D$; 30 mm CYLINDER

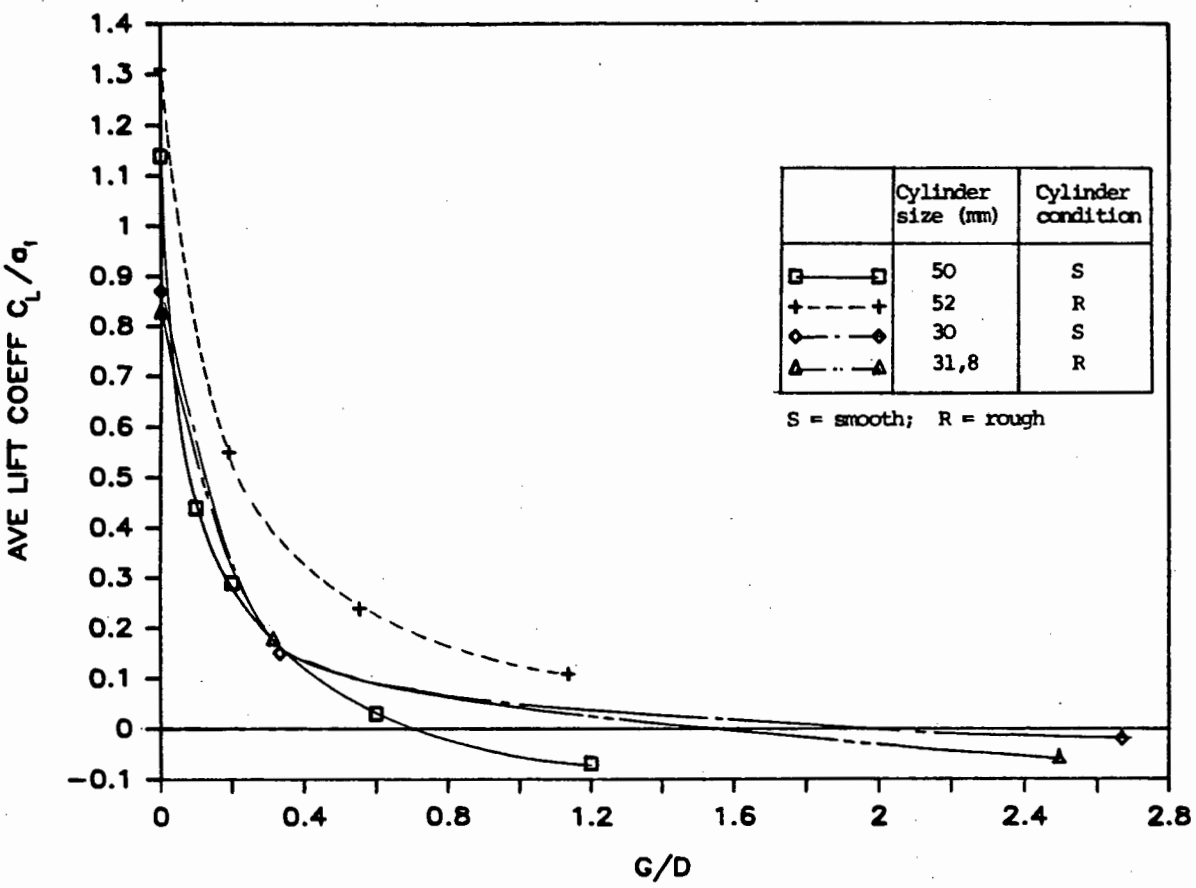

FIG. 5.50: AVERAGE LIFT COEFFICIENTS FOR VARIOUS $G/_D$; SMOOTH BED

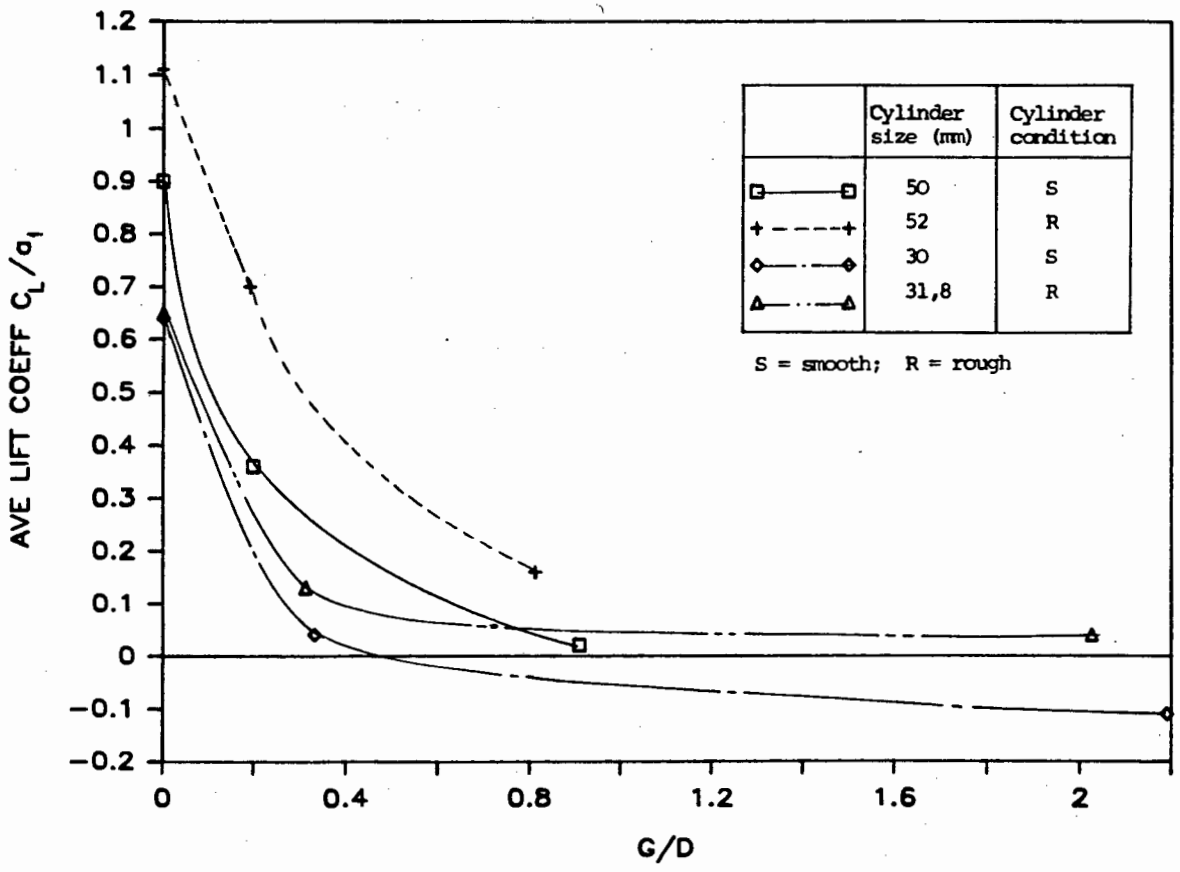

FIG. 5.51: AVERAGE LIFT COEFFICIENTS FOR VARIOUS $G/_D$; ROUGH BED

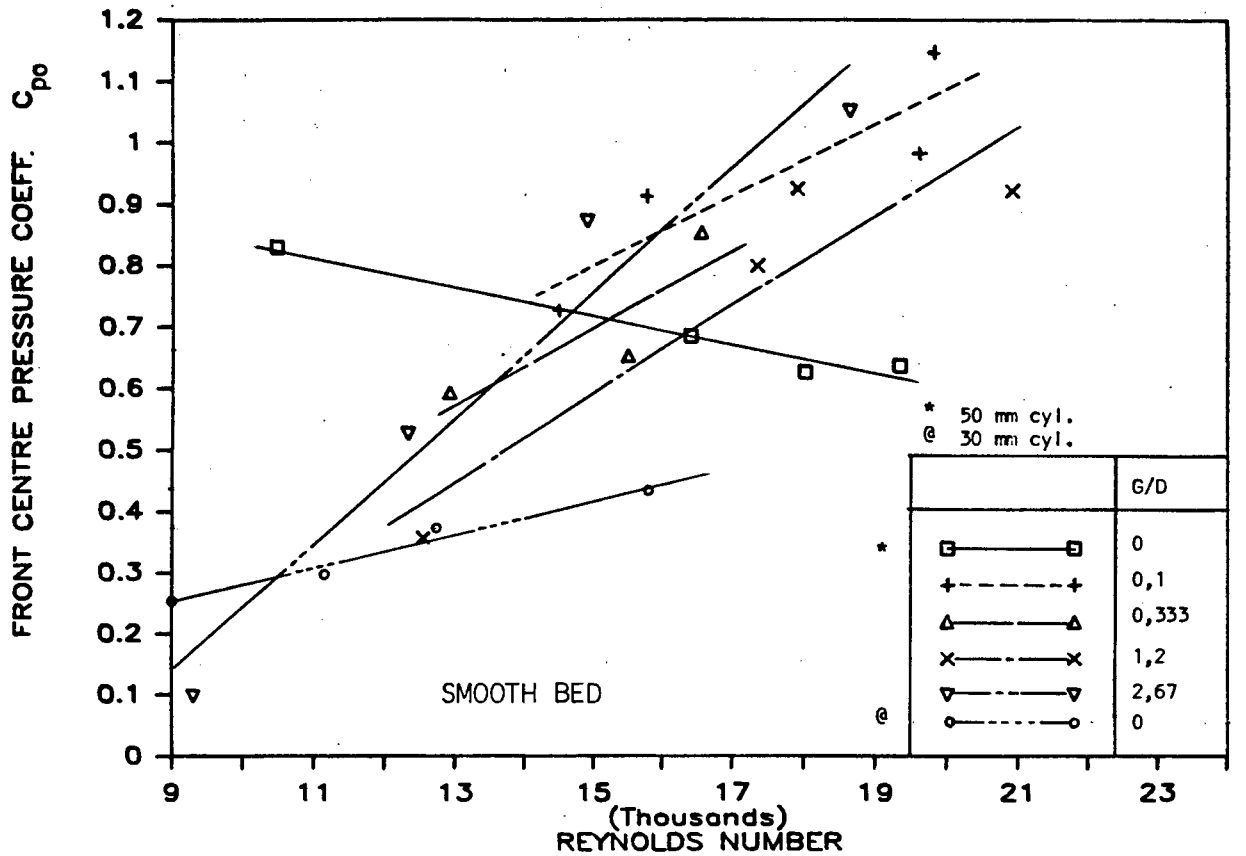

FIG. 5.52: VARIATION OF FRONT CENTRE PRESSURE COEFFICIENT WITH REYNOLDS NUMBER; SMOOTH CYLINDERS

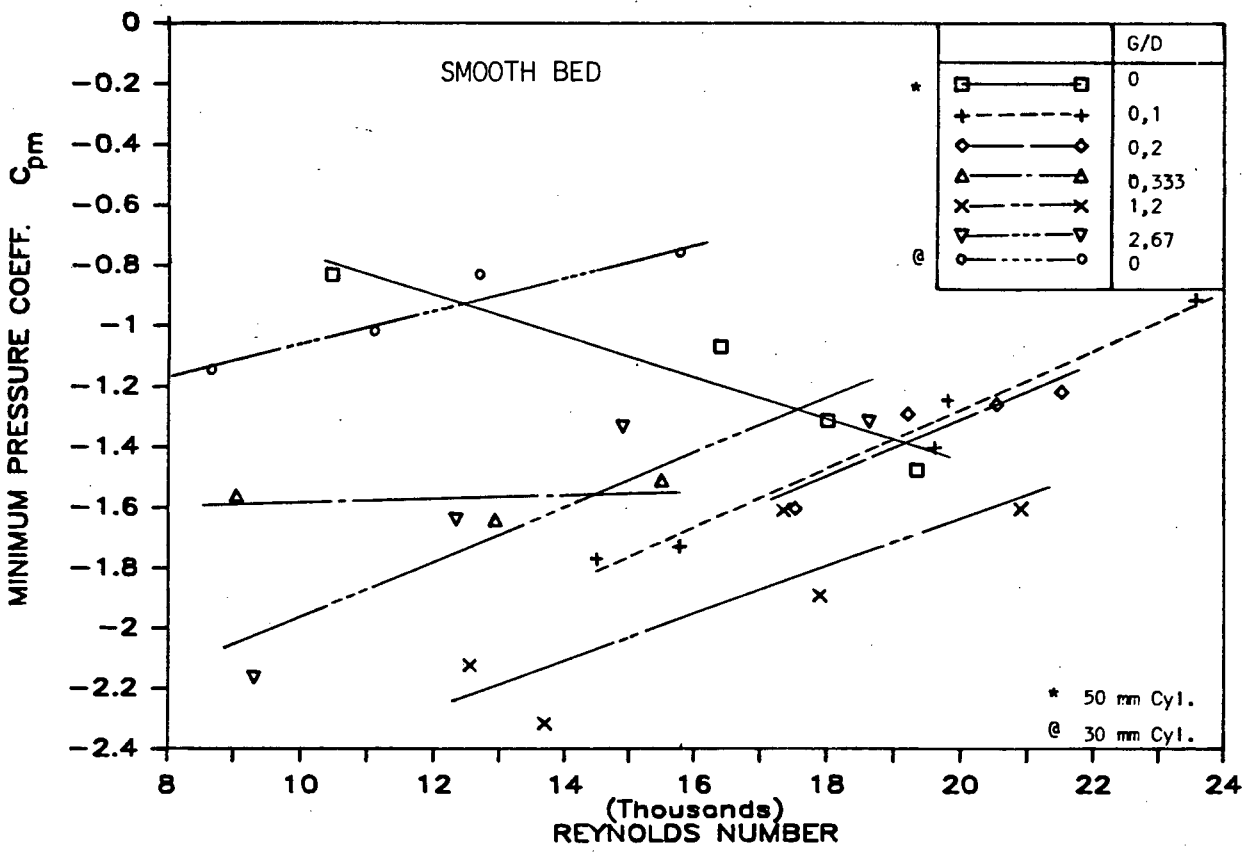

FIG. 5.53 VARIATION OF MINIMUM PRESSURE COEFFICIENT WITH REYNOLDS NUMBER; SMOOTH CYLINDERS

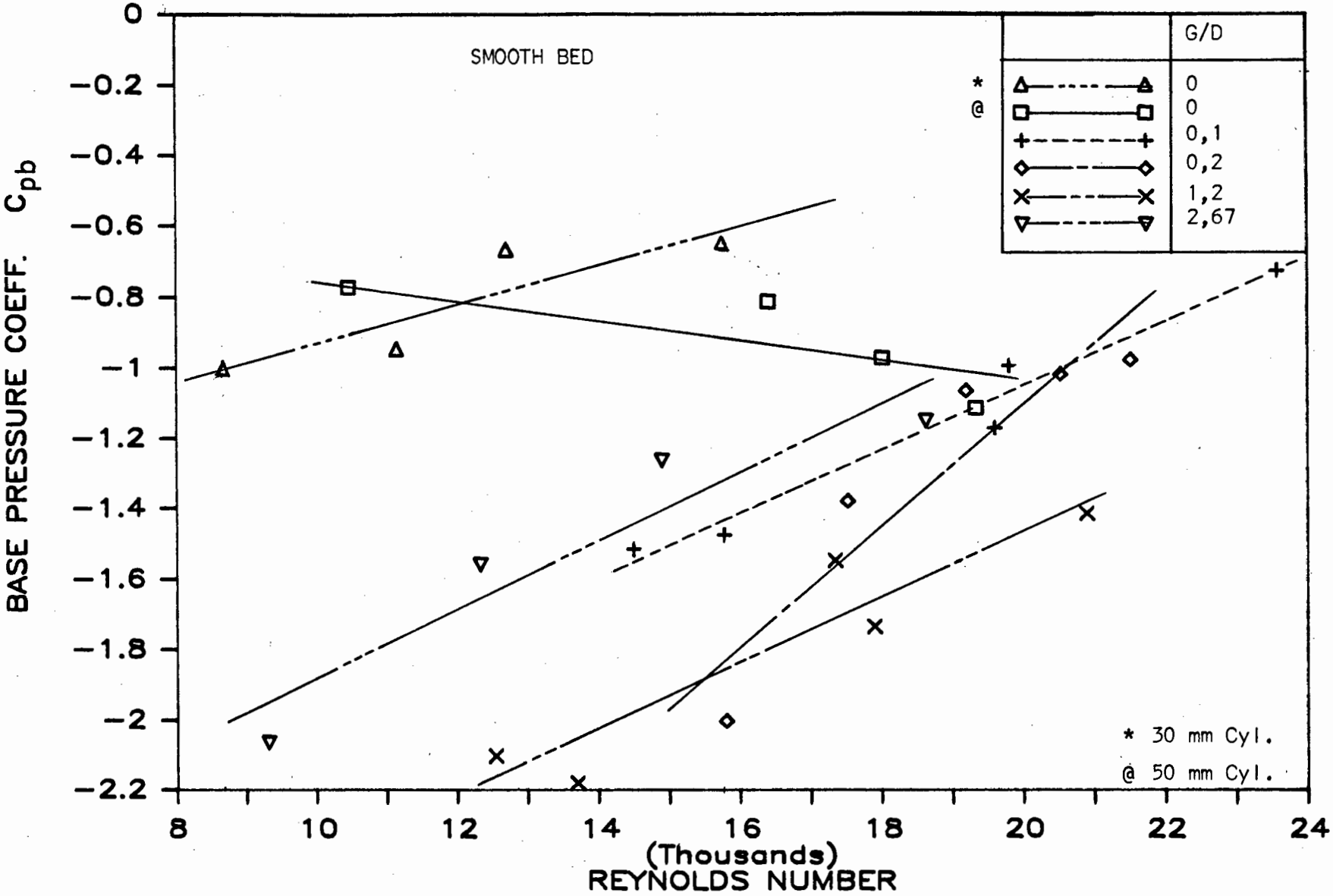

FIG. 5.54: VARIATION OF BASE PRESSURE COEFFICIENT WITH REYNOLDS NUMBER; SMOOTH CYLINDER

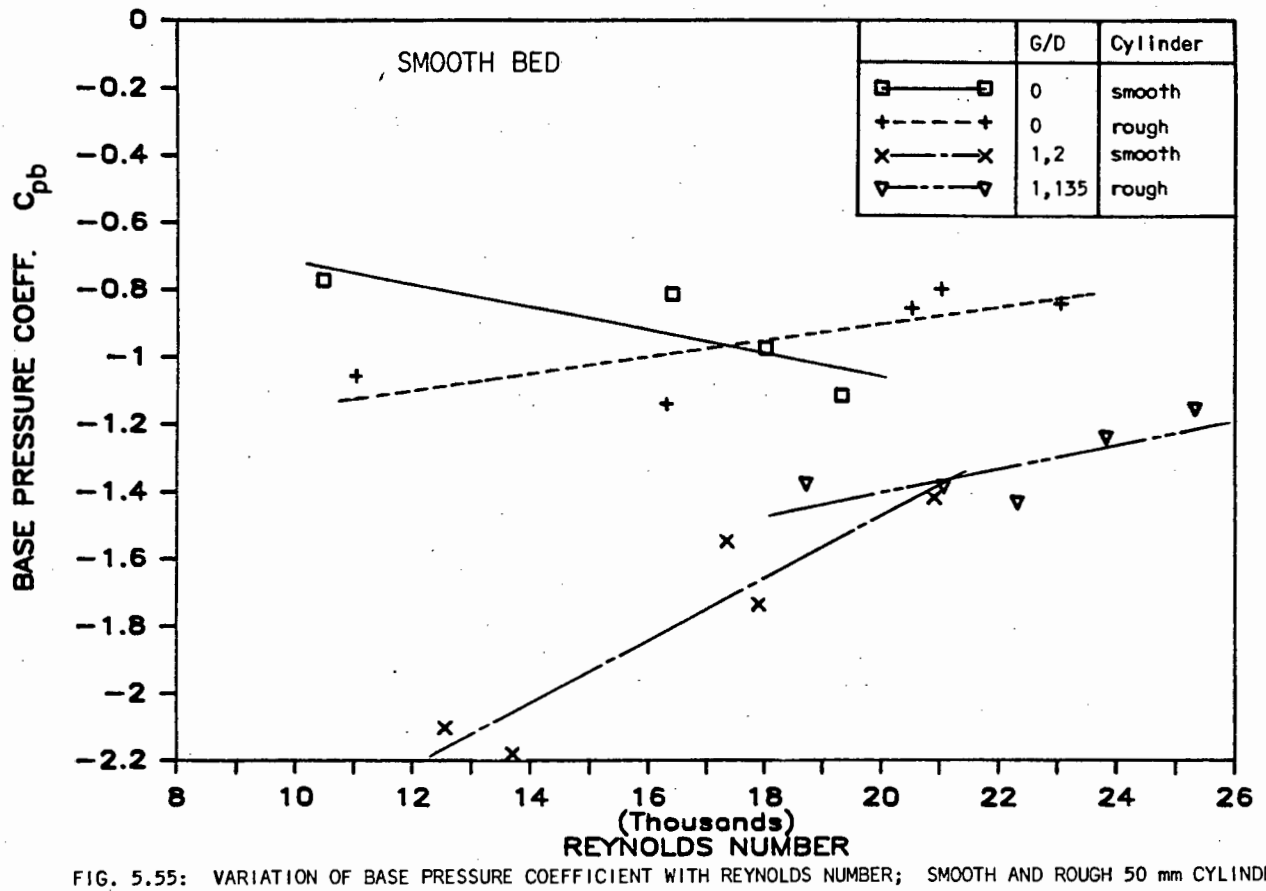

FIG. 5.55: VARIATION OF BASE PRESSURE COEFFICIENT WITH REYNOLDS NUMBER; SMOOTH AND ROUGH 50 mm CYLINDERS

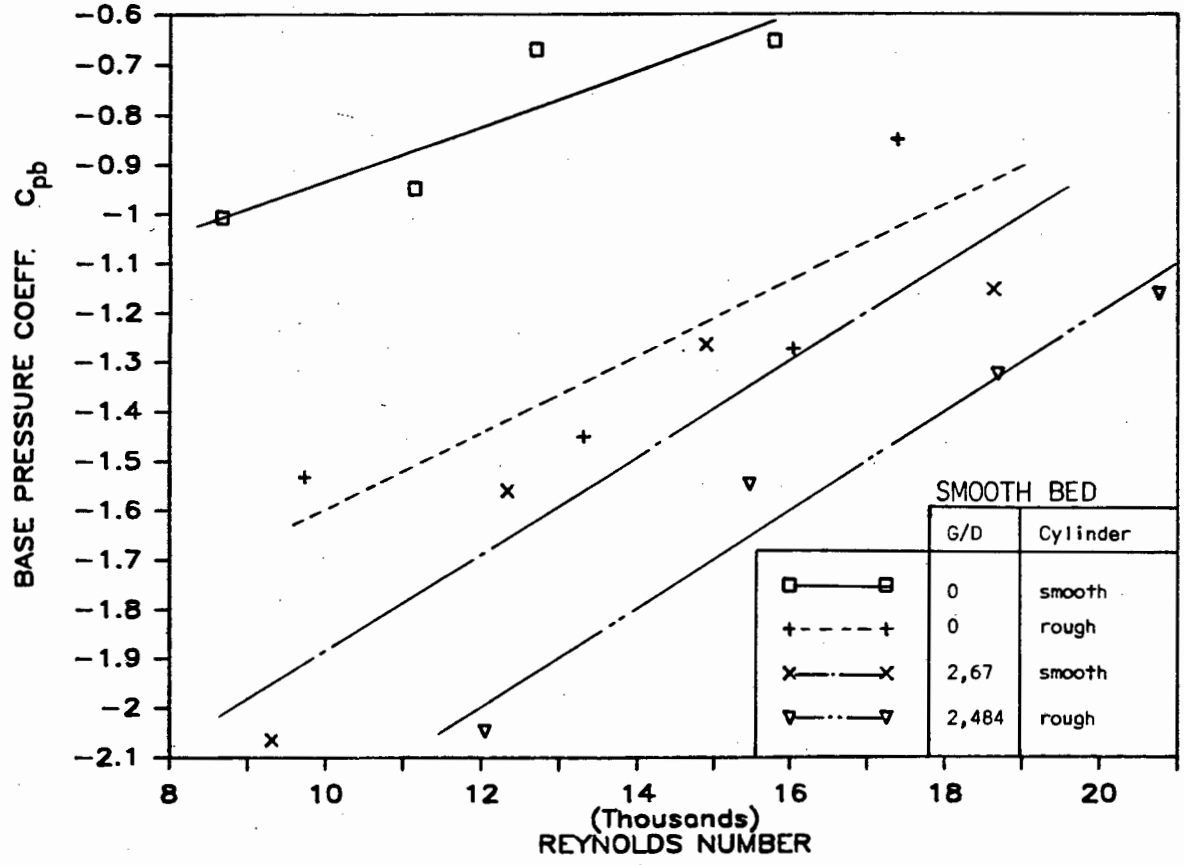

FIG. 5.56: VARIATION OF BASE PRESSURE COEFFICIENT WITH REYNOLDS NUMBER; SMOOTH AND ROUGH 30 mm CYLINDERS

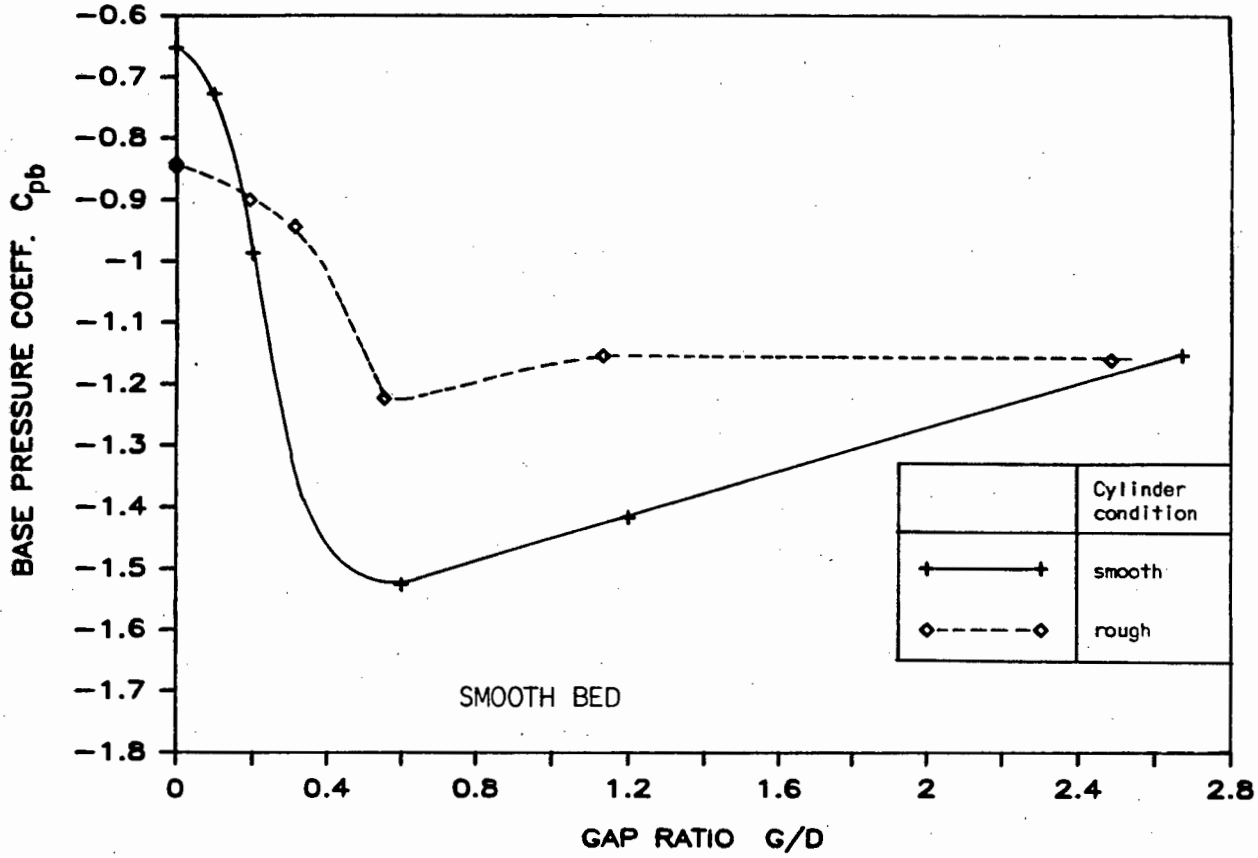

FIG. 5.57: VARIATION OF BASE PRESSURE COEFFICIENT WITH GAP RATIO; R_e = approx 20 000

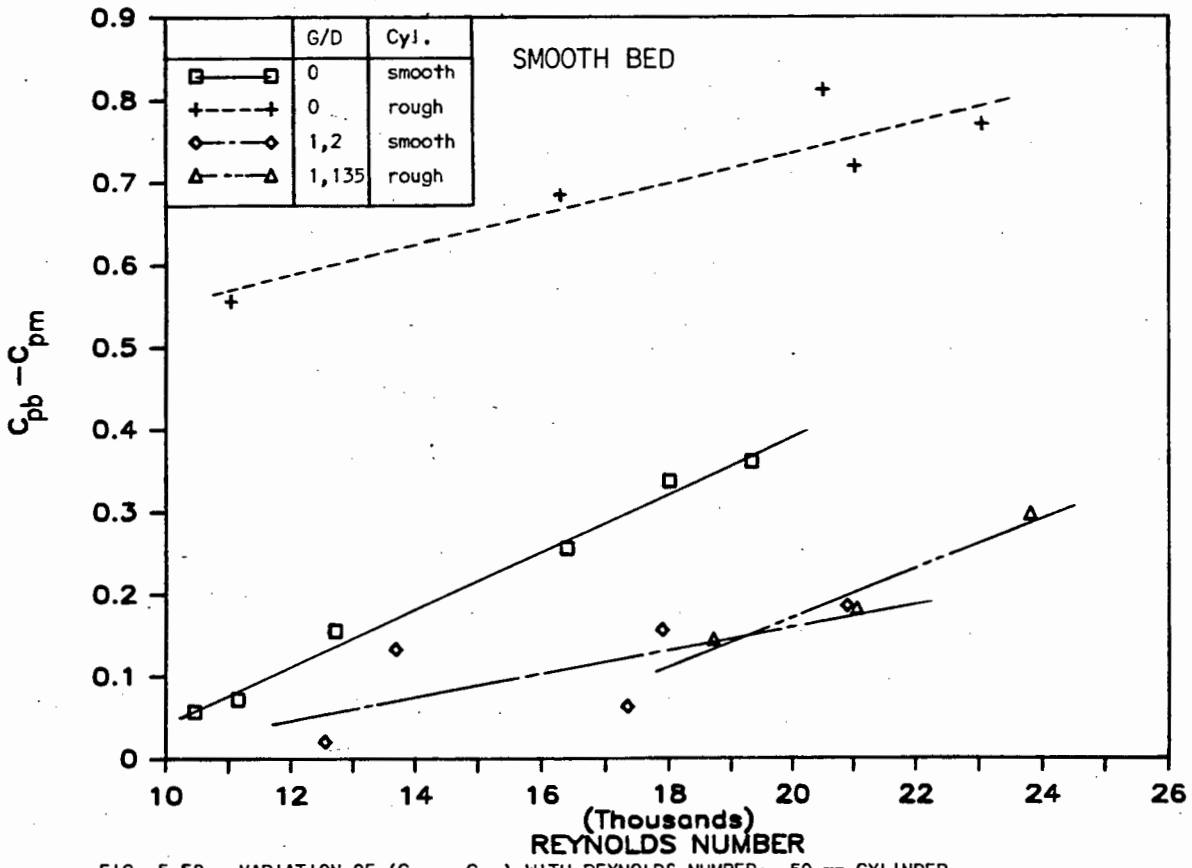

FIG. 5.58: VARIATION OF (C_{pb} - C_{pm}) WITH REYNOLDS NUMBER; 50 mm CYLINDER

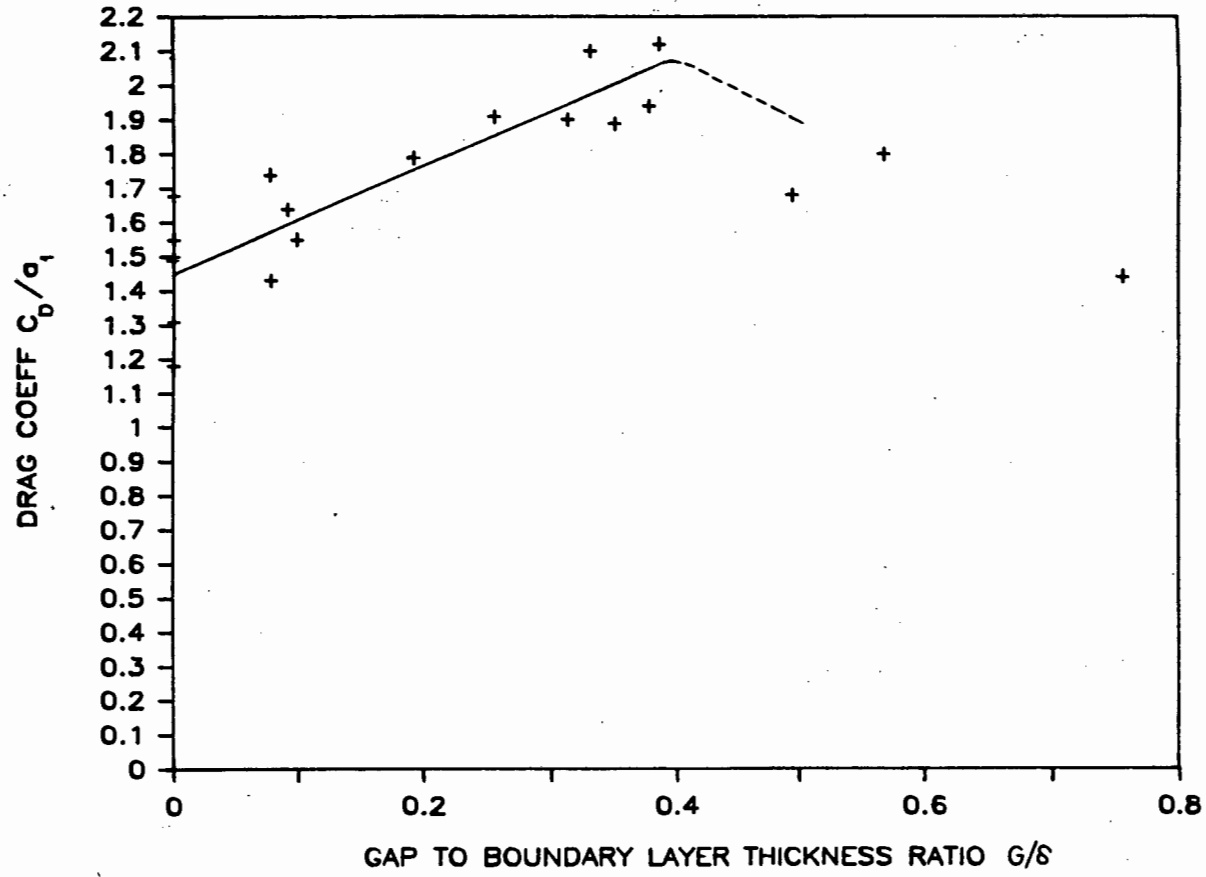

FIG. 5.59: VARIATION OF DRAG COEFFICIENT WITH G/ δ ; SMOOTH BED, SMOOTH CYLINDERS

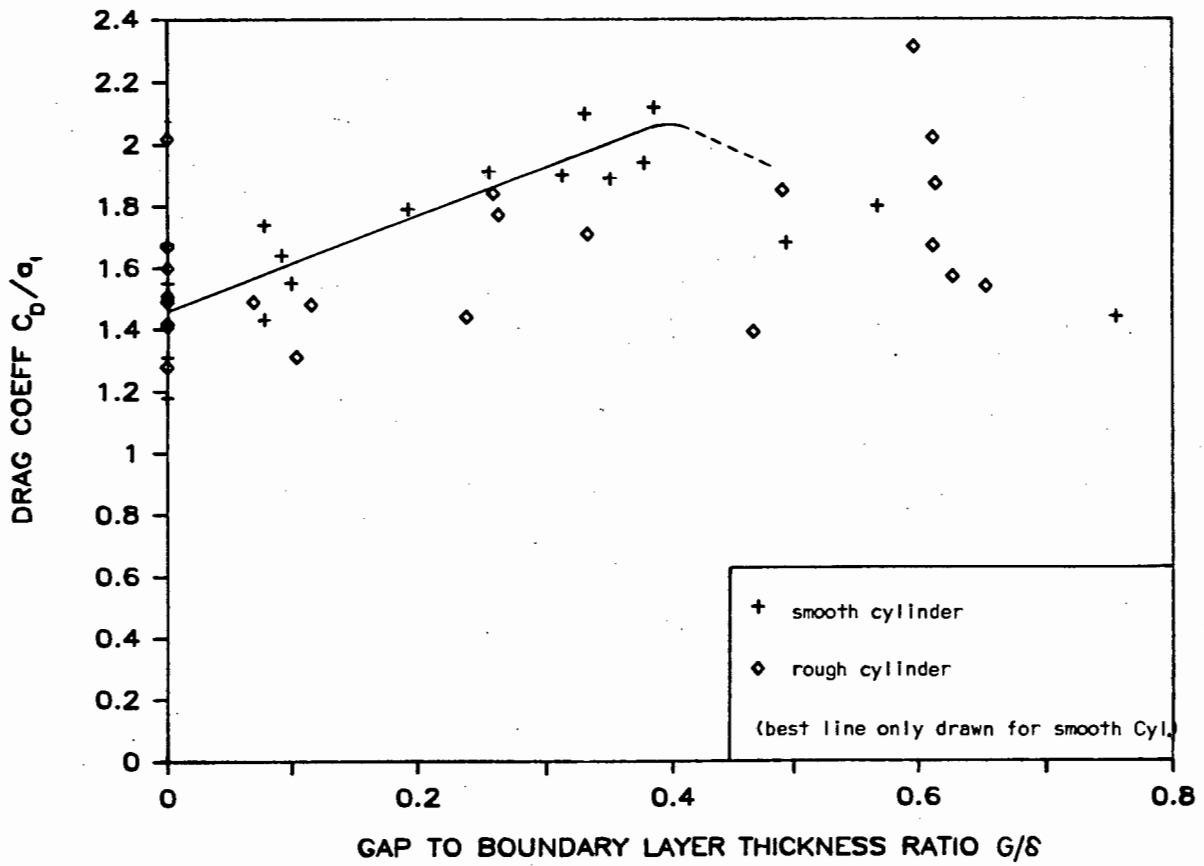

FIG. 5.60: VARIATION OF DRAG COEFFICIENT WITH G/δ; SMOOTH BED, SMOOTH AND ROUGH CYLINDERS

CHAPTER 6 - RESULTS OF FORCE RIG TESTS

6.1 Introduction

The main objective with the tests undertaken with the force rig (experimental details in Chapters 3 and 4), was to determine the drag and lift coefficients by means of an alternative method, in the same water flume and under similar conditions, to serve as a comparison and to gauge the reliability of the two experimental methods utilised.

Tests were only undertaken with a smooth 50 mm diameter cylinder. Only a smooth bed was considered for the 21 test runs, performed at four G/D locations.

Although the force measurements were relatively quick to perform, the velocity readings took at least two hours per test run. One set of readings (Run 16), is shown as an example in Table 6.1. The calculations of the applicable lift and drag forces were straightforward; a brief calculation is also indicated in Table 6.1.

Computations of velocities, and lift and drag coefficients, were similar to those presented in Chapter 5.

The following reference velocities were applied in calculating Reynolds number, and the lift and drag coefficients:

CLEARANCE, G (mm)	G/D	DETERMINATION OF REFERENCE VELOCITY	APPROXIMATE REFERENCE VELOCITY (% OF $U_{D/2}$)
0	0	From eq. (5.9)	97,4
10	0,2	From eq. (5.13)	98,5
30	0,6	From eq. (5.13)	99,7
60	1,2	$U_{D/2}$	

$U_{D/2}$ = velocity at the elevation of the centre of the cylinder.

FORCE DETERMINATION

Clearance = Ø mm
Cylinder: Smooth
Diameter = 5Ø mm
Bottom: Smooth

Distances

(1) Fulcrum to pointer(drag) = 754,3 mm
(2) Fulcrum to cylinder = 631,Ø mm
Fulcrum to cyl. centre = 656,Ø mm

Static readings
Bottom elevation = 5,Ø5 cm

Surface Elev. (cm)	Depth (cm)	Balance(g) (PE6ØØØ)
23,95	18,9Ø	96,Ø
35,4Ø	3Ø,35	51,Ø

(constant = -3,9317g/cm)

"Dynamic" readings
Balances zero at depth = 19,14 cm
(PE6ØØØ, 3ØØØ)

Lift reading (PE 6ØØØ) = -146 g
Drag reading (PE 3ØØØ) = 168 g
Calculations:
LIFT: $-146 + 25{,}9^{*} = \underline{-12Ø\ g}$
DRAG: $168 \times \frac{754{,}3}{656} = \underline{193\ g}$
(* correction for submerged arms of rig)

RUN No.	= 16
DATE	= 19.12.86
TEMP	= 22,Ø C
H	= 7,1 inches
$Q = Ø{,}191\sqrt{H}$	= Ø,Ø5Ø9 m^3/s
Elevation surf	= 3Ø,79 cm
Bottom	= 5,Ø5 cm
* Depth	= 25,74 cm
Flume width	= 6Ø8 mm
Ave. velocity	= Ø,325 m/s
Dia of Pitot	= 16,8 mm

VELOCITY DISTRIBUTION

Dist to wall Hor. (mm)	Balance (PE3ØØ) (g)	(m/s)
2Ø	8,5	Ø,279
3Ø	9,2	Ø,29
4Ø	9,9	Ø,3Ø1
6Ø	1Ø,5	Ø,31
8Ø	1Ø,4	Ø,3Ø8
1ØØ	1Ø,8	Ø,314
15Ø	11,15	Ø,319
2ØØ	1Ø,34	Ø,3Ø7
25Ø	9,85	Ø,3Ø
3Ø4	9,3Ø	Ø,291

TABLE 6.1 EXAMPLE OF SET OF MEASUREMENTS (FORCE RIG)

Run No.	Gap G (mm)	$G/_D$	Temp (°C)	$U_D/_2$ (m/s)	V_{eff} (m/s)	Reynolds No. R_e	Length leff (mm)	Water depth H (cm)	Forces Measured (grams)		Coefficients		Depth parameter a_1	Coefficients	
									F_D	F_L	C_D	C_L		C_D/a_1	C_L/a_1
1	30	0,6	16,5	0,26	0,259	10 791	590,7	29,35	179	11	1,78	0,11	0,830	2,14	0,13
2			16,7	0,075	0,075	4 061	594,8	25,25	15,4	1,3	1,81	0,15	0,802	2,25	0,19
3			21,0	0,121	0,120	5 957	587	24,51	33	2,1	1,55	0,096	0,796	1,95	0,12
4			21,7	0,24	0,239	12 406	587	26,60	143	10	1,68	0,114	0,812	2,07	0,14
5			22	0,31	0,309	16 718	583,5	27,62	243	13	1,71	0,09	0,819	2,09	0,11
6			21	0,18	0,179	8 861	580,5	25,38	84	7,6	1,77	0,16	0,803	2,2	0,20
7	60	1,2	21	0,175	0,175	8 925	586,0	26,32	67	3,0	1,46	0,065	0,810	1,80	0,08
8			21,5	0,223	0,223	11 605	594,7	27,32	122	3,1	1,62	0,041	0,817	1,98	0,05
9			21,5	0,294	0,294	15 300	599	28,57	229	7,6	1,73	0,058	0,825	2,10	0,07
10			21,7	0,31	0,31	16 760	598,6	29,59	214	7,3	1,46	0,05	0,831	1,76	0,06
11			21,7	0,128	0,128	6 660	589,0	25,00	38	2,0	1,56	0,08	0,800	1,95	0,10
12	0	0	21,5	0,11	0,107	5 571	591,0	26,46	26,6	15,8	1,54	0,92	0,811	1,90	1,13
13			21,5	0,13	0,127	6 594	596,7	24,75	44	25	1,78	1,01	0,798	2,23	1,26
14			21,7	0,183	0,178	9 272	594,0	27,78	83	39	1,73	0,81	0,820	2,11	1,00
15			21,7	0,27	0,263	13 684	589,8	25,13	163	96	1,57	0,92	0,801	1,96	1,15
16			22	0,31	0,302	16 538	590,5	25,74	193	120	1,308	0,814	0,806	1,62	1,01
17	10	0,2	17,3	0,0671	0,066	3 333	592,4	28,48	12,2	2,1	1,85	0,31	0,824	2,25	0,38
18			17,5	0,1121	0,11	5 538	594,2	27,34	30	4,5	1,62	0,25	0,817	1,98	0,30
19			17,5	0,143	0,141	7 103	593,6	26,57	51	8,5	1 71	0,28	0,812	2,10	0,35
20			17,7	0,184	0,181	9 140	591,2	26,89	74	12,5	1,51	0,25	0,814	1,85	0,31
21			18	0,233	0,229	11 574	593,8	27,07	133	18	1,67	0,23	0,815	2,05	0,28

Cylinder diameter = 50 mm (smooth)
Smooth bed

TABLE 6.2 SUMMARY OF MEASUREMENTS AND COMPUTATIONS (FORCE RIG)

A summary of measurements and computations is given in Table 6.2. To make realistic comparisons with corresponding tests performed with the pressure rig, account was also taken of the depth parameter a_1 in calculating lift and drag coefficients.

6.2 Velocity Profiles along the Flume Width

Apart from "vertical" velocity profiles, velocity distributions were measured along the width of the flume, at the elevation of the cylinder centre. Selected plots at an elevation of 25 mm, are shown in Fig. 6.1 and at an elevation of 85 mm in Fig. 6.2. The Reynolds numbers indicated, are based on the velocity at the elevation concerned and a cylinder diameter of 50 mm.

For each test run, the velocity curve was meticulously plotted on graph paper by hand, and the effective length of the cylinder determined graphically. Due to the size of the pitot tube, the closest the velocity could be measured to the side wall, was 12 mm; closer locations would have been preferred, as the velocity changed rapidly in the region concerned. The effective lengths of the cylinder are indicated in Table 6.2.

In the region 60 to 140 mm from the side walls, the velocity curves exhibited a hump, particularly at higher velocities. The hump was probably due to a three dimensional flow effect, caused by interference of the wall.

6.3 Drag Coefficient

The drag coefficients C_D/a_1 were plotted for each of the four G/D values. On the same diagrams, the drag coefficients determined by pressure integration were indicated. The diagrams

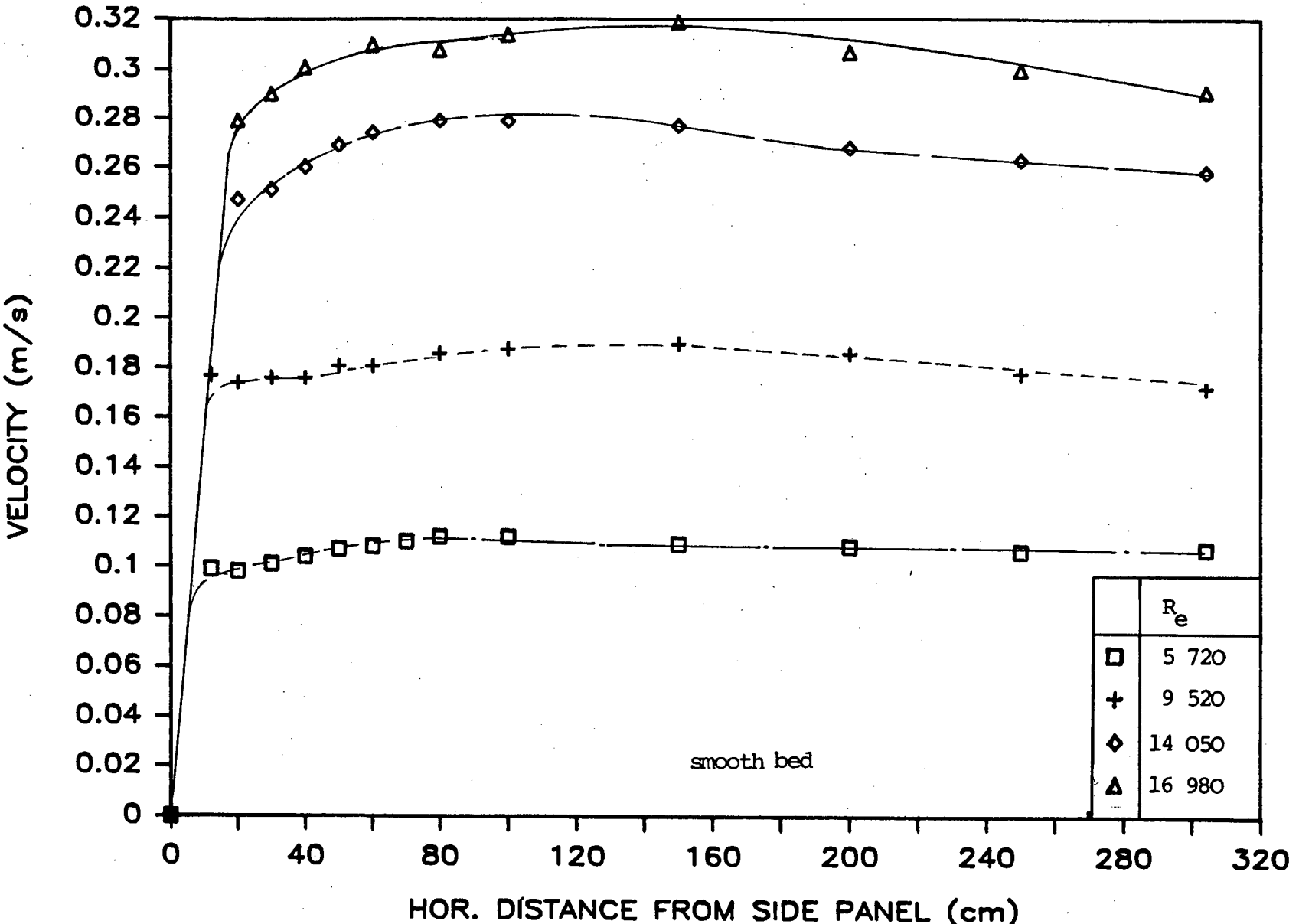

FIG 6.1: VELOCITY PROFILES MEASURED AT AN ELEVATION OF 25 mm ABOVE THE BED (FORCE RIG METHOD)

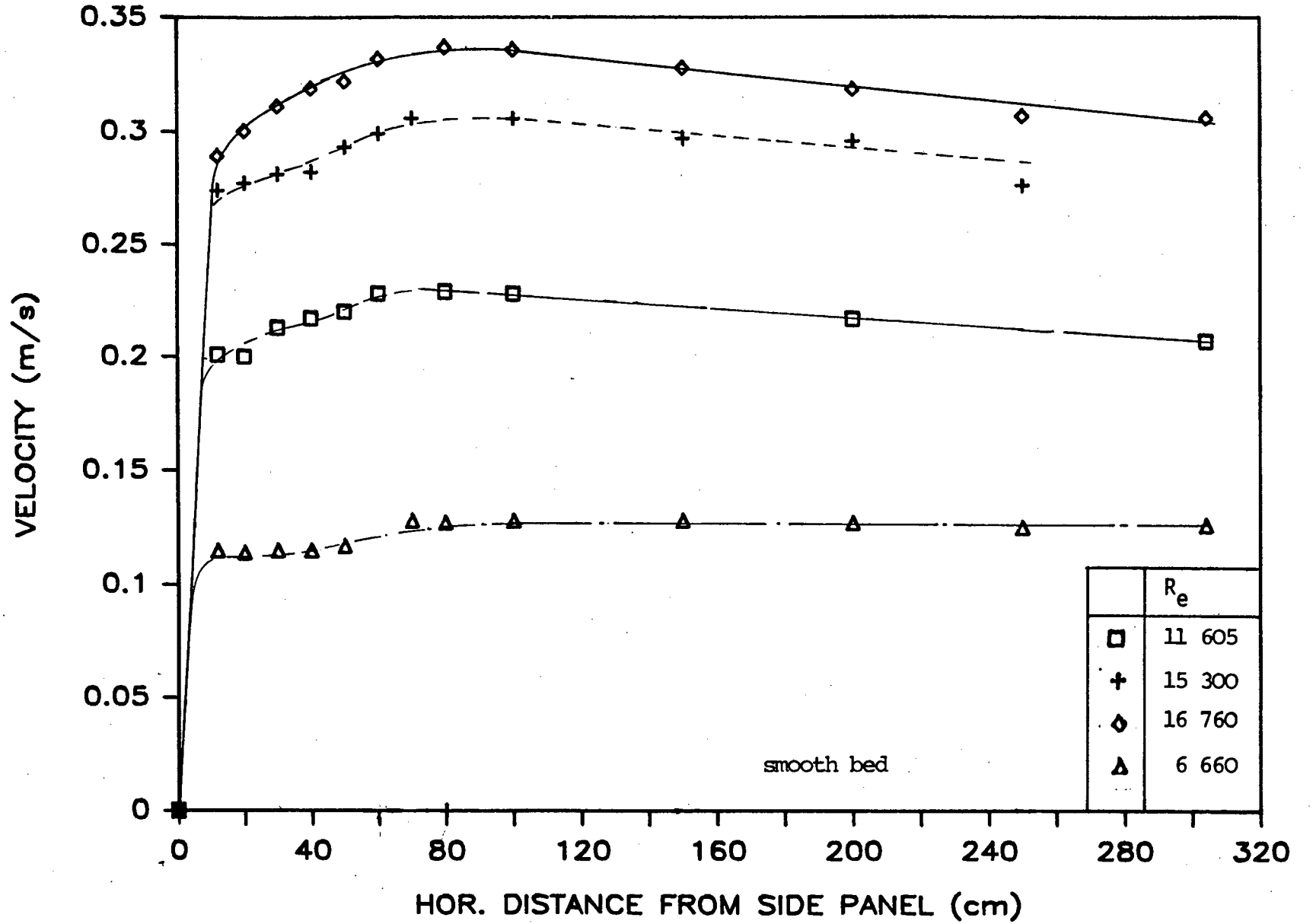

FIG 6.2: VELOCITY PROFILES MEASURED AT AN ELEVATION OF 85 mm ABOVE THE BED (FORCE RIG METHOD)

are shown in Figs. 6.3 to 6.6. The downtrends of particularly Figs. 6.3 and 6.4 could indicate the start of the critical region. Average drag coefficients for various G/D were calculated as was done in Chapter 5. A comparison with values derived by means of pressure integration is indicated in Fig. 6.7. A true comparison of average values is not realistic, as the force rig tests were done at lower Reynolds numbers.

The deviating force coefficients generated by test run 12 with the pressure integration method (and discussed in Section 5.5.2), are responsible for the curvilinear relationships shown in Figs. 6.3 and 6.8. A least squares analysis (for a straight line), showed that the force rig coefficients were generally higher. Higher values were expected, as the direct force measurement also included the skin friction component of the total drag.

The drag coefficients (force rig method) fall in the region of 2,Ø. This value is slightly higher than expected. The following factors possibly contributed to a slightly higher value, as well as the scattering of the results with faster flows:

(i) Three dimensional effects closer to the side panels;

(ii) Vibration of the cylinder, as indicated by slight fluctuations in readings on the "lift" and "drag" balances. (According to Blevins (1977, p.19) "cylinder vibration, at or near the vortex shedding frequency, can increase the drag force.").

6.4 Lift Coefficient

The lift coefficient showed a substantial decrease, as the G/D ratio increased.

Lift coefficients C_L/a_1 compared fairly well with values determined by means of the pressure rig method, for corresponding test runs. A comparison of these values is graphically represented in Fig. 6.8. The reason for the curvilinear relationship for G/D = Ø, with the indirect method, is discussed in Section 5.5.2.

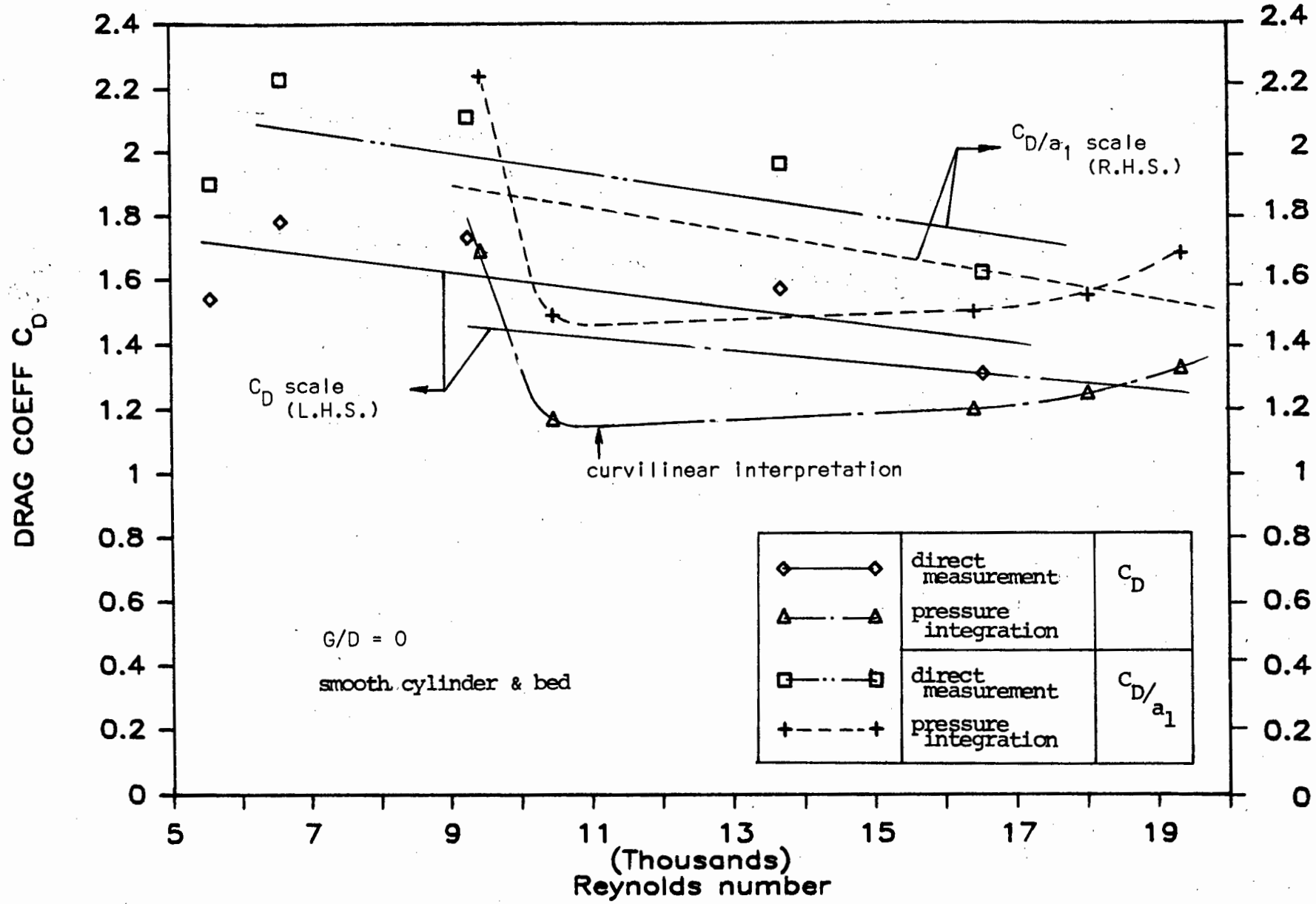

FIG. 6.3: DRAG COEFFICIENT BY DIRECT MEASUREMENT AND PRESSURE INTEGRATION; 50 mm CYLINDER, $G/_D = 0$

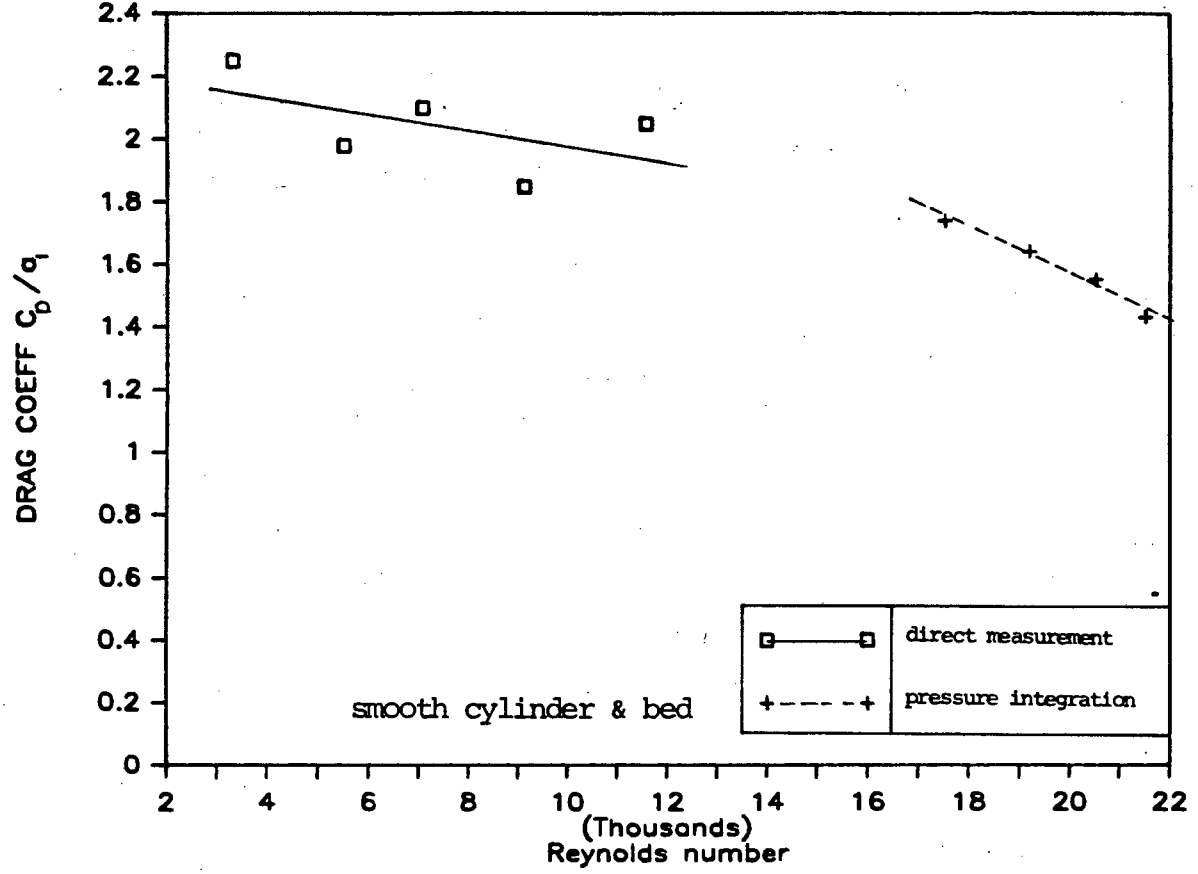

FIG. 6.4: DRAG COEFFICIENT BY DIRECT MEASUREMENT AND PRESSURE INTEGRATION; 50 mm CYLINDER, $G/_D$ = 0,2

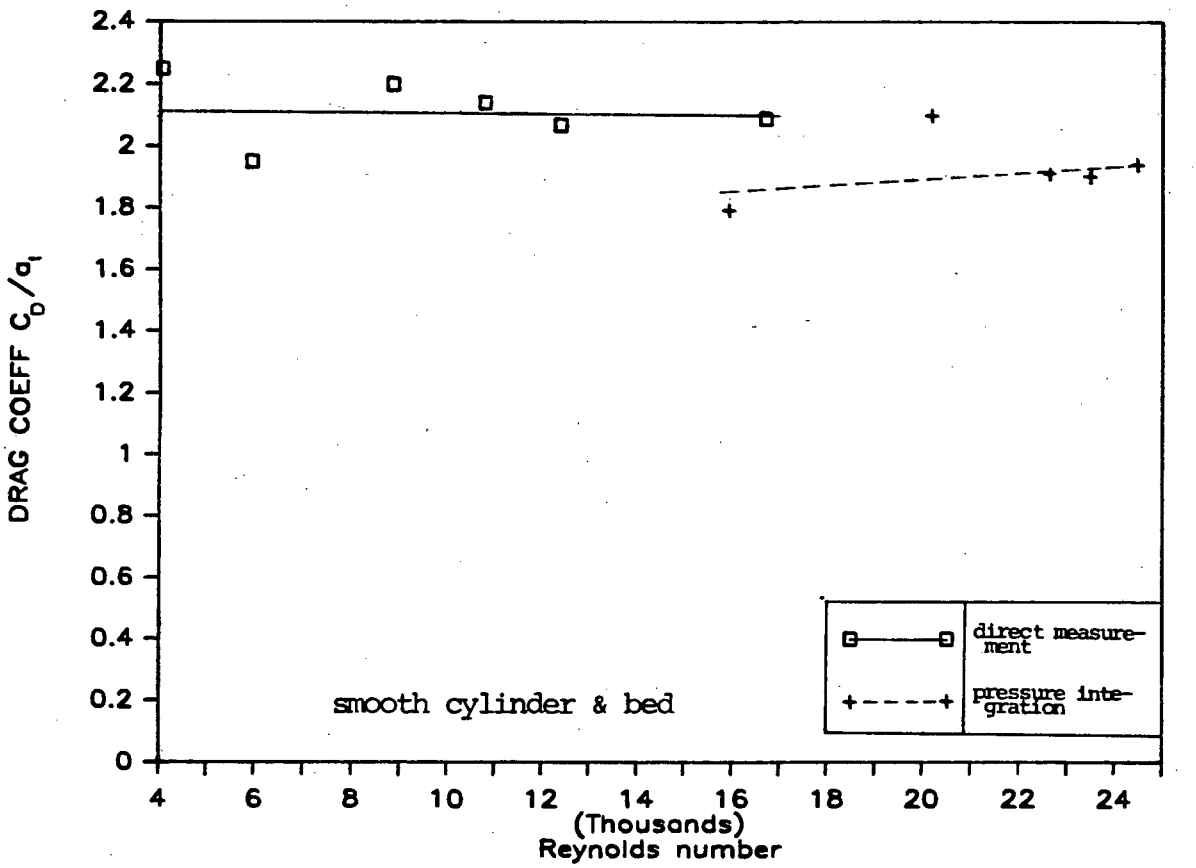

FIG. 6.5: DRAG COEFFICIENT BY DIRECT MEASUREMENT AND PRESSURE INTEGRATION; 50 mm CYLINDER, $G/_D$ = 0,6

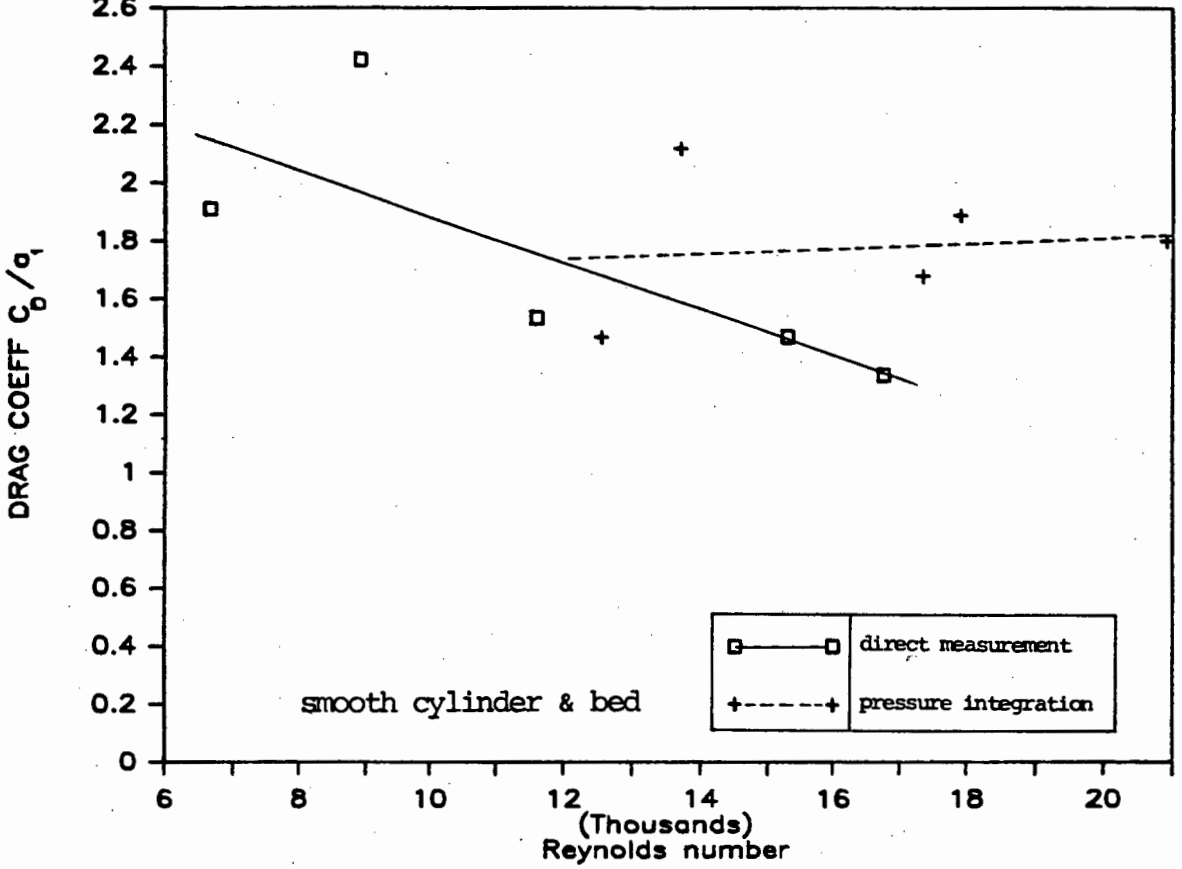

FIG. 6.6: DRAG COEFFICIENT BY DIRECT MEASUREMENT AND PRESSURE INTEGRATION; 50 mm CYLINDER, $G/_D$ = 1,2

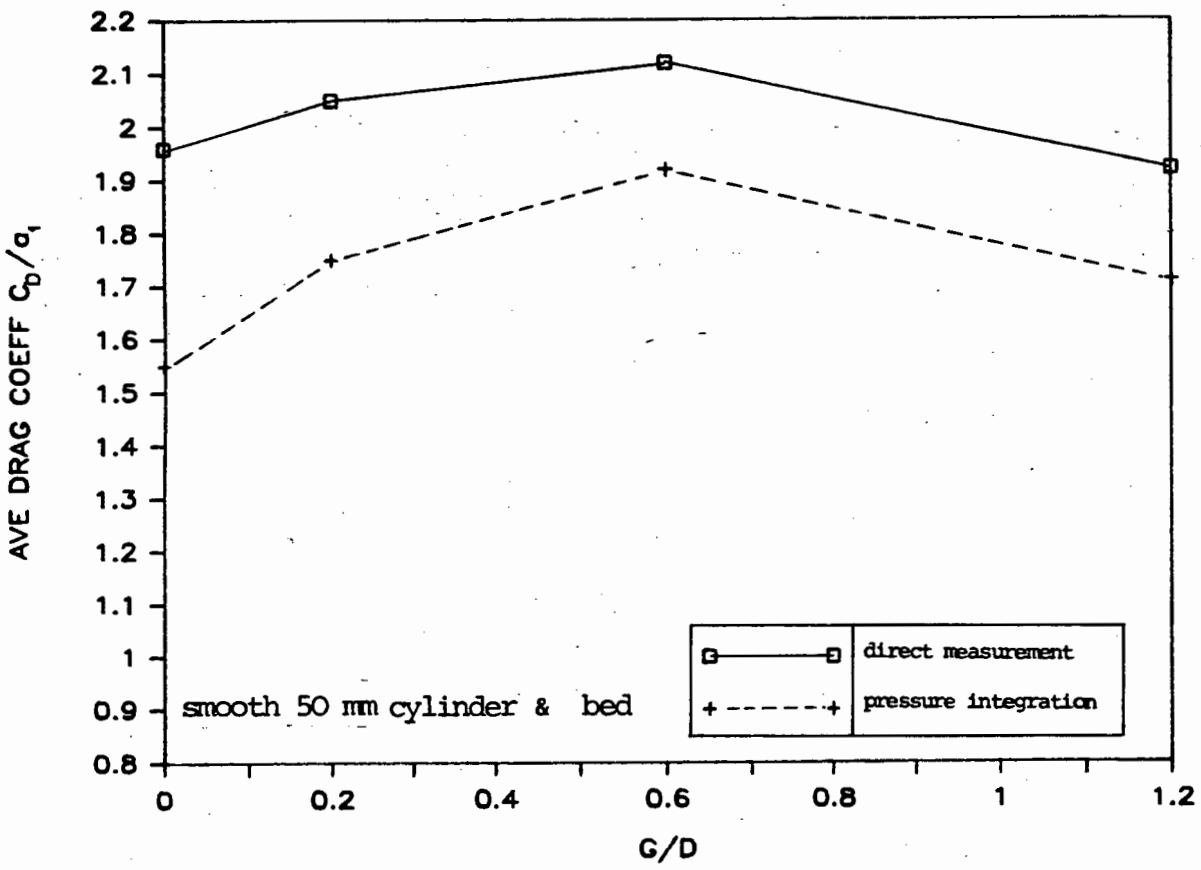

FIG. 6.7: AVERAGE DRAG COEFFICIENTS DUE TO DIRECT MEASUREMENT AND PRESSURE INTEGRATION

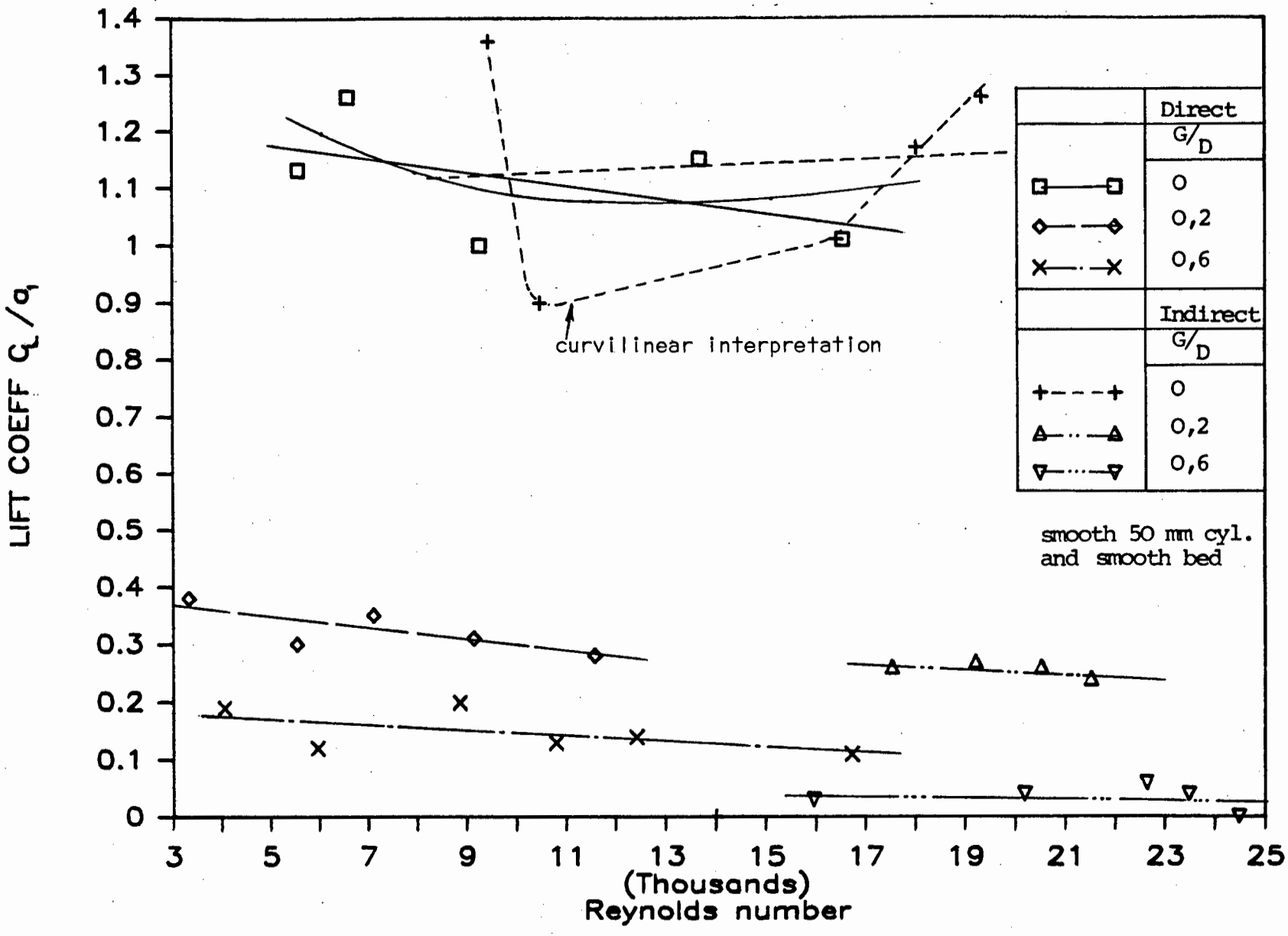

FIG. 6.8: LIFT COEFFICIENTS BY DIRECT MEASUREMENT AND PRESSURE INTEGRATION; 50 mm CYLINDER

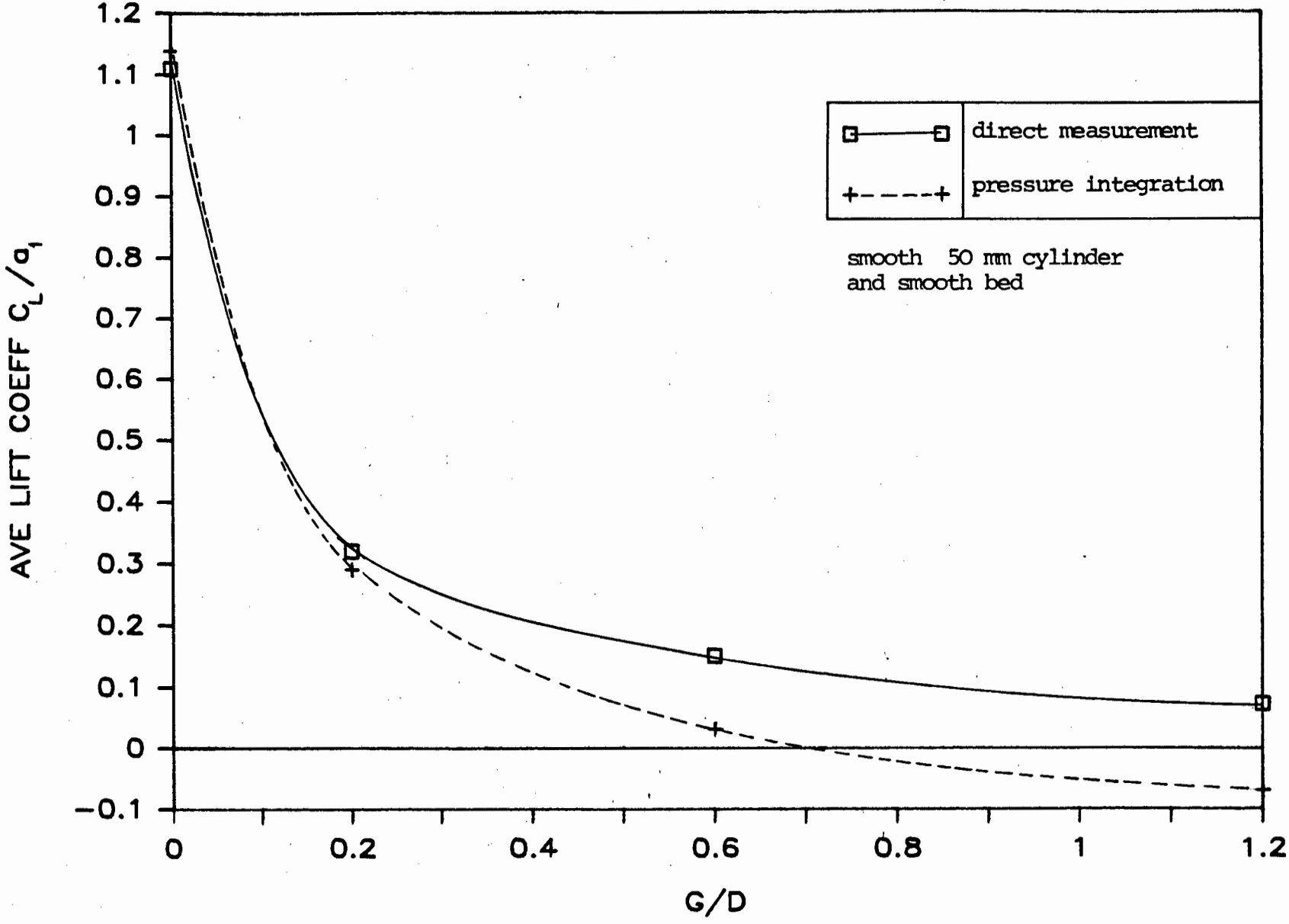

FIG. 6.9: AVERAGE LIFT COEFFICIENTS DUE TO DIRECT MEASUREMENT AND PRESSURE INTEGRATION

Average lift coefficients are also compared in Fig. 6.9. Although the force rig values were obtained with slower flows, the correlation is fairly good.

The "lift" balance was more difficult to read than the "drag" balance at faster flows, due to continuous fluctuation of the readings. The maximum range of "lift" balance readings was about one gram, or a deviation of Ø,42%, which is regarded as satisfactory.

6.5 General Comments

Although the drag coefficients generated by the force rig method, were generally higher than anticipated, the results compared well to the pressure rig values, considering the influence of vibrations and three dimensional flow near the side walls. Further, the murkiness of and the suspended particles in the water, were more noticeable than when the pressure rig tests were performed.

To minimise vibrations of the rig and subsequent fluctuations in readings, the following measures had to be taken:

(i) The water in the flume had to be at least five cylinder diameters deep, to limit cylinder blockage. It was estimated that a drawdown of 3 mm could influence the force coefficients by as much as 1Ø%.

(ii) The velocity measured at the elevation of the cylinder centre, had to be limited to approximately Ø,3 m/s (R_e = 15 ØØØ) - the rig started to vibrate visibly beyond this flow velocity, which in turn resulted in continuous fluctuations of the readings.

(iii) The aluminium frame had to be stabilised by loading it very carefully, directly above the two vertical arms.

Procedure (iii) required much patience to perform, as even the slightest contact with the rig or the flume affected the readings on the balances.

6.6 Conclusions

(i) The force rig method indicated that the method, as described and applied here, is based on a simple yet novel technique.

(ii) The various measures taken and adjustments made (particularly stabilising the frame) to get the apparatus ready for live readings, was of paramount importance for the successful operation of the experimental set-up. It had to be done for every test run and took almost as long as the test run to perform.

(iii) Should the factors which possibly could have influenced the results and the lower Reynolds numbers be taken into account, the results generated by the force rig method (direct measurement) compare favourably with those obtained from the pressure rig method (pressure integration). Further, a comparison between the two methods revealed the reliability of particularly the pressure rig readings.

CHAPTER 7 - FLOW VISUALISATION

Flow visualisation experiments were performed to investigate the flow around the cylinder, particularly the identification of the separation points and the vortex shedding effect.

7.1 Experimental Procedure

The pressure rig arrangement, described in Chapter 3, was utilised for the flow visualisation experiments. The smooth 50 mm diameter cylinder was assembled in the flume. The hollow brass rod, passing through the perspex wall panel of the flume, was coupled to a beaker using plastic tubing. The beaker was supported on top of the flume and filled with dye. The dye was ejected from the single pressure tapping of the cylinder, by means of gravitation. The flow of dye was regulated by means of a laboratory clamp.

The turbidity of the water, supplied by the water tower, did not permit photography through water. As filtering of the water was not successful, the only alternative was to use the municipal drinking water supply, available in the laboratory. Unfortunately the maximum flow attainable with this supply, was only 0,005 m^3/sec. With a water depth of 22,5 cm in the flume, this flow corresponded to a Reynolds number of 2 000. At higher velocities, free stream turbulence prevented flow visualisation.

Trial runs were done with potassium permanganate, as the dye. Although very colourful, the purple dye stream diffused fairly quickly behind the cylinder. It was therefore decided to use Process Black artists' ink (Manufacturer: Winsor and Newton, London) as dye. It proved to be very successful.

The opposite perspex panel of the flume, was covered with white drawing paper on the outside. The paper was illuminated from behind with a single 200 W photographic lamp. A second 200 W lamp

provided diffused illumination of the region behind the cylinder, from above the water. The dye streams were photographed, using 35 mm still photography (1/30 second, ASA 400).

Tests with five cylinder positions, in relation to the bed, were undertaken: (i) G/D = 0 (on bottom); (ii) G/D = 0,1 (5 mm clearance); (iii) G/D = 0,2 (10 mm clearance); (iv) G/D = 0,6 (30 mm clearance); (v) G/D = 1,2 (60 mm clearance)

7.2 Results and Discussion

A photographic record of the flow around the cylinder is provided from Figs. 7.1 to 7.5. As far as could be ascertained, the only previous flow visualisations with a cylinder close to a boundary, were done by Taneda (1965), Littlejohns (1974), Bearman and Zdravkovich (1978) and Grass et al (1984). Taneda's work was very useful, but was unfortunately carried out at a Reynolds of only 170. Littlejohns only considered G/D = 0 cases and used a water channel in the Reynolds number range 5×10^5 to 5×10^6, while Bearman and Zdravkovich used a smoke tunnel at a Reynolds number of 25 000 and a span-diameter ratio (L/D) of only 1. Grass et al visualised the flow field around a cylinder in a water flume, in the Reynolds number range 2 000 to 4 000, using a hydrogen bubble flow tracer method.

7.2.1 Cylinder Resting on Bottom (G/D = 0)

From a photographic viewpoint, flows generating a Reynolds number of 1 850 (velocity at cylinder centre = 0,037 m/s) gave the best results. Beyond this value, the vortices diminished in size and formed, as well as dispersed, very rapidly indeed.

The separation point was observed as being located just beyond the shoulder of the cylinder (Fig. 7.1(a)), approximately at 100° from the front centre point. This compares very well with the measurements from the pressure profiles, indicated in Table 5.6.

The shedding of vortices, in different stages of development, is illustrated in Figs. 7.1(b) and (c). In Fig. 7.1(b) it is noticed how the distance between shed vortices increase as they move downstream. Unfortunately the dye diffused at a distance of approximately three cylinder diameters downstream of the cylinder.

Fig. 7.1(d) illustrates a faster flow (R_e = 2 100) and four vortices can be seen. They were rapidly shed and disappeared as quickly.

7.2.2 G/D = 0,1 (clearance = 5 mm)

Very interesting tests were undertaken at R_e = 1 900. From Fig. 7.2(a) it appears as if the upper separation point is located just beyond the top of the cylinder ($\theta > 90^\circ$).

No vortex formation close to the bed, behind the cylinder, can be observed in Fig. 7.2(b). The dye stream is drawn into the wake zone and disperses in the vortex shedding region, behind the upper shoulder of the cylinder. Taneda (1965) also observed only a single row of vortices at G/D = 0,1 (but a Reynolds number of 170).

It was however interesting to notice that vortices were in fact shed in the region close to the bed, at a Reynolds number of 2 500 (Fig. 7.2(c)). At yet faster flows, the dye stream dispersed too soon to observe anything meaningful.

7.2.3 G/D = 0,2 (clearance = 10 mm)

Tests were performed at R_e = 1 900. The upper separation point of the boundary layer, along the cylinder surface, is clearly visible in Fig. 7.3(a); it is located at the cylinder shoulder (separation angle = 90°). From Fig. 7.3(b) it is clear that the separation closer to the flume bed, occurs slightly downstream from

the lower shoulder. These results are also equivalent to those obtained from pressure profile measurements (Table 5.6).

The vortices shed from the lower side of the cylinder are smaller than those formed on the upper side. This is due to the proximity of the bed, which imposes spatially constrained conditions on the flow, resulting in limited vortex growth in the lower wake zone.

The downstream effect on a vortex shed from the upper side of the cylinder, is illustrated in Fig 7.3(c). The result is due to the rotational motion of the vortex. Soon after the photograph was taken, the vortex dispersed.

7.2.4 G/D = Ø,6 (clearance = 3Ø mm)

Experiments were undertaken at R_e = 2 ØØØ. The upper and lower separation points (Figs. 7.4(a) and (b)) were located at the respective cylinder shoulders.

The development of vortices closer to the bed is very clearly illustrated in Fig. 7.4(b). The formation of alternating vortices, from the upper and lower regions behind the cylinder, is shown in Fig. 7.4(c). This phenomenon was obtained by ejecting dye into the approaching stream, close to the two separation points.

7.2.5 G/D = 1,2 (clearance = 6Ø mm)

Tests were performed at R_e = 2 ØØØ. From the various illustrations (Figs. 7.5(a) to (d)) it is clear that the flow situation almost replicates symmetrical flow.

As in the previous three cases above, the upper and lower separation angles correspond to previous geometrical measurements from pressure profiles. In this case, the separation angles are 9Ø° and 27Ø° (Figs. 7.5(a) and (b)). Vortex formation and movement downstream are illustrated in Figs. 7.5(b) to (d).

7.2.6 Vortex Shedding and Development

From the flow visualisation tests it was clear that immediately downstream of the cylinder there is a formation region where vortices are shed. The vortices then develop a regular pattern. At a distance of three to four cylinder diameters downstream of the cylinder, for $G/D = 0$, the vortices become unstable and disperse due to turbulence. Further away from the bottom, at $G/D = 0,6$ and 1,2, the stable region appeared to be slightly broader.

7.3 Conclusions

Considerable time was spent on observing various flow phenomena during the flow visualisation tests. The photographic record only represents a sample of these observations. The main conclusions are mentioned below.

(i) The experimental technique employed proved to be very effective.

(ii) The separation points identified from the photographic records, are equivalent to those obtained from geometrical means.

(iii) Although flow visualisation tests at a Reynolds number of about 2 000 could only be performed, the results were in agreement with tests undertaken at other Reynolds numbers in the subcritical regime, viz. 170 (Taneda, 1965), 2 000 to 4 000 (Grass et al (1984)), and 25 000 (Bearman and Zdravkovich, 1978).

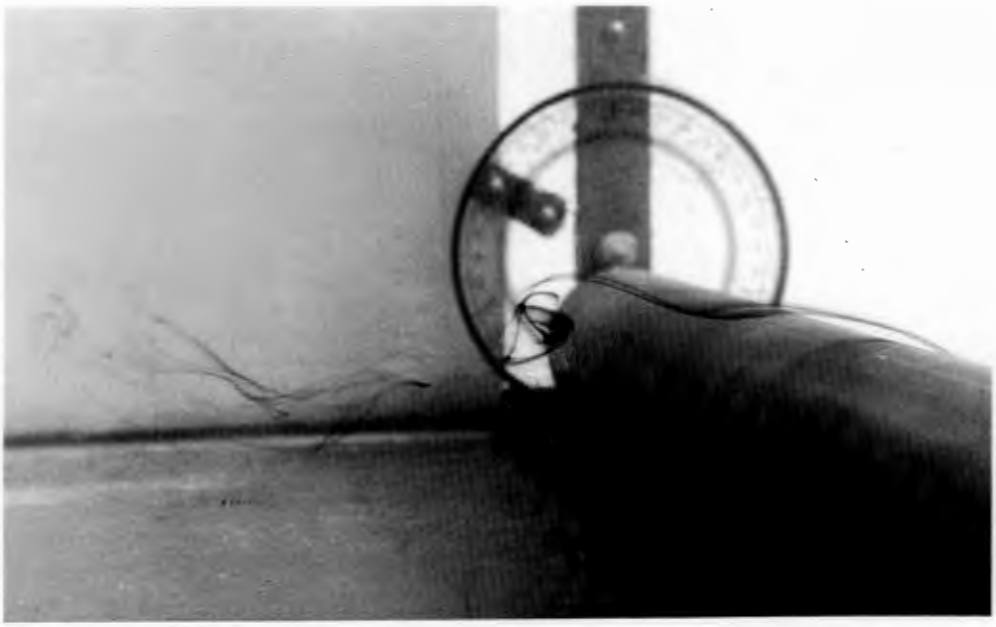

(a)

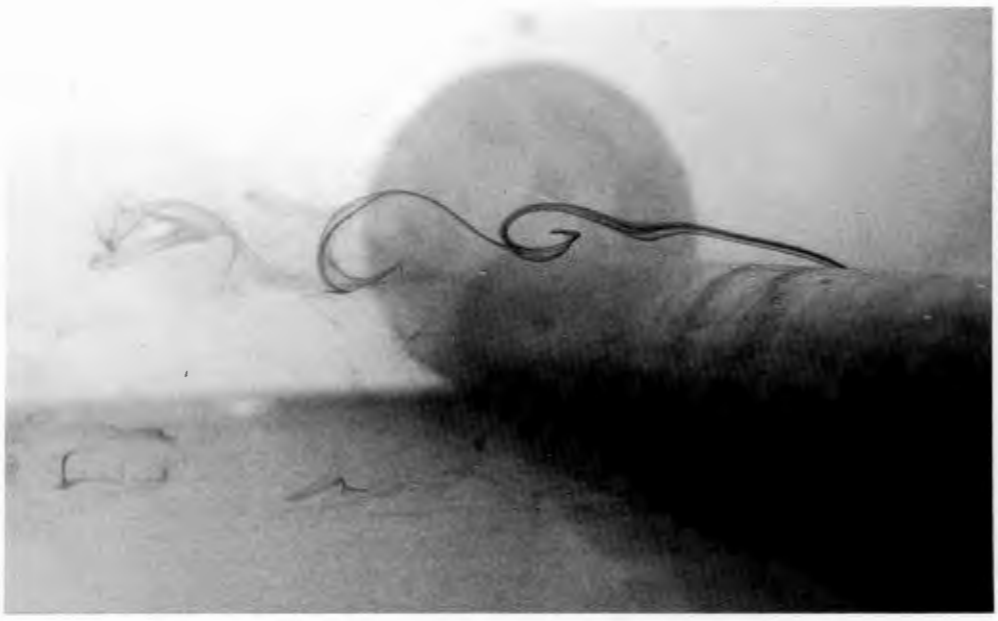

(b)

FIG. 7.1: FLOW VISUALISATION; G/D = 0; R_e = 1 850

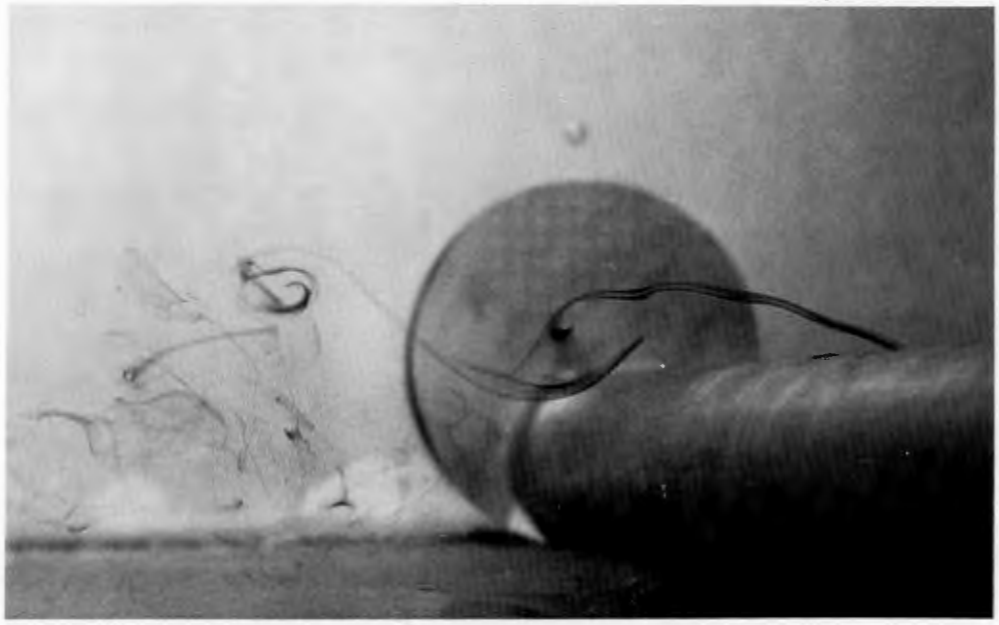

(c) R_e = 1 850

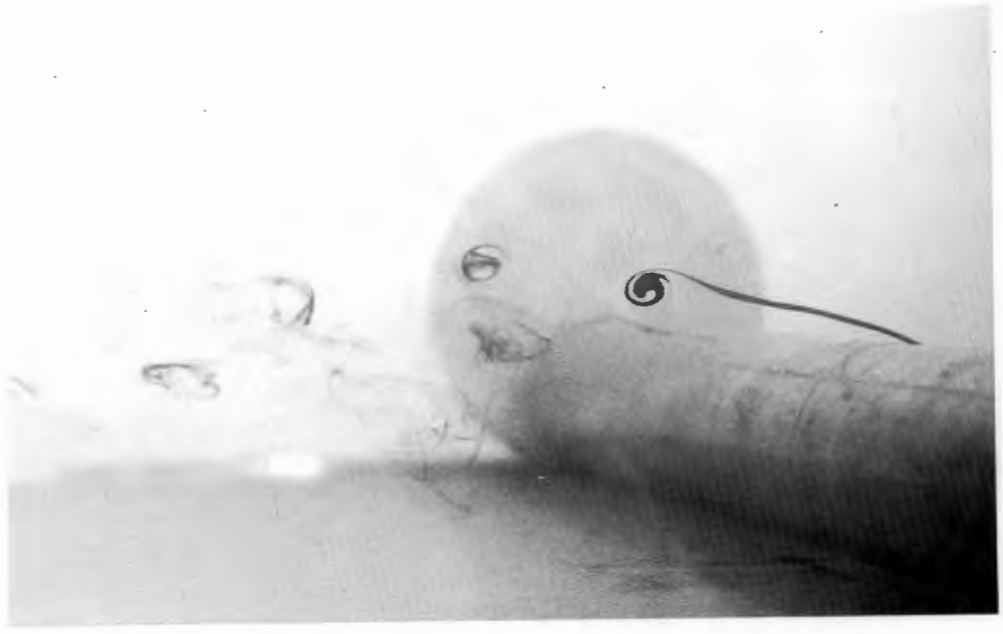

(d) R_e = 2 100

FIG. 7.1: FLOW VISUALISATION; $G/_D$ = 0

(a)

R_e = 1 900

(b)

R_e = 1 900

(c)

R_e = 2 500

FIG. 7.2: FLOW VISUALISATION; $G/_D$ = 0,1

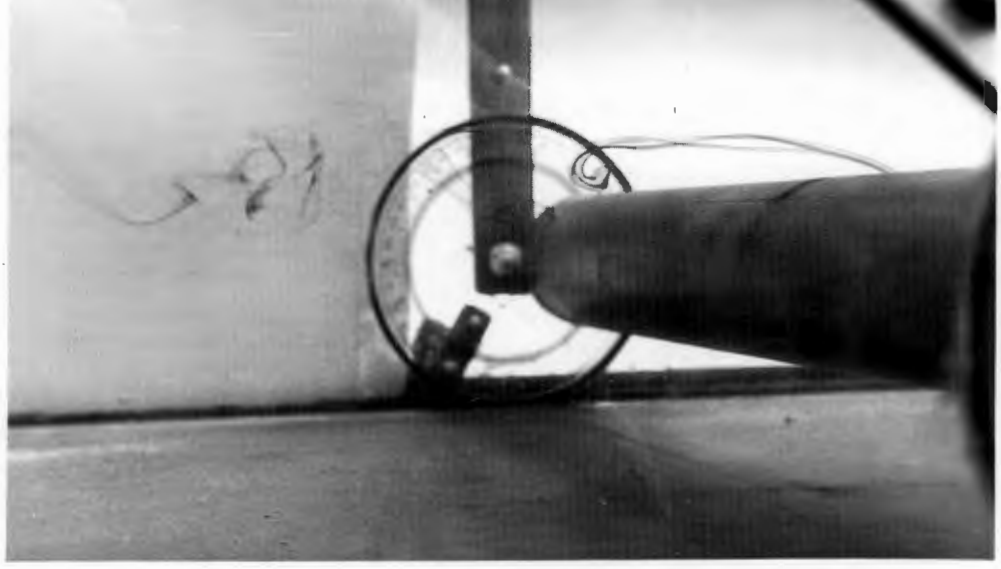

(a)

(b)

(c)

FIG. 7.4: FLOW VISUALISATION; $G/_D = 0,6$; $R_e = 2\ 000$

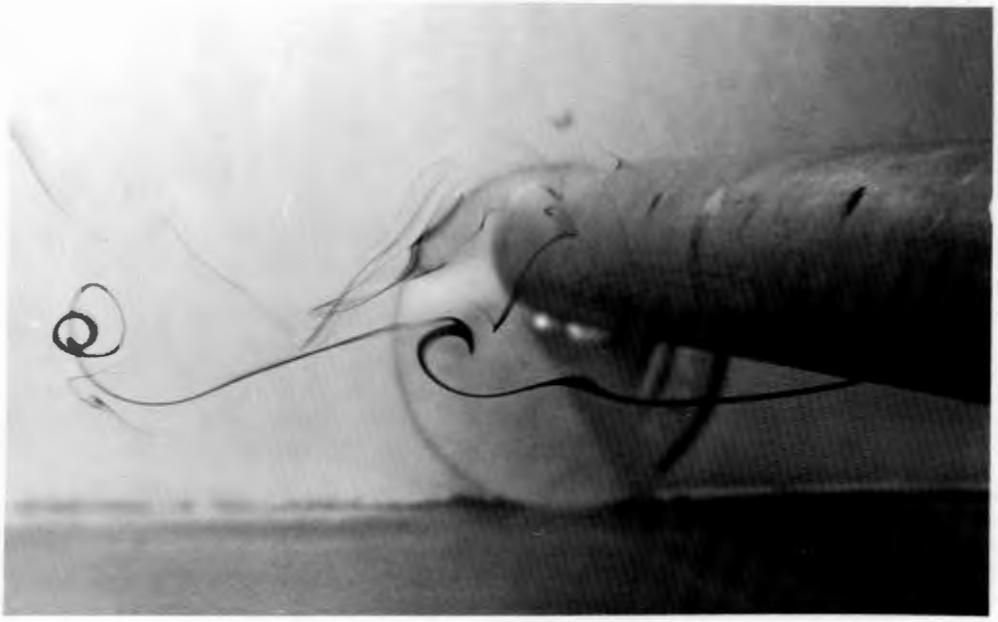

(a)

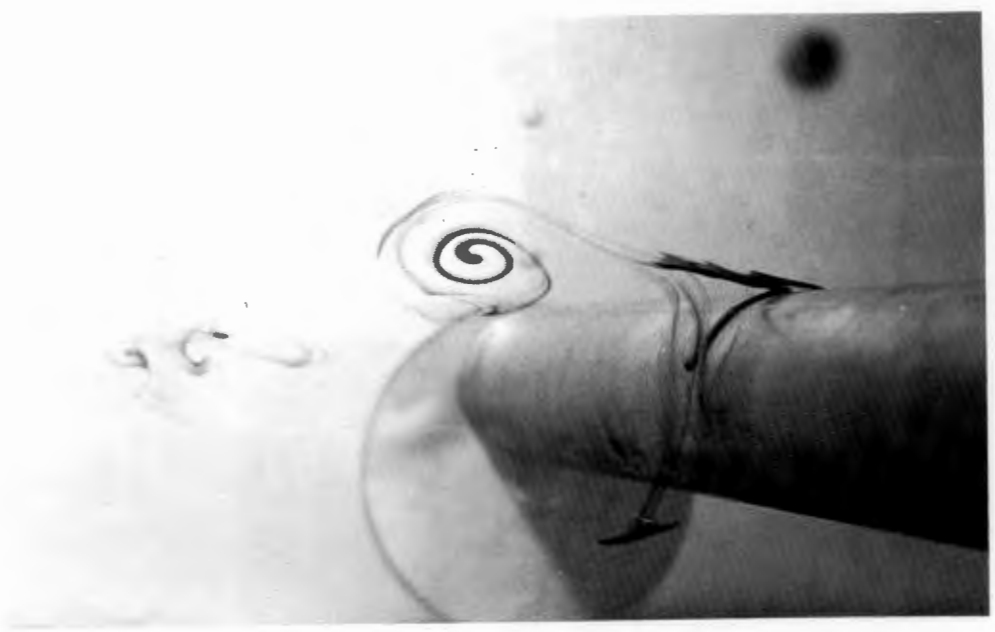

(b)

FIG. 7.5: FLOW VISUALISATION; $G/_D = 1,2$; $R_e = 2\ 000$

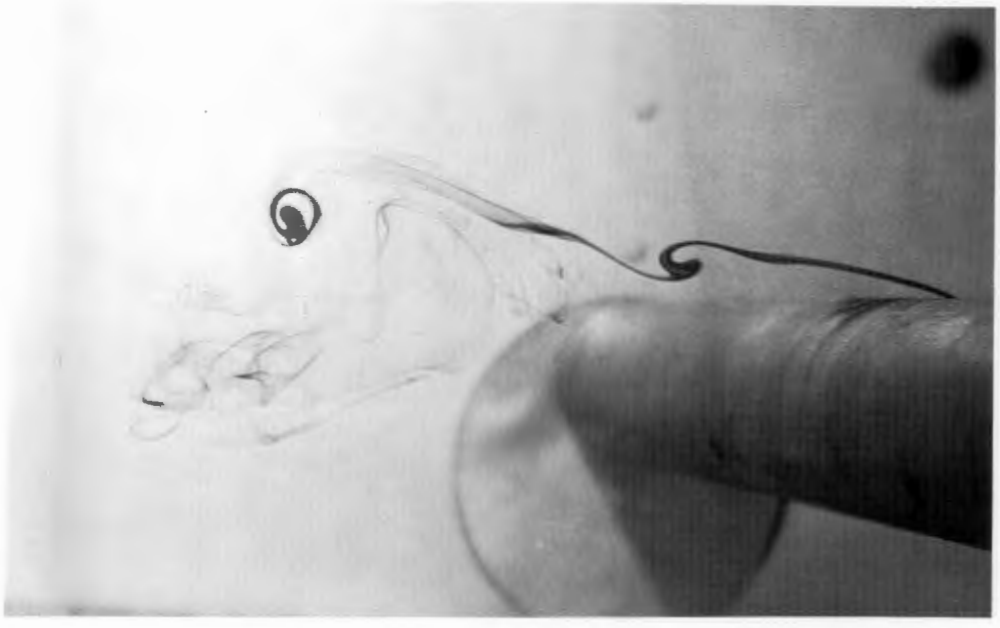

(c)

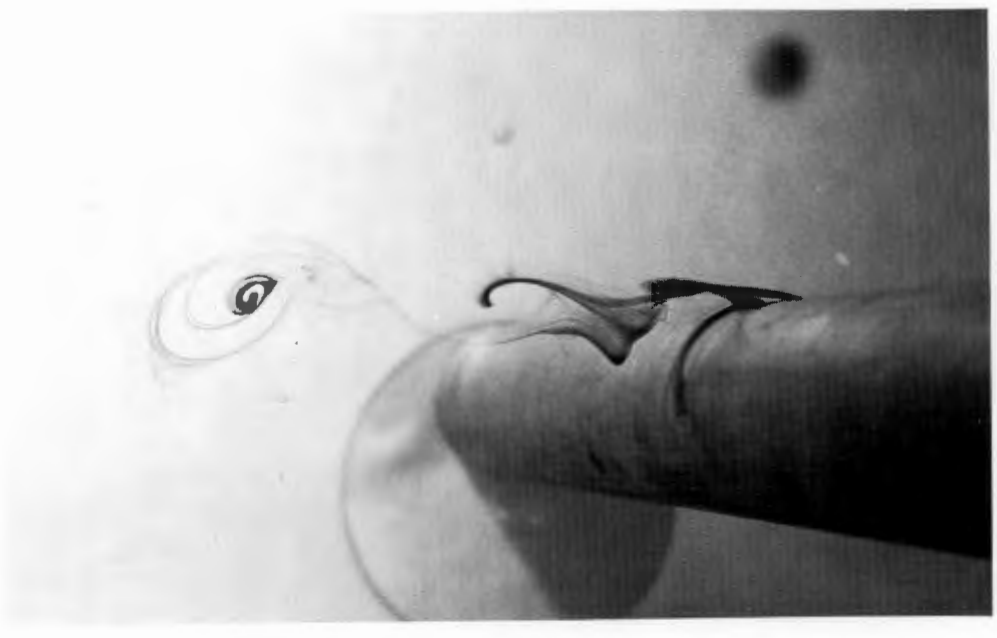

(d)

FIG. 7.5: FLOW VISUALISATION; $G/_D = 1,2; R_e = 2\ 000$

CHAPTER 8 - COMPARISON WITH OTHER EXPERIMENTAL RESEARCH WORK

8.1 Introduction

A number of measurements on lift and drag forces had previously been done on cylinders placed near a boundary. Most of this work was by means of direct measurement, using strain gauges. Very few investigators used the pressure integration method: Beattie et al (1971) were amongst the few researchers who utilised a water medium. All the investigators worked either in a different Reynolds number range, or used another experimental technique. Further, most of the published work, relates to tests in an air medium.

8.2 Pressure Distributions

Beattie et al (1971) provide no information on the pressure distributions on which they based their force calculations.

Bearman and Zdravkovich (1978) used a wind tunnel and measured distributions of mean pressure around a cylinder, at a Reynolds number of 48 000. Pressures were presented non-dimensionally in the form of the pressure coefficient C_p, where

$$C_p = \frac{P_\theta - P_{static}}{\frac{1}{2} \rho U^2} \qquad (8.1)$$

P_θ is the pressure at angle θ from the front centre of the cylinder, P_{static} is the static pressure taken at a reference point and U the reference velocity. Pressure distributions measured by them for two G/D ratios, are indicated in Fig. 8.1; pressure coefficients along the base of the wind tunnel are also shown.

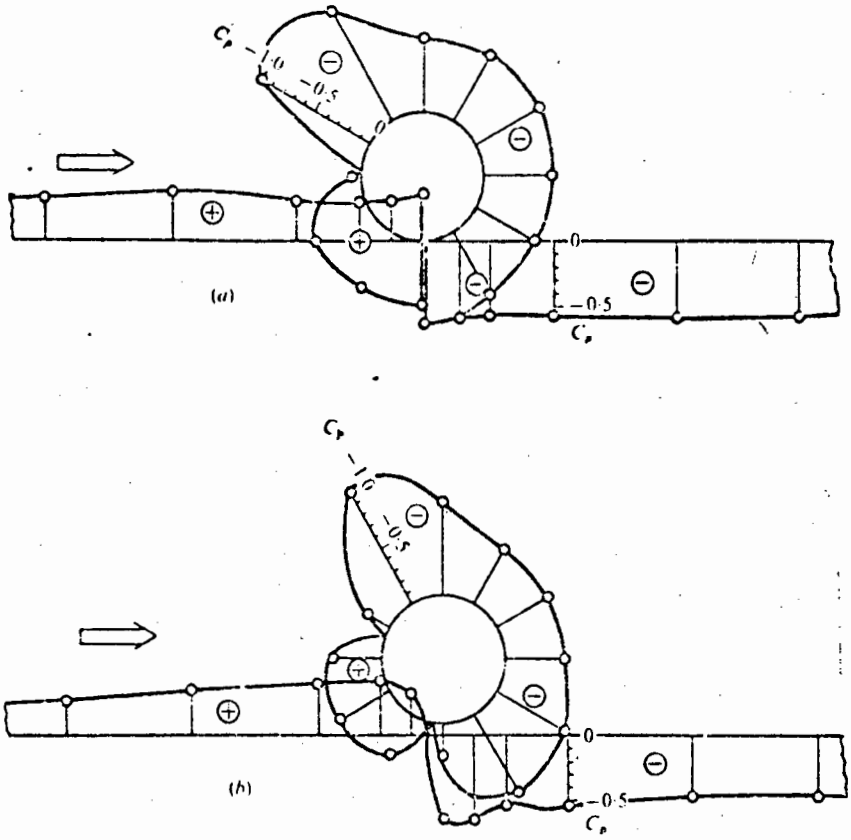

Figure 8.1: Pressure distributions around a cylinder.
a) G/D = 0 ; b) G/D = 0,1 (Bearman and Zdravkovich, 1978)

The above mentioned two pressure distributions (Bearman and Zdravkovich, 1978) are graphically compared to results (test runs 15 and 20 respectively) obtained in the present investigation in Figs. 8.2 and 8.3. For the present study, the pressure coefficients were calculated using Eq. (5.14), i.e. with V_{eff} as the reference velocity.

Although pressure distributions at different Reynolds numbers, viz. 48 000 (Bearman and Zdravkovich) and 20 000 in air and water mediums respectively are compared, similar results are observed regarding the locations of the minimum pressure points and the wake

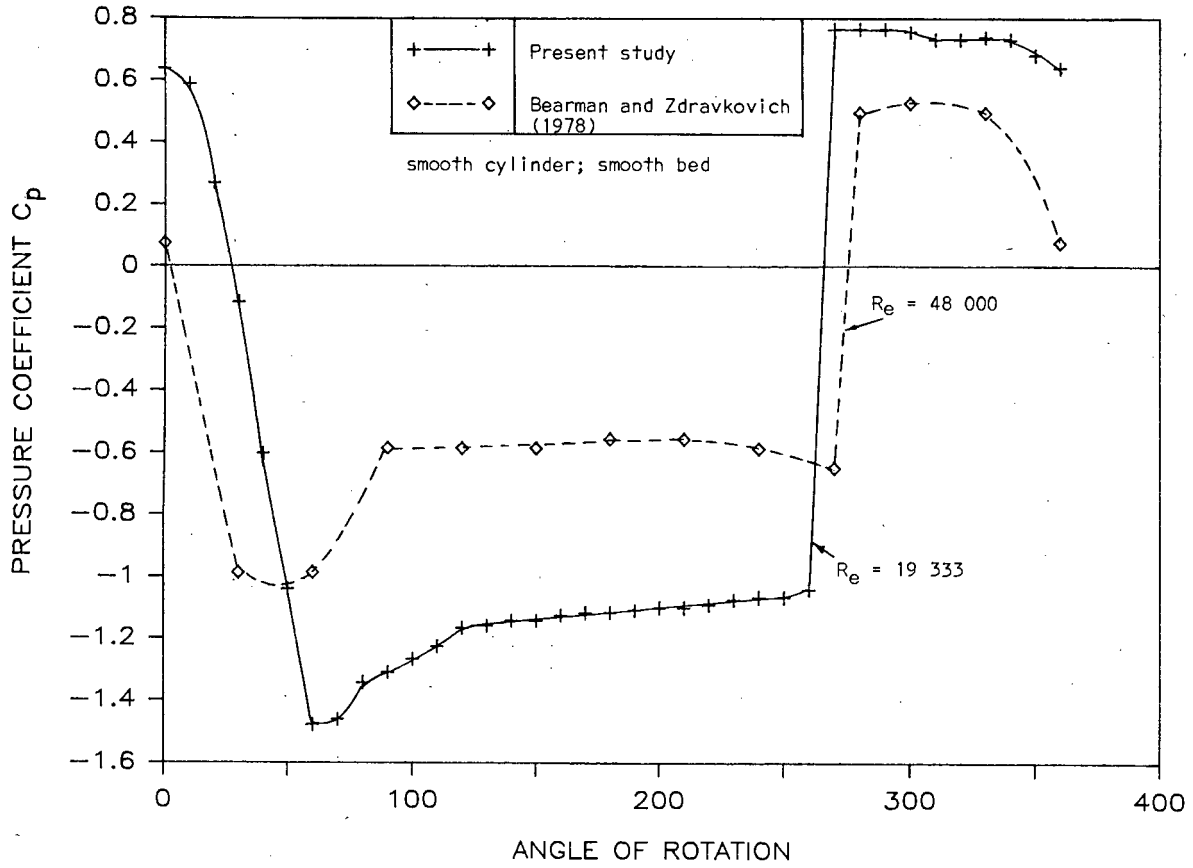

FIG. 8.2: PRESSURE DISTRIBUTION AT G/D = 0; COMPARISON TO BEARMAN AND ZDRAVKOVICH (1978)

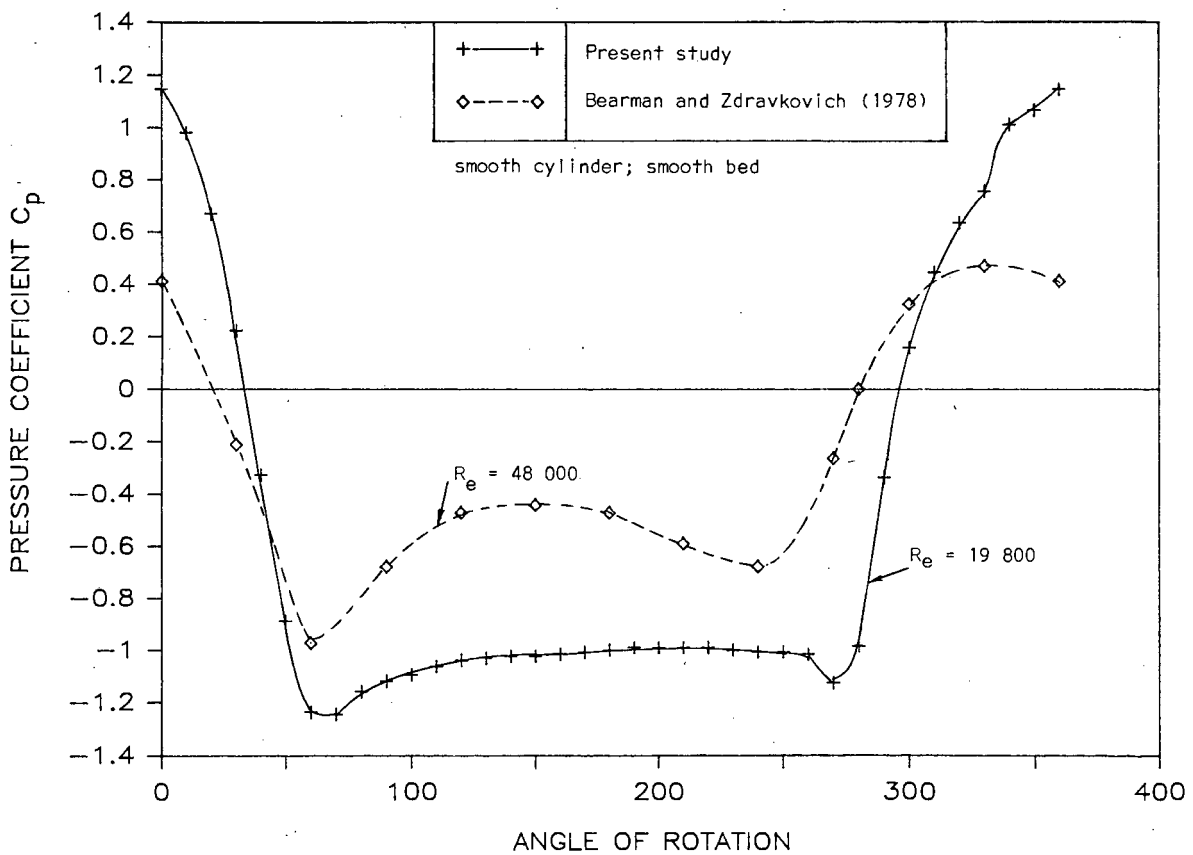

FIG. 8.3: PRESSURE DISTRIBUTION AT G/D = 0,1; COMPARISON TO BEARMAN AND ZDRAVKOVICH (1978)

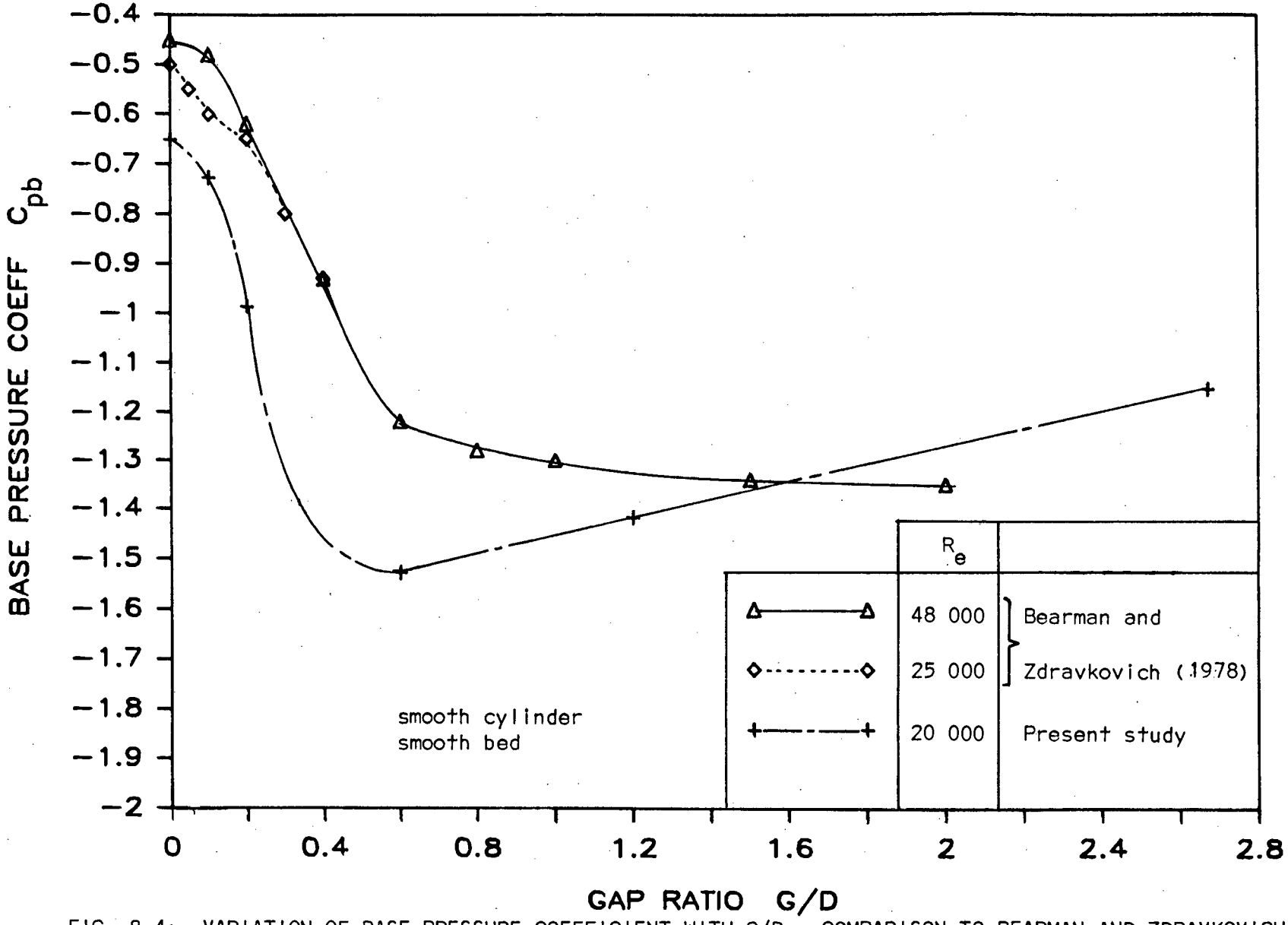

FIG. 8.4: VARIATION OF BASE PRESSURE COEFFICIENT WITH G/D: COMPARISON TO BEARMAN AND ZDRAVKOVICH (1978)

zone pressures. Near the bottom, i.e. at small G/D ratios, the pressure distributions showed a displacement of the front stagnation point, towards the bottom (refer to Table 5.6).

Comparisons between further results of Bearman and Zdravkovich and those obtained from the present work also indicate that a symmetrical flow situation, characterised by the pressure distribution assuming a symmetrical shape about the front centre of the cylinder, is approached at G/D ratios beyond one.

The variation of the base pressure coefficient C_{pb} with the gap ratio G/D, is compared to results obtained by Bearman and Zdravkovich (1978) in Fig. 8.4: The correlation is fairly good.

8.3 Force Coefficients based on Depth Parameter a_2

Littlejohns (1974), in investigating the dependency of the force coefficients on the depth of water H, defined a second correlation factor a_2 as follows:

$$a_2 = \frac{D}{H} \tag{8.2}$$

Force coefficient values based on a_2 were calculated for the 30 and 50 mm cylinders, both smooth on a smooth bed, and are compared to those of Littlejohns (who measured forces directly) in Table 8.1 below, and Figs. 8.5 and 8.6.

Littlejohns (1974)			Present Work				
R_e	Coefficients		D (mm)	R_e	Para-meter	Coefficients	
	C_D/a_2	C_L/a_2			a_2	C_D/a_2	C_L/a_2
100 000	8,0	10,2	50	9 447	0,244	6,917	4,208
115 000	8,5	10,8		10 470	0,215	5,438	3,266
130 000	8,8	11,3		16 411	0,199	6,018	4,058
				18 018	0,190	6,602	4,960
				19 333	0,203	6,570	4,959
			30	8 670	0,135	9,597	5,724
				11 148	0,156	9,434	5,636
				12 713	0,113	9,273	6,325
				15 812	0,106	11,000	6,226

Table 8.1: Force coefficients based on depth parameter a_2; comparison between results of Littlejohns (1974) and the present study.

Both Figs. 8.5 and 8.6 do not correlate particularly well with Littlejohns' force coefficients, should his results be extrapolated. The values for the 30 mm cylinder are obviously higher than those for the 50 mm cylinder, due to a smaller blocking ratio. The amount of scatter, particularly in the drag coefficients is exaggerated with the introduction of the depth parameter a_2. However, the graphical plots show that the lift and drag coefficients are influenced by the depth of water over the cylinder.

8.4 Drag and Lift Coefficients

All drag and lift coefficients dealt with here, include the depth

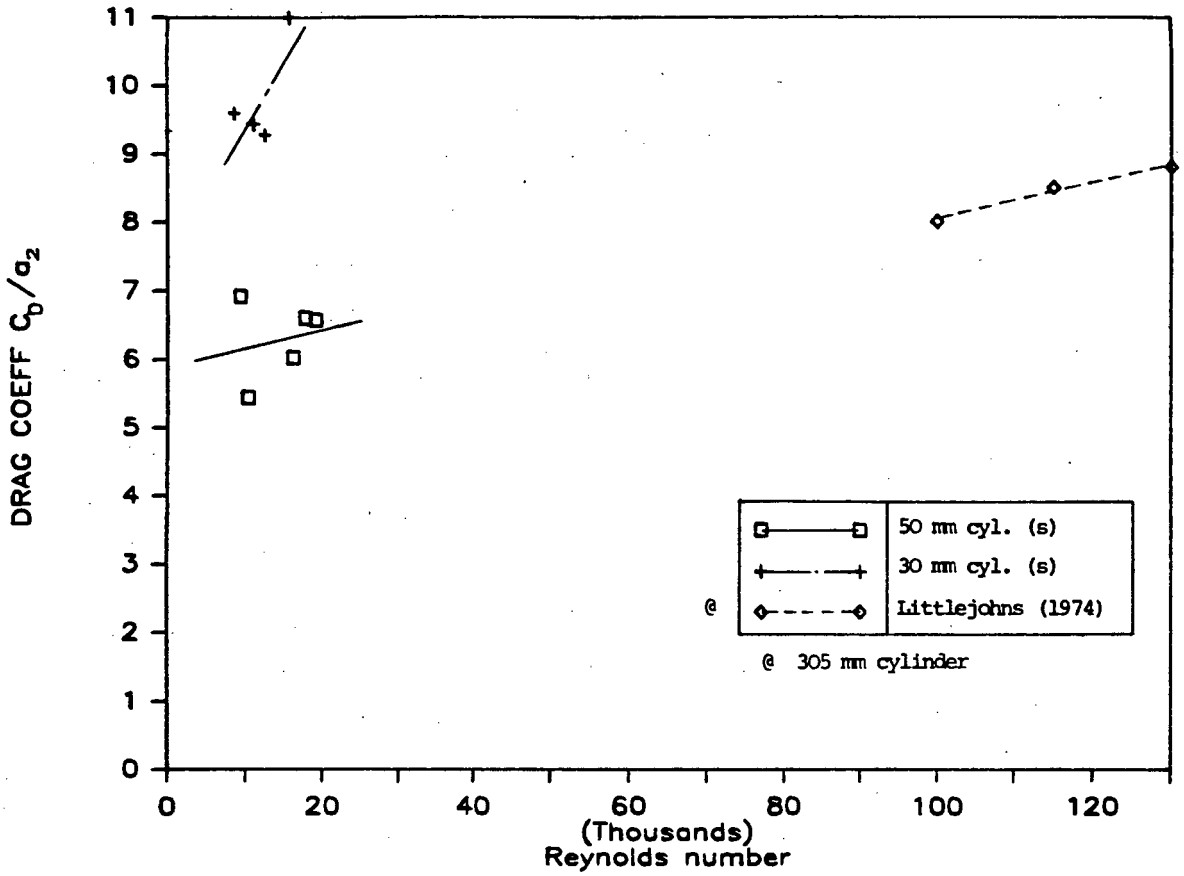

FIG. 8.5: COMPARISON BETWEEN DRAG COEFFICIENT C_D/a_2 , DETERMINED BY LITTLEJOHNS (1974) AND THE PRESENT STUDY; $G/D = 0$

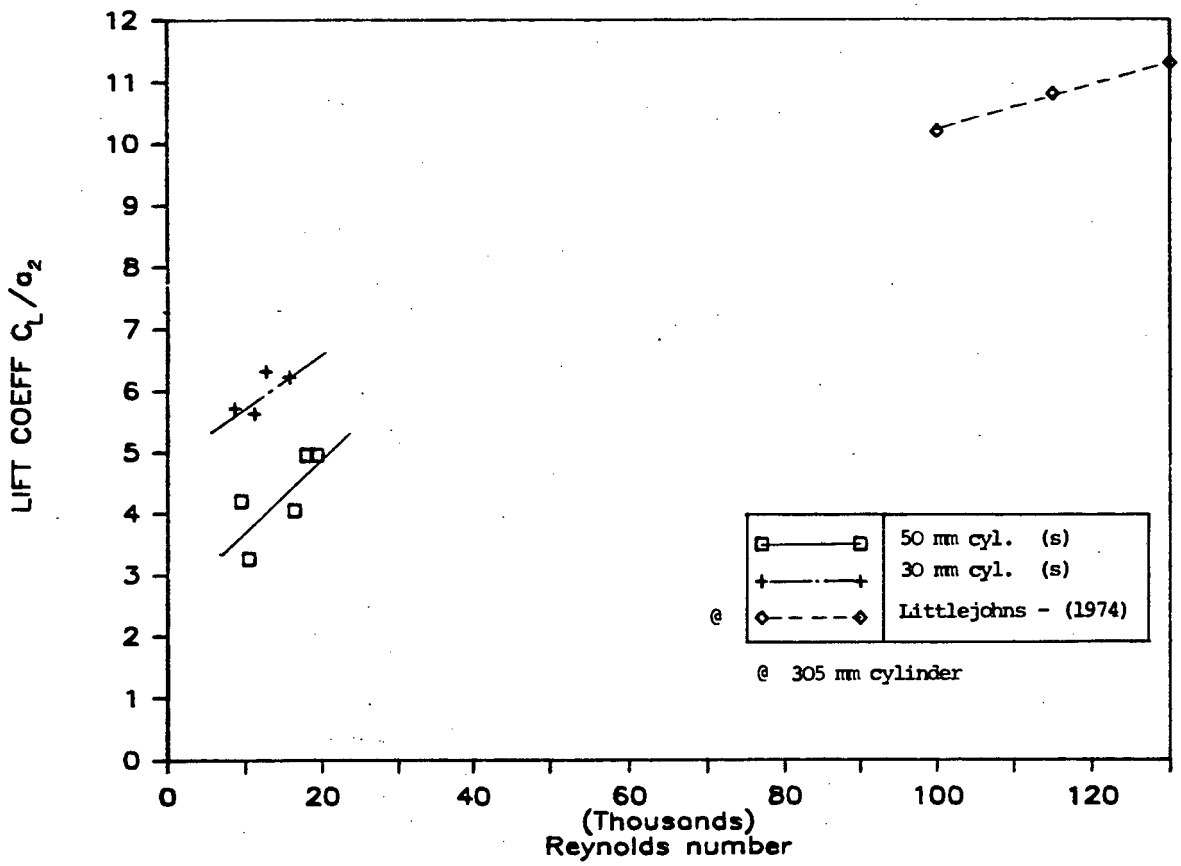

FIG. 8.6: COMPARISON BETWEEN LIFT COEFFICIENT C_L/a_2 , DETERMINED BY LITTLEJOHNS (1974) AND THE PRESENT STUDY; $G/D = 0$

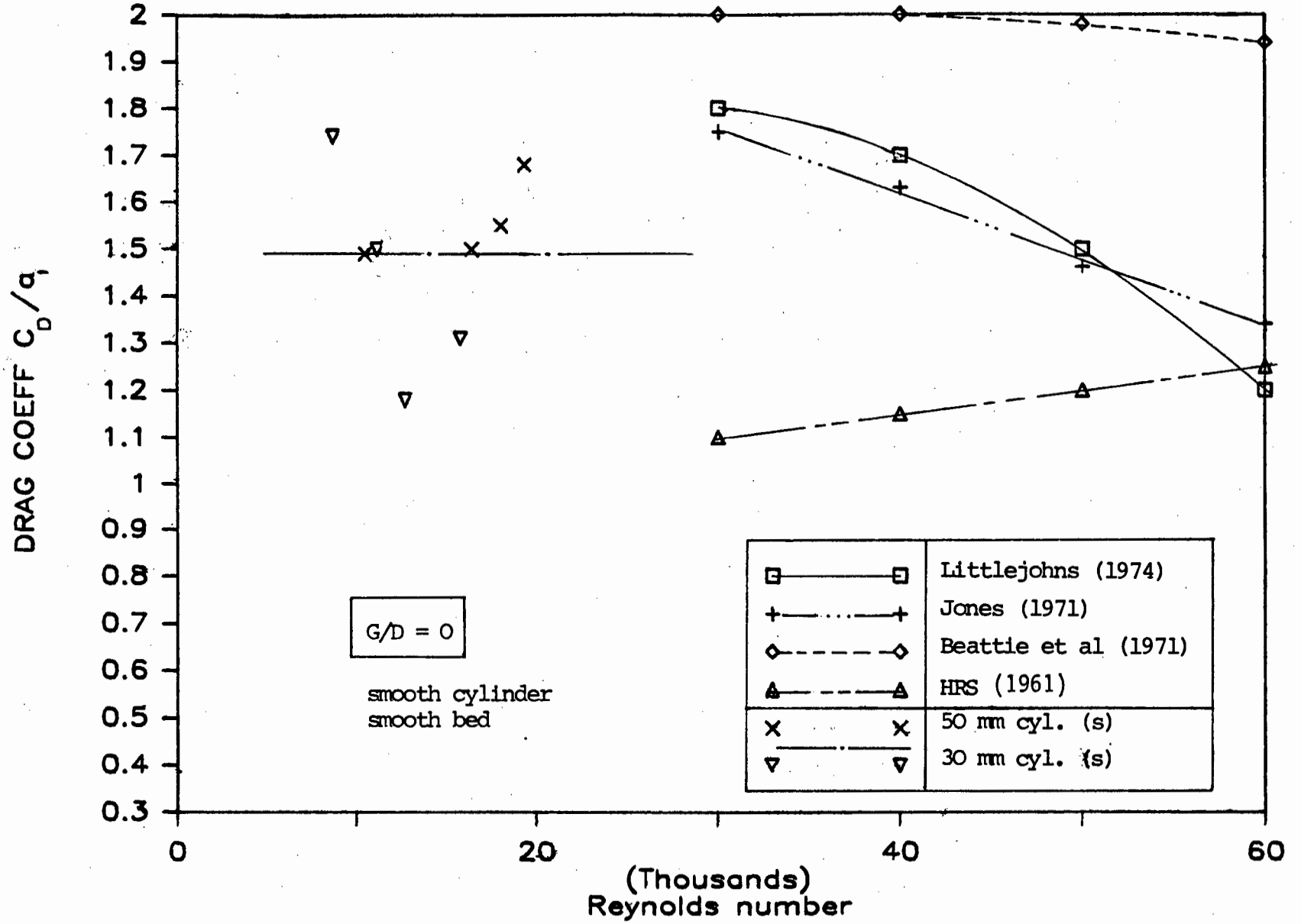

FIG. 8.7 : COMPARISON BETWEEN DRAG COEFFICIENTS, DETERMINED BY OTHER INVESTIGATORS AND THE PRESENT STUDY

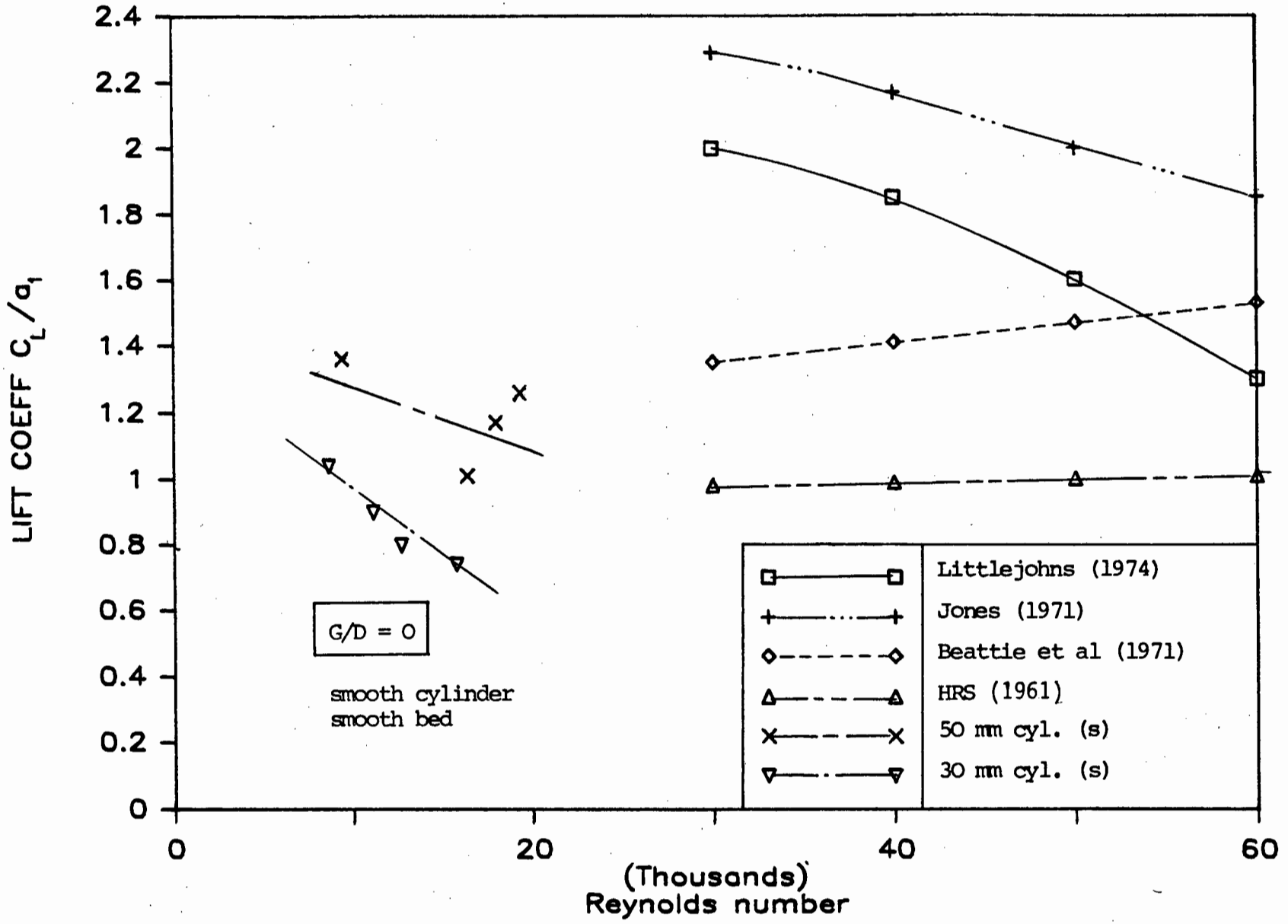

FIG. 8.8: COMPARISON BETWEEN LIFT COEFFICIENTS, DETERMINED BY OTHER INVESTIGATORS AND THE PRESENT STUDY.

parameter a_1 and are indicated as C_D/a_1 and C_L/a_1 respectively.

Drag and lift coefficients are compared to measurements by Beattie et al (1971), Jones (1970, 1971) and Littlejohns (1974), in Figs. 8.7 and 8.8. They all worked in a water medium, performing tests in the field (Littlejohns) or in large scale installations. Only Littlejohns undertook measurements with a free water surface, over the cylinder. The mentioned researchers recorded measurements from a Reynolds number of approximately 30 000 to 500 000, but essentially over the critical Reynolds number zone.

Drag coefficients for a cylinder resting on the bed, are shown in comparison to results of the abovementioned investigators in Fig. 8.7. The large scale tests generated higher values. Littlejohns also indicated a plot of tests done at the Wallingford Hydraulics Research Station in 1961, on 1/3 scale models in a towing tank. These extrapolated results are also indicated in Fig. 8.7, and although at totally different Reynolds numbers, show fair correlation with the present study.

Lift coefficient values of the present work and the researchers above, are compared in Fig. 8.8. The results of Beattie et al, which were also based on the pressure integration method, indicate some correlation with those generated by the 50 and 30 mm cylinders. The downtrends of the latter results is possibly indicative of the start of the critical region.

8.4.1 Force Coefficients at various G/D ratios

Average drag and lift coefficient at various G/D ratios are compared to those obtained by Thomschke (1971), Wilson and Caldwell

(1971), Bagnold (1974), Roshko et al (1975), Fredsoe et al (1985) and Zdravkovich (1985) in Figs. 8.9 and 8.10. Thomschke, Bagnold and Fredsoe et al worked in a water medium, and all the other investigators in air . While the results of the present study are given for the Reynolds number range 10 000 to 25 000, the other investigators worked at Reynolds numbers of 3 000 (Bagnold),20 000 (Roshko et al), 20 000 to 30 000 (Fredsoe et al), 33 200 (Wilson and Caldwell), 61 000 (Zdravkovich) and 92 000 (Thomschke).

The average drag coefficient versus G/D plots of the present study (smooth 30 and 50 mm cylinders) lie approximately midway between those obtained by Wilson and Caldwell (1971) and Roshko et al (1975); refer to Fig. 8.9. The plots of Roshko et al (1975) and Thomschke (1971) are characterised by maximum points at G/D = 0,6 and 0,1 respectively, which correspond to the present study to some degree. Göktun (1975) and Haffen (1975) also found a similar tendency.

The average lift coefficients versus G/D plot of the present study is compared to those of the other investigators in Fig. 8.10. The correlation is excellent. At small G/D values, near the bottom, the lift coefficients approach those obtained by Wilson and Caldwell (1971) and Roshko et al (1975) while the results almost coincide with Thomschke's (1971) and Bagnold's (1974) curves beyond G/D = 0,3.

At G/D > 1,0 a few test runs produced negative lift coefficients (refer Figs. 5.48 to 5.51). In all these cases the maximum pressure points were located slightly above the front centre of the cylinder (Tables 5.3 and 5.6), possibly resulting in a net downward force on the cylinder. Zdravkovich (1985) also measured negative lift coefficients, with a prominent minimum turning point (Fig. 2.15). Lower in the subcritical region, Zdravkovich obtained a less pronounced peak, in the G/D range 0,3 to 1,5. A possible explanation for the negative lift coefficient is given in Chapter 10 of this thesis.

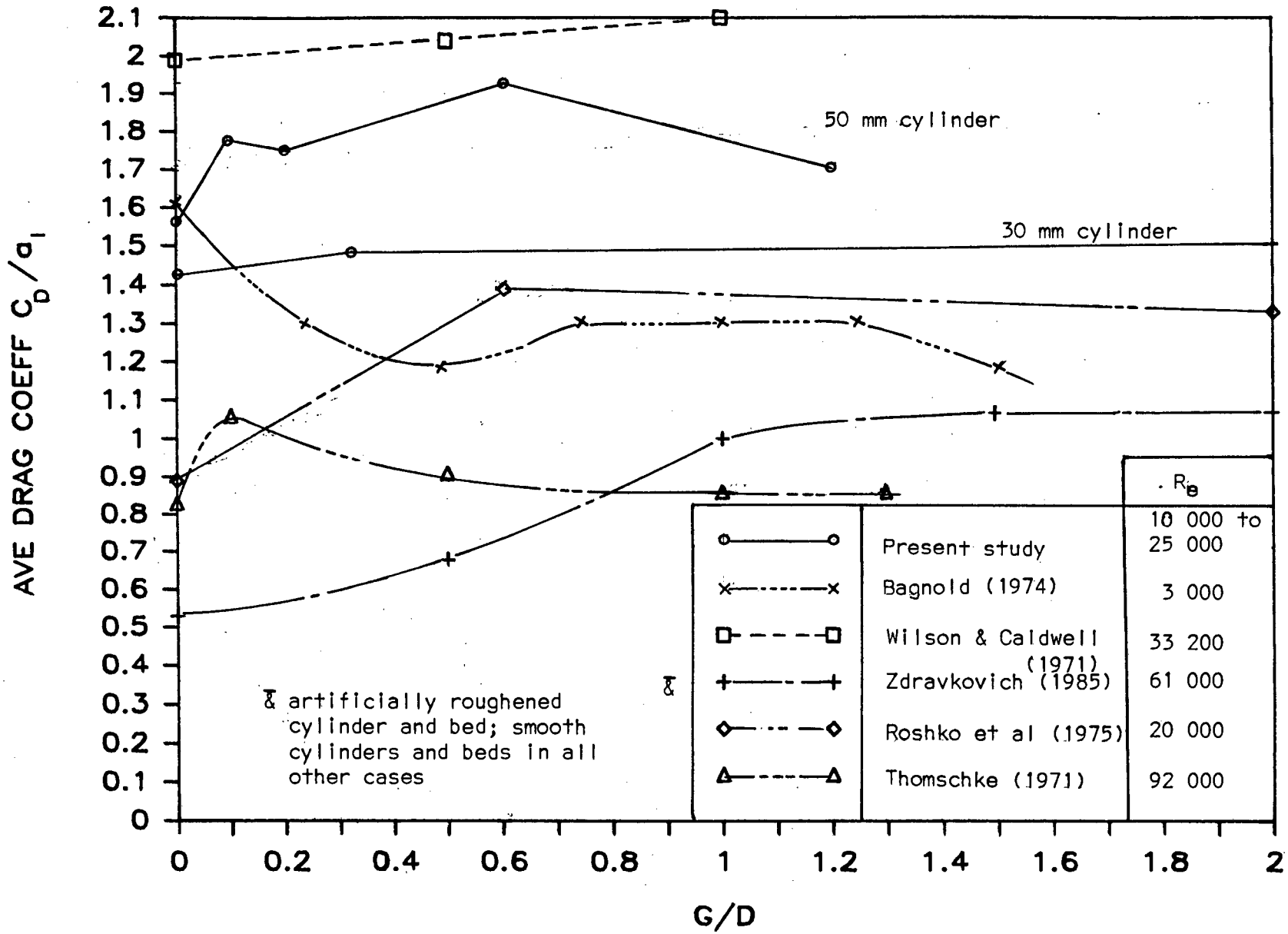

FIG. 8.9: DRAG COEFFICIENTS AT VARIOUS G/D RATIOS: COMPARISON TO OTHER WORK

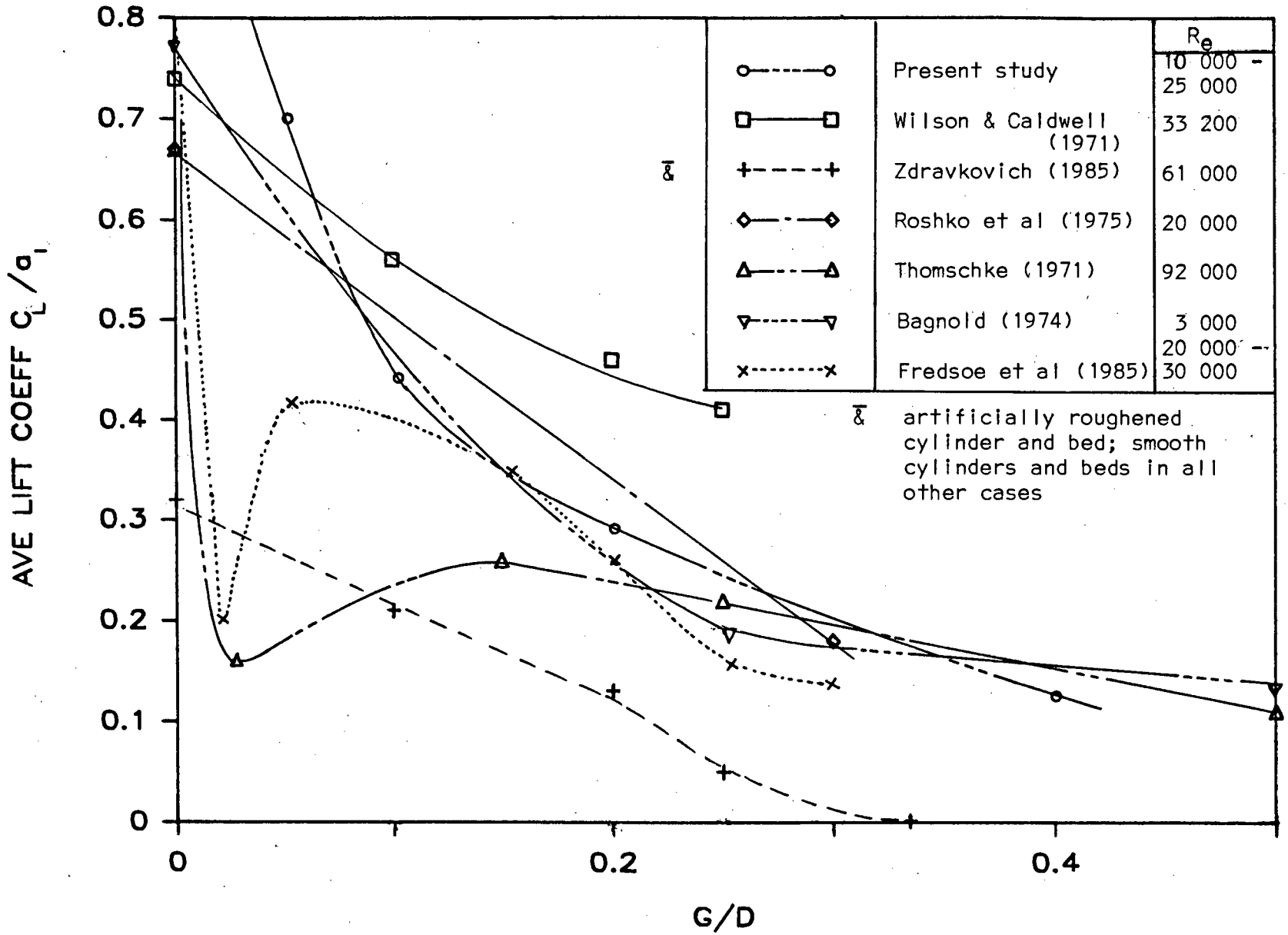

FIG. 8.10: LIFT COEFFICIENTS AT VARIOUS G/D RATIOS: COMPARISON TO OTHER WORK

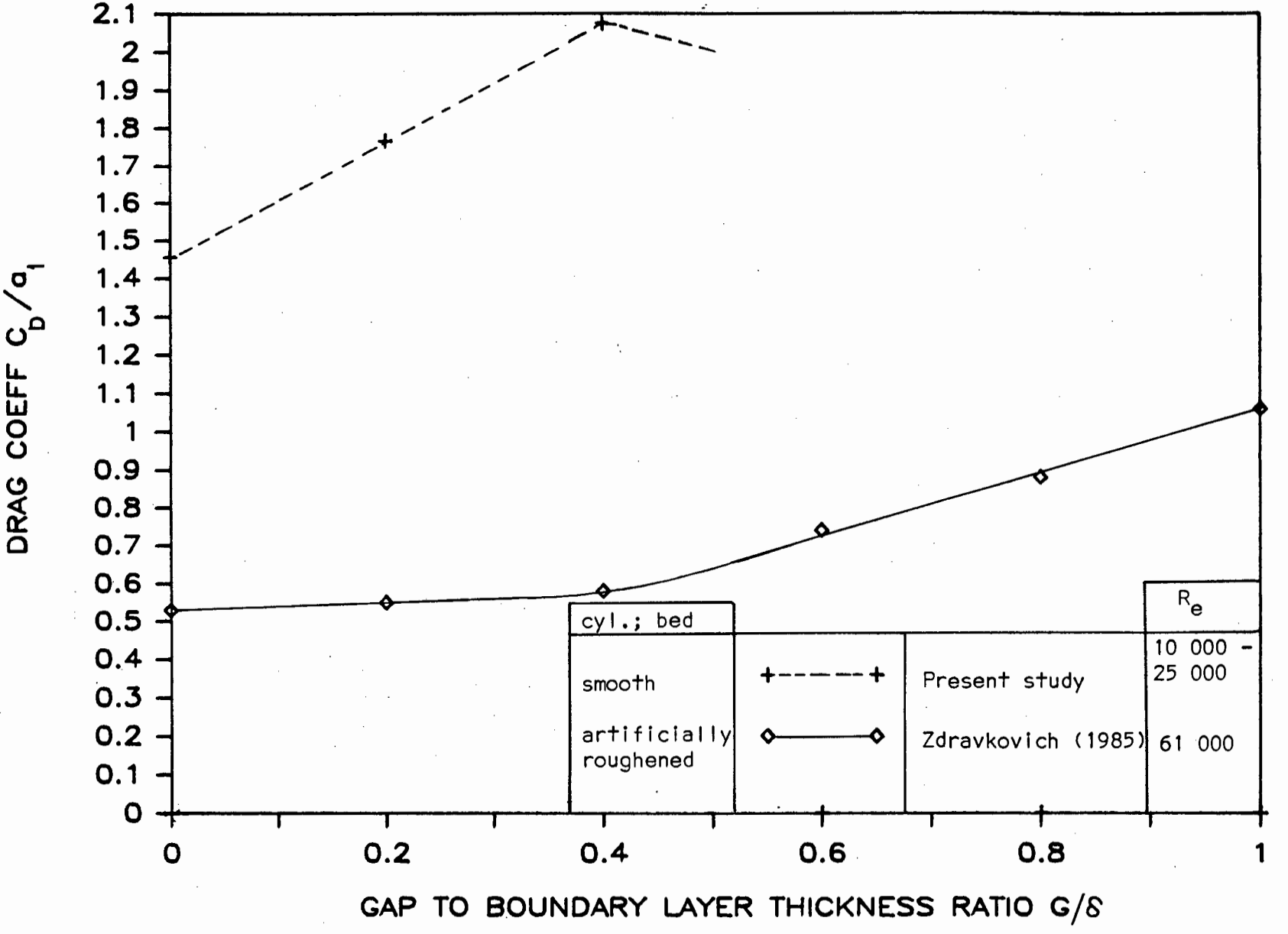

FIG. 8.11: VARIATION OF DRAG COEFFICIENT WITH G/δ; COMPARISON TO ZDRAVKOVICH (1985)

8.4.2 Variation of Drag Coefficient with G/δ

The variation of the drag coefficient C_D/a_1 with the gap to boundary layer thickness ratio G/δ is compared to the results obtained by Zdravkovich (1985) in Fig. 8.11. Although the drag coefficients are equal to more than double Zdravkovich's results at small G/δ values, both plots indicate an increasing tendency. Zdravkovich found that the drag coefficient was almost constant for $G/\delta > 1$, and only started to decrease when the test cylinder was immersed in the boundary layer. The boundary layer thicknesses measured in the present study were all in excess of 1,5 cylinder diameters, resulting in a maximum G/δ ratio of Ø,755; it was therefore not possible to obtain the variation of the drag coefficient beyond $G/\delta = 1,Ø$.

8.4.3 Bed and Cylinder Roughness

Bed roughness did not appear to influence the force coefficients; contradictory results were produced. This corresponds to results obtained by Jones (197Ø) and Littlejohns (1974), at higher Reynolds numbers near the critical flow regime.

Cylinder roughening resulted in a slightly higher drag coefficient for the "rougher" smaller cylinder, with a smooth bed flume. Should a rough bed also be considered, this tendency prevails up to a Reynolds number of approximately 14 ØØØ. All the investigators mentioned earlier in Section 8.4, found a similar result near the critical flow regime. The same researchers found that cylinder roughening, caused a decrease in the lift coefficient. Should their values be extrapolated to the subcritical region of the present study, their "smooth" and "rough" curves either merge or intersect.

The present research indicated that, except for the 50 mm cylinder which caused more flow blockage, cylinder roughening did not have any marked influence on the lift coefficient in the Reynolds number range concerned. Bagnold (1974) performed tests at a Reynolds number of 3 000, and found a very slight increase in the lift coefficient, close to the bed, associated with cylinder roughening.

CHAPTER 9 - REVIEW OF THEORETICAL STUDIES UNDERTAKEN

9.1 Introduction

As indicated in Chapter 2 of this dissertation (Section 2.7), theoretical studies on a cylinder placed in a steady flow close to a boundary, are almost non-existent. A number of theoretical studies was however, undertaken on symmetrical flow past cylinders. The majority of these studies concentrate on numerical calculation methods.

In the discussion that follows, the influence of boundary or wall proximity on wave-induced forces as well as the potential flow are briefly examined. Theoretical models, capable of generating pressure distributions around a circular cylinder located in steady symmetrical flow, are then discussed, followed by an analytical explanation of the upward lift force induced when a cylinder is placed in a steady flow near a boundary.

9.2 Wave-induced Forces

The influence of a nearby plane boundary on the wave-induced forces on a circular cylinder, was theoretically analysed by Yamamoto et al (1974). The cylinder's axis was located parallel to the plane boundary and perpendicular to the wave direction. Only cylinders far from the free water surface were considered. They also carried out experiments to compare with their theoretical results.

Yamamoto et al found the drag force effect negligible in their test program, and consequently omitted drag coefficients from their study. In discussing their work, Grace (1975) indicated that the Keulegan-Carpenter period parameter, K-C, of less than 2 was not typical of real-life situations. (The Keulegan-Carpenter period parameter K-C or "wake parameter", as it was referred to by Yamamoto et al (1976) is represented by

$$K\text{-}C = \frac{U_{max}\, T}{D}$$

where U_{max} = amplitude of the harmonically changing velocity
T = period of oscillation
D = diameter of the cylinder,

is closely related to the phenomenon of wake formation. It can also be shown that K-C is a measure of the relative displacement of water particles.).

Schrecker (1978) reported on experiments performed by Keulegan and Carpenter (1958) on cylinders and plates to examine the flow patterns at various K-C values. They found that no flow separation occurred for K-C $\leq$ 15. For K-C beyond 15, separation was observed, vortices formed and the drag increased considerably. Sarpkaya and Isaacson (1981) identified the following ranges of the K-C values over which the various force components, in oscillatory or unsteady flow, become predominant:

K-C value	Predominant force component
larger than about 15	drag
smaller than about 10	inertia
larger than about 5	lift

In Chapter 2 it was mentioned that the Strouhal number S is related to the vortex shedding frequency in steady flow conditions. The Keulegan-Carpenter period parameter on the other hand, is clearly important in oscillatory flow situations.

9.3 Potential Flow Theory

In their abovementioned analysis, Yamamoto et al (1974) closely investigated lift forces and the effect of varying cylinder clearance G on the lift coefficient. Attention was only devoted to the lift resulting from the asymmetrical flow caused by the nearby plane boundary. Their calculations based on potential flow theory generated a lift coefficient, C_L = 4,49 for the cylinder making contact with the boundary; this flow condition corresponds to uniform, steady inviscid flow without separation. For the same flow situation and cylinder location, Wilson and Reid (1963) found a C_L value of 4,48. This lift force is directed away from the wall when the cylinder touches the boundary.

A lift coefficient value, $C_L = \pi(\pi^2 + 3)/9 = 4.49$ was already derived by Müller in 1929 for potential flow and with G = 0. The case of G = 0 (with no flow under the cylinder) cannot be obtained mathematically from the case where $G \neq 0$ and by letting G approach zero. Yamamoto et al (1976) reported that they mathematically calculated $C_L \rightarrow -\infty$ for $G \rightarrow +0$.

The potential flow theory yields a large net lift force towards the boundary (i.e. negative lift force) even if a very small gap exists between the cylinder and the boundary. With further separation between cylinder and boundary, the lift force towards the boundary decreases until it approaches zero at a gap ratio G/D of approximately 1 (refer to Fig. 9.1). Owing to the effective "compression" of the streamlines, the flow in the gap between the cylinder and the boundary has a higher velocity than at the top of the cylinder. According to the Bernouilli equation, the pressure at the top of the cylinder is higher than at the bottom thereof; a net downward force is therefore exerted on the cylinder. This result demonstrates the inability of the potential theory to deal with the consequence of flow separation.

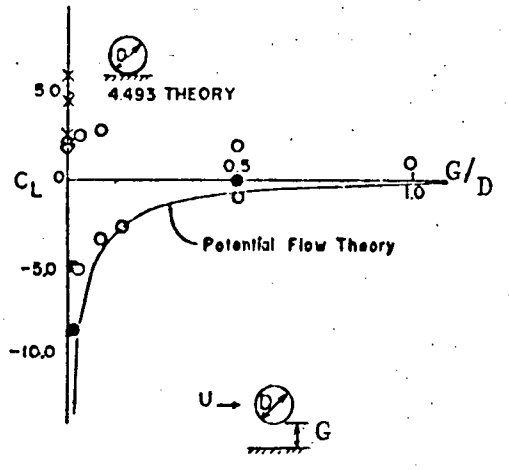

Experimental results:

- o Wright and Yamamoto (1979); D = 300 mm
- • Yamamoto et al (1973); D = 150 mm
- × Schiller (1971); D = 150 mm

Fig. 9.1: Lift Coefficient of Cylinders near Plane Boundary, in Wave Action (from Wright and Yamamoto (1979))

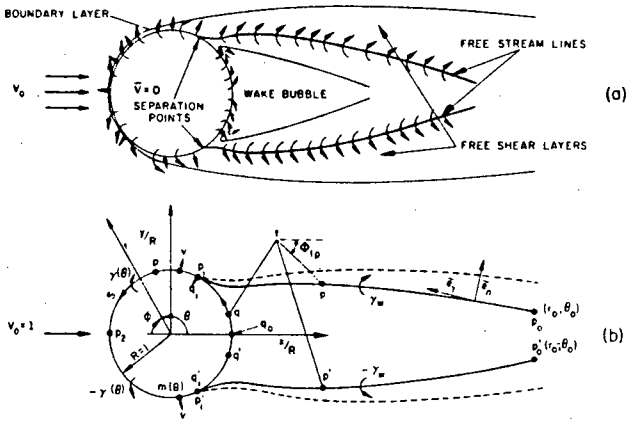

Fig. 9.2: Definition sketches for the mathematical model of Celik et al (1985)

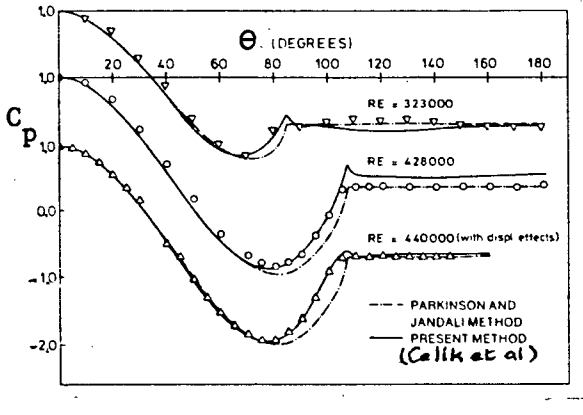

Experimental results:

- ▼ Murphy (1966)
- o Achenbach (1968)
- ▲ Celik (1980)

Fig. 9.3: Comparison of the pressure distributions obtained by the models of Celik et al (1985) and Parkinson and Jandali (1970). (from Celik et al (1985)).

Experimental results of Yamamoto et al (1974) and Wright and Yamamoto (1979), showed good agreement with the C_L versus G/D plot based on the potential flow theory (refer to Fig. 9.1). Also Sarpkaya (1976) obtained lift coefficient values at small K-C numbers, and G = 0, which compared well, regarding the order of magnitude, with Müller's (1929) C_L value of 4,49 for potential flow. However, Grace (1975) questioned the practical importance of negative lift coefficients to the pipeline designer, as downward forces resulted in greater stability. Yamamoto et al's (1976) response was that additional experimental results at larger K-C numbers, showed that a large negative (downward) lift occurred when wake formation was small and a large positive (upward) lift when wake formation became larger; this reversal happened within half a wave cycle.

From the above, it is evident that the theoretical analysis by Yamamoto et al (1974) using potential flow, is related to pure wave action at small Keulegan-Carpenter period parameters, where the wake behind the cylinder is not yet fully developed.

9.4 Symmetrical Flow Past Cylinders : Calculation Methods

During the past two decades, considerable advances were made in the numerical solution of the Navier-Stokes equations (derived in Schlichting, 1979) for fluid flow past bluff bodies, such as circular cylinders. Unfortunately, the results are restricted to laminar flow situations, remote from a boundary, at low Reynolds numbers. This is mainly due to the cost involved and the severe numerical problems encountered when considering higher Reynolds numbers.

Should turbulent flow situations be considered, the numerical solutions of the Reynolds-averaged Navier-Stokes equations not only involve excessive computing times, but are also influenced by uncertainties in the modelling parameters; these uncertainties are mainly in the region of separated flow.

According to Celik et al (1985) a practical and quicker solution is obtained when an inviscid model, representing the most important features of the real flow, is developed. However, free parameters such as the location of flow separation and the base pressure have to be known, and therefore be determined from alternative methods, for the model to generate realistic results.

Celik et al (1985) identified models which assume steady flow to be one of three categories, namely (i) free-streamline models, using conformal mapping techniques, (ii) surface-singularity models and (iii) free-streamline models with surface and wake singularities. In all these models the flow field consists of the boundary layer on the body, the wake and the flow region outside the boundary layer and wake.

The free-streamline models with surface and wake singularities (refer to category (iii) above), are based upon the assumption "that the vorticity in the wake region is concentrated in relatively thin shear layers" (Celik et al, 1985). The vorticity is a vector quantity, of the same nature as angular velocity. According to Lugt (1983) vorticity is the angular velocity of a fluid at a point in space.

Celik et al referred to a model developed by Dvorak et al (1979). This two-parameter model involved the wake bubble length and the base pressure coefficient. The wake bubble length is the distance between the body and its image. Dvorak et al's model produced satisfactory results for flat plates, regarding streamline patterns. However, applications of the model adapted for the circular cylinder, indicated the dependence of the results on the wake fineness ratio; the latter defines the wake length which is a free parameter for which a value has to be prescribed.

Dvorak et al's model assumes the vorticity on the streamlines to be constant and equal to its value at the point of separation. The

position of the separating streamlines is determined by an iterative procedure. Briefly the method is as follows:
An initial shape of the vortex sheets is assumed, and the vorticity distribution satisfying the required velocity condition on the body and the position of the new streamline (corresponding to the previous singularity distribution) is determined; the procedure is iterated until a satisfactory position for the streamlines is obtained. Dvorak et al (1979) did not provide details of a convergence criterion or the numerical method used in their report.

Celik et al (1985) cited examples of a few irrotational-flow models, analogous to the above model of Dvorak et al. All these models involve some free parameters of which the values have to be determined beforehand, either from experimental investigations or other means. To minimise empirical inputs and reduce the number of free parameters, Celik et al utilised boundary layer theory in a model they developed, which was similar in some respects to the Dvorak et al model. The Celik et al model generates pressure distributions around a cylinder placed in various symmetrical flows.

9.4.1 The model of Celik et al (1985)

9.4.1.1 Assumptions

To simulate the real separated flow past a circular cylinder to an approximate degree, the model was based on the following assumptions (refer Fig. 9.2):

(i) The flow field is steady.

(ii) The boundary layer on the cylinder and the free shear layers are sufficiently thin, such that they can be represented by vortex sheets. (According to Goldstein (1950), vortex sheets "may be regarded as an idealization, for inviscid fluids, of thin layers of vorticity in a fluid whose viscosity is small but not zero"). Further, it is assumed that the vorticity in the shear layer and in the

boundary layer, is concentrated on the free streamline appearing beyond the point of separation and along the contour of the cylinder.

(iii) The wake bubble, behind the cylinder, has negligible vorticity.

(iv) In the near wake region, the vorticity strength on the free streamline is constant.

(v) Stagnation points are located on the cylinder, just downstream of the points of separation.

(vi) The boundary layer's influence, prior to the occurrence of separation, is represented by a source distribution such that the normal velocity is given by

$$v(\theta) = \frac{d}{d\theta} (2 U_e \delta^*/D) \qquad (9.1)$$

where θ = angle measured from the rear stagnation point,

δ^* = boundary-layer displacement thickness,

U_e = tangential velocity (outside the boundary layer region),

D = cylinder diameter

It is also assumed that $v(\theta)$ is negligible beyond the point of separation.

9.4.1.2 Equations and Solution

The assumptions and boundary conditions mentioned above, lead to a so-called Neumann problem. The solution of such a problem, lies in the construction of a system of singularity distributions comprising a source distribution $m(\theta)$ and a vortex sheet $\gamma(\theta)$ (on the circle), a vortex sheet of constant strength γ_w on the shear layers, and a uniform flow field having a velocity $V_o = 1$. The source distribution satisfies the boundary condition $v_r = v$, while the vortex distribution can be found to satisfy the following conditions:

(a) The normal velocity on the circle (see Fig. 9.2(b)) is zero.

(b) The vorticity is conserved at the point of separation, i.e. $\gamma_s = \gamma_w + \gamma_d$; s and w refer to the upstream and downstream sides of the separation point on the exterior and d refers to the downstream side in the interior.

(c) The tangential velocity at a position θ_d, due to the vortex distribution is equal and opposite to that caused by the source distribution (according to assumption (v) of the previous Section 9.4.1.1.).

With reference to Fig. 9.2(b), the velocity in the r-direction at point t due to a unit source element and in the θ-direction at point p due to a unit vortex element, is given by the following expression, in terms of polar co-ordinates:

$$G(p,t) = \frac{\partial \ell_n (r_{tp})}{\partial r_t} = \left[r_t - r_p \cos (\theta_p - \theta_t)\right]/r_{tp}^2 \quad (9.2)$$

The source distribution $m(\theta_t)$, on the circle, which satisfies the boundary condition in Eq. (9.1) is given by

$$\pi\, m (\theta_t) + \int_0^{2\pi} m (\theta_q)\, G (q,t)\, d\, \theta_q = v(\theta_t) \quad (9.3)$$

According to condition (a) above, the fluid within the circle is assumed to be at rest. This condition generates the following equation for the vortex sheets on the circle and the free streamlines:

$$- \pi \gamma(t) + \int_{q_0}^{q_1} \gamma(q) \left[G(q,t) - G'(q',t) \right] d\theta_q$$

$$+ \int_{p_0}^{p_2} \gamma(p) \left[G(p,t) - G(p',t) \right] ds_p - \sin \theta_t = 0 \qquad (9.4)$$

where $G(p',t) = G(r_p, -\theta_p, t)$

s_p = arc length at point p.

The required outflow $v(\theta)$ at the circle is not disturbed by this vortex distribution. The source distribution does, however, contribute to the tangential velocity on the circle.

Celik et al (1985) subsequently showed that the total tangential velocity U is given by

$$U = -\sin \theta + u + \pi\gamma + \gamma_w Q$$

$$= 2\sin \theta + u + \frac{(u_s - 2\sin \theta_s)Q}{(\pi - Q_s)} \qquad (9.5)$$

where u_s = tangential velocity on the circle due to the source distribution

Q = a wake influence function

Q_s = the wake influence function at $\theta = \theta_s$

u = boundary-layer displacement effect

The first and third terms on the right-hand side of Eq.(9.5) are the velocity due to the uniform stream, and the combined effect of the boundary layer and the wake respectively.

9.4.1.3 Wake Length Parameter

As the streamlines which arise from the separation points are not known initially, the computations must commence with a guess; the locations of the vortex sheets must therefore be determined by an iterative procedure.

Celik et al's constant-vorticity model requires that a wake length parameter w_ℓ be introduced. This parameter can be regarded as the effective wake length which represents the influence of the whole wake on the pressure distribution around the cylinder. This model thus involves the two parameters θ_s and w_ℓ. The separation angle θ_s can be determined from boundary-layer calculations using the method described by Celik and Patel (1982), which in turn utilises the numerical scheme and turbulence model of Cebeci and Bradshaw (1977). The wake length parameter w_ℓ is determined by a trial-and-error procedure such that the calculated value of the minimum pressure coefficient C_{pm} matches its experimental value.

9.4.1.4 Base Pressure Coefficient

The base pressure coefficient C_{pb} is given by

$$C_{pb} = 1 - U^2 + \overline{\Delta H} \qquad (9.6)$$

where U = non-dimensional tangential velocity

$\overline{\Delta H}$ = mean value of the non-dimensional total pressure head jump

= $4 \pi \gamma_s (\pi \gamma_s - U_o)$; U_o being the non-dimensional tangential velocity on the exterior side of the vortex sheet.

9.4.2 Pressure Distributions

A comparison of the results (in the critical regime) obtained from the Celik et al model, with and without

displacement effects, and the model of Parkinson and Jandali (1970) is shown in Fig. 9.3; the application of the model of Parkinson and Jandali is briefly discussed below in Section 9.4.3. Although both models assume the same separation position, the Celik et al model uses the minimum pressure coefficient C_{pm}, while the model of Parkinson and Jandali uses the base pressure coefficient C_{pb}; C_{pm} exhibited less experimental scatter than C_{pb}.

In the vicinity of the separation point, the method under discussion exhibits a small kink; this is due to the fact that a constant total head difference ΔH is assumed across the vortex sheet. The same tendency is observed in the subcritical regime.

The model of Celik et al (1985) shows good comparison with experimental results regarding pressure distributions. However, the results suffer from uncertainties as the calculations use the experimental values of the minimum pressure coefficient C_{pm}.

9.4.3 Flow past rough-walled cylinders : Application of the Model of Parkinson and Jandali (1970)

Güven et al (1977) developed an analytical model for the steady flow past a circular cylinder at very large Reynolds numbers. The model was required to accommodate rough-walled cylinders and was based on the wake-source potential-flow model of Parkinson and Jandali (1970). According to the latter model, the pressure distribution can be calculated provided the pressure coefficient at separation C_{ps} and the angle of separation θ_s are given. The wake-flow details are not considered and it is assumed that $C_{pb} = C_{ps}$.

As consideration of the development and separation of the boundary layer as well as the compatibility of the wake flow with the external potential flow is essential to generate the C_{pb} , θ_w (approximate angle of beginning of the wake region defined in Fig. 9.4(a)), and the pressure distribution, an extension of the Stratford-Townsend theory for turbulent boundary-layer separation was used (Güven et al (1977). This theory makes provision for rough-walled cylinders due to the fact that (C_{pb} - C_{pm}) is a function of the surface roughness ratio k/D, the Reynolds number, the free stream turbulence and the pressure distribution (up to the minimum pressure point θ_{min}).

Güven et al (1977) unfortunately did not indicate any graphical pressure distributions, based on the extension of the Stratford-Townsend theory. However, their comparisons of the Parkinson and Jandali theory with experiment for both smooth and rough cylinders are respectively shown in Figs. 9.4(a) and (b). These comparisons correlate fairly well, particularly up to the minimum pressure points.

9.5 Steady Flow Near a Boundary : Explanation of Upward Lift Force

Fredsoe and Hansen (1984) introduced a modified description of the potential flow around the upstream part of a cylinder, in close proximity to a boundary. The purpose of their analysis was to explain why a cylinder, in a steady flow, experiences an upward lift force when placed in contact with or close to a plane boundary.

9.5.1 Velocities Above and Below the Cylinder

To investigate the influence of the wake, aft of a cylinder, they carried out a series of flow velocity measurements. The flow velocity above and below a 89 mm diameter cylinder, placed in 450 mm deep water in a 2 metre

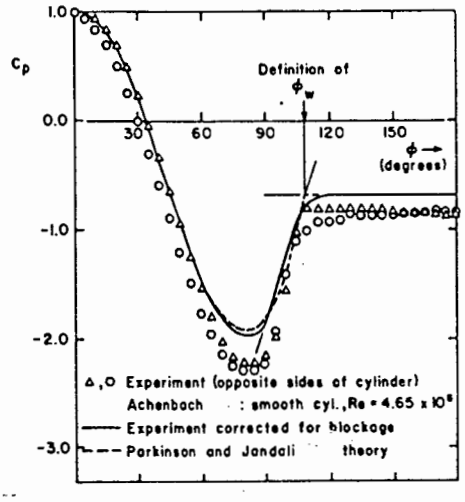

(a) Smooth cylinder

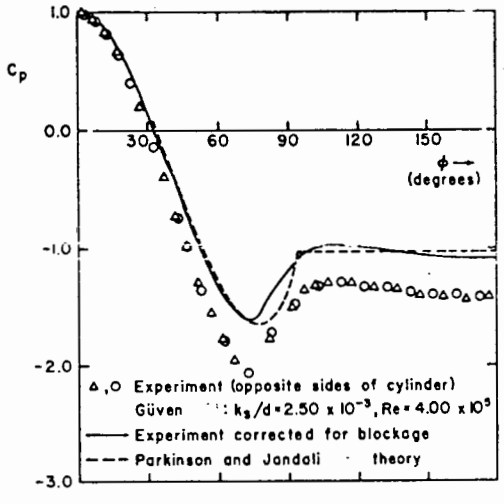

(b) Rough cylinder

Fig. 9.4: Comparison of the theory of Parkinson and Jandali with experiment (from Güven et al, 1977)

wide water flume, was measured using a small (6 mm diameter) propeller. Measurements were taken with the cylinder towed through still water (non-shear flow) and in steady flow conditions with the cylinder at rest (shear flow). The experimental details which also involved the measurement of lift forces experienced by the cylinder suspended on springs, are given by Fredsoe et al (1985).

The velocity measurements were compared with the velocity obtained from the potential flow theory, as described by Müller (1929). For comparison purposes the velocities were normalised with values predicted from potential theory at a depth equivalent to four cylinder diameters, i.e. sufficiently remote from the solid boundary.

The shear flow velocities just slightly above and below the cylinder, U_{top} and U_{bottom} respectively, were approximately equivalent at each G/D ratio for the shear flow case. The potential flow theory predicted a U_{bottom} value larger than U_{top}; from an extremely large difference at G = 0 (cylinder-wall contact), the velocity U_{bottom} decreased swiftly to approach U_{top} at approximately G/D = 1 (refer to Fig. 9.5). With a gap under the cylinder, in shear flow, separation occurs at locations of about 90° and 270° from the front cylinder centre (refer to Chapter 5 of this study, particularly Table 5.6) for smooth cylinders. The wake pressure in the 90° to 270° region is roughly constant. No wake is present upstream of the cylinder, which makes the Bernouilli equation valid for the upstream section of the cylinder. As the streamlines experience a constant curvature along the cylinder up to separation, it is evident that the velocities at the two separation points must be virtually equal.

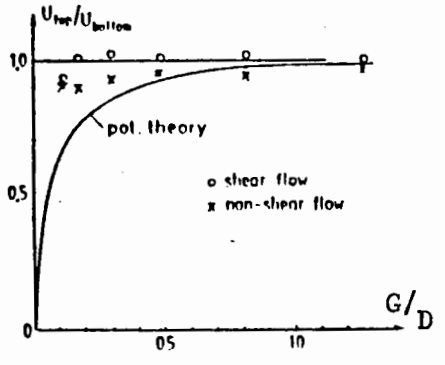

Fig. 9.5: Variation in U_{top}/U_{bottom} with gap ratio G/D (from Fredsoe and Hansen, 1984)

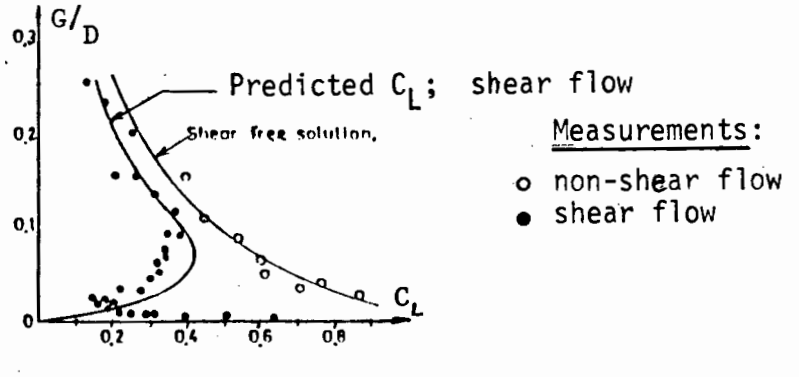

Fig. 9.6: Comparison between predicted and measured lift coefficients; R_e = 25 000 (from Fredsoe and Hansen, 1984)

9.5.2 Displacement of Front Stagnation Point

The fact that U_{top} virtually equals U_{bottom}, means that the top and bottom pressures also become almost equal. These pressures can therefore not contribute to the transverse lift force on the cylinder. However, when the cylinder moves closer to the boundary and the gap is reduced, the front stagnation point (i.e. the point where the maximum pressure occurs) moves from the cylinder centre line towards the wall, due to the reduction in the cross section available to flow under the cylinder. The displacement of the front stagnation point was recorded in the experimental component of the present study (refer to Table 5.6) and also observed by Bearman and Zdravkovich (1978). Further, this displacement results in a positive (upward) lift force exerted on the cylinder.

9.5.3 Modified Potential Theory

To estimate the magnitude of the lift force, Fredsoe and Hansen (1984) adjusted the flow description of the potential theory in front of the cylinder, such that the velocity U_{top} was equal to U_{bottom}. They consequently superimposed on the flow, described according to Müller's (1929) potential flow derivation, a vortex body around the cylinder. The direction of rotation of the vortex body was clockwise, when the non-viscous approach flow was directed from left to right (refer to Fig. 5.2).

The potential flow description of Müller, as used by Fredsoe and Hansen is as follows:

The complex potential ω being a function of z, the complex coordinate where $z = x + iy$ and x and y defined as in Fig. 5.2, is given by the expression

$$\omega_1 = - U_o z - \sum_{j=0}^{\infty} \left(\frac{m_j}{(z-z_j)} + \frac{m_j}{(z - \bar{z}_j)} \right) \qquad (9.7)$$

where

$$m_o = U_o \frac{D^2}{4}$$

$$m_{j+1} = m_j \frac{D^2}{4(2a - Y_j)^2}; \quad Y_o = a \text{ (See Fig. 5.2)}$$

$$Y_{j+1} = a - \frac{D}{2(2a - Y_j)}$$

$z_j = i\, Y_j$
U_o = far field velocity in shear-free flow
a = distance from the bed to the cylinder centre
D = cylinder diameter

The complex potential ω_1 describes the flow, with velocity U_o, around a cylinder placed a gap distance of $(a - D/2)$ from the boundary.

To compensate for the influence of the wall on the circulation around the cylinder, Fredsoe and Hansen (1984) applied the following modified potential flow description of the vortex. They obtained the vortex by the composition of two vortex bodies with their centres in

$c_1 = (0; \sqrt{a^2 - D^2/4})$ and $c_2 = \bar{c}_1$ the complex conjugate. The vortex bodies had equal strengths and opposite rotational directions. This caused the wall to "automatically become a streamline". The complex potential became

$$\omega_2 = K [i\, \ell n\, (z - c_1) - i\, \ell n\, (z - c_2)] \qquad (9.8)$$

where

K = a constant.

Fredsoe and Hansen proved, using geometry, that a circle coinciding with the cylinder becomes a streamline, i.e.

Eq.(9.8) fulfilled the requirement of a vortex body. The strength of the vortex, characterised by Eq.(9.8) was subsequently adjusted for different gap ratios such that the total complex potential

$$\omega = \omega_1 + \omega_2 \qquad (9.9)$$

would meet the requirement of U_{top} being equal to U_{bottom}.

9.5.4 Determination of Lift Force

The pressures on the upstream face, between θ = 270° and 90°, was now simply determined by means of the Bernouilli equation. On the rear side of the cylinder the constant wake pressure was not considered as it did not contribute to the lift force. The vertical component of the pressures on the front face of the cylinder was integrated to generate a positive (upward) lift force at all gap ratios. The lift coefficient calculated, decreased with increasing gap ratios, i.e. as the front stagnation point (where the pressure is a maximum) moved upward towards the front centre point of the cylinder.

Fredsoe and Hansen obtained experimental values for the lift coefficient in shear-free flow by towing a cylinder, fixed to a carriage, through still water; lift coefficients in shear flow (i.e. with a stationary cylinder in steady flow) were also determined. The experimental C_L values at various G/D ratios, compared favourably (particularly for shear-free flow) with the corresponding values predicted by the modified potential flow description (refer to Fig. 9.6).

9.5.5 Comparison to Potential Flow Theory

From the above it is clear that while Fredsoe and Hansen's (1984) analysis and measurements (refer Fredsoe et al, 1985) indicate that the flow velocities at the top and bottom of a cylinder, placed in a steady flow near a

boundary are the same, the potential theory predicts a larger velocity at the bottom than at the top of the cylinder. This contradictory prediction of the potential flow theory results in a downward lift force when the cylinder is located close to a boundary, which is certainly not possible (refer to the experimental results of the present study, summarised in Chapter 5).

Although the qualitative analysis of Fredsoe and Hansen (1984) does not describe the detailed variation of the lift coefficient C_L exactly for shear flow, their experimental results exhibit the same trend as the results obtained by Bagnold (1974) and Thomschke (1971) close to the wall.

9.6 Steady State Solution: State of Affairs

Already in 1967 Schubert mathematically analysed the influence of fluid flowing over a cylinder lying on a wall. Unfortunately only slow flows of Reynolds numbers up to values of only one were considered. Solutions were obtained when the motion far from the cylinder was of uniform shear. According to Schubert (1967), the transverse force exerted by the fluid on the cylinder is zero. He stated that neither the pressure forces nor the viscous forces can exert a net lift on the cylinder. He explained that this was possibly due to the slow motion of the fluid.

Since the unsatisfactory attempt made by Schubert, not much progress was made regarding the steady state solution. Earlier in this Chapter (Section 9.3) it was shown that the potential flow theory does not yield realistic results when a very small gap exists between the cylinder and the boundary, due to a large net lift force being generated towards the latter. A major shortcoming of the potential theory is the fact that it does not accommodate flow separation, a flow phenomenon which should be considered in real flow situations. Further, the simplistic

potential theory does not cater for turbulence. In moderate fluid flows the boundary layer close to the wall is turbulent. It is therefore evident that any steady state solution should relate to turbulent approaching flows.

When discussing calculation methods in symmetrical flow in Section 9.4, reference was made to the numerical solutions achieved by means of the Reynolds-averaged Navier-Stokes equations. In turbulent flow situations the solutions of the Navier-Stokes equations are adversely influenced by uncertainties in the modelling parameters, particularly in the separated flow regions. When a cylinder is located in close proximity to a boundary, these uncertainties would be further accentuated. Further, the inviscid flow model which Celik et al (1985) developed to represent steady symmetrical flow does not generate important characteristics such as the location of flow separation and the base pressure directly. These free parameters have to be determined from alternative methods. An iterative procedure is then used to generate inter alia the pressure distributions around a cylinder placed in various symmetrical flows. It is clear that this model cannot be readily adapted to meet the requirements for wall cylinders.

In the foregoing it was also reported that Güven et al (1977) applied the model of Parkinson and Jandali (1970) to rough-walled cylinders in symmetrical flow. They used an extension of the Stratford-Townsend theory for turbulent boundary-layer separation. However, the pressure distribution can only be calculated provided the pressure coefficient at separation and the angle of separation are given. Although Güven et al's application is an improvement on the Celik et al (1985) model, it is as limited regarding its adaptability to simulate real fluid flows past wall cylinders.

Fredsoe and Hansen's (1984) modified potential theory provides an useful description of the fluid flow around the upstream part of

a cylinder placed close to a boundary. Their analysis (Section 9.5) results in an acceptable explanation of the upward lift force experienced by a cylinder placed in contact or near a plane boundary, in a steady flow. Although their method generated lift coefficients which compared favourably with experimental values, it does not accommodate flow separation and turbulence.

In summary, it is evident that flow turbulence is the main problem to be addressed before an acceptable steady state solution for wall cylinders will be realised. Various attempts by the author have indicated that a realistic numerical analysis of the steady flow past wall cylinders warrants a study in its own right.

CHAPTER 10 - DISCUSSION AND THEORETICAL ANALYSIS

10.1 Introduction

It is mentioned in Chapter 1 that one of the objectives set for this study, was to obtain a better conception of the various characteristics of the fluid flow around a circular cylinder, placed in a steady transverse flow near a boundary; only the subcritical Reynolds number region is considered, due to the limitations of the experimental arrangement to achieve higher Reynolds numbers. However, the downtrends of the drag coefficient plots, could indicate the start of the critical region. Unfortunately the influence of cylinder roughness and turbulence intensity on the critical Reynolds number could not be ascertained.

An attempt is made in this Chapter, to explain how the flow and force coefficients are influenced by boundary proximity. The explanation is based on an interpretation of the various experimental results generated (Chapter 5) and the flow visualization tests undertaken (Chapter 7); the lift phenomenon is also explained. The discussion is therefore largely related to the pressure distribution diagrams, obtained for various combinations of the following variables: cylinder size, gap to diameter ratio (G/D), cylinder roughness, bed roughness and approach velocity.

Although it is not the intention with this dissertation to propose a mathematical model for steady flow past a cylinder near a wall, some simple calculations are provided. These calculated values are compared to those produced from experimental observations.

10.2 Cylinder at various G/D locations

The main features of the pressure distributions, viz. the front stagnation point, the minimum pressure point, the separation point and the wake zone, are discussed. Special reference is made to flow separation, which is regarded as a key phenomenon in explaining the flow past a circular cylinder.

10.2.1 G/D > 1,1

At these locations, the pressure distribution diagrams (see e.g., Figs. 5.14 and 5.26 for the smooth cylinder) approach the symmetrical flow situations, as graphically represented by Flachsbart's (1932) measurements in Fig. 2.7.

The points where the flow separates from the cylinder surfaces, were determined to be located exactly at the upper and lower shoulders of the cylinder, i.e. at 90° and 270° respectively from the front cylinder centre (Tables 5.3 and 5.8). The front stagnation point (maximum pressure location) was generally located at the front cylinder centre.

Although the lift coefficient approached zero, the experimental observations for some test runs produced a slightly negative value (refer Table 5.3). It could not be ascertained accurately what the exact location of the separation point was for these cases; measurements taken, indicated approximate locations of 90° and 270°. However, from the pressure distribution diagrams it was clear that the front stagnation points, for the test runs that generated negative lift coefficients, were displaced slightly above the front cylinder centre. A more detailed explanation of the phenomenon of lift, is offered later in this Chapter.

The variation of drag coefficient with Reynolds number plots (Fig. 5.43), showed that the drag coefficient is only slightly influenced by faster approach flows and cylinder size; it displayed a downward tendency at increasing Reynolds numbers. Calculations of the average base pressure coefficient, revealed that the pressure in the wake zone (see plots in Figs. 5.54 to 5.56) increased with Reynolds number. Comparisons between values in Tables 5.3 and 5.8 showed that if C_{pb} increases, the drag coefficient decreases. This implies that there is indeed a slight decrease in the drag coefficient with increasing Reynolds numbers, for this situation where symmetrical flow is approached. Further, this is possibly the start of the critical region.

Bed roughness did not influence the force coefficients such that a logical conclusion could be reached; the plots in Fig. 5.47 produce contradictory results, regarding the drag coefficients for smooth and rough cylinders, while the lift coefficient plots in Figs. 5.48 and 5.49 do not provide corresponding deductions when compared.

Cylinder roughening resulted in the earlier commencement of turbulence in the boundary layer of the cylinder. This led to the mobile separation points being displaced downstream, to be located at 110° and 250° from the front cylinder centre (Table 5.8). The difference in the base and minimum pressure coefficients, $C_{pb} - C_{pm}$ calculated for smooth and rough cylinders at $G/D > 1{,}1$ for corresponding Reynolds numbers (Fig. 5.58), is virtually equivalent. This implies that the drag coefficient is not much affected by cylinder roughening; Fig. 5.46 illustrates that "smooth" and "rough" plots for the 50 mm diameter cylinder, almost coincide.

However, when the 30 mm diameter cylinder is considered, $(C_{pb} - C_{pm})$ values at corresponding Reynolds numbers are smaller for the rough cylinder (refer Table 5.8). According to Güven et al (1975), their surface roughness tests on cylinders, performed in symmetrical flow beyond the "critical regime", indicated that lower $(C_{pb} - C_{pm})$ values are linked to thicker and retarded boundary layers. Such boundary layers are caused by larger wall shear stresses and lead to earlier flow separation and an increase in the total drag coefficient. All the tests done for the present study, were executed in the subcritical flow regime and produced delayed flow separation for rough cylinders in near-bed locations. The average smooth bed drag coefficients for the 30 mm cylinder, (Fig. 5.47), showed that cylinder roughening

resulted in a higher drag coefficient. Should the results for the larger cylinder be ignored, due to its blocking ratio being higher, it is evident that cylinder roughening leads to a higher drag coefficient, in the subcritical flow regime concerned. A possible explanation of the flow mechanism causing the increase in the drag coefficient, is given in Section 10.3.

Although cylinder roughening resulted in a somewhat higher lift coefficient for the 50 mm cylinder, virtually no change was recorded with the smaller cylinder (Fig. 5.50); the results for the 50 mm cylinder can therefore not be regarded as conclusive.

Flow visualisation tests performed at G/D = 1,2 confirmed that a symmetrical flow situation was approached. Regular vortex formation took place whereby vortices were alternately shed from the region immediately downstream from the separation points, on the upper and lower shoulders of the cylinder.

10.2.2 Near-bed locations: $0 < G/D < 1,1$

Very interesting observations were made as the cylinder was moved closer to the bed of the flume, i.e. as the cylinder was partly or wholly immersed in the thick boundary layer along the bottom of the flume.

Due to the boundary interfering with the flow around the cylinder, as the cylinder approaches the boundary, the symmetrical shape of the pressure distribution diagram is somewhat distorted (see e.g., Figs. 5.22 and 5.23): The centre of the wake zone moved upwards from 180° to 175° (Fig 5.8) with respect to the front cylinder centre, and the minimum pressure peak under the cylinder diminished rapidly. Further, both the upper and lower separation points moved downstream. The location of the lower minimum pressure peak was also displaced downstream, while the position of the upper peak was almost unaffected.

From a careful analysis of the pressure distribution data and the corresponding graphical plots, it is evident that the front stagnation point is displaced towards the boundary as the clearance between the cylinder and the boundary is reduced.

Below G/D = Ø,5 the base pressure coefficient increased rapidly; the plots in Fig. 5.57 represent the variation in base pressure coefficient at a Reynolds number of approximately 2Ø ØØØ. The higher base pressure coefficient at smaller clearances, suggest a smaller or flatter curvature for the streamlines adjacent to the unstable wake region, behind the cylinder. The flow visualisation photographs (Fig. 7.3(a) and 7.4 (a)), confirm the fact that the downstream streamlines are less curved.

As the cylinder-to-boundary gap G was reduced, the vortex shedding action was suppressed at the boundary side of the cylinder (refer Fig. 7.2 (c) for the G/D = Ø,1 location of the cylinder). This was evidently due to the bed interfering with vortex shedding in the lower energy boundary layer along the bed of the flume.

Although little change was observed in the drag coefficient, the lift coefficient increased dramatically, particularly close to the boundary.

At all the near-bed locations the drag coefficient exhibited a slight decrease as the Reynolds number increased. The average drag coefficient versus G/D plots, indicate peak values at G/D = Ø,3 for the 3Ø mm cylinder and between G/D = Ø,1 and Ø,2 for the larger cylinder (Figs. 5.46 and 5.47); drag coefficients for the rough bed show a reversed tendency.

The relationship between the drag coefficient and the gap to boundary layer thickness ratio (Fig. 5.59) facilitated the

possibility of accommodating both the 30 mm and 50 mm cylinder on the same plot. The plot shows that the drag coefficient decreases a little, as the cylinder approaches the boundary. It therefore appears that the lower energy in the boundary layer closer to the boundary, results in a smaller drag coefficient; a value of 1,45 was recorded when the cylinder touched the boundary (Fig. 5.59).

Although there was a slight increase in the drag coefficient due to bed roughness, at G/D = Ø,1, it could not be established beyond all doubt whether bed roughness had any influence on the force coefficients. However, cylinder roughening apparently had some effect on the drag coefficient. The 3Ø mm cylinder's surface roughness ratio k/D was $3 \times 1Ø^{-2}$ compared to $2 \times 1Ø^{-2}$ for the 5Ø mm cylinder. It is therefore not surprising that the results for the 3Ø mm cylinder were more conclusive, for both smooth and rough beds: cylinder roughening caused an increase in the drag coefficient up to a Reynolds number of about 14 ØØØ.

Although cylinder roughening produced higher lift coefficients for the 5Ø mm cylinder at G/D values beyond Ø,3, no change was observed for the smaller cylinder.

1Ø.2.3 On-bed location: G/D = Ø

The on-bed position of the cylinder generated the most interesting results of the entire experimental program.

As the flow under the cylinder was obstructed, separation could only occur on the upper side of the cylinder. For all the smooth bed situations, separation was recorded at an angle of $1Ø5^{o}$ from the front cylinder centre; the separation locations with a rough bed were naturally inconsistent, due to flow "leakage" under the larger cylinder (refer Table 5.6).

Should one only consider the smooth bed situations, it is observed that the separation point was displaced slightly downstream for the smooth cylinder and slightly upstream for the rough cylinder, in comparison to near-bed locations of the cylinder.

The location of the separation point for a smooth bed, was confirmed by flow visualisation tests (Fig. 7.1 (a)). Although not shown by the photographic record, an almost "dead" zone was observed immediately in front of the cylinder on the boundary; little recirculation took place, as suspended particles accumulated there during test runs.

The smooth bed pressure distributions showed a sharp rise between the 260° and 270° pressure tapping locations. A dramatic pressure rise was only expected at 270°. The error resulting from the minor flow leakage which occurred under the cylinder due to bed irregularities, was estimated as less than 0,5% (based on total depth); too small an error to have any influence on the pressure distributions. No displacement of the minimum pressure point concerned (located at 70°), was observed in comparison to cylinder locations close to the boundary.

The drag coefficient showed a downward tendency at increasing Reynolds numbers. A similar trend was noticeable in the lift coefficient versus Reynolds number plots for the smaller cylinder. As pointed out before, the lift coefficient was a maximum when the cylinder was placed on the bed of the flume.

Except for the 50 mm smooth cylinder, all the pressure coefficient plots, viz. C_{po}, C_{pm} and C_{pb}, exhibited a slightly upward trend at increasing Reynolds numbers (Fig. 5.52 to 5.56). The C_{po} and C_{pm} plots for the smooth 30 mm cylinder at G/D = 0 (Figs. 5.52 and 5.53), indicate very consistent results. Further, the values are respectively lower and higher than those for the other plots. This is evidently due to the 30 mm cylinder being located in the lower energy boundary layer along the bed of the flume. The fluid particles in the cylinder's boundary layer

However, with a smooth bed flume, it appears that cylinder roughening resulted in a smaller drag coefficient in the G/D range 0,5 to 0,9 (Figs. 5.46 and 5.57 compared). From geometrical measurements it was estimated that in virtually all cases, surface roughness caused separation to occur further downstream (Table 5.8). This is probably due to the turbulence produced by the rough surface, imparting energy to the cylinder's boundary layer from the surrounding flow. The boundary layer is consequently further accelerated, such that it remains adjacent to the cylinder's surface over a larger distance. It can therefore withstand the adverse pressure gradient better, leading to the separation point shifting downstream. The base pressure in the wake region is recovered, leading to a reduction of the drag coefficient. This recovery in base pressure is noticeable when the pressure distributions of the 50 mm cylinder, where G/D equals about 0,6, are compared for smooth and rough cylinders (Figs. 5.12 and 5.13).

However, cylinder roughening did result in some increase in the drag coefficient of the smaller (30 mm) cylinder. Up to a Reynolds number of approximately 14 000, this change applied to all locations of the 30 mm cylinder where tests were executed; smooth as well as rough beds. At a Reynolds number of about 20 000 and a G/D value beyond 2,0, "smooth" and "rough" C_{pb} values were almost equivalent (Fig. 5.57).

Measurements with a smooth bed, indicated that the smaller cylinder was immersed in a relatively thicker boundary layer. When compared to the larger cylinder, a boundary layer thickness of 3 to 5 cylinder diameters were measured compared to 1,5 to 3 cylinder diameters for the larger cylinder. It is believed that the flume's boundary layer therefore had a greater influence on the flow past the 30 mm cylinder. Although estimates indicated that (except for the on-bed location) cylinder roughening caused separation to occur further downstream, implying a smaller drag coefficient, the

C_{pb} values (refer Fig. 5.56) reflect a slightly higher drag coefficient, which was in fact measured; this was more evident closer to the boundary.

At very small clearances between the cylinder and the boundary, the drag coefficient is not essentially determined by the width of the wake but partly also by the magnitude of the pressure in the 270° to 360° region. The rough 30 mm cylinder was immersed in a thinner boundary layer along the flume's bed (Test run 74 compared to runs 55 and 56, Table 5.8). More energy would therefore be available to exert pressure on the cylinder in the 270° to 360° region, leading to a higher drag coefficient. Alternatively, at the same clearance a thinner boundary layer results in a larger G/δ ratio, such as test run 67 compared to run 62; this implies a higher drag coefficient (refer Fig. 5.59).

10.4 The Phenomenon of Lift Explained

In Chapter 2 of this thesis, potential flow past a cylinder was discussed. It was pointed out that for symmetrical flow, the theoretical pressure distribution is given by the following relationship (from Eq. (2.10)):

$$p = p_o + \tfrac{1}{2}\rho U^2 \ (1-4 \sin^2\theta)$$

The front and rear stagnation points occur at $\theta = 0°$ and 180°, where the pressures are a maximum. It is evident that this symmetrical pressure distribution does not cause any net drag and lift forces on the cylinder.

In a real fluid, flow separation will occur leading to a wake region being formed. The drastic reduction in the pressure behind the cylinder, results in a total fluid force (or drag force) acting on the cylinder in the direction of flow. However, the pressure

distribution is still symmetrical about the front or rear cylinder centres, and the position of the front stagnation point is unaffected; no net transverse or lift force is therefore possible.

In the present study, the latter situation was approached by all cylinder locations where G/D > 1,1. It is interesting to note, that although the lift coefficient approached zero in many cases, a negative value was recorded for a few test runs; for some rough bed situations at a G/D value of as low as 0,91. In these cases of negative lift coefficients, the boundary layer thickness was at least equal to two cylinder diameters. Further, the front stagnation point was located just above the front cylinder centre, while separation was estimated to have occurred virtually at the upper and lower shoulders of the cylinder at $\theta = 90^{o}$ and 270^{o}. The sketch in Fig. 10.1(a) gives a relative indication of the locations of the front stagnation point A and the separation points S_1 and S_2.

As the cylinder approaches a boundary, an asymmetrical flow pattern develops (refer Fig. 2.9), due to the obstruction caused by the boundary. The pressure distribution around the cylinder becomes distorted (Figs 5.22 and 5.23), and a vertical force component (the lift force) acting away from the boundary, is induced. In the present study it was shown that the front stagnation point was displaced towards the boundary, as the boundary was approached. Both the upper and lower separation points were displaced downstream. At the on-bed location of the cylinder, separation naturally only occurred on the upper side at $\theta = 105^{o}$, for both smooth and rough cylinders on a smooth bed (Fig. 10.1(b)). In summary, when a smooth cylinder approaches a boundary, the upper separation point is displaced downstream, and the front stagnation point towards the boundary; their displacements are therefore in opposite directions.

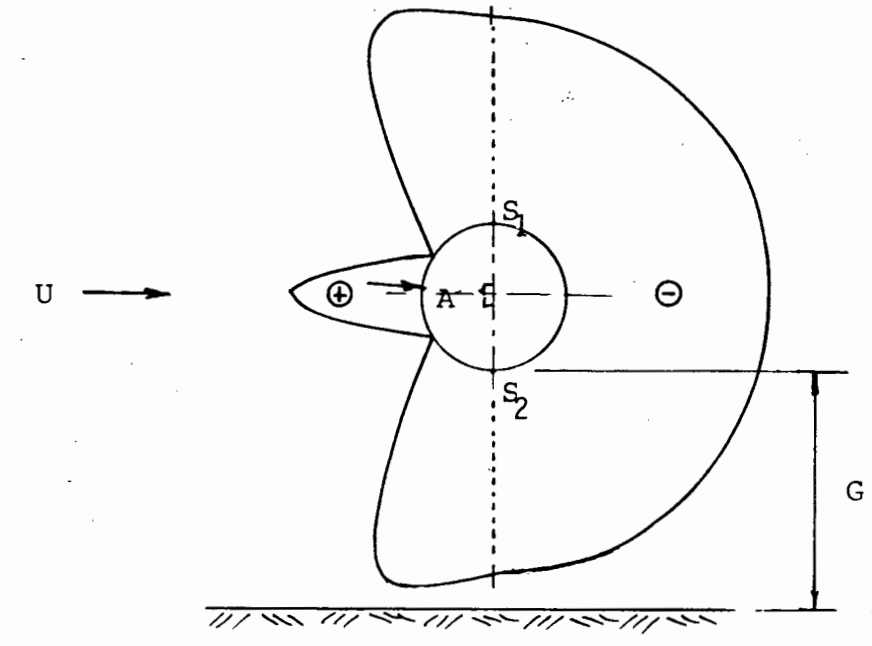

(a): G/D 1,1

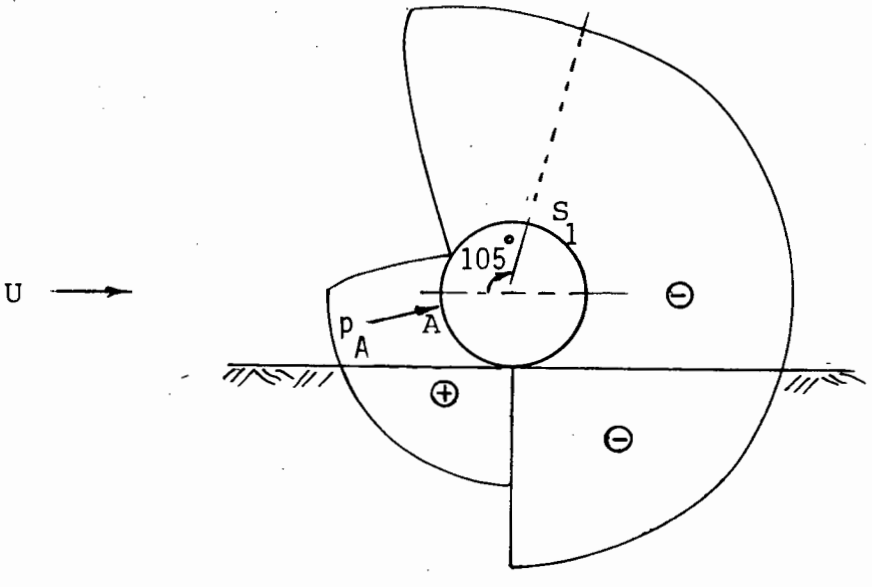

(b): G/D = 0

FIG. 10.1 : Relative indication of pressure distributions, and front stagnation and separation points

10.4.1 Cylinder Resting on the Bed

In the light of the foregoing and with reference to Fig. 10.1(b), the following explanation for the lift force which is induced when a cylinder rests on a plane boundary in steady flow, is offered:

(i) A region of stagnant fluid (a "separation bubble") is created in front of the cylinder, due to the blocking of the fluid between the body and the boundary. This region is characterised by an almost constant positive pressure up to the front cylinder centre (Fig. 5.6).

(ii) The fluid particles are accelerated to the point of minimum pressure (estimated at 70° in the present study), and then decelerated to the point of separation.

(iii) It is believed that the fluid particles which are diverted around the stagnant fluid region, are faster than the surrounding flow. They therefore transfer more energy to the boundary layer of the cylinder, enabling it to overcome the increasing pressure up to the wake zone to some degree. The result is, separation (discussed in more detail in Section 2.3.1) is delayed further downstream, in comparison to symmetrical flow past the cylinder.

(iv) The negative pressure in the wake region remains constant, virtually from the separation point to the cylinder-bed contact point, at $\theta = 270^{\circ}$ (Fig. 10.1(b)). It is therefore clear that the wake pressure cannot influence or contribute to any possible vertical transverse force on the cylinder.

(v) Measurements showed that the front stagnation (maximum pressure) point is located slightly below the front cylinder centre. It is also evident from Fig. 10.1(b) that there is a net upward force exerted on the cylinder. Apart from the constant positive pressure in the 270° to 360° region in front of the cylinder, the negative pressure around the minimum pressure point (estimated at $\theta = 70°$), supports the upward net force even further.

From the relative pressure distribution in Fig. 10.1(b), it is observed that the location of the separation point could be an indication of the magnitude of the lift force; separation further downstream denotes an increase in the lift force.

10.4.2 Cylinder Near the Bed

When a small gap is created between the cylinder and the boundary, fluid particles are partially channelled through the gap. This results in the rapid diminishing of the separation bubble in front of the cylinder and the subsequent reduction in the pressure in that region. The total upward force is drastically reduced. In the present study, the lift coefficient decreased by about 30 % when the gap ratio G/D increased from zero to 0,055 (Run 16, Table 5.3).

At larger clearances the separation bubble disappears and the flow velocities at the bottom and the top of the cylinder, are virtually equivalent (according to measurements carried out by Fredsoe and Hansen, 1984). The latter finding is contrary to the potential flow theory, which predicts a larger "bottom" flow velocity at small gaps. It was confirmed by flow visualisation tests (Chapter 7), that vortex shedding already occurs at the lower side of the cylinder at a gap ratio G/D of 0,1. At

G/D = 0,2 the locations of the separation point were estimated as 90° and 260° for the smooth cylinder (Table 5.6).

As the gap further increases, an almost symmetrical pressure distribution develops around the cylinder (refer to Fig. 5.10, G/D = 0,333). However, a slightly higher pressure region is still in existence in front of the cylinder between $\theta = 270^{\circ}$ and 360°; this results in a net upward lift force prevailing.

As mentioned earlier, a few test runs at $G/D \geq 1,2$ locations produced negative lift coefficients. A careful analysis of the pressure distribution diagrams concerned (Figs. 5.14, 5.16, 5.17 and 5.28), revealed a larger negative pressure under the cylinder than over its top. Obviously this implies a downward force, or negative lift, on the cylinder. Further, the velocity at the bottom of the cylinder was apparently very slightly higher than over its top; measurements by Fredsoe and Hansen (1984) indicated that U_{bottom} was just greater than U_{top} at G/D = 1,26. This can possibly be attributed to the higher energy in the turbulent boundary layer (along the bed of the flume), directly below the cylinder compared to its upper side. The upper side was virtually located in the more stable free stream velocity region of the flume; the boundary layer thickness concerned (refer Table 5.8) substantiates this theory. The flume's boundary layer was also sufficiently thick, to have virtually attained a velocity equal to that of the free stream, at a point located at the bottom of the cylinder. More energy was consequently imparted to the cylinder's boundary layer on the lower cylinder surface, resulting in a higher velocity at the lower minimum pressure point. With the smooth cylinder, separation occurred at the upper and lower shoulders of the cylinder.

Further, for all these "negative lift" situations, the front stagnation point was located slightly above the front cylinder centre.

10.4.3 Location of Front Stagnation Point

From the above, it is clear that the location of the front stagnation point can be regarded as a useful indicator of the direction in which the transverse lift force acts on the cylinder.

When the cylinder is resting on the bed in a boundary layer of moderate thickness, an upward lift force is recorded and the front stagnation point is displaced towards the boundary. As the cylinder is moved away from the bed, the maximum pressure point moves in phase with it. When a symmetrical flow situation is reached remote from a boundary, there will be no net lift force and the cylinder will be located exactly at the front cylinder centre.

However, should the cylinder be immersed in a boundary layer of at least two cylinder diameters thick, there are $G/D > 1,0$ locations at which a downward force (negative lift) acts on the cylinder. In such cases, the front stagnation point is located slightly above the front cylinder centre.

Therefore, when the front stagnation point is located below the front cylinder centre, the lift force acts upwards and when located above the centre point, there is a downward lift force.

10.5 Semi-empirical Calculations

In Chapter 9 it is demonstrated that the mathematical modelling of symmetrical flow past a cylinder, can be fairly intricate should separation and vortex shedding be involved. Near a boundary the

(i) The front stagnation point is located at the front cylinder centre, at $\theta = 0°$. The pressure at that point is equal to $\frac{1}{2} \rho U^2_{D/2}$.

(ii) The shear flow pressure distribution around the cylinder is roughly sketched in Fig. 10.1(b). The main pressure contributions towards the lift force are considered to be the 270° to 360° pressure region and the negative pressure zone around the negative peak at 70° (Table 5.8). The average negative pressure in this "peak" region is assumed to be double the maximum pressure at $\theta = 0°$; essentially the 60° to 80° region (refer to Fig. 5.6). The wake region is not considered to contribute towards the lift force at all.

The total predicted lift force per unit length of cylinder F_L, can then be derived as follows:

$$F_L \text{ (predicted)} = \Sigma \text{ Pressure } p \times \text{Area}_{elem}\, dA \times \sin\theta$$

$$= \Sigma \, (p_1 \, dA_1 \, \sin\theta_1 + p_2 \, dA_2 \, \sin\theta_2)$$

$$= \Sigma \, (p_1 \, r\Delta\theta_1 \sin\theta_1 + p_2 \, r\Delta\theta_2 \, \sin\theta_2)$$

(refer to Fig. 5.1)

$$= \tfrac{1}{2}\rho U^2_{D/2} \, D/2 \, \Sigma \, (\sin\theta_1 \, \Delta\theta_1 + 2 \, \sin\theta_2 \, \Delta\theta_2)$$

where $p_1 = \frac{1}{2}\rho U^2_{D/2}$ (assumption (i) above)

and $p_2 = 2p_1$

$$= \tfrac{1}{2}\rho U^2_{D/2} \, D/2 \left| \left(\int_{270°}^{360°} \sin\theta \, d\theta - 2 \int_{60°}^{80°} \sin\theta \, d\theta \right) \right|$$

$$= \tfrac{1}{2}\rho U^2_{D/2} \, D/2 \, \left(\cos\theta \Big|_{270°}^{360°} - 2\cos\theta \Big|_{60°}^{80°} \right)$$

$$= \tfrac{1}{2}\rho U^2_{D/2}\ D/2\ (1 + 0{,}653)$$

$$= 0{,}826\ (\tfrac{1}{2}\rho D\ U^2_{D/2}) \qquad (10.1)$$

The actual lift force $F_L = \tfrac{1}{2}\ C_L\ \rho\ D\ V^2_{eff}$

$= \tfrac{1}{2}\ C_L\ \rho\ D(0{,}974)^2\ U^2_{D/2}$ from the Table on page 5-22

Therefore, the predicted lift coefficient C_L can be found from

$$F_{L(actual)} = F_{L(predicted)}$$

$$\tfrac{1}{2}C_L\rho D(0{,}974)^2\ U^2_{D/2} = 0{,}826\ (\tfrac{1}{2}\rho D\ U^2_{D/2})$$

$$C_L = \frac{0{,}826}{(0{,}974)^2}$$

$$= 0{,}87$$

The observed and predicted lift coefficients compare fairly well:

*Observed C_L : 0,76 (30 mm cylinder)
0,90 (50 mm cylinder)
Predicted C_L : 0,87
(*average values from Table 5.4(c))

10.5.2 Drag Coefficient

Two different methods were used to calculate the drag coefficient. The first method is directly related to the wake width and the second based on similar assumptions as those outlined in Section 10.5.1 above.

10.5.2.1 Drag related to wake width

This method is based on the fact that the drag coefficient does not change appreciably from the on-bed location to a position remote from the boundary, i.e. symmetrical flow. Roshko (1961) approximated the drag coefficient in symmetrical flow as follows:

$$C_D = - C_{pb}\left(\frac{\text{Wake width}}{\text{Cylinder diameter}}\right) \qquad (10.2)$$

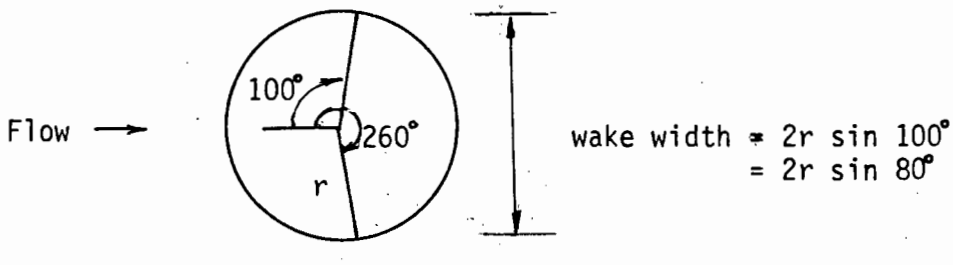

Fig. 10.2: Calculation of wake width

If it is now assumed that the wake spans the region 100° to 260° behind the cylinder, then from Fig. 10.2:

Wake width $= 2r \sin 80°$

$= 0,985\ D$

and $C_D = - C_{pb} \frac{0,985D}{D}$

$= - 0,985\ (-1,510)$ ($\bar{C}_{pb} = -1,51$ for 30 mm cylinder at G/D = 2,67)

$= 1,487$

10.5.2.2 Drag related to pressure distribution

This method is based on similar assumptions as set out in Section 10.5.1. From Fig. 10.1(b) it is clear that the regions in the pressure distribution diagram contributing mainly to the drag force, are the wake zone (stretching from 90° to 270°) and the 270° to 360° region in front of the cylinder. The minimum peak region (60° to 90°) would "reduce" the drag. Except for the wake region where a pressure equal to 1,5 times the stagnation point pressure is assumed, the pressures in the other regions are as before.

The drag force per unit length of cylinder, can be derived in a similar way as for the lift force in Section 10.5.1:

$$F_D = \tfrac{1}{2}\rho U^2_{D/2}\ D/2 \left(\int_{270°}^{360°} \cos\theta\ d\theta - 2\int_{60°}^{90°} \cos\theta\ d\theta - 1,5 \times 2 \int_{90°}^{180°} \cos\theta\ d\theta\right)$$

$$= \tfrac{1}{2}\rho U^2_{D/2}\ D/2\ (1 - 0,268 + 3)$$

$$= \tfrac{1}{2}\rho D\ U^2_{D/2} \times 1,866$$

The drag coefficient can now be calculated:

$$C_D = \frac{F_{L\ predicted}}{F_{L\ actual}}$$

$$= \frac{\frac{1}{2}\rho D\ U^2_{D/2} \times 1,866}{\frac{1}{2}\rho D\ V^2_{eff}}$$

$$= \frac{1,866}{(0,974)^2} \qquad V_{eff} = 0,974\ U_{D/2}$$

$$= 1,97$$

The calculated and measured drag coefficients compare as follows:

Calculated values	Measured values (G/D = Ø)
1,49 (wake width method)	1,25 (30 mm cylinder)
1,97 (pressure distr.)	1,33 (50 mm cylinder)

Apart from the calculated values being slightly higher, the correlation is fair. For the 50 mm cylinder the maximum drag coefficient was 1,54 at G/D = Ø,6.

Although the above calculations could be regarded as rather simplistic, the results do give a fair indication of the order of magnitude of the force coefficient concerned.

CHAPTER 11 - CONCLUSIONS

11.1 Lift and drag forces have been measured on stationary cylinders placed in the turbulent boundary layer of a steady flow, in an open flume. The author believes that the novel experimental techniques utilised, produced accurate pressure distributions and velocity profiles. The two methods used, were respectively based on pressure integration and direct force measurements; velocity measurements were taken simultaneously. The simple yet novel experimental techniques employed, generated substantially similar results under comparable flow and boundary proximity conditions. Due to the sensitivity of the apparatus to vibrations, very careful experimental procedures had to be followed. However, the results proved to be fairly accurate.

11.2 To compare the force coefficients at different flow conditions, a depth parameter a_1 was introduced to compensate for the varying water depth with a free water surface. Although the larger cylinder generated slightly higher force coefficients, its maximum average values (estimated at 80 % of C_L/a_1 and C_D/a_1), are recommended for the subcritical flow region concerned (R_e = 6 000 to 26 000):

Lift coefficient C_L (at G/D = 0) = 0,90
Drag coefficient C_D (at G/D = 0,6) = 1,54

The semi-empirical calculations in Section 10.5 compare favourably to these values.

11.3 A thorough analysis was undertaken before deciding on the reference velocity to be used in determining the force coefficients. The method developed by Jones (1970, 1971) is recommended for a turbulent boundary layer. This method is based on the 1/7th power law for approximating the velocity profile in the boundary layer (refer to Eqs. (5.8), (5.9) and (5.13)).

11.4 Bed roughness did not have any appreciable influence on the force coefficients. The rough bed results therefore followed a similar trend as the smooth bed values.

11.5 Comprehensive tests were performed, regarding the influence of cylinder roughening. The lift coefficient was virtually unaffected, particularly at near-bed locations. The drag coefficients for the two cylinders yielded dissimilar results. The roughened 50 mm cylinder produced a slightly lower drag coefficient in the G/D range 0,5 to 0,9; the geometrically estimated displacement of the separation point downstream, led to a smaller wake. The "rougher" 30 mm cylinder produced a higher drag coefficient, particularly closer to the boundary. This was attributed to the influence of the boundary layer along the bed of the flume.

11.6 The project led to a better understanding of the various flow phenomena around a cylinder. The approximate measurements of the locations of the minimum pressure, stagnation and separation points, made it possible to provide an explanation for the phenomenon of lift as well as other flow features (refer Chapter 10). It was also shown that the locations of the front stagnation and separation points, provide an indication of the direction of the lift force.

11.7 The limited flow visualisation tests undertaken at a Reynolds number of 2 000, confirmed the estimated position of the separation points, as well as the suppression of vortex shedding close to the boundary.

11.8 The lift coefficient was a maximum at the on-bed location of the cylinder and reduced rapidly to approach zero at $G/D > 1,1$. The measurement of the boundary layer thickness along the flume's bed, proved to be very useful in explaining the few cases, all at $G/D \geq 1,2$, where a downward lift force was measured (refer

Section 10.4.2)

11.9 Plots of the force coefficients against Reynolds number exhibited a slightly downward trend as the Reynolds number increased. This tendency corresponded with the base pressure coefficient plots, which showed an expected upward trend.

11.10 Plots of the variation of the drag coefficient with the gap-to-diameter ratio G/D, indicated a minimum drag coefficient at G/D = 0 and maximum points at G/D values of 0,1 and 0,6. The plots of the drag coefficient against the gap to boundary layer thickness ratio G/δ, showed a steadily increasing trend from G = 0. The latter relationship is recommended as a useful parameter for studies related to flows past bluff bodies placed near a boundary.

11.11 The various coefficients obtained in the present study, compared favourably with previously published values, although the latter values were essentially obtained at higher Reynolds numbers near the critical flow regime. The downtrends of the force coefficients at increasing Reynolds numbers are indicative of the start of the critical region.

CHAPTER 12 - FUTURE WORK

The work reported in this thesis relates to conditions experienced with a pipeline in a river estuary. Unfortunately the velocities attained with the experimental arrangements were generally lower than those experienced in normal estuarial flow. Further, it would be worthwhile to extend the work of this thesis, by investigating the turbulent boundary layer along the flume's bed, with a cylinder in place, in more detail.

Rig improvements, additional experiments and mathematical modelling that might supplement the work, are mentioned below.

12.1 Improvements to Present Apparatus

(a) Force Rig

The force rig provided relatively quick and accurate results, but was very sensitive to vibrations. A better method of stabilising the aluminium frame during test runs, or an alternative design, should be considered. Obviously a shorter frame would be more rigid, but unfortunately the height of the flume mountings dictate the height of the frame.

(b) Pressure Rig

Very accurate pressure readings were obtained with the pressure rig arrangement. A motorised rotating device fixed to the test cylinder and set to stop for a predetermined period of time at specific locations, would assist the experimenter a great deal. Even more essential is the development of a data logging system coupled to the

"pressure" balance, such that for every position of the pressure tapping, time-averaged pressures could be logged after a set time period. The data logging systems that currently can be coupled to Mettler balances, only record fluctuating pressures. Consideration could also be given to a system by which a range of pressure tappings are simultaneously sampled. It would however be difficult to fit a number of tappings to a test cylinder.

(c) Water Supply

Velocities up to only Ø,5 m/s were possible with the current water supply in the laboratory. Faster flows are required to achieve higher Reynolds numbers such that investigations closer to the critical Reynolds number could be undertaken. To obtain faster flows an additional reservoir and pumping system would have to be utilised.

12.2 Additional Experiments

(a) Larger experimental arrangement

A larger experimental arrangement would make it possible to extend the Reynolds number range to approximately 8Ø ØØØ. The Reynolds number region up to about 8Ø ØØØ has not been investigated thoroughly, regarding the influence of cylinder roughening on the force coefficients.

(b) Boundary layer investigation

Interesting results such as a negative lift force, were obtained in the present experimental investigations. It is believed that the interaction of the flume's boundary layer with the cylinder and possibly its boundary layer, led to the downward lift force as well as the minimum drag coefficient at G/D = Ø. A thorough investigation of both these boundary layers, is required to gain a better understanding about these mentioned phenomena.

(c) Blockage ratios

It is desirable that a thorough investigation be undertaken on the influence of blockage ratios on the force coefficients of wall cylinders, when a wide range of blockage ratios are considered. To date the only studies on this subject were done for free cylinders. The effect of the drawdown of the water surface in intermediate water depths should also be investigated further.

(d) Flow visualisation

Few flow visualisation tests had been performed in water at subcritical Reynolds numbers beyond 2 000. The technique employed in the present study to eject dye from the single pressure tapping in the test cylinder, was very effective. It would be very interesting to observe flow phenomena at faster flows, at various G/D settings, to gauge the influence on separation and the wake region. Tests with roughened cylinders could also reveal interesting features. Due to turbulence, video recording would probably have to be utilised.

12.3 Mathematical modelling

As far as could be ascertained, no realistic mathematical modelling regarding the steady flow of viscous fluid past a cylinder near a boundary, had been undertaken to date; essentially due to all the flow complexities involved. A realistic prediction of the pressure distribution, the minimum and separation points and the wake region would assist pipeline designers a great deal. It is hoped that such a study would be undertaken in the not too distant future.

REFERENCES

A. References actually consulted

Achenbach, E.	1968	Distribution of local pressure and skin friction around a circular cylinder in cross-flow up to $Re = 5 \times 10^6$. J. Fluid Mechanics, Vol. 34, part 4, pp. 625-639.
Achenbach, E.	1971	Influence of surface roughness on the crossflow around a circular cylinder. J. Fluid Mechanics, Vol. 46, pp. 321-335.
Acrivos, A., Leal, L.G., Snowden D.D. and Pan, F.	1968	Further experiments on steady separate flows past bluff objects. J. Fluid Mechanics, Vol. 34, part 1, pp. 25-48.
Acrivos,A., Snowden, D.D., Grove, A.S. and Petersen, E.E.	1965	The steady separated flow past a circular cylinder at large Reynolds numbers. J. Fluid Mechanics, Vol. 21, part 4, pp. 737-760.
Bagnold, R.A.	1974	Fluid forces on a body in shear flow; experimental use of stationary flow. Proc. Roy. Soc. London, Series A, Vol. 340, pp. 147-171.
Batham, J.P.	1973	Pressure distributions on circular cylinders at critical Reynolds numbers. J. Fluid Mechanics, Vol. 57, pp. 209-229.
Bearman, P.W. and Zdravkovich, M.M.	1978	Flow around a circular cylinder near a plane boundary. J. Fluid Mechanics, Vol. 89, part 1, pp. 33-47.
Beattie, J.F., Brown, L.P. and Webb, B.	1971	Lift and Drag Forces on a Submerged Circular Cylinder. Offshore Technology Conference, Houston, Texas, Preprints, Vol. 1, pp. 319-328.

Bishop, R.E.D. and Hassan, A.Y. 1964 The Lift and Drag Forces on a Circular Cylinder in a Flowing Fluid. Proc. Royal Soc., London, Vol. 277A, pp. 32-50.

Blevins, R.D. 1977 Flow - Induced Vibration. Van Nostrand Reinhold, New York.

Brown, R.J. 1967 Hydrodynamic Forces on a Submarine Pipeline. ASCE, J. of the Pipeline Div., Vol. 93, No. PL1, pp. 9-19.

Buresti, G. 1983 Appraisal of Universal Wake Numbers From Data for Roughened Circular Cylinders. ASME, J. Fluids Eng., Vol. 105, pp. 464-468.

Cebeci, T and Bradshaw, P. 1977 Momentum Transfer in Boundary Layers. Hemisphere Publishing Corporation, Washington.

Celik, I. and Patel, V.C. 1982 Boundary - Layer Development on Circular Cylinders. Boundary - Layer Meteorology, Vol. 24, pp.281-293.

Celik, I., Patel, V.C. and Landweber, L. 1985 Calculation of the Mean Flow Past Circular Cylinders by Viscous-Inviscid Interaction. ASME, J. Fluids Eng., Vol. 107, pp. 218-223.

Coutanceau, M. and Bouard, R. 1977 Experimental determination of the main features of the viscous flow in the wake of a circular cylinder in uniform translation. Part 1. Steady Flow. J. Fluid Mechanics, Vol 79, part 2, pp. 231-256.

Dalton, C. and Chantranuvatana, B. 1980 Pressure Distribution Around Circular Cylinders in Oscillating Flow. ASME, J. Fluids Eng., Vol 102, pp. 191-195.

Dean, R.G. and Harleman, D.R.F. 1966 Interaction of Structures and Waves. Ippen, A.T. (Editor): Estuary and Coastline Hydrodynamics, McGraw-Hill Book Co., New York, London, pp. 341-403.

Font, J.B. 1967 Discussion of "Hydrodynamic forces on a Submarine Pipeline", by Brown, R.J. ASCE, J. of the Pipeline Div., Vol. 93, No. PL3, pp. 77-79.

Fredsoe, J. and Hansen, E.A. 1984 Lift forces on Pipelines in Steady Flow. Institute of Hydrodynamics and Hydraulic Eng., Technical Univ. of Denmark, DCAMM report 295.

Fredsoe, J., Sumer, B.M., Andersen, J. and Hansen, E.A. 1985 Transverse Vibrations of a Cylinder very close to a Plane Wall. Fourth International Offshore Mechanics and Arctic Eng. Symposium, Dallas, Texas, pp. 601-609.

Gerrard, J.H. 1961 An experimental investigation of the oscillating lift and drag of a circular cylinder shedding turbulent vortices. J. Fluid Mechanics, Vol. 11, pp. 244-256.

Goldstein, S. 1950 Modern Developments in Fluid Dynamics. 2 vols. University Press, Oxford.

Grace, R. 1975 Discussion of "Wave Forces on Cylinders near Plane Boundary", by Yamamoto, et al. ASCE, J. of the Waterways, Harbors and Coastal Eng. Div., Vol. 101, No. WW3, pp. 305-308.

Grass, A.J., Raven, P.W.J., Stuart, R.J. and Bray, J.A. 1984 The influence of boundary layer velocity gradients and bed proximity on vortex shedding from free spanning pipelines. Trans. ASME, Journal of Energy Resources Technology, Vol. 106, pp. 70-78.

Grove, A.S., Shair, F.H., Petersen, E.E. and Acrivos, A. 1964 An experimental investigation of the steady separated flow past a circular cylinder. J. Fluid Mechanics, Vol. 19, pp. 60-80.

Güven, O. , Farell, C. and Patel V.C. 1980 Surface-Roughness Effects on the Mean Flow Past Circular Cylinders. Journal of Fluid Mechanics, Vol. 98, pp. 673-701.

Güven, O., Patel, V.C. and Farell, C. 1975 Surface roughness effects on the mean flow past circular cylinders, Iowa Inst. Hydraulic Res. Rep. No. 175.

Güven, O., Patel, V.C. and Farell, C. 1977 A model for high-Reynolds-number flow past rough-walled circular cylinders. Trans. ASME I, J. Fluids Eng., Vol. 99, pp. 486-493.

Jeffreys, H. 1929 On the transport of sediment by streams. Proc. Camb. Philos. Soc., Vol. 25, pp. 272-276.

Jones, W.T. 1970 Forces on a Transverse Circular Cylinder in the Turbulent Boundary Layer of a Steady Flow. Ph.D. dissertation, Rice Univ., Houston, Texas.

Jones, W.T. 1971 Forces on Submarine Pipelines from Steady Currents. ASME, Petroleum Mech. Eng. with Underwater Technology Conference, Paper No. 71-UnT-3.

Jones, W.T. 1978 On-bottom Pipeline Stability in Steady Water Currents. J. Petroleum Technology, pp. 475-484.

Kacker, S.C., Pennington, B. and Hill, R.S. 1974 Fluctuating lift coefficient for a circular cylinder in cross flow. ASME, J. Mech. Eng. Science, Vol. 16, No. 4, pp. 215-224.

Larock, B.E. 1967 Discussion of "Hydrodynamic Forces on a Submarine Pipeline", by Brown, R.J., ASCE, J. of the Pipeline Div., Vol. 93, No. PL3, pp. 75-77.

Le Méhauté, B. 1976 An Introduction to Hydrodynamics and Water Waves. Springer Verlag, New York, Heidelberg, Berlin.

Littlejohns, P.S.G. 1972 Submarine Pipeline Research: Review of literature of lift and drag of cylinders in unidirectional flow. Hydraulics Research Station, Wallingford, Internal Report 109.

Littlejohns, P.S.G. 1974 Current-induced forces on Submarine Pipelines. Hydraulics Research Station, Wallingford, Internal Report 138.

Lugt, H.J. 1983 Vortex flow in Nature and Technology. John Wiley and Sons Inc., New York, London.

Masch, F.D. and Moore, W.L. 1960 Drag Forces in Velocity Gradient Flow. ASCE, J. Hydraulics Div., HY7, pp. 1-11.

Müller, W. 1929 Systeme von Doppelquellen in der ebenen Strömung, insbesondere die strömung um zwei kreiszylinder. Zeitschrift für angewandte mathematik und mechanik, Vol. 9, Deft 3, pp. 200-213.

Murphy, V.S. and Rose, W.C.	1978	Detailed Measurements on a Circular Cylinder in Cross Flow. Amer. Inst. of Aeronautics and Astronautics Journal, Vol. 16, No. 6, pp. 549-550.
Parkinson, G.V. and Jandali, T.	1970	A Wake Source Model for Bluff Body Potential Flow. Journal of Fluid Mechanics, Vol. 40, pp. 577-594.
Ramamurthy, A.M. and Ng, C.P.	1973	Effect of Blockage on Steady Force Coefficients. ASCE, J. of the Eng. Mech. Div., Vol. 99, No. EM4, pp. 755-772.
Roshko, A.	1961	Experiments on the Flow past a Circular Cylinder at very high Reynolds Numbers. J. Fluid Mechanics, Vol. 10, No. 3, pp. 345-356.
Roshko, A., Steinolfson, A., and Chattoorgoon, V.	1975	Flow forces on a cylinder near a wall or near another cylinder. Proc. 2nd US Conf. Wind Eng. Research, Fort Collins, paper IV-15.
Rotem, Z.	1967	The heated surface probe for measuring shear stress at the wall in laminar boundary layers. Canadian J. of Chemical Eng., Vol. 45, pp. 175-178.
Rouse, H.	1938	Fluid Mechanics for Hydraulic Engineers. McGraw-Hill Book Co., New York & London.
Rouse, H.	1946	Engineering Hydraulics. John Wiley and Sons, Inc., London.
Sarpkaya, T.	1976	Forces on cylinders near a plane boundary in a sinusoidally oscillating fluid. Trans. ASME, J. Fluids Eng., Vol. 98, pp. 499-505.

Sarpkaya, T. and Isaacson, M. 1981 Mechanics of wave forces on offshore structures. Van Nostrand Reinhold, New York.

Savkar, S.D., So, R.M.C. and Litzinger, T.A. 1980 Fluctuating Lift and Drag Forces induced on large span bluff bodies in a turbulent cross flow. ASME, Heat Transfer Div., Vol. 9, pp. 19-26.

Schlichting, H. 1979 Boundary Layer Theory. McGraw-Hill, New York, 7th ed.

Schrecker, A.M. 1978 Wave Forces on Submarine Pipelines: A Review. M.Sc thesis, University of Cape Town, South Africa.

Schubert, G. 1967 Viscous flow near a cusped corner. J. Fluid Mechanics, Vol. 27, part 4, pp. 647-656.

Shaw, T.L. 1971 Effect of side walls on flow past bluff bodies. ASCE, J. Hydr. Div., Vol. 97, HY1, pp. 65-79.

Sheddin, R. and Lin, S.P. 1983 Drag-force fluctuation on a cylinder. J. Fluid Mechanics, Vol. 127, pp. 443-452.

Smith, C. 1969 An Experimental Investigation of the Variation with water depth of Lift and Drag Coefficients of a body on or near the bottom of a flowing stream. M.Sc thesis, Rice University, Houston, Texas.

Smith, C. 1971 The influence of the interaction between wake and free surface on hydrodynamic drag forces. Ph.D. thesis, Rice University, Houston, Texas.

Sutko, A.A. 1967 Discussion of "Hydrodynamic Forces on a Submarine Pipeline", by Brown, R.J. ASCE, J. of the Pipeline Div., Vol. 93, No. PL3, pp. 79-80.

Taneda, S	1965	Experimental investigation of vortex streets. J. Phys. Soc. Japan, Vol. 20, No. 9, pp. 1 714-1 721.
Tanida, Y., Okajima, A. and Watanabe, Y.	1973	Stability of a circular cylinder oscillating in uniform flow or in a wake. J. Fluid Mechanics, Vol. 61, part 4, pp. 769-784.
Thomschke, H.	1971	Experimentelle Untersuchung der stationären Umströmung von Kugel und Zylinder in Wandnähe. (An experimental investigation of the stationary flow around spheres and cylinders close to a wall). Ph.D. dissertation, Faculty of Mech. Eng., Karlsruhe University.
Townsend, D.R. and Farley, D.W.	1973	Design Criteria for Submarine Pipeline Crossings. ASCE, J. Hydraulics Div., Vol. 99, No. HY10, pp. 1 659-1 673.
Tritton, D.J.	1959	Experiments of the flow past a circular cylinder at low Reynolds numbers. J. Fluid Mechanics, Vol. 6, pp. 547-567.
Vennard, J.K. and Street, R.L.	1976	Elementary Fluid Mechanics, 5th edition, John Wiley & Sons, Inc., New York, London, Sydney, Toronto.
Wilson, B.W. and Reid, R.O.	1963	Discussion of "Wave Force Coefficients for Offshore Pipelines", by Beckmann and Thibodeaux, ASCE, J. of the Waterways and Harbors Div., Vol. 89, No. WW1, pp. 61-65.

Wilson, J.F. and Caldwell, H.M.	1971	Force and Stability Measurements on Models of Submerged Pipelines. ASME, Journal of Eng. for Industry, pp. 1 290-1 298.
Wright, J.C. and Yamamoto, T.	1979	Wave Forces on Cylinders near Plane Boundaries. ASCE, J. of the Waterways, Harbors and Coastal Eng. Div., Vol. 105, No. WW1, pp. 1-13.
Yamamoto, T., Nath, J.H. and Slotta, L.S.	1974	Wave Forces on Cylinders near Plane Boundary. ASCE, J. of the Waterways, Harbors and Coastal Eng. Div., Vol. 100, No. WW4, pp. 345-359.
Yamamoto, T., Nath, J.H. and Slotta, L.S.	1976	Final discussion of "Wave Forces on Cylinders near Plane Boundary". ASCE, J. of the Waterways, Harbors and Coastal Eng. Div., Vol. 102, No. WW2, pp. 275-277.
Zdravkovich, M.M.	1985	Forces on a circular cylinder near a plane wall. Applied Ocean Research, Vol. 7, No. 4, pp. 197-201.

B. References not actually consulted

Celik, I 1980 Mean Flow Past Circular Cylinders. Ph.D. thesis, Dept. of Mechanics and Hydraulics, Univ. of Iowa, Iowa City, Iowa.

Dementiev 1934 Transactions, Science Research Inst. of Hydrotechnics, Vol. 12, Leningrad.

Dvorak, F.A., Maskew, B. and Rao, B.M. 1979 An investigation of Separation Models for the Prediction of C_{Lmax}. Final Technical Report, Contract, DAAG 29-76-C-0019, Analytical Methods, Inc., Bellevue, Washington.

Flachsbart, O. 1932 Winddruck auf Gasbehälter. Reports of the AVA in Göttingen, IVth Series, pp. 134-138.

Göktun, S. 1975 The Drag and Lift Characteristics of a Cylinder Placed near a Plane Surface. M.Sc thesis, US Naval Postgraduate School, Monterey, California.

Haffen, B. 1975 Forces on a Transverse Circular Cylinder in a Steady Uniform Flow near a Plane Boundary. M.Sc thesis, Oregon State University.

Hama, F.R. 1954 Boundary-Layer Characteristics of Smooth and Rough Plates. Trans. Soc. of Naval Architects and Marine Engineers, Vol.62, p. 333.

Hinze, J.O. 1959 Turbulence, An Introduction to its Mechanism and Theory. McGraw-Hill Book Co., New York.

Homann, F. 1936 Einfluss grosser Zähigkeit bei Strömung um Zylinder. Forschg. Ing.-Wes. 7, pp.1-10.

Hydraulics Research Station	1961	Submarine Pipelines. An investigation into drag and lift at high Reynolds numbers. HRS, Wallingford, Report No. 168.
Keulegan, G.H. and Carpenter, L.H.	1958	Forces on Cylinders and Plates in an Oscillating Fluid. J. of Research of the National Bureau of Standards, Vol. 60, No.5, pp. 423-440.
Knoblock and Troller		Tests on the Effect of Sidewind on the Ground Handling of Airships. Report of tests conducted at the Daniel Guggenheim Airship Institute.
Murphy, J.C.	1966	The Effects of Non-steady Flow on the Pressure Distribution About a Circular Cylinder. Thesis, US Naval Postgraduate School, Monterey, California.
Schiller, F.C.	1971	Wave Forces on a Submerged Horizontal Cylinder. M.Sc thesis, US Naval Postgraduate School, Monterey, California.
Stratford, B.S.	1959	The Prediction of Separation of the Turbulent Boundary Layer. Journal of Fluid Mechanics, Vol. 5, pp. 1-16.
Townsend, A.A.	1962	The Behaviour of a Turbulent Boundary Layer near Separation. Journal of Fluid Mechanics, Vol. 21, pp. 536-554.
Yamamoto, T., Nath, J.H. and Slotta, L.S.	1973	Yet Another Report on Cylinder Drag or Wave Forces on Horizontal Submerged Cylinders. Engineering Experiment Station Bulletin No.47, Oregon State University, Corvallis, Oregon.

APPENDIX 1 - COMPUTER PROGRAMS

To calculate the lift and drag forces generated, as well as all the actual flow velocity values, for each of the 134 test runs, relatively simple computer programs were written in BASIC. The programs are shown in Tables A1.1 and A1.2. A Tektronix 4052 micro computer was utilised to execute the programs.

A pressure integration method was applied to compute the drag and lift forces; 36 pressure readings had to be keyed in per test run. A sample solution is indicated in Table 5.2.

The simple flow velocity program was necessary to produce flow velocity distribution profiles for the various approach flows in the flume; some velocity profiles are shown in Figs. 5.32 to 5.36.

```
100 INIT
110 SET DEGREES
120 PAGE
130 DIM A(36)
140 L=36
150 FOR I=1 TO L
160 PRINT
170 PRINT "ANGLE: ";I*10-10;"    MASS ?"
180 INPUT A(I)
190 NEXT I
200 PAGE
210 PRINT "ANGLE","MASS "
220 PRINT
230 FOR I=1 TO L
240 PRINT I*10-10,A(I)
250 NEXT I
260 PRINT
270 PRINT "DO YOU WANT TO CHANGE ANY MASS  ?  (Y/N)    "
280 INPUT O$
290 IF O$<>"Y" THEN 350
300 PRINT "AT WHICH ANGLE?"
310 INPUT A6
320 PRINT "CORRECT  MASS ?"
330 INPUT A((A6+10)/10)
340 GO TO 200
350 S1=0
360 S2=0
370 PAGE
380 AXIS @1:20,5,0,10
390 PRINT @41:
400 PRINT @41:
410 PRINT @41: USING 420:"ANGLE","MASS","HEAD","H SIN B","H COS B"
420 IMAGE 8A , 4(10A)
430 B=PI*44.7*44.7/400
440 PRINT @41:
450 MOVE @1:0,A(1)/B
460 FOR I=1 TO L
470 C=I*10-10
480 PRINT @41: USING 490:I*10-10,A(I),A(I)/B,A(I)/B*SIN(C),A(I)/B*COS(C)
490 IMAGE 3D,4(6D.3D)
500 REM CALCULATE TOTALS
510 S1=S1+A(I)/B*SIN(C)
520 S2=S2+A(I)/B*COS(C)
530 REM PLOT GRAPH
540 DRAW @1:(I-1)*3,A(I)/B*3
550 NEXT I
560 PRINT @41:
570 PRINT @41: USING 580:"TOTALS : ",S1,S2
580 IMAGE 15T,9 A,2(6D.3D)
590 PRINT @41:
600 PRINT @41:
610 D=2.6*PI*9.81/180
620 PRINT @41: USING 640:"LIFT FORCE :  ";S1*D
630 PRINT @41: USING 640:"DRAG FORCE : ";S2*D
640 IMAGE 15A,4D.3D
650 END
```

TABLE A1.1: COMPUTER PROGRAM FOR DETERMINATION OF LIFT AND DRAG FORCES

APPENDIX 2 - DETAILS OF LINEAR REGRESSION LINE ANALYSIS

To draw the best line through the points plotted for a number of the relationships represented graphically in Chapters 5,6 and 8, linear regression line (least squares straight-line) analyses were carried out. A Lotus 1-2-3 software package (Version 2, 1985) was used. The equation of the regression line is $y = mx + c$, where m is the gradient coefficient and c the y-intercept constant. The various m and c values calculated are indicated below. Details on the standard errors of estimate are available from the author.

Figure	Line	Gradient coefficient m	Constant c
5.37	C_D/a_1 : smooth cyl.	- Ø,ØØØ Ø64 44	2,2112
	rough cyl.	- Ø,ØØØ Ø65 46	2,5994
	C_D : smooth cyl.	- Ø,ØØØ Ø45 78	1,7983
	rough cyl.	- Ø,ØØØ Ø43 33	2,Ø443
5.38	5Ø mm cyl.: smooth	- Ø,ØØØ Ø35 6	2,2166
	rough	- Ø,ØØØ Ø39 67	2,2925
	3Ø mm cyl.: smooth	- Ø,ØØØ Ø64 44	2,2112
	rough	- Ø,ØØØ Ø65 46	2,5994
5.39	5Ø mm cyl.: smooth	- Ø,ØØØ Ø91 189	3,4583
	rough	- Ø,ØØØ 1Ø4 3	3,8Ø8
	3Ø mm cyl.: smooth	- Ø,ØØØ 117 145	2,69782
	rough	- Ø,ØØØ 156 532	3,3151
5.4Ø	C_L/a_1 : smooth cyl.	- Ø,ØØØ Ø42 39	1,3823
	rough cyl.	- Ø,ØØØ Ø44 6	1,4573
	C_L : smooth cyl.	- Ø,ØØØ Ø3Ø 69	1,1259
	rough cyl.	- Ø,ØØØ Ø32 89	1,1745
5.41	smooth cyl.	Ø,ØØØ ØØ3 617 7	1,Ø866
	rough cyl.	- Ø,ØØØ ØØ1 Ø75 9	1,3253

Figure	Line	Gradient coefficient m	Constant c
5.42	smooth cyl.	Ø,ØØØ ØØ9 379	Ø,2Ø22
	rough cyl.	- Ø,ØØØ Ø27 67	1,5452
5.43	G/D = Ø,314; smooth bed	- Ø,ØØØ 118 54	3,7Ø36
	= 2,484; smooth bed	- Ø,ØØØ Ø59 72	2,7277
	= Ø,314; rough bed	Ø,ØØØ ØØ3 229	1,6894
	= 2,Ø25; rough bed	- Ø,ØØØ Ø24 7Ø	1,9884
5.44	G/D = Ø	Ø,ØØØ ØØ3 618	1,Ø866
	= Ø,2	- Ø,ØØØ Ø25 978	Ø,7813
	= Ø,6	- Ø,ØØØ ØØØ 913 6	Ø,Ø537
5.45	G/D = Ø	- Ø,ØØØ Ø44 6	1,4573
	= Ø,314	Ø,ØØØ Ø1Ø Ø3	Ø,Ø112
	= 2,484	Ø,ØØØ ØØ7 672	- Ø,1422
5.52	G/D = Ø (5Ø mm cyl.)	- Ø,ØØØ Ø23 466 2	1,Ø721
	= Ø,1	Ø,ØØØ Ø57 889 8	- Ø,Ø649
	= Ø,333	Ø,ØØØ Ø62 692 9	- Ø,2395
	= 1,2	Ø,ØØØ Ø72 557	- Ø,4944
	= 2,67	Ø,ØØØ 1Ø3 492 9	- Ø,7898
	= Ø (3Ø mm cyl.)	Ø,ØØØ Ø27 233 6	Ø,ØØ936
5.53	G/D = Ø (5Ø mm cyl.)	- Ø,ØØØ Ø68 557 9	- Ø,Ø711
	= Ø,1	Ø,ØØØ Ø97 293 1	- 3,2251
	= Ø,2	Ø,ØØØ Ø93 529 6	- 3,1835
	= Ø,333	Ø,ØØØ ØØ5 894	- 1,6426
	= 1,2	Ø,ØØØ Ø79 312 3	- 3,2155
	= 2,67	Ø,ØØØ Ø9Ø 851 4	- 2,8662
	= Ø (3Ø mm cyl.)	Ø,ØØØ Ø57 692 5	- 1,6313

Figure	Line	Gradient coefficient m	Constant c
5.54	G/D = Ø (3Ø mm cyl.)	Ø,ØØØ Ø55 287	- 1,4863
	= Ø (5Ø mm cyl.)	-Ø,ØØØ Ø33 351 2	- Ø,3834
	= Ø,1	Ø,ØØØ Ø9Ø 443	- 2,8645
	= Ø,2	Ø,ØØØ 173 219 4	- 4,5666
	= 1,2	Ø,ØØØ Ø93 673	- 3,341
	= 2,67	Ø,ØØØ Ø97 413 5	- 2,8539
5.55	G/D = Ø; smooth cyl.	- Ø,ØØØ Ø33 351 2	- Ø,3834
	= Ø; rough cyl.	Ø,ØØØ Ø25 13Ø 2	- 1,3999
	= 1,2; smooth cyl.	Ø,ØØØ Ø93 673	- 3,34Ø9
	= 1,135; rough cyl.	Ø,ØØØ Ø35 449 5	- 2,1Ø74
5.56	G/D = Ø; smooth cyl.	Ø,ØØØ Ø55 281	- 1,48636
	= Ø; rough cyl.	Ø,ØØØ Ø77 733 7	- 2,3725
	= 2,67; smooth cyl.	Ø,ØØØ Ø97 413 5	- 2,8539
	= 2,484; rough cyl.	Ø,ØØØ Ø99 4Ø3 3	- 3,1839
5.58	G/D = Ø; smooth cyl.	Ø,ØØØ Ø35 Ø61 1	- Ø,3Ø827
	= Ø; rough cyl.	Ø,ØØØ Ø18 732 5	+ Ø,36462
	= 1,2; smooth cyl.	Ø,ØØØ Ø14 274 3	- Ø,12384
	= 1,135; rough cyl	Ø,ØØØ Ø3Ø 367 2	- Ø,43507
5.59	C_D/a_1 vs. G/δ (up to G/D = Ø,4)	1,544 857 5	1,4571
6.3	C_D : direct measurement	- Ø,ØØØ Ø27 855	1,8733
	pressure integration	- Ø,ØØØ Ø21 Ø4	1,638
	C_D/a_1 : direct measurement	- Ø,ØØØ 341 96	2,3173
	pressure integration	- Ø,ØØØ Ø35 6	2,2166

Figure	Line	Gradient coefficient m	Constant c
6.4	direct measurement	- Ø,ØØØ Ø25 84	2,2355
	pressure integration	- Ø,ØØØ Ø75 33	3,Ø734
6.5	direct measurement	- Ø,ØØØ ØØ4 663	2,1623
	pressure integration	Ø,ØØØ Ø1Ø 77	1,6981
6.6	direct measurement	- Ø,ØØØ Ø8Ø 18	2,6861
	pressure integration	Ø,ØØØ ØØ9 469 5	1,6359
6.7	direct measurement	- Ø,Ø46 42	2,Ø357
	pressure integration	+ Ø,1Ø5 952	1,6795
6.8	Direct: G/D = Ø	- Ø,ØØØ Ø11 722 1	1,2311
	= Ø,2	- Ø,ØØØ ØØ9 84Ø 6	Ø,3962
	= Ø,6	- Ø,ØØØ ØØ4 642 5	Ø,1938
	Indirect: G/D = Ø	Ø,ØØØ ØØ3 617 7	1,Ø866
	= Ø,2	- Ø,ØØØ ØØ4 618 1	Ø,3484
	= Ø,6	- Ø,ØØØ ØØØ 913 6	Ø,Ø537
8.5	5Ø mm cylinder	Ø,ØØØ Ø26 878	5,912
	3Ø mm cylinder	Ø,ØØØ 193 Ø11	7,493
8.6	5Ø mm cylinder	Ø,ØØØ 119	2,525
	3Ø mm cylinder	Ø,ØØØ Ø86	4,928
8.7	3Ø and 5Ø mm cylinder	- Ø,ØØØ ØØØ 114 2	1,4953
8.8	5Ø mm cylinder	- Ø,ØØØ Ø16 98	1,468
	3Ø mm cylinder	- Ø,ØØØ Ø42 39	1,382

19 JAN 1989